

12-2013

Systematic parameter analysis for selective laser melting (SLM) of silver-based materials.

Harald Rieper, 1979-
University of Louisville

Follow this and additional works at: <https://ir.library.louisville.edu/etd>



Part of the [Industrial Engineering Commons](#)

Recommended Citation

Rieper,, Harald 1979-, "Systematic parameter analysis for selective laser melting (SLM) of silver-based materials." (2013). *Electronic Theses and Dissertations*. Paper 1205.
<https://doi.org/10.18297/etd/1205>

This Doctoral Dissertation is brought to you for free and open access by ThinkIR: The University of Louisville's Institutional Repository. It has been accepted for inclusion in Electronic Theses and Dissertations by an authorized administrator of ThinkIR: The University of Louisville's Institutional Repository. This title appears here courtesy of the author, who has retained all other copyrights. For more information, please contact thinkir@louisville.edu.

SYSTEMATIC PARAMETER ANALYSIS FOR SELECTIVE LASER MELTING
(SLM) OF SILVER-BASED MATERIALS

By

Harald Rieper

Dipl.-Ing. (FH), Aachen University of Applied Sciences, Aachen, Germany, 2006

MBA, Aachen University of Applied Sciences, Aachen, Germany, 2008

A Dissertation

Submitted to the Faculty of the

J.B. Speed School of Engineering of the University of Louisville

In Partial Fulfillment of the Requirements

For the Degree of

Doctor of Philosophy

Department of Industrial Engineering

Speed School of Engineering

University of Louisville

Louisville, Kentucky

December 2013

Copyright 2013 by Harald Rieper

All rights reserved

SYSTEMATIC PARAMETER ANALYSIS FOR SELECTIVE LASER MELTING
(SLM) OF SILVER-BASED MATERIALS

By

Harald Rieper

Dipl.-Ing. (FH), Aachen University of Applied Sciences, Aachen, Germany, 2006

MBA, Aachen University of Applied Sciences, Aachen, Germany, 2008

A Dissertation approved on

August 26, 2013

By the following Dissertation Committee:

Dissertation Director: Dr. Brent Stucker

Dr. Andreas Gebhardt

Dr. Gail W. DePuy

Dr. Thomas Starr

DEDICATION

This PhD dissertation is dedicated to my parents

Mrs. Margret Katharina Rieper

And

Mr. Hermann Johann Josef Rieper (†1996)

Who supported me in my education with their invaluable love.

ACKNOWLEDGEMENTS

I would like to thank my major professors Dr. Brent E. Stucker and Dr. Andreas Gebhardt for their guidance and patience. I would also like to thank the other committee members Dr. Gail DePuy and Dr. Thomas Starr for their support. I would also like to express my thanks to my partner in life Dr. Janine Hellenbrand, for her understanding and patience during those times when there was no light at the end of anything. Also, many thanks to everyone from Aachen University of Applied Sciences who supported me in running the tests series like Dr. Gereon Elbers, Ms. Mirjam Knothe, Ms. Miranda Fateri, Mr. Frank-Michael Schmidt, Mr. Hans Lingers, Mr. Andreas Vollmann, Mr. Ulrich Figge, Dr. Stephan Kallweit and especially Mr. Prasanna Rajaratnam and Mr. Alexander Schwarz. Thanks to the faculty members of the University of Louisville for the support during the studies and courses. Furthermore, I would like to thank Mr. Horst Reichert from Micromeritics Analytical Service Europe, Mr. Ellwyn Purrio from ISF Aachen and everyone else who contributed to my work and is not mentioned here.

ABSTRACT
SYSTEMATIC PARAMETER ANALYSIS FOR SELECTIVE LASER MELTING
(SLM) OF SILVER-BASED MATERIALS

Harald Rieper

August 26, 2013

Selective Laser Melting (SLM) is a growing technology for the additive manufacturing of parts and structures. Based on a powder layer technique, a laser locally melts the powder and forms new structures. [1] In this approach, silver-based alloy powders will be used. The processing of this kind of material is considered difficult compared to other powder materials such as mild steels or tool steels. Silver powder is a highly reflecting material and has excellent thermal conductivity. Both properties make it difficult to process using Selective Laser Melting. Due to its high price, industries use silver parts as economically as possible so that the parts tend to be thin and light weight. Therefore, one limiting constraint should be the manufacturing of thin, hollow parts. The second constraint is the usage of a laser with small power output. The reasons why this machine will be used is that it is affordable for a large amount of companies, that it can be placed nearly everywhere and that it economically beats large workshops with cast and milling facilities. Since AgCu7 is a typical artwork material and AgCu28 is a typical technical material, this work is related to further

research on the processing of both materials. Processing maps were developed using the response surface method.

The dissertation covers the questions why silver is used, what was done, which methods are available to answer upcoming questions and which solutions are proposed. Chapter one provides an introduction to the topic. Chapter two covers information that is available about different precious materials, physical relations and other aspects that are necessary to understand what happens in the melt pool. Chapter three deals with important parameters and collects some fundamental approaches to uncover new relations. Chapter four shows the pretests, powder distributions, absorptivity measurements, and necessary steps to manufacture hollow structures. In chapter five, six, and seven the experiments for AgCu7 and AgCu28 are described. Factorial designs and the response surface method were used in order to analyze the dependency of process parameters on porosity. In chapter eight, the results of the materials are compared. Chapter nine presents the summary and future perspectives.

TABLE OF CONTENT

DEDICATION	iii
ACKNOWLEDGEMENTS.....	iv
ABSTRACT	v
LIST OF TABLES	xiii
LIST OF FIGURES	xvi
LIST OF EQUATIONS.....	xxiv
1 INTRODUCTION	1
1.1 Scope	1
1.2 Changes in industries caused by additive manufacturing	2
1.3 Selective Laser Melting process	4
1.4 Silver as a material with special properties	6
1.4.1 Relation to industry sectors	7
1.4.2 Example: Manufacturing of conductors for flexible solar cells	7
1.4.3 Medical applications	8
1.5 New possibilities for artificial designs.....	8
2 LITERATURE REVIEW	9
2.1 State of the art	9
2.2 SLM of non-precious metals	9

2.2.1	Research about high alloy steels and tool steels	9
2.2.2	Investigations related to titanium and its alloys.....	13
2.2.3	Research into copper-based materials	15
2.2.4	Research into aluminum-based materials.....	17
2.2.5	Research into nickel-based materials	17
2.3	SLM of precious materials	18
2.3.1	Research related to gold.....	18
2.4	Research related to silver and its alloys	20
2.5	Research generally related to the SLM process	21
2.5.1	Investigations related to powder physics	22
2.5.2	Research into binding mechanisms	25
2.6	Research related to parameter analysis	26
2.7	Research related to DoE approaches.....	28
2.8	Research related to additive manufacturing and FEA.....	31
2.9	Research related to thermal and electrical conductivity.....	33
2.9.1	Investigations about conductive material	33
2.10	Reflectivity and absorbtion rates.....	38
2.11	Summary of findings.....	38
3	FUNDAMENTAL STEPS IN SILVER PROCESSING	40

3.1	Physical properties about silver and its alloys	40
3.2	SLM approaches.....	42
3.2.1	Realizer SLM 50	42
3.3	Path to thin walled, hollow parts	43
3.4	Design of experiments to detect parameter fields.....	44
3.4.1	Supply of powders and machinery.....	45
4	PRETESTS.....	48
4.1	Material AgCu7 from literature.....	48
4.2	Material AgCu28 from literature.....	49
4.3	Particle distribution tests for AgCu7.....	49
4.3.1	Particle diameter test description.....	50
4.3.2	Particle diameter tests for AgCu28	57
4.4	Absorption tests.....	61
4.5	EDX Analysis.....	65
4.6	SEM Analysis	67
4.7	Evaluation of first tracks.....	70
4.8	Manufacturing of hollow section parts.....	72
5	SCREENING EXPERIMENTS WITH AGCU7	74
5.1	Test set up.....	74

5.2	Parameter fields.....	77
5.3	Limits of scan speed and linear energy density	79
5.4	Analysis of produced samples- microscopy.....	83
5.4.1	Measurement of surface porosity	83
5.5	Microsections - sample preparation.....	85
5.6	Factorial design - definitions	88
5.6.1	ANOVA	89
5.7	Data analysis	91
5.7.1	Data analysis of test series 1	91
5.7.2	Model adequacy checking	93
5.7.3	Data analysis of test series 2, 3, and 4 - failed parts	103
5.7.4	Test series 2, 3, and 4	105
5.7.5	Model adequacy checking of test series 2, 3, 4	106
5.8	Microscopy	112
5.8.1	Test series 2	113
5.8.2	Test series 3	117
5.8.3	Test series 4	120
5.8.4	Results and conclusion of the screening experiments.....	123
5.8.5	Test series 5	124

5.8.6	Test series 6	130
5.8.7	Test series 7	131
5.8.8	Test series 8	133
5.8.9	Results and conclusion of experiments 5 to 8:	135
6	RESPONSE SURFACE METHOD AGCU7	136
6.1	Theoretical background	136
6.2	Model and data points for test series 9	138
6.3	Responses.....	143
7	RESPONSE SURFACE METHOD AGCU28.....	150
7.1	Screening experiments for AgCu28.....	150
7.1.1	Test series 10	150
7.1.2	Test series 11	156
7.2	Response surface for AgCu28.....	158
7.3	Responses.....	164
8	COMPARISON OF AGCU7 AND AGCU28	170
8.1	T-test on means.....	170
8.2	Process maps.....	174
9	SUMMARY AND FUTURE PERSPECTIVE, CONCLUSIONS	177

9.1	Summary and findings	177
9.2	Future work.....	182
	REFERENCES.....	185
	APPENDICES	196
	Symbols and explanations	196
	Narrow paths.....	200
	Selective Laser Melting process.....	202
	Measurement of laser power	203
	Preparation of powder for additional test runs.....	204
	Manufacturing of silver powder	205
	Comparison of dimensions.....	207
	CURRICULUM VITAE	208

LIST OF TABLES

Table 1: Absorption rates and thermal conductivities - literature values.....	38
Table 2: Electrical and thermal properties of silver [93] [90]	40
Table 3: Mechanical properties; tensile strength of silver [93]	40
Table 4: Mechanical properties; elongation of silver [93].....	41
Table 5: Other properties of silver [93]	41
Table 6: Fundamental data of SLM 50 [95] [96].....	42
Table 7: Fundamental parameter overview	45
Table 8: Some powder suppliers	46
Table 9: Some machinery suppliers	47
Table 10: Chemical analysis (spectrum) of AgCu7.....	68
Table 11: Chemical analysis (spectrum) of AgCu28.....	70
Table 12: Summary of scan speeds	83
Table 13: Data for AgCu7-screening test series 1:.....	91
Table 14: Run order scheme for test series 1	92
Table 15: Factors and levels for test series 1	96
Table 16: MINITAB output for ANOVA test series 1	97
Table 17: Parameters of selected samples (figure 52)	102

Table 18: Data for test series 2, 3, and 4.....	105
Table 19: Model of test series 2, 3, 4.....	110
Table 20: ANOVA output for test series 2,3,4.....	110
Table 21: Parameters of selected tracks (figure 61)	114
Table 22: Parameters of selected tracks (figure 62)	115
Table 23: Parameters of selected samples (figure 63)	118
Table 24: Parameters of selected samples (figure 64)	118
Table 25: Parameters of the scan tracks in figure 65	121
Table 26: Parameters of test series 4, 60 μm (figure 66).....	121
Table 27: Parameters of test series 5, 30 μm (figure 69).....	126
Table 28: Parameters of test series 5, 60 μm (figure 70).....	128
Table 29: Parameters of test series 6 (figure 71).....	130
Table 30: Parameters of test series 7 (figure 72).....	132
Table 31: Parameters of test series 8, 30 μm (figure 73).....	133
Table 32: Parameters of test series 8, 60 μm (figure 74).....	134
Table 33: Initial parameters for the model of the response surface	138
Table 34: Factorial design collection sheet in order to analyze the factors to be included in the model.....	140
Table 35: MINITAB output: estimated regression coefficients for porosity [%] .	141

Table 36: MINITAB output: ANOVA of response surface AgCu7	142
Table 37: Parameters of test series 10, 30 μm layer thickness (figure 83)	152
Table 38: Parameters of test series 10, 60 μm layer thickness (figure 84)	155
Table 39: Parameters of test series 11, 30 μm layer thickness (figure 85)	156
Table 40: Parameters of test series 11, 60 μm layer thickness (figure 86)	157
Table 41 : Factors and levels of the response surface AgCu28	158
Table 42: Data of response surface for AgCu28.....	160
Table 43: MINITAB output: Estimated Regression Coefficients for porosity [%]162	
Table 44: MINITAB output: ANOVA of response surface AgCu28	163
Table 45: MINITAB output: unusual observations for porosity [%].....	163
Table 46: MINITAB output: two sample T-test.....	172
Table 47: Chemical elements	196
Table 48: Greek letters	196
Table 49: Units	197
Table 50: Abbreviations	197

LIST OF FIGURES

Figure 1: Scheme of the SLM process	5
Figure 2: Conductivity of typical conductor materials [82].....	35
Figure 3: Development of silver and copper prices 2011-2013 [83-86]	36
Figure 4: Comparison of thermal and electrical properties as a function of temperature [89, 90]	37
Figure 5: Realizer SLM 50 desktop machine	43
Figure 6: Alloy phase diagram system AgCu [100].....	48
Figure 7: Data derived from powder supplier, AgCu7	50
Figure 8: Laser fraction measurement (left) and X-ray sedimentation measurement.....	51
Figure 9: Empirical cumulative distribution function of particle diameter, coarse powder, AgCu7, laser fraction	52
Figure 10: Scatterplot of particle diameter distribution, coarse powder, AgCu7, laser fraction	53
Figure 11: Scatterplot of particle diameter distribution, fine powder, AgCu7, laser fraction.....	54
Figure 12: CDF of particle diameter, fine powder, AgCu7, laser fraction.....	55

Figure 13: Plot of particle distribution, fine powder, AgCu7, sedimentation technology	56
Figure 14: Plot of CDF, fine powder, AgCu7, sedimentation technology	57
Figure 15: Plot of particle distribution, AgCu28, sedimentation technology	58
Figure 16: Plot of particle distribution, AgCu28, laser fraction	59
Figure 17: Plot of CDF, AgCu28, sedimentation technology	59
Figure 18: Plot of CDF, AgCu28, laser fraction.....	60
Figure 19: Ulbricht ball and Michelsen interferometer	61
Figure 20: Absorbance measured for the test probes AgCu7 and AgCu28.....	62
Figure 21: Absorption rates, literature values [5, 39, 91] compared with experimental measurements	64
Figure 22: SEM and EDX analyzer Gemini LEO 1530	65
Figure 23: Spectrum of AgCu7	66
Figure 24: Spectrum of AgCu28	67
Figure 25: SEM of AgCu7, topography, magnification 500-fold.....	68
Figure 26: SEM of AgCu28, topography, magnification 500-fold.....	69
Figure 27: Wedge and ring [110] and [104]	72
Figure 28: Silver Nefertiti, manufactured at Aachen University of Applied Sciences.....	73

Figure 29: Arrays for test series 3 and 4, separated into 30 μm and 60 μm layer thickness	75
Figure 30: Unused, milled base plates (copper left, stainless steel 1.4301 right) 76	
Figure 31: Example of manufactured parts after cleaning, test series 1, 30 μm layer thickness.....	77
Figure 32: AgCu7- proportional scheme of overlapped spot distances for spot distances = 5 μm , 7 μm , 15 μm , 20 μm (top down)	78
Figure 33: Scheme of exposures, peak time per spot for a pulse time = 20 μs , 40 μs , 80 μs (from left to right) and spot distances = 5 μm , 7 μm , 15 μm , 20 μm (top down).....	79
Figure 34: Mean speeds for 20 μs pulse time.....	80
Figure 35: Regression of scan speed (scheme)	80
Figure 36: Mean speeds for 40 μs pulse time.....	81
Figure 37: Mean speeds for 60 μs pulse time.....	82
Figure 38: Mean speeds for 80 μs pulse time.....	82
Figure 39: Digital microscope Keyence VHX-100, VH-Z20 with inspection software.....	84
Figure 40: Scheme of optical inspection.....	84
Figure 41: Example of optical inspection, test series 3.1, specimen 6, spot OM	85
Figure 42: Spots for porosity measurements (a-d)	87

Figure 43: Sample of image processing	87
Figure 44: a) Outer boundary removed b) test area c) inner boundary removed	88
Figure 45: Normal probability plot of the residuals.....	93
Figure 46: Histogram of the residuals, test series 1.....	94
Figure 47: Residuals versus fitted values, test series 1	95
Figure 48: Residuals versus the order of the data	96
Figure 49: Histogram of surface porosity, AgCu7, test series 1	99
Figure 50: Main effect plot of test series 1, AgCu7	100
Figure 51: Interaction plot for surface porosity.....	101
Figure 52: Selected samples of test series 1: a) run order 2, b) run order 16, c) run order 19, d) run order 20	102
Figure 53: Scatter plot of failed parts test series 2-4, AgCu7	103
Figure 54: Scatter plot of failed parts, test series 2-4, power vs. preexposure and scan speed	104
Figure 55: Histogram of standardized residuals, test series 2, 3, 4	106
Figure 56: Normal probability plot of standardized residuals, test Series 2, 3, 4	107
Figure 57: Run order plot of test series 2, 3, and 4.....	108
Figure 58: Plot of Standardized Residuals versus Fitted Values	109
Figure 59: Interaction plot of test series 2, 3, 4.....	111
Figure 60: Main effects plot for test series 2, 3, 4	112

Figure 61: Selected tracks, test series 2 a) 06, b) 27, c) 24, d) 26, e) 18, f) 04, g) 15, h) 31, i) 14, j) 03, k) 23	113
Figure 62: Selected tracks, test series 2 a) 19, b) 10, c) 30, d) 09, e) 29, f) 12, g) 32, h) 21, i) 01, j) 02.	115
Figure 63: Selected samples of test series 3 a) 25, b) 28, c) 22, d) 27, e) 32, f) 16, g) 03, h) 26, i) 04, j) 21, k) 29, l) 06.	117
Figure 64: Selected samples of test series 3 a) 01 b) 10, c) 13, d) 08, e) 09, f) 18.	119
Figure 65: Selected tracks, test series 4 a) 06, b) 27, c) 24, d) 26, e) 16, f) 13, g) 18, h) 04, i) 15, j) 31, k) 14, l) 07, m) 08, n) 03, o) 23	120
Figure 66: Selected samples, test series 4, 60 μm layer thickness a) 22, b) 19, c) 10, d) 30, e) 25, f) 09, g) 29, h) 12, i) 32, j) 21, k) 01, l) 02.	122
Figure 67: Schematic comparison of test series 1-4 and test series 5.....	124
Figure 68: Example of a hollow cube, 10 offsets, height 10 mm.....	125
Figure 69: Selected samples, test series 5 a) 01-21, b) 01-12, c) 01-16, d) 01-23, e) 01-7, f) 01-29, g) 01-02, h) 01-08.	127
Figure 70: Selected samples, test series 5, 60 μm , a) 1-28, b) 1-17, c) 1-26, d) 1-19, e) 1-22, f) 1-9.....	129
Figure 71: Selected samples, test series 6: a) 2-6, b) 2-24, c) 2-4, d) 2-31, e) 2-3.	131
Figure 72: Selected samples, test series 7 a) 3-16, b) 3-26, c) 3-21, d) 3-6.....	132
Figure 73: Selected samples, test series 8, 30 μm layer thickness a) 4-24, b) 4-16, c) 4-13, d) 4-31.....	133

Figure 74: Selected samples, test series 8, 60 μm layer thickness, a) 4-22, b) 4-10, c) 4-49, d) 4-32, e) 4-1.....	135
Figure 75: RSM a) factorial points, b) axial points c) factorial and axial points .	137
Figure 76: Model adequacy checking of response surface.....	142
Figure 77: Response surface plot of porosity [%] vs. power [W] and pulse time [μs].....	144
Figure 78: Contour plot of porosity [%] vs. power [W] and pulse time [μs].....	144
Figure 79: Response surface plot of porosity [%] vs. spot distance [μm] and pulse time [μs].....	146
Figure 80: Contour plot of porosity [%] vs. spot distance [μm] and pulse time [μs].....	147
Figure 81: Response surface plot of porosity [%] vs. power [W] and spot distance [μm].....	148
Figure 82: Contour plot of porosity [%] vs. power [W] and spot distance [μm]..	149
Figure 83: Selected samples, test series 10, a) 21, b) 31, c) 12, d) 5, e) 16, f) 23, g) 14, h) 7, i) 32, j) 29, k) 25, l) 8, m) 27.	151
Figure 84: Selected samples, test series 10 a) 28, b) 17, c) 11, d) 13, e) 15, f) 19, g) 24, h) 22, i) 30, j) 9, k) 1.	154
Figure 85: Selected samples, test series 11: a) 24, b) 15, c) 31, d) 14, e) 23. .	156
Figure 86: Selected samples, test series 11: a) 19, b) 30, c) 12, d) 32.....	157
Figure 87: Residual plots for porosity	161

Figure 88: Surface plot of porosity vs. power and pulse time	164
Figure 89: Contour plot of porosity vs. power and pulse time	165
Figure 90: Surface plot of porosity vs. power and spot distance	166
Figure 91: Contour plot of porosity vs. power and spot distance	167
Figure 92: Surface plot of porosity vs. spot distance and pulse time	168
Figure 93: Contour plot of porosity vs. spot distance and pulse time.....	169
Figure 94: Histogram of the response of AgCu7.....	170
Figure 95: Histogram of the response of AgCu28.....	171
Figure 96: Boxplot of both materials	172
Figure 97: Process map of AgCu7.....	175
Figure 98: Process map of AgCu28.....	175
Figure 99: University of Louisville Logo - a) CAD File, b) STL File c) manufactured Minerva batch	200
Figure 100: Manufactured University of Louisville Minerva batch a) as printed b) eyes 20 x magnification c) and d) details 20 x magnification	201
Figure 101: Scheme of Selective Laser Melting process.....	202
Figure 102: Boundary, offset and hatch vectors	203
Figure 103: Calibration of laser power [106].....	204
Figure 104: Vibratory sieve shaker with 45 μ m test sieve.....	205
Figure 105: Scheme of the silver powder manufacturing process [125-127]....	206

Figure 106: Proportional comparison of dimensions..... 207

LIST OF EQUATIONS

Equation 1: Break up time for a liquid cylinder without viscosity and gravity [21]	12
Equation 2: Marangoni effect [23].....	12
Equation 3: Plasma speed.....	14
Equation 4: Empirical plasma formation threshold [28].....	14
Equation 5: Estimation of recoil pressure [28]	15
Equation 6: Critical repetition rate [28].....	15
Equation 7: Max. density estimation for two different powder diameters	16
Equation 8: Factor for energy input parameters	24
Equation 9: Radial thermal diffusion time [56]	25
Equation 10: Dimensionless scan rate [56]	26
Equation 11: Energy density [56].....	26
Equation 12: Stability condition, Plateau-Rayleigh analysis [58] and [59].....	27
Equation 13: Stability condition by Yadroitsev et al.	27
Equation 14: Wiedemann-Franz law [87].....	36
Equation 15: Simplified factor of Wiedemann-Franz-law [88]	37
Equation 16: Wave length	62
Equation 17: Wave number	62

Equation 18: Lambert-Beer law	63
Equation 19: Calculation of transmission.....	63
Equation 20: Essential ANOVA equation [118].....	89
Equation 21: Symbolic denotation of the fundamental ANOVA equation [118] ..	90
Equation 22: Model to describe the response [119].....	90
Equation 23: Calculation of residuals [119]	90
Equation 24: Estimation of residuals	90
Equation 25: Calculation of Coefficient of Determination (R^2) [120].....	98
Equation 26: Calculation of Adjusted Coefficient of Determination [121].....	98
Equation 27: First-order model [122]	136
Equation 28: Second-order model [122].....	136

1 INTRODUCTION

1.1 Scope

The scope of this work is to provide a deepened scientific knowledge of the processing of Selective Laser Melting of silver alloys using a low energy laser source. Therefore, a typical desktop machine (Realizer SLM 50) was used which had a small footprint. The advantages and usability of this machine was described by Gebhardt et al. [2]

Silver based alloys are highly reflective materials that are used in medical applications, as conductive material, for biochemical purposes, in high frequency electronic applications such as GSM antennas, and traditionally in the field of jewelry making. It is difficult to laser process due to its comparably high reflectivity and its high thermal conductivity. Both physical properties slow down the process. For obtaining a stable process with repeatable results, the characteristics of the material should be explained. Furthermore, the processing using a Selective Laser Melting machine should be investigated. Important parameters should be determined and varied for the optimization of the results. The approach encompassed a systematic parameter analysis, for which the influence parameters were categorized. Finally, the porosity was analyzed and significant factors were determined.

Since the scientific analysis of silver material was not very well known, this work covers this particular area. For this approach, the silver alloys AgCu7 and AgCu28 were used.

The order of this documentation does not follow the experimental timeline. The EDX and SEM analyses were conducted at the same time whereas the absorption measurements and the powder distribution measurements occurred with a time gap of several months. The manufacturing and analysis of the material, the microscopy and the microsections were conducted by working with AgCu7 first, then followed by AgCu28. In order to compare the results, and to avoid repetitions of the process descriptions, the experiments were structured and summarized in this dissertation.

1.2 Changes in industries caused by additive manufacturing

In general, additive manufacturing technologies are developing very quickly. They will influence modern design, time to market and offer new possibilities for logistics and decentralized manufacturing.

Additive manufacturing provides us the possibility to rethink logistic systems. One popular vision is that in the future, every household will own a small additive manufacturing machine to produce parts and components that are needed. It also provides the possibility to highly customize products for individual needs. There exist several approaches that show the advantages of highly decentralized logistic structures. One example is the actual printing on demand of books (www.lulu.com). Book publishers realized that they need large

warehouses and stocks of resources if a large amount of print work would be produced in the traditional way. That generally increases costs. Furthermore, transport of the goods over large distances is uneconomical. But in the age of digital printing, a decentralized digital printing machine can print on demand which reduces warehouse costs and, in case of a close distance to the customer, transportation costs.¹ [3]

For additive manufacturing, there are some supporting arguments that should be named:

- Resources are limited and economically manufactured parts benefit from less material usage.
- Transportation and warehouse systems are costly.
- Subtractive methods cannot provide freeform fabrication.
- Usage of powder and a layer-by-layer addition of materials open up the constraints for a wide range of geometric shapes.

Actually, the idea of a decentralized manufacturing network is very popular. It would benefit from all key drivers that are mentioned above. Limited resources make it necessary to use material and energy in an efficient manner. For an additive manufacturing process, it is known that the layer based production method consumes a lot less material than subtractive methods. For the vision that was mentioned previously, just powders must be transported to local workshops or households. The last benefit is that freeform fabrication gives

¹ Examples inspired and derived from a presentation of Dr. Piller, DDMC 2012

new possibilities to design parts and structures that cannot be produced using subtractive methods. This argument is the most powerful for the success of additive manufacturing.

1.3 Selective Laser Melting process

Additive manufacturing first was developed for plastics and resins, resulting in molds to cast metals. The disadvantage is that further steps are necessary. In comparison to that, the Selective Laser Melting (SLM) process is an approach for the direct digital manufacturing of functional parts. Selective Laser Melting was developed for many years. It can be subordinated to powder bed fusion processes. [1] The method was described in the literature. [1, 4, 5] Nevertheless, for a better understanding of the process, a short description will be given.

A typical SLM machine consists of two different bins that are mounted in a process chamber. Comparably to a piston, the bottom of at least one of the bins can be moved up and down via elevating screws. A single-component powder is inserted into the first chamber. Then, the bottom of the chamber is moved downwards, and a wiper, doctor blade or a roller pushes the first layer of the material. Oxygen is evacuated and the chamber is flushed out by an inert shielding gas (typically Argon or Nitrogen), so that the working atmosphere prevents oxide reactions. Next, a focused laser beam melts a portion of the powder bed where the future contour shall be created. The contour solidifies instantaneously by thermal conduction into the surrounding powder when the laser beam is travelling forward. For contouring, a scanner unit is typically used

in combination with an F-Theta lens. Layer thickness can be adjusted by changing the distance between wiper and build platform. For building a part, its shape is mathematically sliced into two-dimensional contours that can be processed by a PLC. Figure 1 shows a schematic of the SLM process.

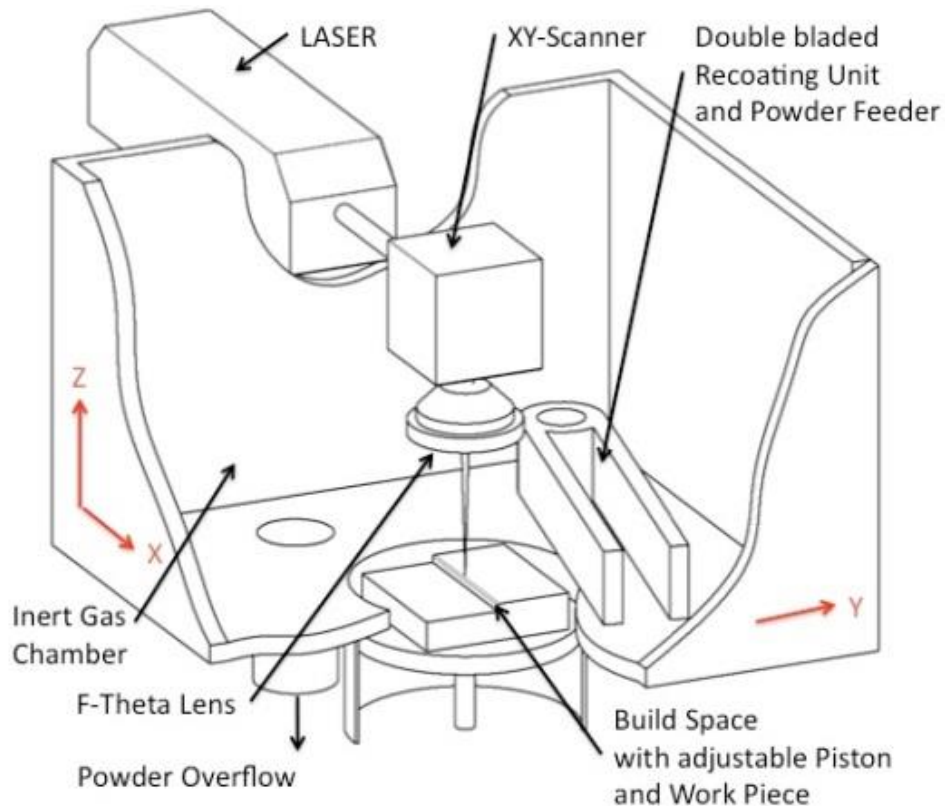


Figure 1: Scheme of the SLM process

After finishing of the first layer, the platform is lowered by the amount of one layer thickness and the wiper adds a new layer of fresh material. The wiper of the Realizer SLM 50 desktop machine rotates around an axis. The wiper blades, which can be lowered and lifted, contain powder which is poured between the blades either manually or via an automated screw feeder. Surplus

material is returned to the second chamber which serves as storage. Therefore, it is lowered just before each new layer arrives.

After finishing of the last contour and cooling down of the entire powder cake, the part can be removed, cleaned and prepared for further use, e.g. polishing. The SLM process was well investigated for many materials. Stainless steels and aluminum were reported by several researchers (see chapter 2.2.1).

For silver alloys, comprehensive parameter studies in relation to Selective Laser Melting are not available.

1.4 Silver as a material with special properties

Silver and its alloys were used since ancient times. The lack of corrosion made it famous as currency for many centuries. Tableware, forks and spoons were available in sterling silver for a long time as well. Products made out of sterling silver are marked with the label “925” since the chemical composition contains 92.5% silver.

In more recent times, silver compounds were used for photography, for water disinfection and for brazing. Additionally, silver is well known as a conductive material and can be found in many switches from the range between 3 volts and 500,000 volts. [6]

Silver has a unique optic trait once it is polished and manufactured well. That is the reason why it is used for outstanding jewelry, for timeless household equipment or for high class car interiors [6]. Besides some marketing information of different machine suppliers, additive manufacturing of silver alloys has not

been investigated fully. This dissertation reports on the application of Selective Laser Melting to this material to cover this gap in the materials that can be successfully processed with this technology.

1.4.1 Relation to industry sectors

One main focus was to use a low power desktop machine to prove that silver structures can be manufactured in a decentralized manner. Potential industry sectors are dental applications, jewelry, artwork, workshops that want to provide service for electric mobility, industries that need independence of logistic systems such as aerospace industries or on-site repair shops, biochemists, producers of medical implants or heart steppers, and many more.

1.4.2 Example: Manufacturing of conductors for flexible solar cells

Silver can be used as a colloid dispersed ink so that it can be processed in 3D printing machines. New approaches show that antennas, electrical paths and connectors can be manufactured using silver ink instead of etching and soldering a printed circuit board. For example, Glasschroeder et al. tested the manufacturing of printed lines using PMMA with binder and silver ink. [7] The conductivity was comparably poor due to the chosen material and processing parameters. [7] Better results were obtained by Hedges and Marin. [8] They presented printed antennas using aerosol jet printing, resulting in a line width down to 10 μm . [8] These approaches used inks with binders and therefore, they needed an additional drying or curing process. Although these techniques were

not related to Selective Laser Melting, it could be derived that methods exist that can produce 3D silver paths in a precise manner.

1.4.3 Medical applications

Early additive manufacturing applications in the medical sector were conducted using additive manufacturing methods. In 1997 for instance, Berry et al. presented studies of Selective Laser Sintering of medical parts such as skulls and bones. [9] Less work was published using additive manufactured silver parts for medical purposes.

1.5 New possibilities for artificial designs

As explained in chapter 1.2, additive manufacturing in general provides new chances for industry processes. It can be either used to scale models of future parts for testing purposes. [10] For instance, Quincieu et al. noted that Selective Laser Sintering help to improve the design of parts before costs occur that could be avoided, proved with a case study for aerospace design [11]. In advance, several tests were performed, as for example mechanical fit check, tooling fit check etc. [11] The knowledge was used to improve the design of transport boxes after the fit check was performed. [11] For silver alloys, new hollow structures are possible that are difficult to cast. There is no need to manufacture solid rings that can be produced in a cheaper manner with different technologies, but there exist fewer technologies to produce open structures as internal meshes with curved outlets. For example, this advantage can be used in manufacturing a ring-curved stent tube with new designs. [1]

2 LITERATURE REVIEW

2.1 State of the art

An aim of this literature review was to investigate which materials have been successfully processed and compare those to silver. In general there existed two main metal areas that were of interest. The first area covered the beginning of Selective Laser Melting and considered ferrous materials such as mild steels or tool steels. Also, the processing of high alloy steels could be subordinated into this section. General problems occurring for the validation of a new material could be derived from the literature and could help to find appropriate solutions. The other area of interest covered non-ferrous metals and alloys such as copper alloys, titanium and gold. The reason why these materials could contribute to the understanding of silver processing is that the high reflectivity and both, thermal and electrical conductivity are comparable to silver which led to the simple hypothesis that the problems to solve were comparable, too.

2.2 SLM of non-precious metals

2.2.1 Research about high alloy steels and tool steels

For different tool steels and stainless steels, Childs et al. compared theoretical results with experiments. A CO₂ laser source was used with 10 to

200 W power and scan speeds up to 50 mm/s. Argon shielding gas was used. [12]

Morgan et al. [13] described the production of cubes made from stainless steel 316L. In previous work, they found that upscaling of the parameters for thin walls caused a porosity of approximately 20%. [14, 15] A continuous wave Nd:YAG laser source was used. They reported about the wave pattern due to higher energy input at higher levels. First, they manufactured ten thin walls with increasing wall height (one additional layer each) and varied the scan length. Next, they investigated scan strategies and hatch strategies using different kinds of overlaps (positive / negative overlap) or different assemblies of the welding paths. [13]

Wei et al. [16] investigated all steps from single track, single layer to solid cubes using stainless steel 316L. For single layer experiments, four scan strategies were used: 1) vertical lines, 2) single line blocks that were patterned orthogonally versus each other, 3) lateral increasing squares and 4) "jumping and turning". [16] For 1) and 3), they observed balling and deformation or metal accumulation due to thermal stress accumulation. Scan method 2) showed similar problems at the boundaries of each square. Best results were obtained with method 4). [16]

In 1998, O'Neill et al. [17] worked on different methods to examine the best laser parameters for a Nd:YAG-laser. Single layer plates were manufactured using austenitic steel powder. Finally, they presented a process map that helped

to predict the behavior of the powder bed dependent on pulse frequency and laser power. [17]

One year later in 1999, O'Neill et al. pushed forward their previous work for multilayer systems. [18] The size of the plates was 3 x 3 mm, working with stainless steel. They noted that, due to the high laser power, rapid vaporization caused a shock wave and, hence caused recoil forces. The curling of the material hindered a flat powder level. [18]

Tolosa et al. manufactured tensile test specimen from 1.4404 (X2CrNiMo17-12-2), according to steel grade 316L. They used a layer thickness between 30 μm and 100 μm , scan speed: up to 1,000 mm/s and a laser spot size between 80 μm and 300 μm . [19] The powder size distribution was between 10 μm and 45 μm . [19]

Jerrard et al. produced specimens that were mixed between austenitic and martensitic steel grades. They tested mechanical and magnetic properties using micro hardness tests and "magnetic adherence" forces. Finally, they found that customized properties can be achieved. For this set of material, densification can be improved by a higher proportion of martensitic steel powder. [20]

Rombouts et al. [21] worked with different types of steel powders. One way they explained balling phenomena was based on Rayleigh instability. Plateau and Rayleigh developed the following equation: [21]

$$t_{break} = \left\{ 0.3433 * \frac{\gamma LV}{\rho \left(\frac{W_p}{2}\right)^3} \right\}^{-1}$$

Equation 1: Break up time for a liquid cylinder without viscosity and gravity [21]

where γLV represents surface tension, W_p width of the pool, and ρ density of the liquid [21]. The next effect that was noted by Rombouts et al. [22] is the Marangoni effect, which can be estimated using the following equation:

$$M_a = \frac{d\gamma LV}{dT} \frac{dT}{dr} \frac{L}{2\eta\alpha}$$

Equation 2: Marangoni effect [23]

where dT/dr is the temperature gradient, L length of the melt pool, and α thermal diffusivity. [21] Furthermore, they summarized that oxides that were created from remaining oxygen in the build chamber, reacted exothermically. The provided energy led to a larger melt pool. For iron, the energy from exothermic reaction was approximately a factor of 10 compared to the latent heat (2.4 kJ/g vs. 0.25 kJ/g). Furthermore, they noted that by the influence of oxides, the melting point was slightly decreased (which increased the melt pool) and the laser absorptance was decreased. In comparison to welding technologies, where large amounts of oxygen are used to reduce the surface tension, the surface tension for higher oxygen contents did not affect Marangoni convection because the surface tension gradient did not change significantly within the typical window (0.1-3wt%). However, the presence of oxygen caused balling problems. [21] Using a special camera system, they measured the dependence of melt pool dimensions on different factors. [21]

A detailed mathematical description of Bernard-Marangoni convection can be found in Boeck and Thess. [24] They investigated the influence of Prandtl-numbers on the Marangoni number and provided numerical solutions. [24]

Furthermore, Boeck and Thess [23] analyzed Marangoni convection using an electron beam and a vacuum chamber.² They explained that "after melting, a free surface is built between liquid metal and vacuum. Surface tension σ causes tensile forces that load every element of the surface, originating from the surface that surrounds the element. For most liquids, surface tension decreases with increasing temperature. Highest temperature can be expected in the middle of the melt pool, so that the surface tension increases to the borders of the pool." That means if a single element is considered, there is a gradient from the inner face to the outer face of this element. The forces facing each other are not compensated so that a resulting force exists. This resulting force is directed to the border of the melt pool and induces a current. The current that is created by surface tension gradients is called the Marangoni effect. [23]

2.2.2 Investigations related to titanium and its alloys

A large quantity of sources was available that dealt with Ti 6-4. There were some other material combinations and alloys that should be mentioned. For titanium, Gu et al. investigated the manufacturing of TiC/Ti₅Si₃ composites using

² This explanation of the Marangoni effect is translated and paraphrased from German

the Selective Laser Melting method. [25] Tension tests and ductility tests were analyzed by Facchini et al. for titanium alloy specimens that were produced using SLM. [26]

Yasa et al. analyzed Charpy impact tests for titanium and steel alloy specimens that were produced using SLM. They used maraging steel powder X3CoNiMo18-9-5 (hardens building martensite), 1.4453 (stainless steel 316L) and titanium alloy Ti-6Al-4V. [27]

Fischer et al. [28] worked on the thermal interaction between laser pulse and metal powder. They defined three different stages of repetition rates: first, plasma domain, where a single pulse is able to build a melt pool and plasma, second stage is the same as first but without plasma, third stage needs more than one pulse to melt the material and last stage is comparable to continuous wave. [28] Titanium powder was used and different fundamental equations were presented. [28] Furthermore, Fischer et al. provided some estimation equations:

$$v_{plasma} = \frac{P_0}{\tau_p \pi r_b^2 I_{plasma}}$$

Equation 3: Plasma speed

where P_0 represents laser power, τ_p pulse duration, r_b laser beam radius and I_{plasma} “estimated empirical plasma formation threshold.” [28]

$$I_{plasma} = \frac{4 * 10^4}{\sqrt{\tau}}$$

Equation 4: Empirical plasma formation threshold [28]

$$P_{rec} \approx 0.54p(T_s)$$

Equation 5: Estimation of recoil pressure [28]

They combined these parts into a “critical repetition rate” for calculating a molten surface in one single laser pulse: [28]

$$v_m = \frac{2A_b P_0}{\pi r_b^2 k_b \Delta T_m} \sqrt{\frac{k_b}{\tau_p \pi}}$$

Equation 6: Critical repetition rate [28]

where P_0 is laser power, τ_p pulse duration, r_b laser beam radius and A_b absorptivity

2.2.3 Research into copper-based materials

Before additive manufacturing methods were available, tools and electrodes were manufactured using subtractive methods such as milling or by conventional sintering. Copper is widely used for the manufacturing of resistance welding electrodes due to its high electrical conductivity. Since pressure is applied, tungsten-stabilized copper alloys were used, but it is always a tradeoff between wear behavior, conductivity and machinability. For this reason, research was conducted for new manufacturing methods.

In 1999, Zaw et al. compared different materials by use of a common sintering process and an additive manufacturing sintering process. The scope was the improvement of manufacturing methods for electrical discharge machining electrodes. Furthermore, they conducted a comparison with a Rapid

Tool EDM electrode. One of the conventional materials was CuW and 100% copper. [29]

Focusing on tool manufacturing in 2003, Zhu et al. [30] used a two component copper mixture, consisting of pure copper and the three phase alloy SCuP as binder. They compared the results for the manufacturing of a mold. [30]

In 2007, Zhu et al. investigated the influence of the powder density (apparent density) on the final product for Selective Laser Sintering. [31] Different copper powders were used and powder packing models were considered. [31] They noted that there exists an influence of surface roughness and shape of the powder on the packing density. [31] If two different powder sizes were used, the limiting density can be calculated with: [31, 32]

$$\rho = \rho_L + \frac{\rho_s}{1 - \rho_L}$$

Equation 7: Max. density estimation for two different powder diameters

where ρ = density, ρ_L = density of large powder diameter, and ρ_s = density of small powder diameter.

Gu and Shen focused on balling effects of copper-based metal alloys. [33] They determined three different principles that cause balling. Fundamental mixing was 30% CuSn 10% CuP and the rest was pure copper. They used a CO₂ laser source with a maximum power output of 2 kW. Powder thickness was 200 μ m before melting. Spot size was 300 μ m, power 300-500 W and scan speed 30-70 mm/s. The hatch distance was 150 μ m and no shielding

gas was used. “first lines scan balling” is caused by a high thermal gradient at the beginning of the process. Surface tension depends on temperature. Shrinkage induced balling was observed for higher scan speeds and is caused by the contraction of liquid material while cooling down. “Self balling” is the same effect, but caused by a low scan speed and a high energy input. [33]

2.2.4 Research into aluminum-based materials

A work group from Fraunhofer ILT, Aachen [34] aimed to increase the SLM process efficiency using aluminum-based powder. They separated into primary and auxiliary process time, pointing out that the main variables were scan speed, hatch distance and layer thickness. The experimental setup was able to increase laser power and scanning speed, using a fiber-coupled disk laser. Findings were that with scan speeds up to 1,200 mm/s and a laser power of 500 W, nearly fully dense parts could be manufactured. [34] They investigated density, hardness and tensile strength. [34]

Similar machine parameters were used by Wang. [35] The manufacturing parameters were 1,000 mm/s, with 195 W and a scan spacing of 0.9 mm. [35] Wang manufactured specimens for tensile tests and bend tests from Hastelloy X, using an EOS machine. Some specimens were treated with hot isostatic pressing. Fatigue tests were performed as well. [35]

2.2.5 Research into nickel-based materials

Lots of research is available since nickel-based alloys were widely used in industries. For example, Yadroitsev et al. from Loughborough University used

nickel-based powder (Inconel 625) for their studies. [36] They investigated the optimal hatch distance in relation to porosity and applied a scan method with dual heating of the powder bed. [36] This study indicated that a higher pulse energy (8 and 9 J) led to less porosity. [36]

In a similar manner as Yadroitsev et al., Mumtaz et al. [37] investigated the behavior of a commercial nickel superalloy. They measured the contact angle and bead geometry, respectively, and analyzed the bonding behavior using metallographic micro sections. Different parameters were changed, e.g. pulse width, percentage overlap, hatch strategy and scan strategy etc. They depicted the results in a process map, displaying pulse width against specific energy. [37]

2.3 SLM of precious materials

2.3.1 Research related to gold

Copper, silver and gold belong to group 11 of the periodic table. From this group, gold was processed by Khan and Dickens, who presented parameter studies into Selective Laser Melting in 2008. [38] They used 24 carat gold. First, the particle size distribution (dispersion in isopropanol, laser diffraction technique) was found to be between 3.3 μm and 46 μm . SEM showed that gold particles were commonly spheres. [38] They also measured the tap density according to different standards (constant weight or constant volume). [38] For the test series, Khan and Dickens used a SLM 100 machine with 50 W cw laser power. They obtained better results from a single-scan concerning the structure

of the surface. They detected more melted particles within the cross-scanned samples. The thickness of single scan layers was more than 20% less than cross scanned layers since more powder was molten and more energy was applied. Finally, they concluded that surface roughness was almost the same. [38]

In 2010, Khan and Dickens deepened the previous work and produced cubes out of pure gold (edge length 4 mm). [39] They investigated the reflection of gold powder for the fiber laser wave length area (85%). For manufacturing, they preheated the powder bed to 100 °C and investigated the process window for gold, depending on laser power and laser scan speed. They found that good results were obtained for 50 W and 65 mm/s. [39]. The density was described for ground cross sections, resulting in approx. 88% dense parts. The porosity mainly occurred between layers. Varying the hatch distance did not lead to significant differences. [39]

For the silver manufacturing process, it can be learned from Khan and Dickens that the machine configuration of a SLM 100 for gold meets the possible configuration of the SLM 50 machine, related to laser power and scan speed. [39]

Klotz [40] described different methods for the surface coloring of gold jewelry. None of them used Selective Laser Melting. Surface tests were conducted using the test scheme of DIN 1811 (“The Reference Test Method for Nickel Release”, artificial sweat) and ISO 10271 (“Dental Metallic Materials, Corrosion Test Methods”). [40]

Fischer-Bühner et al. [41] extended the study of colored gold intermetallics to investment casting. They used a fall test to estimate the influence of different micro alloys on the ductility. [41] A potential application of this material was in jewelry which was underlined by different examples. [41]

2.4 Research related to silver and its alloys

Since silver is considered a very expensive material, the usage of it is limited. From a material science perspective, it is used in soldering processes but the physical binding mechanism is different than Selective Laser Melting. Therefore, silver-based soldering materials were not considered.

In some alloys, traces of silver were used as alloying elements. For example Kermanidis et al. published about corrosion of an aluminum alloy that contained silver as an alloying element. Silver alloyed aluminum is known as the hardest aluminum alloy that can be processed. They found that the fatigue limit is reduced by almost half due to corrosion effects. [42]

Besides that, silver itself can be alloyed with lots of elements, many of them showing an appropriate phase diagram with solutions. For example, the systems Ag-Au shows 100% solubility, whereas Ag-Cu and Ag-Ge show phase diagrams with eutectics. [43] The system Ag-Fe has no solubility for large temperature regions. [43] Some early investigations (1981) of Ag-Cu and laser melting were published by Beck et al. [44] They worked on different alloys of the system Ag-Cu and analyzed the metastable behavior when the alloy is quenched. [44]

Wielage et al. observed microstructure and mechanical properties of silver composites. They focused on contact material, but the research was more related to powder production. [45] A short description of the powder manufacturing process that is important for the silver study of this dissertation is presented in the appendices.

Extensive material properties of pure silver were described by Smith and Fickett. [46] They collected many references to the investigation of most relevant physical properties. [46]

Gisario et al. [47] analyzed the butt welding behavior of different silver alloy sheets (800 and 925 silver alloy, system Ag-Cu). They used a diode laser (0.94 μm wave length) with higher laser powers (range 500 to 800 W). Sheet dimensions were 0.5 x 200 x 300 mm. They varied laser power, scan speed and welding time. They analyzed the material using SEM and Energy Dispersive X-Ray Spectrometers (EDXS). They defined an analytical expression for oxides. [47]. This work did not contain powder based materials.

This short literature review shows that more research was necessary for a better understanding of silver in the Selective Laser Melting process. Next section overviews collected information regarding the SLM Process.

2.5 Research generally related to the SLM process

Terry Wohlers [48] publishes actual data annually in his report that encompasses industry growth, information related to system suppliers and to international markets.

Levy et al. [49] distinguished between four different material forms: powder, metal sheets, wire, metal spray. Furthermore, this source is about different SLS materials. Levy distinguished between different stages, dependent on the number of steps that were necessary.

In 2010, Levy et al. analyzed the future perspective of lasers in general additive manufacturing processes. [50] The source contained historical aspects from the development of additive manufacturing processes, the developments until today (rising influence of electron beam melting), the main influence parameters of layer-based manufacturing methods and its effects on quality and productivity. Furthermore, this work covered density and accuracy effects and showed some future aspects and suggestions for further development. [50]

Sreenivasan and Bourell [51] explained the resource consumptions and its relations to the total selective melting process. This included energy consumptions for the laser source, drives, heaters and other loads. [51]

2.5.1 Investigations related to powder physics

Yadroitsev and Smurov [52] noted that absorptivity is dependent "... on the physicochemical properties of the powder material, ... on granulomorphometry and apparent density of the powder ...". Furthermore, they noted that absorption by powder is higher than absorption in a bulk base material. They distinguish between the properties of a single track (depending on the known parameters: power, speed, layer thickness, and other properties) and

the properties of the final part (only depending on single track and single layer). [52]

A PM 100 from Phenix was used, with a maximum laser power of 50 W, maximum scan speed of 3 m/s and a laser spot size of 70 μm . The machine could be preheated up to 900 °C. Powder suppliers were TLS Technik GmbH & Co. and Sandvik Osprey. They used tool steel H13, SS 316L, 904L, Inconel 625 Co212-F. They investigated single track properties and observed typical effects that were already known (Marangoni effect, instability at minor scanning speeds etc.). [52]

Furthermore, they stated that “latent heat of fusion influences the heat balance”, so materials with higher latent heat can be processed at lower speeds. [52] They explained the reason why SLM parts were less ductile and can bear higher strengths. Manufactured part size was 50 x 20 x 4 mm (cross scanning strategy). For Young’s modulus, they detected anisotropy due to manufacturing direction (0°, 45°, 90°). [52]

Gusarov and Kovalev [53] modeled a numerical approach to describe the heat-related processes in powder layers. One assumption is an equal sphere diameter. Different packing models returned different conductivity factors: [53]

- Face centered cubic (FCC): $\lambda = 2.828$
- Body centered cubic (BCC): $\lambda = 1.732$
- Simple cubic (SC) $\lambda = 1$

With these conductivity factors, the theoretical conductivity can be adjusted.

Simchi [54] investigated the influence of different powder diameter ranges on laser sintering. Fine powders tended to agglomerate and coarse powders tended to segregate. [54] They used a standard test method for comparing e.g. particle size distribution properties, apparent and tap density and the flow rate. [54] Most of the powders were water atomized. [54] Simchi found that the fractional density depends on the mean particle diameter and on the scan rate. There seemed to be an optimal value around 30 μm that was shifted to a higher mean particle size for faster scan rates [54]. Best results were obtained for low scan rates (50 mm/s). [54] Furthermore, he noted that there is an influence between orientation and size of the pores, depending on particle size distributions. [54]. Different O_2 -concentrations led to different pore patterns, increasing length with lower oxygen concentration within the atmosphere. [54] Furthermore, he noted a ψ -factor from previous work, combining all significant energy input parameters: [54]

$$\psi = \frac{P}{vdh}$$

Equation 8: Factor for energy input parameters

where P is laser power, v scan speed, d layer thickness, and h hatch distance.

For iron powder, Simchi observed a critical ψ (approx. 0.2 kJ/mm³) which served as a boundary for the increase of density. [54]

2.5.2 Research into binding mechanisms

Kruth et al. [55] differentiated binding mechanisms of solid freeform fabricated parts. They categorized into four main categories (solid state sintering, chemically induced binding and melting (partial / full)). They pointed out that available SLM metals were stainless steel 1.4404, tool steel 1.2343, and TiAl6V4.

In 2006, Simchi [56] published a general approach to explain binding and sintering mechanisms and the kinetics of the weld pool for the direct laser sintering process. Powder was obtained from BASF, Schlenk Metallpulver GmbH (Germany), Quebec Metal Powders Limited (Canada), Osprey Metals (UK), and Hoeganaes (Sweden). Some fundamental relationships were gathered. Furthermore, he collected information concerning densification methods and noted that the change in density during laser exposure and agglomeration led to different absorbance rates. [56] He provided some thoughts about time and energy while the laser works, concluding that particle diameter was larger than the distance the heat could progress during the interaction time.

The equation for radial thermal diffusion time is

$$\frac{d^2}{4 \alpha} = \text{radial thermal diffusion time}$$

Equation 9: Radial thermal diffusion time [56]

whereas

$$v^* = \frac{d^2}{4 \alpha}$$

Equation 10: Dimensionless scan rate [56]

Energy density as a function without geometrical properties is

$$Q = \frac{\pi \eta P}{4 d v}$$

Equation 11: Energy density [56]

Furthermore, void fractions and its empirical effects on the densification were described. [56] For process parameters, a densification coefficient K was used. They noted that oxidation increases the absorption rate. [56]

2.6 Research related to parameter analysis

While working at Fraunhofer ILT in Aachen, Meiners defined in his PhD thesis the following main influence parameters: [5]

- Laser power
- Scan speed
- Layer thickness
- Hatch distance
- Powder size
- Scan vector length
- Shielding gas flow

Furthermore, he noted energy relations equations in order to explain the energy input. [5]

Yadroitsev et al. worked on “the influence of the hatch distance and thickness of powder layer on morphology of the first layer”. [57] They reported that if the hatch distance was too large, undesired surface effects were the consequence. [57]

In previous research, the influence parameters for building a single line was investigated by Yadroitsev et al. [58]. The relation of heat conductivity and absorptivity was important for the obtained mechanical properties. Surface tension forces caused a cylindrical shape. They investigated capillary instabilities. Track width and remelted depth linearly decreased both with scan speed and power. Furthermore, they derived a new condition, compared to Plateau and Rayleigh:

$$\frac{\pi D}{L} > 1$$

Equation 12: Stability condition, Plateau-Rayleigh analysis [58] and [59]

$$\frac{\pi D}{L} > \sqrt{\frac{2}{3}}$$

Equation 13: Stability condition by Yadroitsev et al.

where L is the length of the molten pool and D is the diameter. The difference between equation 12 and equation 13 is explained by geometrical reasons.

Kruth et al. determined important parameters using statistical methods: [60] “scan speed, layer thickness, scan spacing, laser power, powder size and its

distribution, scanning strategy, base platform temperature and atmosphere.” [60] They pointed out hardness (Brinell), density (principle of Archimedes, ethanol), and surface roughness, measured with a FormTalysurf 120L. [60]

Zhang et al. [61] determined the influence factors of a magnesium-aluminum mixture with less than 10% aluminum. They used a MCP 250 II SLM machine with a Nd:YAG laser and produced cubes with 5 mm edge length. Further parameters were: layer thickness 50 μm , hatch spacing 80 μm , particle size 42 and 17 μm . Compared to Yadroitsev et al., density measurement occurred via the principle of Archimedes, (weighed in air, covered with wax, weighed in water, increasing of volume measured). Furthermore, they measured the microhardness and inspected the parts using optical and scanning electron microscopes. Additionally, they depicted the results in a process map displaying the relationship between power and scanning speed. They used seven levels for power and eight levels for scanning speed, respectively. [61] Finally, they reported that for high energy inputs (60-110 W, all speeds, and 30 W at low speeds) they could not form solid lines due to evaporation of Mg. For lower inputs (speeds 0.08 m/s and above, 10–30 W) bonding mechanisms did not occur sufficiently. Best results were obtained within the “forming zone” of low powers and low scanning speeds although stratification, balling, and “cauliflower-like” grains were reported. [61]

2.7 Research related to DoE approaches

There was a lot of literature available concerning Design of Experiments approaches. Most of them related to different additive manufacturing methods or

different materials. For instance, Chatterjee et al. described a DoE approach to observe the dependence of layer thickness and hatching distance on the density, hardness and porosity of the sintered products. [62] Carbon steel powder was used. [62] From statistical analysis, they found that layer thickness influenced the density by a power of two and that the hardness inversely proportionally increased with layer thickness. Porosity was linearly dependent both on layer thickness and hatching distance. [62]

Hsin-Te et al. investigated pulse frequencies and pulse durations of laser beams and times of strikes to point out the effects on the sintering process. With some restrictions, Taguchi's method and ANOVA were used. [63]

Bacchewar et al. used a DoE approach to measure the effects on surface roughness related to build orientation, laser power, layer thickness, beam speed, and hatch spacing. Polyamide was used. [64]

Singh et al. built a DoE model to forecast the density of parts, manufactured with laser sintering. A two level factorial design, a FEM with ANSYS for heat gradients and polyamides were used. [65] They found that the density is affected by laser power and hatch distance. [65]

Kechagias [66] statistically analyzed errors in the laminated object manufacturing process, using heater temperature, heater speed, layer thickness and the speeds of feeder and platform for an orthogonal experiment. Two levels of each factor were used (Taguchi design), followed by ANOVA and analysis of means. [66]

Yadroitsev et al. [67] manufactured single lines and walls, varying vectors and energy inputs. They conducted a parametric analysis using INOX 904 L powder on a Phenix PM 100 machine. [67] Maximum laser power was 50 W, cw, wave length 1.075 μm , laser spot size 70 μm . They measured that 95% of the diameters of the powder particles were less than 20 μm . Furthermore, they observed that the width of a single wall increased with an increasing number of layers. Finally, they recommended correcting the difference between the CAD model and the manufactured part using a correction factor. [67]

Singh and Prakash [68] adjusted analytical equations for sintering and scanning for an ANSYS code. The obtained data was analyzed using the response surface method, finding an analytical approach for density calculations, depending on the factors laser power, scan speed and hatch distance and interactions. [68]

Raghunath and Pandey [69] discussed the refinement of geometrical shape and its effecting factors using a Taguchi approach. Polyamide powders were used. They noted three steps were necessary: system design, parameter design and tolerance design. [69]

Dingal et al. [70] modeled a L8 Taguchi orthogonal design for Selective Laser Sintering of iron powder. [70] They selected peak power density, particle size, interval- spot ratio, layer thickness, stepping distance, pulse on-time and scan speed as factors and gained density, porosity, surface microhardness and mean cross hardness as responses. They noted that Taguchi could be

considered as a fractional factorial experimental design that reduced the number of tests that must be run for a full factorial design. [70]

It can be learned from the different Design of Experiments used by other researchers, that Taguchi reduces the number of experiments compared to a full factorial design. But there are some limitations if the processes are not robust in any cases. For that approach, a full factorial design is a better choice.

2.8 Research related to additive manufacturing and FEA

Since calculations of thermal effects are multi-dimensional problems, modern research on this topic is done using Finite Elements Analysis (FEA). The literature provided various approaches for calculating stresses, energy balances or to predict the behavior of the parts that should be built. For example, Matsumoto et al. studied the effect of temperature gradient and elastic deformation using a finite elements approach. [71] They focused on a single track on a plane. [71]

It can be learned from Matsumoto et al. that the Young's modulus was simulated as a function of temperature. [71]

Osakada and Shiomi compared physical parts to a FEM model. [72] The parts were manufactured with a laser power of 50 W, scan speed of 4-8 mm/s and a hatch distance of 0.75 mm. Base materials were aluminum, copper, iron, stainless steels, chromium, titanium and nickel-based alloys. A single powder layer with large thickness was used (10 mm) in order to detect the optimal

powder for the tests. Balling and linear solidification were detected. [72] Furthermore, they reported about different post treatment methods such as annealing and hot isostatic pressing. [72]

For the transferal of the Osakada and Shiomi's findings onto silver processing, the stress distribution showed a wave shape and it was concluded that cracks will occur. [72] In the case of a very ductile material like silver, this tension gradient may lead to a wave pattern as well.

Zaeh et al. compared specimens manufactured from tool steel 1.2709 (X3NiCoMoTi 18-9-5) with a FEA model and simulated residual stresses. [73] The evaluation of the theoretical data was performed using neutron diffractometry for the measurement of residual stresses. [73] It is reported that distortion decreased with increasing layer thickness, and increasing preheating temperature. [73]

Based on titanium powder, Kolossov et al. [74] formulated a heat conductivity model for Selective Laser Sintering and compared it with measurements, using an infrared camera for heat detection. [74]

For the silver analysis, from Kolossov et al. it can be transferred that both, the heat capacity and thermal conductivity, were modeled as function of temperature. [74]

Since the manufacturing of thin hollow structures is challenging due to known problems like balling and distortion, other researchers worked in this area with different additive manufacturing methods. For example , Neela and De [75]

analyzed a single wall for LENS using FEA. They found that the build parameters, laser power combined with scan speed and powder mass flow rate, had an influence on thermal behavior. Furthermore, the idle time to the next application of laser energy for the manufacturing of the next layer influenced the thermal behavior as well. [75]

Hu and Kovacevic [76] kept the molten pool constant while manufacturing a single wall. This was done using a circuit that adjusted the laser power if necessary. They compared the results with ANSYS FEA calculations for explaining thermal aspects of the weld pool. [76]

Although Hu and Kovacevic used the laser-based additive manufacturing method (LBAM), it can be learned that the imaging and control of the weld pool can be achieved with a NIR-camera, once the camera is calibrated. [76] This could be applied to Selective Laser Melting as well.

2.9 Research related to thermal and electrical conductivity

2.9.1 Investigations about conductive material

Based on aluminum, Khailov et al. [77] described a special method for the measuring of electrical conductivity, derived from aerospace engineering. The specimens were aluminum-based. [77]

Lorente et al. discussed the manufacturing of RF (Radio Frequency) components for microwave filters. Six different filters were manufactured, using titanium and aluminum alloys. They measured the Q-factor (Gaussian failure integral) of the raw parts, surface roughness, and the Q-factor of machined parts.

They found that at least 75% (titanium) and 70% (aluminum alloys) of simulated Q can be achieved. [78]

Lin et al. explained the surface application of silver powders (ink) for conductive thick films. Those powders were applied with screen printing technology. [79]

Heringhaus et al. [80] wrote about the improvements for high power conductors made from silver-tin blends. The conductors were powder based which was produced using dual-jet precipitation. [80]

In many sources, silver is considered as the material with the highest electrical conductivity. For example, Ivers-Tiffée and Münch [81] noted that the best conductive materials were silver, copper, gold, aluminum, sodium, magnesium, zinc, and iron, listed with decreasing conductivity. [81] For practical applications, conductivity values are tabled in common handbooks such as the German "Table Book of Electrical Engineering". [82] In figure 2 the conductivity values are displayed as proportional bars.

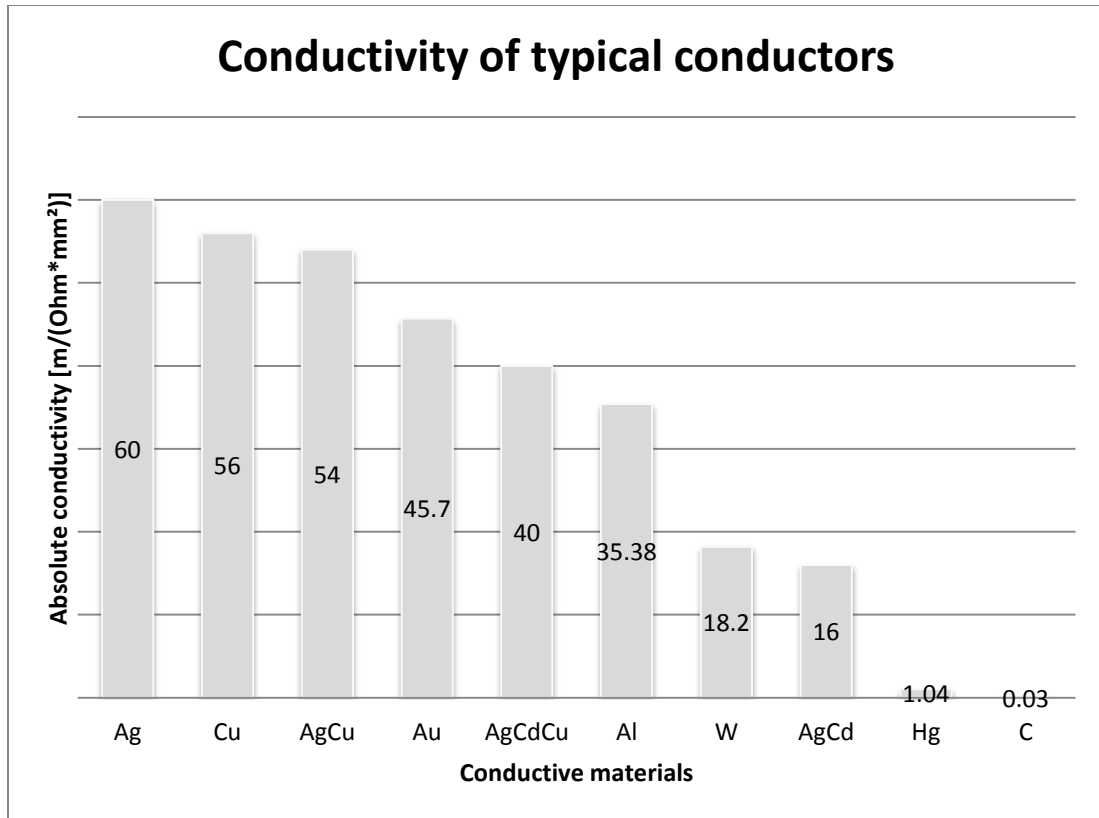


Figure 2: Conductivity of typical conductor materials [82]

It can be seen from the chart that silver has the highest conductivity of all materials that are typically used as conductors. It even conducts better than copper but is much more expensive. From this reason, figure 3 depicts the current development of both raw materials. Please note that there is a factor of more than 100 between both prices.

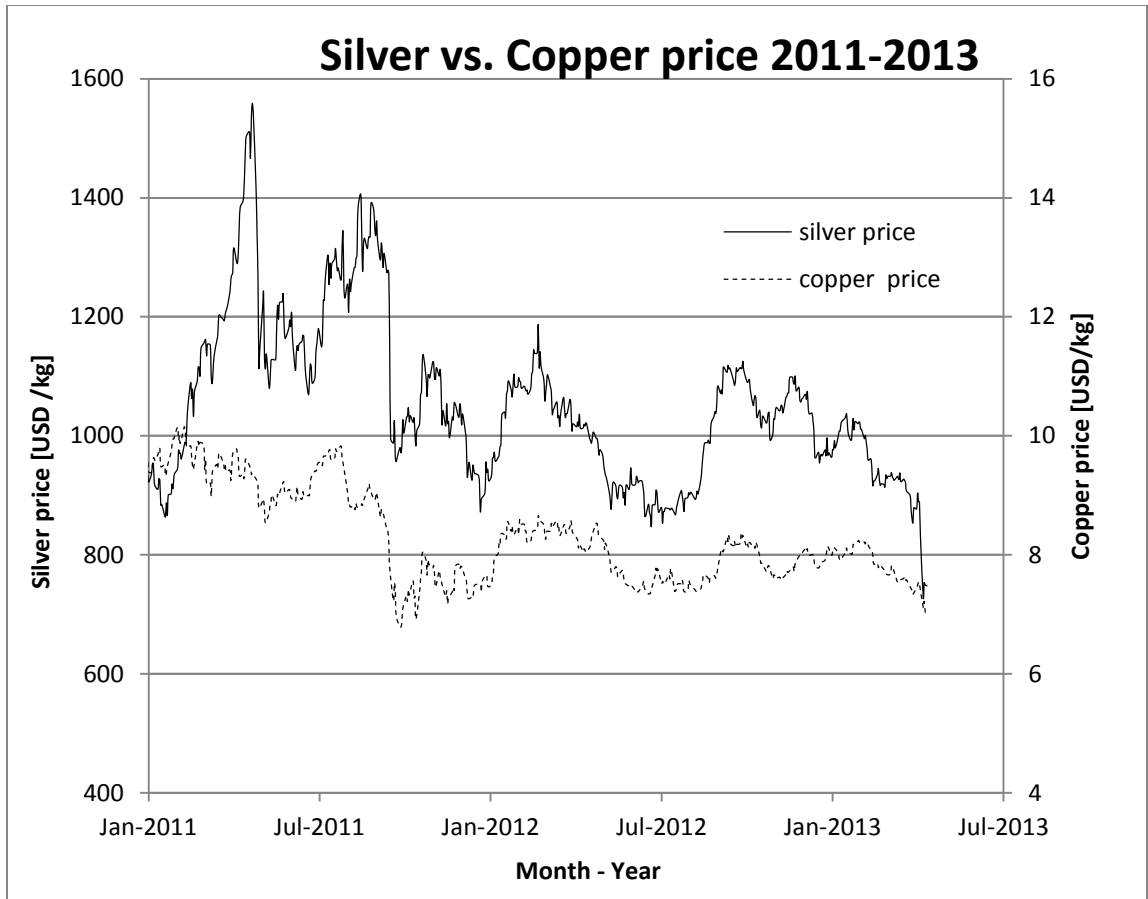


Figure 3: Development of silver and copper prices 2011-2013 [83-86]

The American code ASTM E1004 - 09 is a standard test method for determining electrical conductivity using the electromagnetic (Eddy Current) method. This method was used by Zaw et al. [29, 77]

Thermal (λ) and electrical conductivity (σ) are directly related by the Wiedemann-Franz law:

$$\frac{\lambda}{\sigma} = a * T$$

Equation 14: Wiedemann-Franz law [87]

For metals, the following constant approximation is known: [87]

$$a \approx 3 * \frac{k^2}{e^2}$$

This constant can be calculated with Boltzmann-Constant $k = 1.3806488 * 10^{-23} \text{ J/K} = 8.6173324 * 10^{-5} \text{ eV/K}$ and the elementary charge $e = 1.602176565 * 10^{-19} \text{ C}$ and yields:

$$\frac{\lambda}{\sigma * T} = 2.45 * 10^{-8} \left(\frac{\text{V}}{\text{K}} \right)^2$$

Equation 15: Simplified factor of Wiedemann-Franz-law [88]

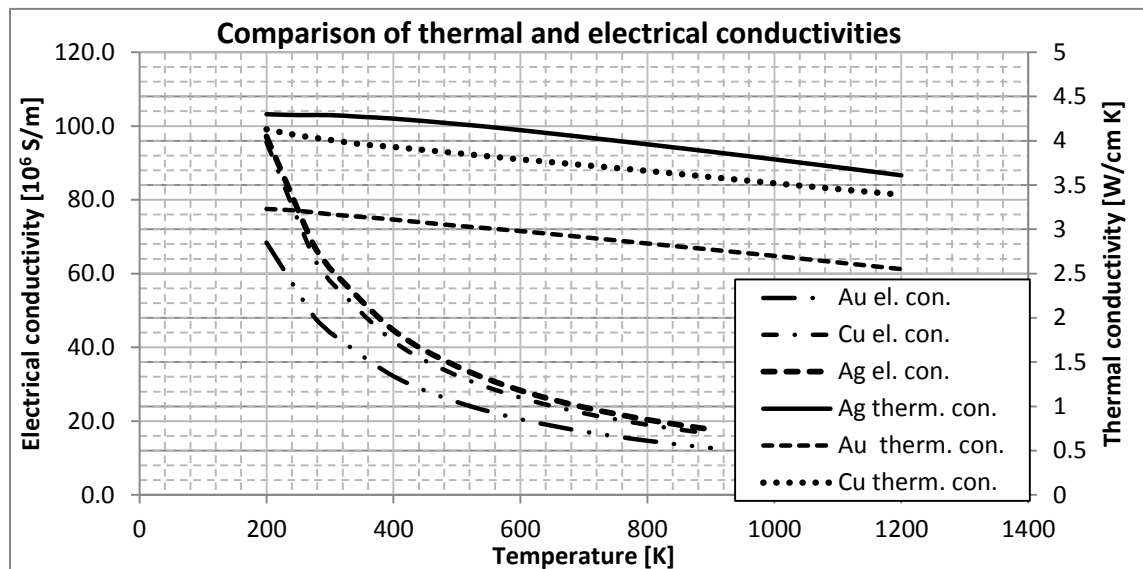


Figure 4: Comparison of thermal and electrical properties as a function of temperature [89, 90]

Figure 4 depicts the dependency of thermal conductivity and temperature (right, decreasing, linear curves) and the dependency of electrical conductivity and temperature (left, decreasing quadratic curves). Both properties are displayed for silver, copper, and gold, respectively. It can be seen that silver has higher conductivities than gold and copper.

2.10 Reflectivity and absorption rates

The reflectivity of the material is important at the wavelength of the laser that is used. The powder size distribution and the temperature influence the absorption rate as well. Different researchers investigated the absorption rates of the material that was used for their studies. Table 1 lists some values about different materials.

Table 1: Absorption rates and thermal conductivities - literature values

Material	Absorption rate [-]	Source	Thermal Conductivity [W/(cm K)]	Source
Pb	0.79	[91]	0.353	[92]
Ti	0.77	[91]	0.219	[92]
Sn	0.66	[91]	0.666	[92]
Ni	0.64	[5]	0.907	[92]
Fe	0.64	[91]	0.802	[92]
Cu	0.59	[91]	4.01	[92]
Al	0.51	[5]	2.37	[92]
Au	0.15	[39]	3.17	[92]

The absorption rates are measured for the wave length of a Nd:YAG laser (1.064 μm). The thermal conductivities were measured at room temperature (27°C). If the metal powder has a sufficient layer thickness the transmittance converges to zero. Below an absorption rate of 0.5, more energy is reflected (or transmitted) than absorbed. In table 1, gold is considered as a highly reflective material with an absorption rate of 0.15. Copper, aluminum, and gold are considered as materials with high thermal conductivity.

2.11 Summary of findings

The literature review showed that different materials have been investigated using the Selective Laser Melting process. This encompassed high

alloyed steels, tool steels, aluminum or titanium alloys. For precious materials, Khan and Dickens worked successfully with a similar machine as the machine used in this work. [38, 39] Several researchers investigated mechanical properties such as porosity. Throughout the scientific investigations, Design of Experiments approaches were used for the statistical analysis of different tasks. The best methods are depending on the specific questions that needed to be answered.

The balling phenomenon has been investigated regarding to Marangoni convection and plasma building. It is caused by a high thermal gradient at the beginning of the process. The Marangoni convection is a current induced by surface tensions. Plasma is build above a critical threshold depending on laser parameters. From the literature review, the existing knowledge about the influences of parameters such as laser power, layer thickness, particle size distribution, and scan speed was used in order to find parameter sets.

3 FUNDAMENTAL STEPS IN SILVER PROCESSING

3.1 Physical properties about silver and its alloys

Table 2: Electrical and thermal properties of silver [93] [90]

Property	Electrical resistivity at 0 °C [$\mu\Omega \cdot \text{cm}$]	Electrical conductivity at 27°C (300 K) σ in [S/m]	Linear coefficient of thermal expansion [$\mu\text{in./in./}^\circ\text{C}$]
	1.59	$61.39 \cdot 10^6$	19.68
Source	ASM handbook	CRC handbook	ASM handbook

Table 2 shows some major information related to pure silver. The data was derived from commonly available handbooks. Depending on the alloy type, the properties change more with increasing content of the alloying elements.

Table 3: Mechanical properties; tensile strength of silver [93]

Property	Tensile strength, as-worked wire [MPa]	Tensile strength, annealed wire [MPa]
	290	125-186
Source	ASM handbook	ASM handbook

Since silver is a conductive material, wire made out of silver is available. Table 3 lists the following tensile strength properties: as worked wire, the tensile strength of silver is nearly twice the tensile strength after annealing (290 MPa vs.

approximately 150 MPa). That is because annealing leads to homogeneous grains and hence increases the ductility. The annealing temperature is slightly above (about 50 °C) the lower limit of the Ag austenitic region. The annealing temperature steeply increases with increasing copper content, starting from approximately 400 °C for pure silver to approx. 790 °C at the eutectic line.

The hardness of pure silver is expected to be below 80 HB [94] , increasing with alloying of copper.

Table 4: Mechanical properties; elongation of silver [93]

Property	Elongation in 50 mm, as-worked wire, [%]	Elongation in 50 mm, annealed wire, [%]	Young's modulus at 20 °C , static, [GPa]
	3-5	43-50	74
Source	ASM handbook	ASM handbook	ASM handbook

Table 4 shows that annealing increases the elongation by approximately a factor of 10. Young's modulus is approximately a third of the modulus of mild steel (210 GPa) and even less than aluminum (depending on the alloy, approximately 140 GPa). Since Young's modulus is the ratio of elongation over stress, the curve would appear with a lower slope in the stress-strain diagram.

Table 5: Other properties of silver [93]

Property	Crystal structure	Density at 20 °C, [g/cm ³]	Melting point [°C]
	Face center cubic	10.49	961.9
Source	ASM handbook	ASM handbook	ASM handbook

Table 5 lists that the crystal structure is face centered cubic. This crystal structure is typical for the austenitic region in the alloy phase diagram. Due to the higher density, the same volume would be heavier than steel. The melting point decreases with increasing alloying elements.

3.2 SLM approaches

3.2.1 Realizer SLM 50

For this series of tests a Realizer SLM 50 was used, shown in figure 5. The scope of the machine was described in [2]. Fundamental data of the machine is provided by table 6.

Table 6: Fundamental data of SLM 50 [95] [96]

Powder bed diameter:	Ø 70 mm
Max. powder bed height:	40 mm
Shielding gas:	Argon
Shielding gas consumption:	2-3 l / min
Remaining oxygen:	approx. 0 – 0.2% while operating
Laser beam compensation	0.16 mm
Layer thickness	typically 30 - 60 µm
Laser type	fiber laser 20 – 100 W
Wave length	1.070 µm
Spot diameter	5.4 mm (without F-Theta Lens) [95] Focused min. 15 - 20 µm

The standard Realizer SLM-50 machine was updated using an F-Theta lens. This lens made it possible to keep the focus spot constant while scanning. Without an F-Theta lens, the spot diameter would be different at the outsides of the build chamber compared to the center. Figure 5 depicts the machine consisting of build chamber, laser source, computer interface and powder feeding unit.



Figure 5: Realizer SLM 50 desktop machine

3.3 Path to thin walled, hollow parts

Due to the size of the chamber, there were some limitations in specimen production. Nevertheless, for the manufacturing of tracks and walls, different parameters could be varied that were not affected by the geometrical limits.

The first step was optical inspection while manufacturing (microscope available) and after manufacturing. Microscopy of the specimen detected cracks and porosity. Additionally, the researcher could pay attention to the optical impression (adherence of powder material, buckling, balling, annealing colors, evaporated material etc.). These properties could be documented using microscope cameras and were needed to improve the weld pool stability.

3.4 Design of experiments to detect parameter fields

Filling the gap between single dots, single hatches, single areas, and solid freeform fabrication, Design of Experiments (DoE) was applied. Since fundamental research was necessary, a full factorial design or the response surface method could be applied.

Both, for obtaining solid parts with high density and for thin, hollow sections, the understanding of producing single lines is fundamental. Those lines are helpful in understanding the manufacturing of planes and single surfaces, finally resulting in additive layers. If the first lines show poor manufacturing traits, the next line built on top will show poor properties again. This may result in failure propagation and consequences can be that the process must be stopped and started again. Therefore, an analytic approach for the investigation of a new material should start with single lines. Previous researchers covered this problem in a similar manner, but with different materials (see section 2). For a Design of Experiments approach, the understanding of effects is fundamental. Table 7 depicts a selected, fundamental parameter overview with different effects. It should be noted that the individual tests were conducted under certain

constraints. Therefore, it would be necessary to pay attention to the literature, mentioned in the last column.

Table 7: Fundamental parameter overview

Property	Effects if increased	Effects if decreased	Source
Energy input	increases density until certain limit		[56]
Energy input	decreases density if too high (due to cracks etc.)		[56]
Hatch distance	decreases density		[5]
Hatch distance		increases density	[56]
Laser power	increases density		[5, 56]
Layer thickness		increases density	[5]
Layer thickness	decreases density		[56]
Oxide layer on the particle sphere	increases absorption		[97]
Oxygen content in gas chamber	larger droplets		[21]
Oxygen content of powder	increases melt pool length		[21]
Particle size distribution		increases density, unstable	[56]
Particle size distribution		higher sintering activity	[97]
Particle size distribution	higher absorption increases temperature		[97]
Particle size distribution		increases reflectivity	[97]
Particle size distribution		leads to agglomeration	[54]
Powder size		increases density	[98]
Scan rate	increases density		[56]
Scan speed	decreases Linear energy density		[5, 61]
Scan speed	intermediate: balling, high speed: droplets	no balling	[21]
Scan speed	increases melt pool length, later decreases if too fast		[21]
Scan vector length	decreases density		[56]
Temperature	increases absorptance		[28]

3.4.1 Supply of powders and machinery

All researchers who work with powders need powder supply sources. Therefore, companies that are able to produce powder material were determined.

The next table lists some powder suppliers, but further suppliers might be available.

Table 8: Some powder suppliers

Company	Country
BASF	Germany
ChemPur Feinchemikalien und Forschungsbedarf GmbH	Germany
DODUCO GmbH	Germany
FINETEC Metallpuder GmbH & Co. KG	Germany
Hoeganaes	Sweden
Metalor Technologies SA	Switzerland
Osprey Metals	United Kingdom
Progold	Italy
Quebec Metal Powders Limited	Canada
Schlenk Metallpulver GmbH	Germany
TLS Technik GmbH & Co. Spezialpulver KG	Germany
State 2012-03-28	

The shape of the powders vary from spherical to more inappropriate shapes, depending on the manufacturing process. Literature distinguishes at least 15 other shapes. It was observed that gas atomized powders are mainly spherical whereas water atomized powders are irregular. [56]

Metal powder bed fusion machinery is available from many suppliers. Table 9 lists some major suppliers who operate world-wide.

Table 9: Some machinery suppliers

Company	Country	web
3D-Micromac AG	Germany	http://3d-micromac.de/
3D Systems	United States	http://www.3dsystems.com/
Arcam AB	Sweden	http://www.arcam.com/
CONCEPT Laser GmbH	Germany	http://www.concept-laser.de/
EOS GmbH	Germany	http://www.eos.info/
Phenix Systems	France	http://www.phenix-systems.com/
Realizer GmbH	Germany	http://www.realizer.com/
Renishaw plc	United Kingdom	http://www.renishaw.com/
Sintermask GmbH	Germany	http://www.sintermask.com/
SLM Solutions GmbH	Germany	http://www.slm-solutions.com/
See also [99]		
State 2012-03-28		

Most companies that produce and sell machinery for Selective Laser Melting are situated in Europe, many of them in Germany. It can be expected that the number of companies will continuously increase if the technology succeeds.

4 PRETESTS

4.1 Material AgCu7 from literature

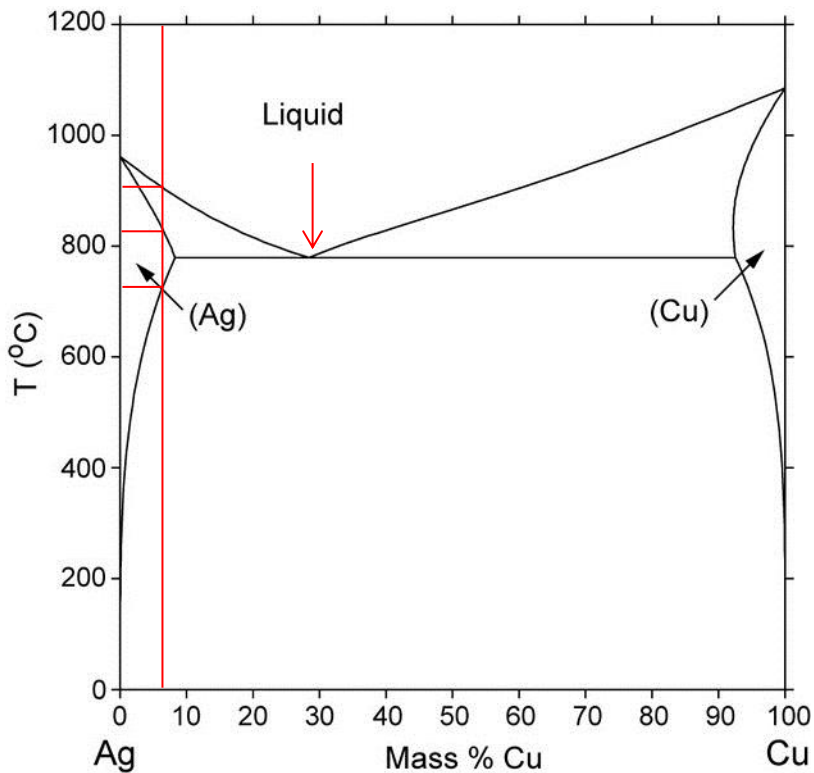


Figure 6: Alloy phase diagram system AgCu [100]

The material that was selected first was AgCu7, containing 7% copper. It can be seen from the alloy phase diagram that silver alloy AgCu7 is completely liquid above a temperature of 890 °C. Compared to pure silver, alloying with 7% copper reduces the liquidus line about 70 °C. Between 890 °C and 820 °C, liquid and α -mixed crystals can be expected. Furthermore, the alloy phase diagram

shows that between the temperatures of 730 °C and 820 °C, the entire phase consists of α -mixed crystals. Below that temperature, α -mixed crystals and β -mixed crystals can be expected.

Generally, alloy phase diagrams are designed for a stable, infinite time process. If the thermic equilibrium is not achieved, the phase lines can be shifted to other regions. Metastable systems were drawn by Beck et al. [44]

Digilov developed a prediction model to calculate the cohesion energy and surface tensions as function of the melting point. For silver and copper, both prediction models return good fits compared to experimental data. [101]

4.2 Material AgCu28 from literature

Considering figure 6, there is a eutectic reaction at 28.1% copper in silver, depicted with an arrow. It can be obtained from the alloy phase diagram that the energy that must be applied for liquidation will be less than for any other combinations of these elements. The melting point is at 779 °C. Below that point, all material will be solid and above that point, all material will be liquid. In comparison to the other combinations of silver and copper, there is no range of temperatures at which liquid and solid material coexist. AgCu28 is the second material that was investigated in this work.

4.3 Particle distribution tests for AgCu7

Before starting the test series, a particle size distribution was obtained from the material supplier and verified by in-house testing. The analysis showed

that the particle diameter had a mean of 27 μm and the standard deviation was 15 μm , as shown in figure 7.

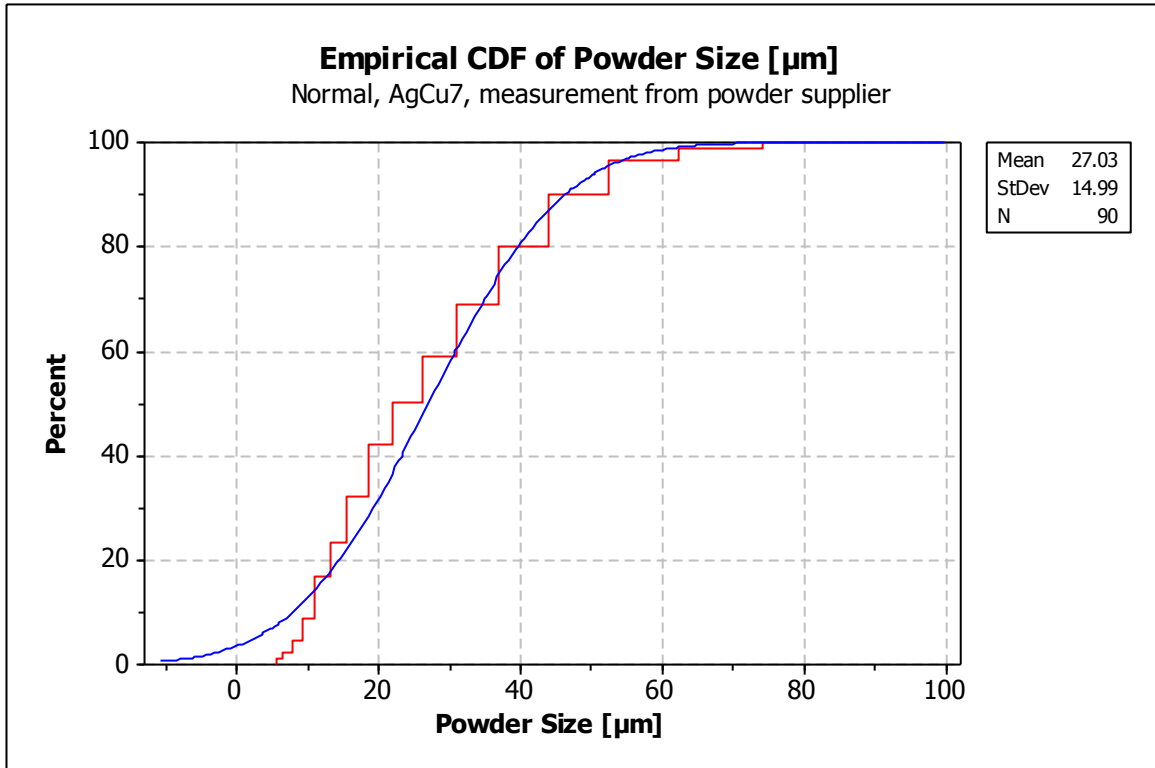


Figure 7: Data derived from powder supplier, AgCu7

4.3.1 Particle diameter test description

For the analysis of the particle diameter distribution, two different tests were conducted. The first test was laser scattering using a Micromeritics Saturn DigiSizer II (figure 8). This test procedure used a laser that could be adjusted in several angles. Scattering was detected by a CCD detector.³ [102] The specimen was prepared in a 40% sucrose dispersion. The second test was a sedimentation test using an X-ray unit that detected the absorption of particles in liquid medium

³ Information also provided by Mr. Horst Reichert, Micromeritics Analytical Service Europe

while settling by gravity. For this purpose, a SediGraph III V1.04 from Micromeritics was used, shown in figure 8. “Stokes law” was used for the particle diameter calculations.⁴ [103]

For each test, two levels were used. The first level was the original powder and the second level was powder that was prepared using a 20 μm sieve. The analysis of the coarse powder showed that the particle diameter had a mean of 26 μm and the standard deviation was 14 μm .



Figure 8: Laser fraction measurement (left) and X-ray sedimentation measurement⁵

For all particle diameter tests, the evaluation was carried out using MINITAB 16. Figure 9 shows the empirical cumulative distribution function. It can be seen that the range was comparably large. The laser fraction results were comparable to the results given by the powder supplier in figure 7.

⁴ Information also provided by Mr. Horst Reichert, Micromeritics Analytical Service Europe

⁵ Particle diameter test series and discussion of the results: courtesy of Mr. Horst Reichert, Micromeritics Analytical Service Europe

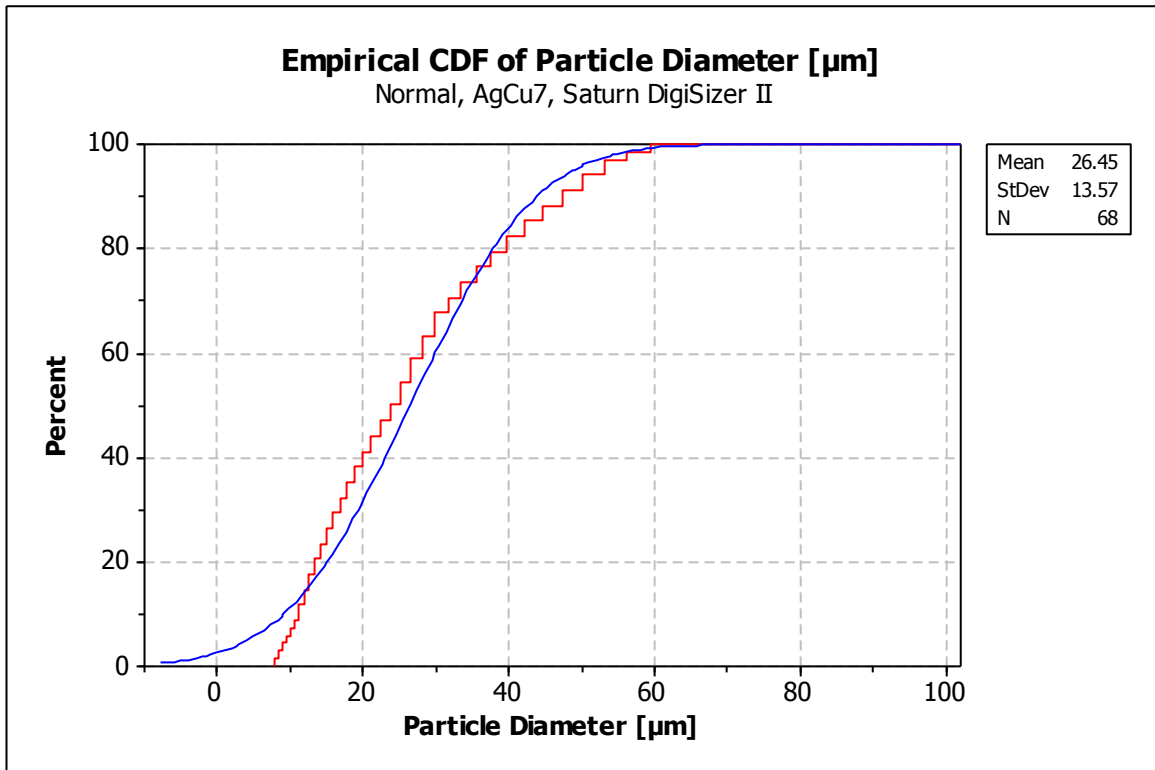


Figure 9: Empirical cumulative distribution function of particle diameter, coarse powder, AgCu7, laser fraction

The scatterplot shows that there was a peak between 20 µm and 30 µm, but the tails of the distribution showed coarse particle diameters (around 80 µm) at one side and very fine at the other side. (Figure 10). Please consider the appendices for a proportional depiction of different powder sizes.

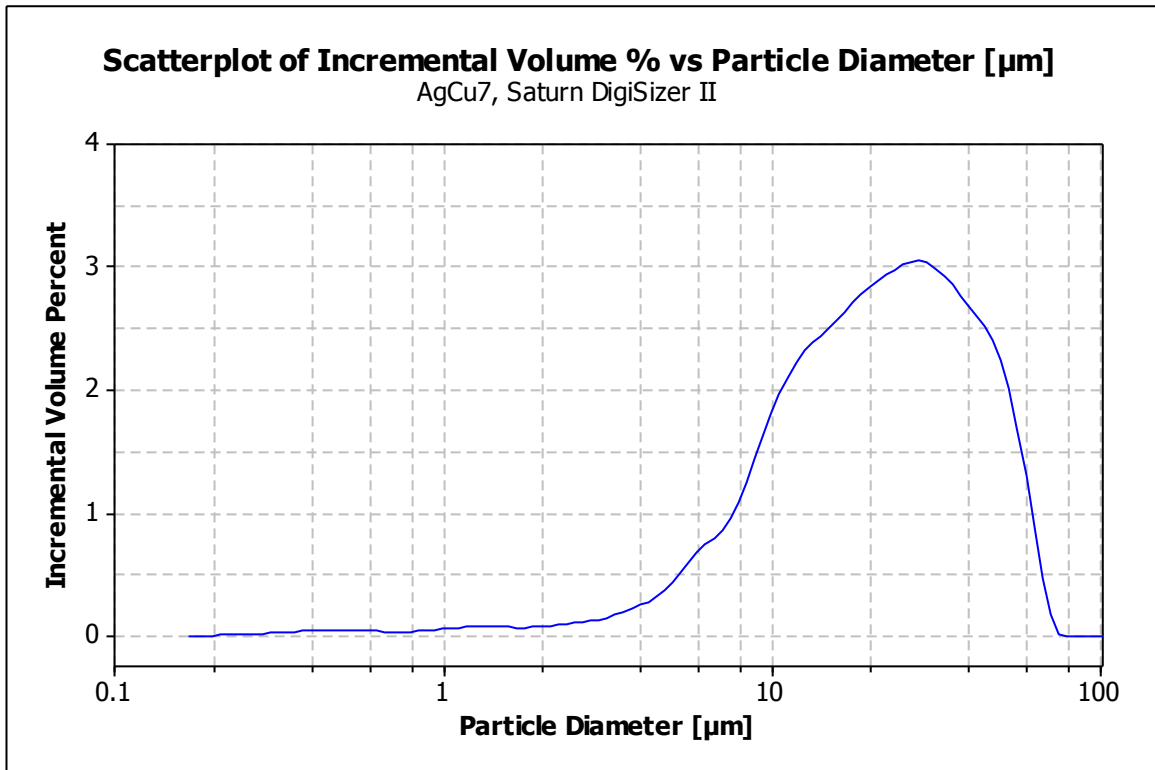


Figure 10: Scatterplot of particle diameter distribution, coarse powder, AgCu7, laser fraction

For the fine powder, the scatterplot shows a straight limit at 20 µm which was the limit of a sieve according to a standard test sieve. Figure 11 depicts that there is an indentation at 10 µm and some fine dust was detected. It cannot be excluded that due to the sieving process, the powder was mechanically milled a little bit and that the very fine powder that was evenly distributed before sieving, was collected in the sieving specimen since it had less mechanical resistance pouring through the sieve mesh. A mean value of nearly 9 µm was determined.

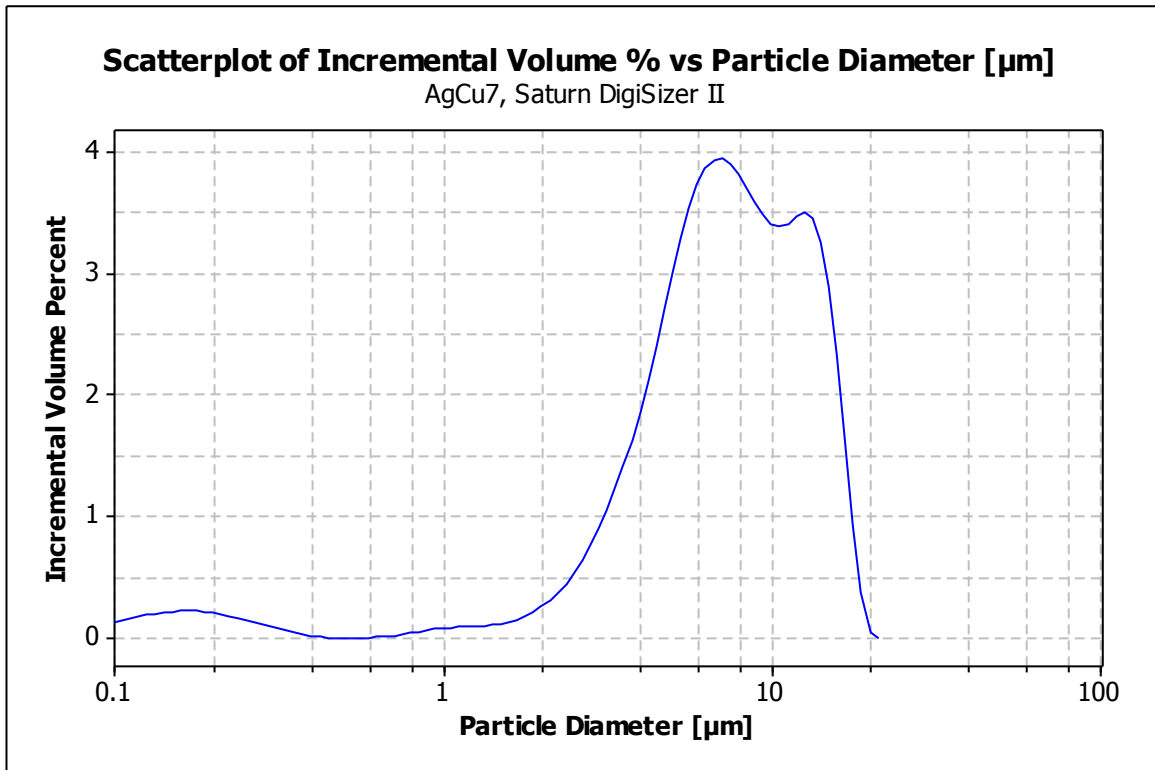


Figure 11: Scatterplot of particle diameter distribution, fine powder, AgCu7, laser fraction

The empirical distribution function of figure 12 and figure 14 are rather similar, although two different physical measurement types were used. It can be expected that there are slight differences because the laser fraction was dependent on the orientation of the small and large axis of the particle if the powder is not exactly spherical. As opposed to this, the sedimentation technology averaged the diameter and measurement failure increased with finer powder.

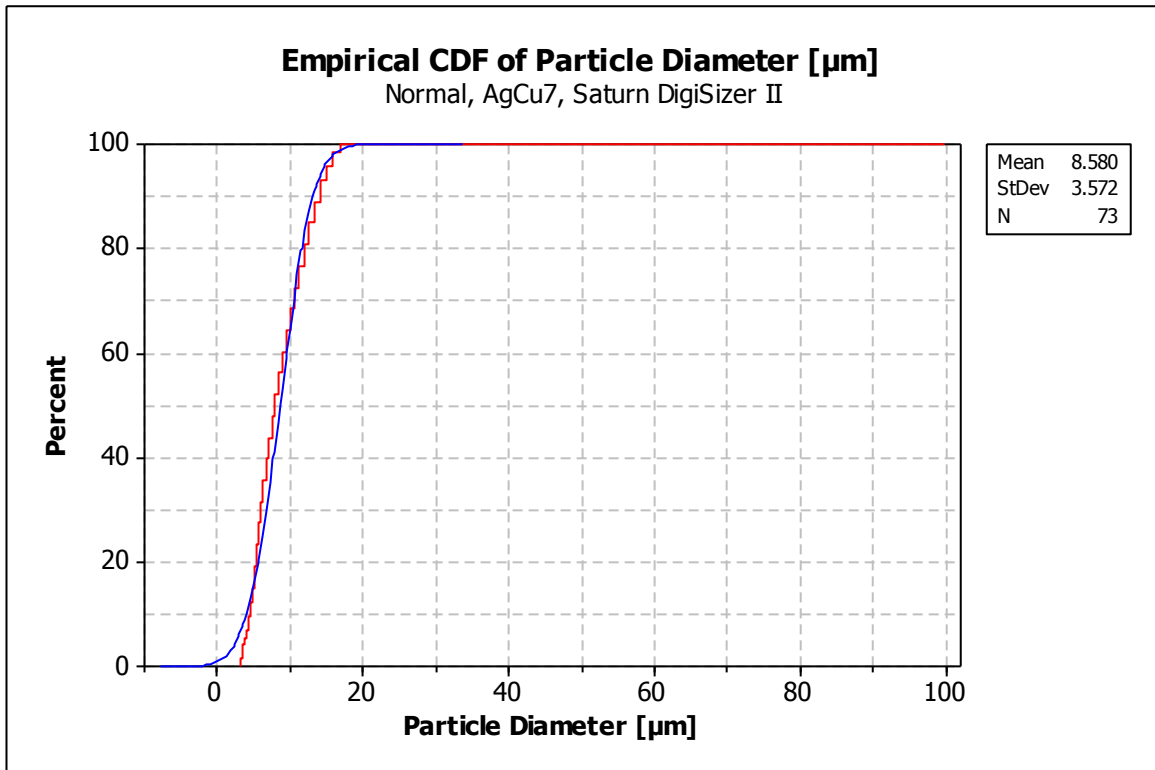


Figure 12: CDF of particle diameter, fine powder, AgCu7, laser fraction

Figure 13 shows that there was a small amount of particles with a larger diameter than 20 µm. Within the accuracy of the sieve, it could be concluded that these particles obtained at least one axis with a diameter of 20 µm so that the powder fit through the mesh.

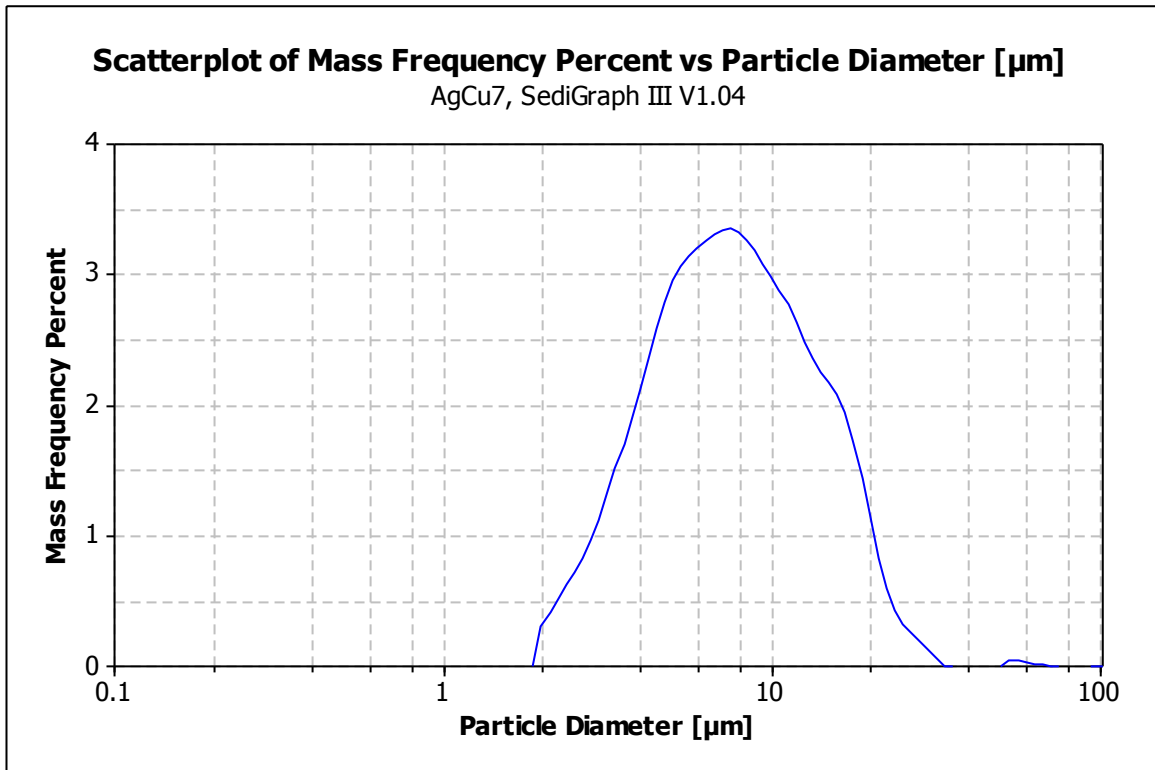


Figure 13: Plot of particle distribution, fine powder, AgCu7, sedimentation technology

Figure 14 shows the empirical cumulative distribution function of the fine powder, measured with the sedimentation technology. As previously stated the mean value was measured as approx. 9 μm with a standard deviation of 4 μm.

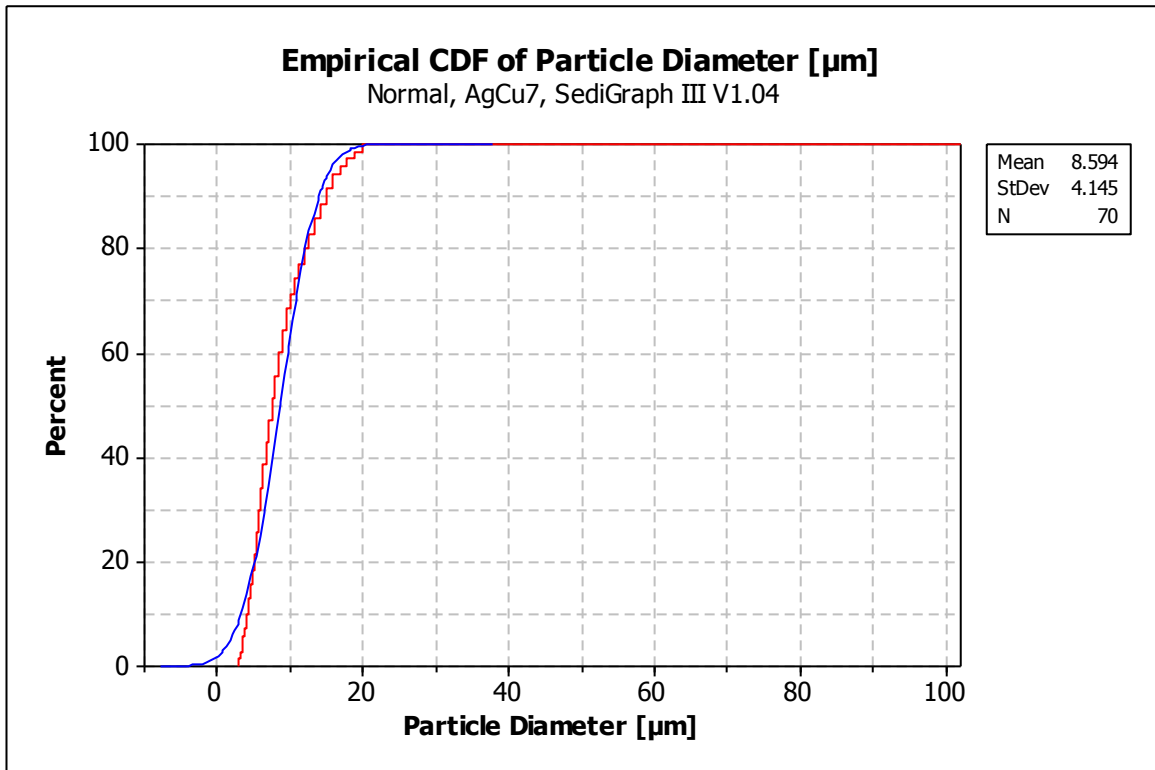


Figure 14: Plot of CDF, fine powder, AgCu7, sedimentation technology

Comparing the results, it was shown that both test methods led to similar particle diameter distributions. The mean of the original powder was the same value as data provided by the supplier. Furthermore, the result was obtained that sieving was a very effective technology since there was no significant increase in diameter beyond 20 µm.

4.3.2 Particle diameter tests for AgCu28

For the analysis of AgCu28, laser fraction and the sedimentation technology were used. For laser fraction, a Micromeritics Saturn DigiSizer II was used, whereas for the sedimentation technology, a Micromeritics Sedigraph III

was used. Figure 15 shows the scatterplot of the particle distribution, measured with sedimentation technology.

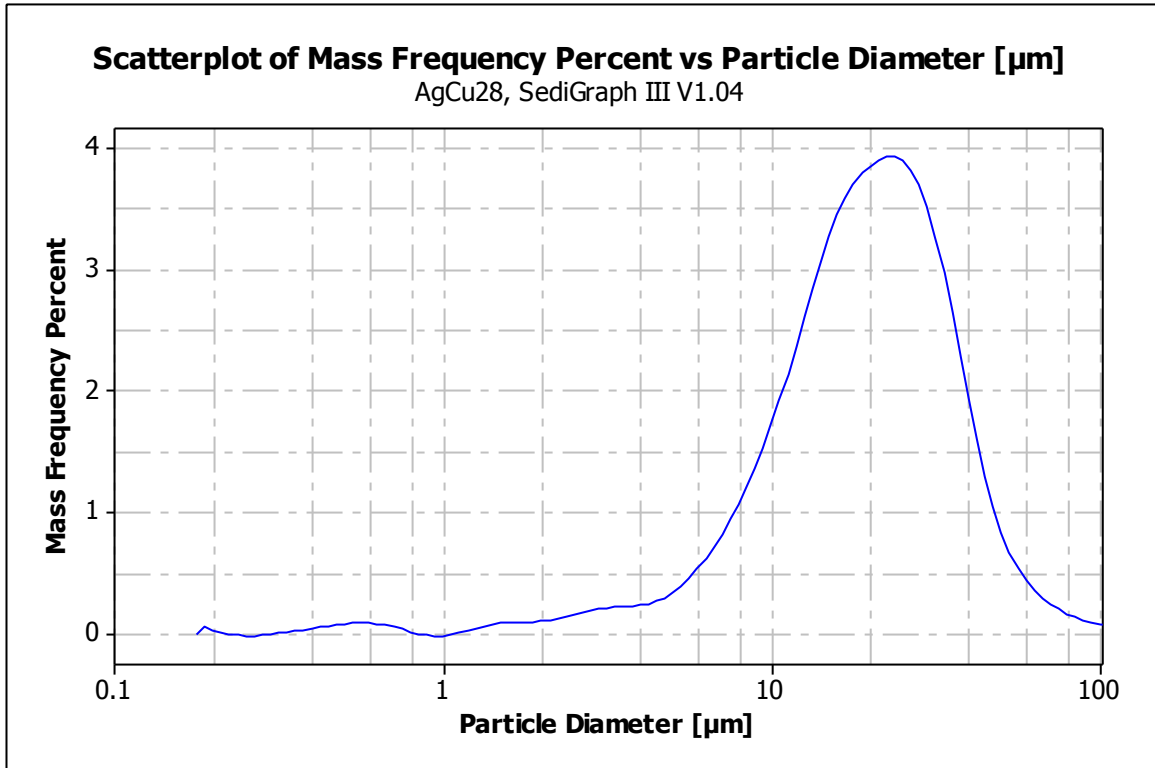


Figure 15: Plot of particle distribution, AgCu28, sedimentation technology

Using the sedimentation technology, the scatterplot of AgCu28 shows particle diameters between approximately 1 and maximum 100 μm. The peak of the graph is around 25 μm (figure 15). In comparison, figure 16 shows the scatterplot of the particle diameter test using laser fraction. In comparison to the tests of AgCu7, a significant difference in the distributions could be reported. The Sedigraph scatter plot was a mean of three different methods and was shifted to higher diameters due to early sedimentation of the fine powder particles. The laser fraction was independent of sedimentation.

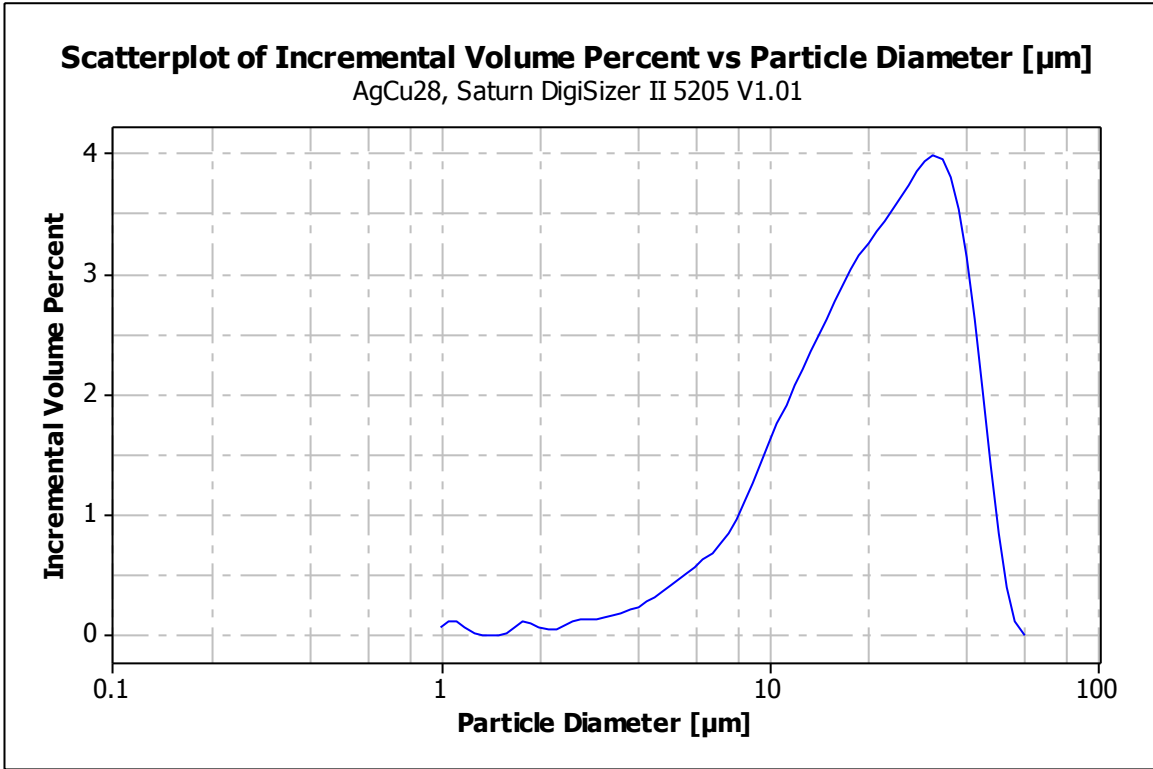


Figure 16: Plot of particle distribution, AgCu28, laser fraction

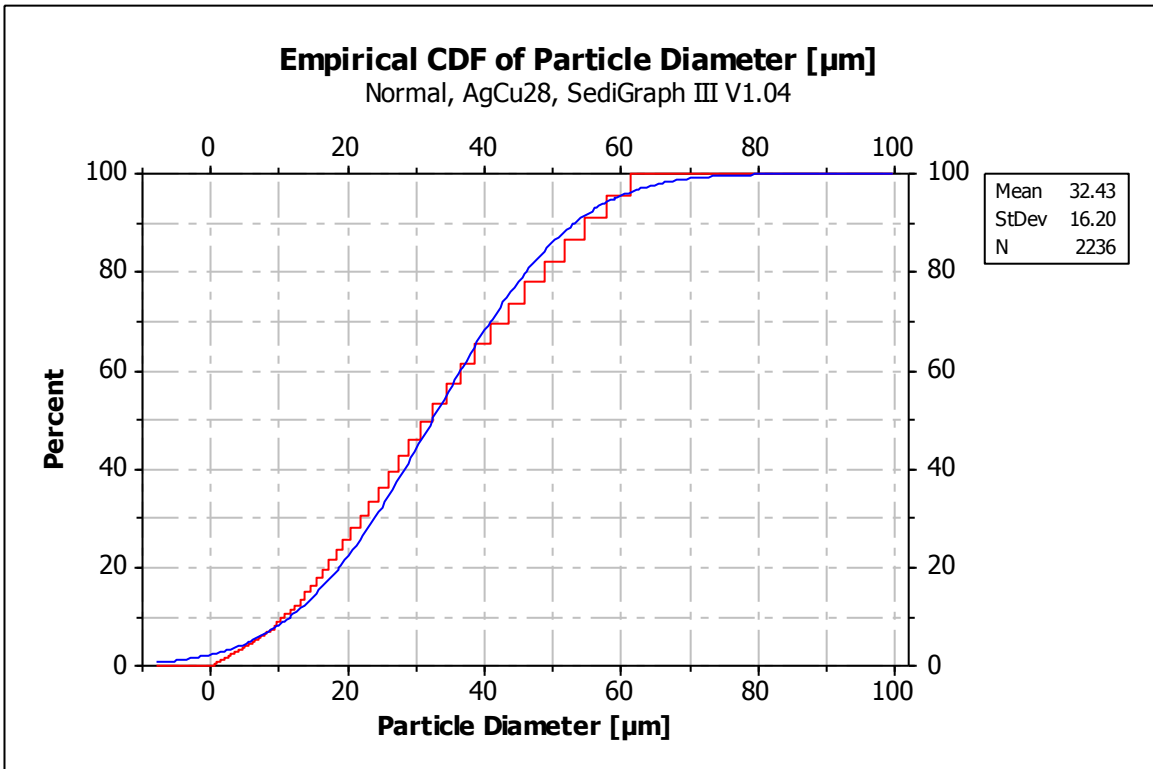


Figure 17: Plot of CDF, AgCu28, sedimentation technology

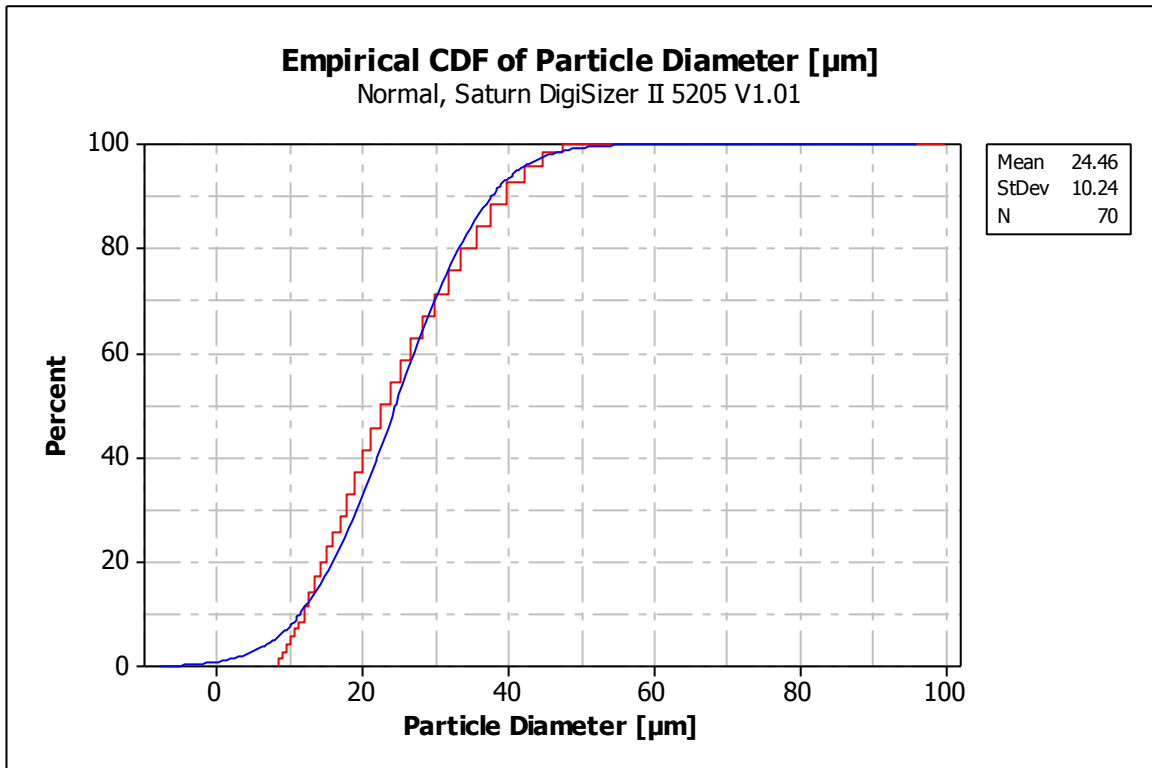


Figure 18: Plot of CDF, AgCu28, laser fraction

Figure 17 shows the empirical cumulative distribution function of the sedimentation experiment. The mean was approximately 32 µm and the standard deviation was approximately 16 µm. Figure 18 depicts the empirical cumulative distribution function of the laser fraction experiment. It shows a mean of 24 µm and a standard deviation of 10 µm. The specification of the material showed that the particle diameters should be below 45 µm, which was proved by the experiment. The measurement reports of the supplier (CILAS 920⁶) showed a mean of 25 µm which fit to the results of the laser fraction. For the assessments

⁶ Information provided by Mr. Phillip Ludwig, TLS Technik GmbH & Co Spezialpulver KG, Bitterfeld, Germany

of the tests, the mean of the laser fraction was used since it equaled the results provided by the powder manufacturer (TLS Technik GmbH).

4.4 Absorption tests

The next step was the detection of the absorption behavior of the silver powder. It is known that due to the highly scattering surface, the absorption rates of powders are different than that of plane, flat material. The surface conditions also influence the absorption behavior. The measurements were conducted using an Ulbricht ball and Michelson Interferometer. Figure 19 shows the test equipment and figure 20 depicts the measurement plots. Once the background scan was conducted, the machine ran 64 measurements and averaged the points after subtracting the background scan.



Figure 19: Ulbricht ball and Michelson interferometer

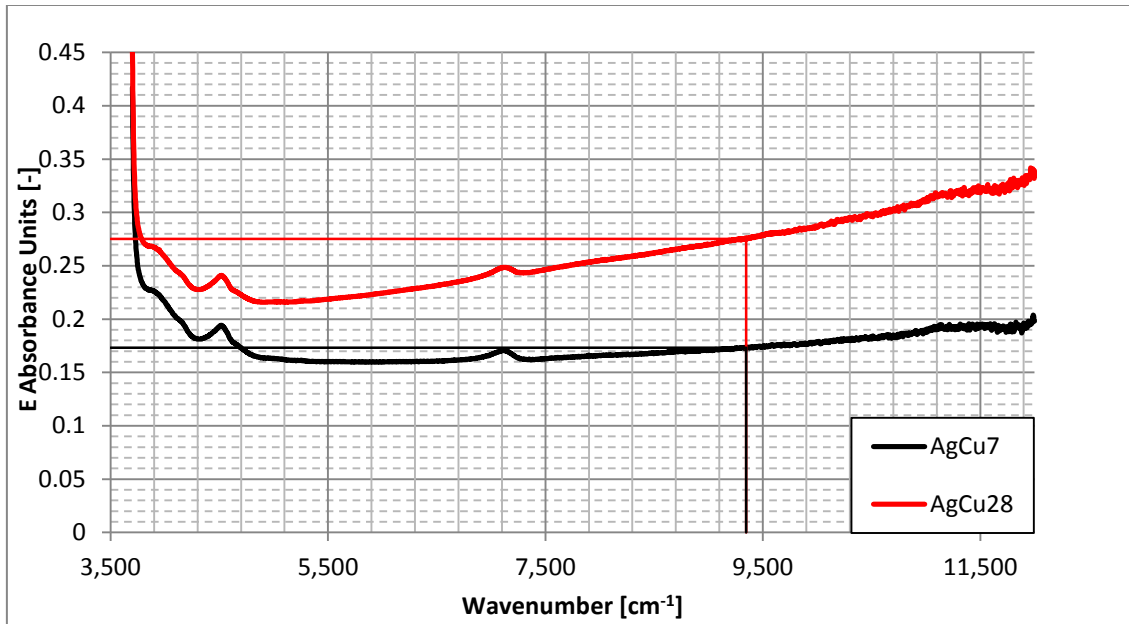


Figure 20: Absorbance measured for the test probes AgCu7 and AgCu28

In figure 20⁷ the wave number is plotted versus the absorbance units (dimensionless). The wave number is proportional to the frequency. Hence, it is also proportional to the energy. That is the historic reasons for using wave numbers instead of directly using wave lengths. The wave length (λ) of interest can be expressed as:

$$\lambda = 1,070 \text{ nm} = 1.070 * 10^{-4} \text{ cm}$$

Equation 16: Wave length

The wave length is simply the reciprocal of the wave number (ν):

$$\nu = \lambda^{-1} = 9345.79 \text{ cm}^{-1}$$

Equation 17: Wave number

⁷ Absorption measurements and discussion of the results: courtesy of Prof. Gereon Elbers / FH Aachen University of Applied Sciences / department Jülich

For AgCu7, we find from the graph that absorbance units are 0.173.

Using Lambert-Beer law, we find the extinction (E):

$$E = -\log\left(\frac{I}{I_0}\right) = -\log(T)$$

Equation 18: Lambert-Beer law

The calculation of the transmission (T) returns:

$$T = 10^{-E} = 10^{-0.173} = 0.67143 \approx 67\%$$

Equation 19: Calculation of transmission

The absorption is simply the balance to 1 and in this case, it equals 33%. Compared to other materials, this value is not very high for this value of interest. For AgCu28, we find from the graph that absorbance units are 0.275. The calculation of the reflection returns 0.53, so that the absorption yields to 0.47.

For single component powders, different absorption rates were investigated by e.g. Tolochko et al. [91] (depicted as blue bars), Meiners [5] (depicted as white bars), and Khan et. al. [39] (depicted as yellow bar).

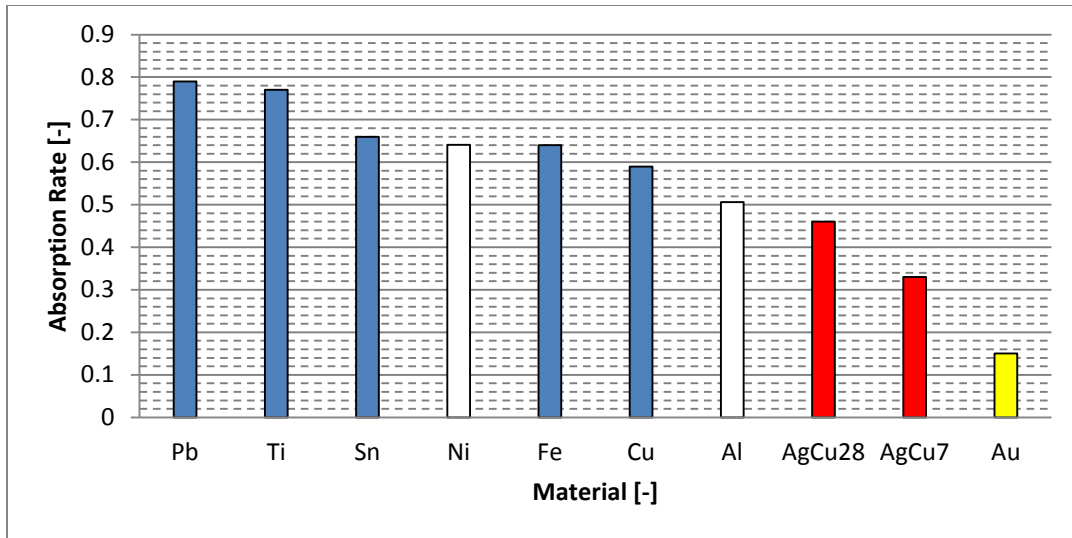


Figure 21: Absorption rates, literature values [5, 39, 91] compared with experimental measurements

Figure 21 shows the literature values compared to the values derived from the measurements mentioned before. Both silver alloy absorption rates were lower than the absorption rates of the other materials except gold. The absorption rate of AgCu7 powder is approximately half of the absorption rate of copper powder and approximately 40% of lead and titanium powder. It can be seen that the silver alloy AgCu28 (0.47), containing 28% copper, is approximately halfway between the absorption rates of AgCu7 (0.33) and pure copper (0.59).

4.5 EDX Analysis

EDX Analysis was conducted at ISF Aachen⁸. A Gemini LEO 1530 was used.



Figure 22: SEM and EDX analyzer Gemini LEO 1530

⁸ Measurements and discussion of the results: courtesy of Ellwyn Purrio, ISF Aachen

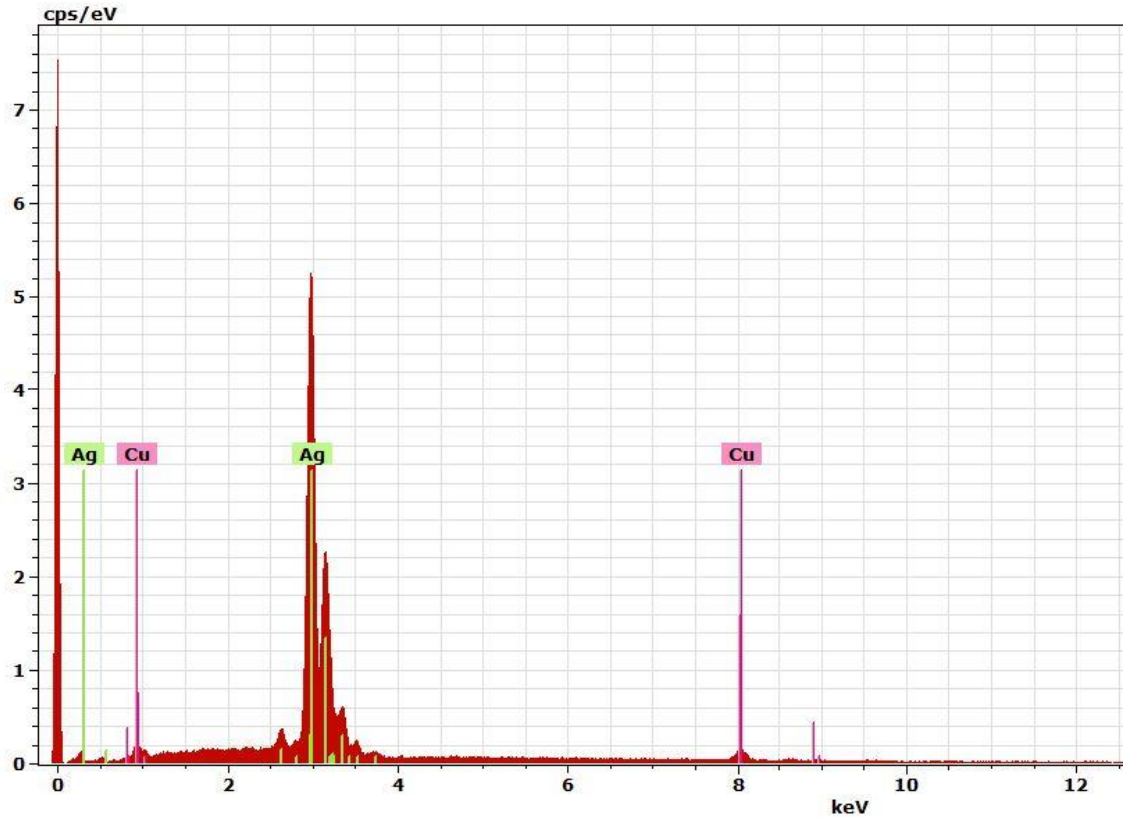


Figure 23: Spectrum of AgCu7

The spectrum of AgCu7 shows that the material consisted of silver and copper. Since the manufacturing method of this commercial powder was not exactly known, oxides or nitrates could be expected. Besides the main elements Ag and Cu, no other alloying element was detected.⁹

⁹ Measurements and discussion of the results: courtesy of Ellwyn Purrio, ISF Aachen

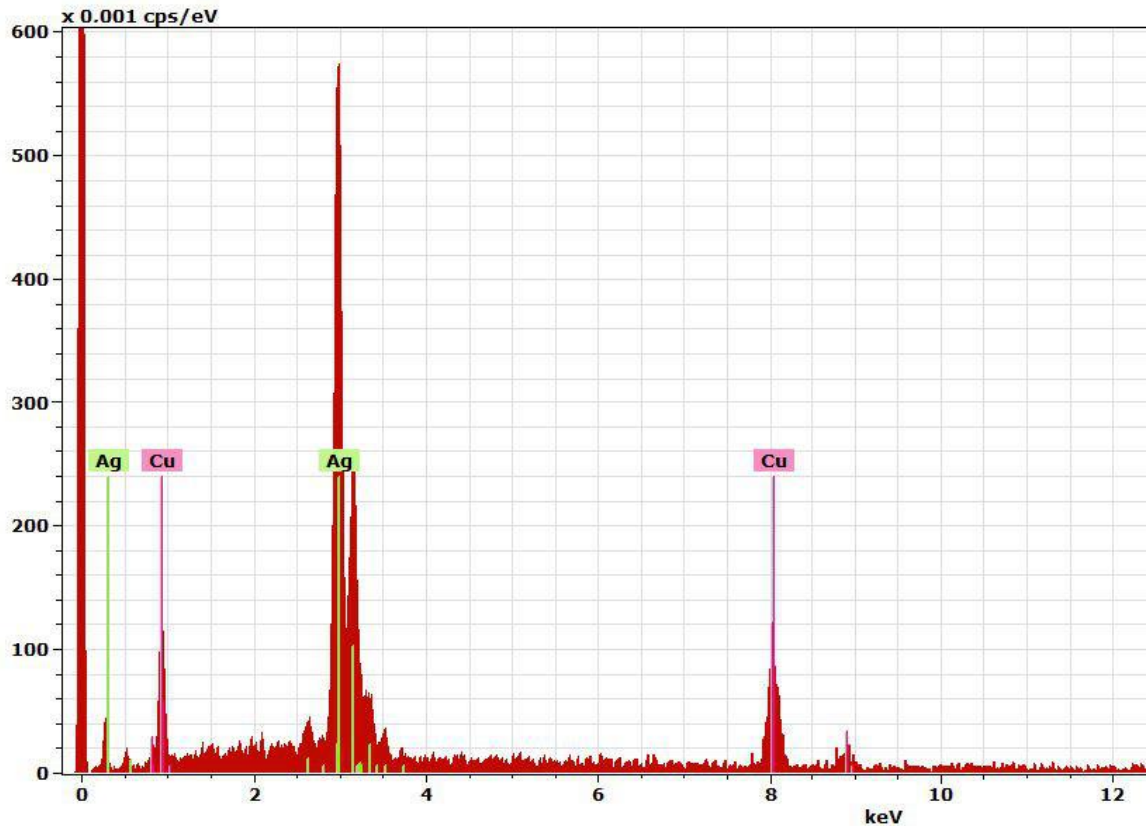


Figure 24: Spectrum of AgCu28

The spectrum of AgCu28 shows that the material consisted of silver and copper. Besides some background noise, no unexpected elements were detected.

4.6 SEM Analysis

SEM was conducted at ISF Aachen¹⁰. A Gemini LEO 1530 was used again.

¹⁰ Measurements and discussion of the results: courtesy of Ellwyn Purrio, ISF Aachen

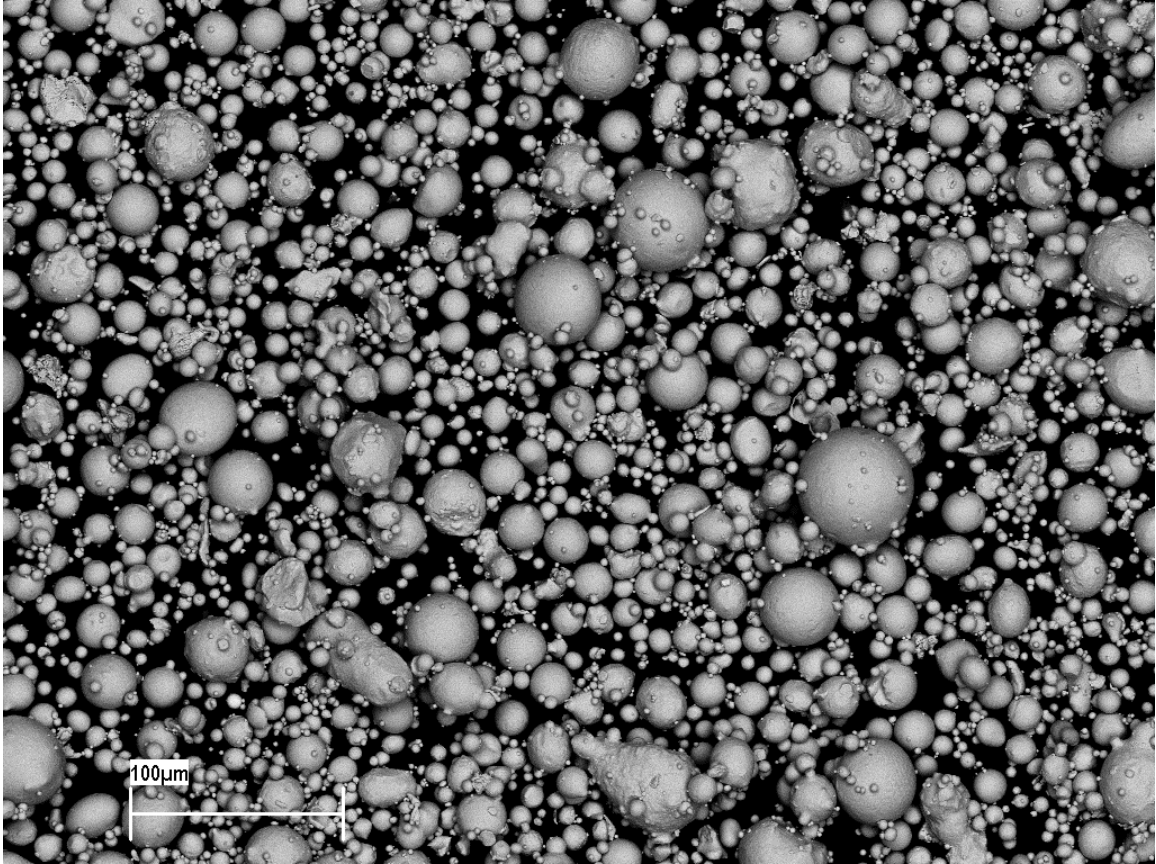


Figure 25: SEM of AgCu7, topography, magnification 500-fold

The topography of AgCu7 shows that the shape of the material was spherical as is typical for a gas sprayed powder. The size of the spheres fit to the results obtained from the particle diameter distribution function.

Table 10: Chemical analysis (spectrum) of AgCu7

Element	Atomic number	Series	[Weight%]	[At.%]
Ag	47	L-Series	94.44	90.91
Cu	29	K-Series	5.56	9.09
		Total:	100	100

The spectrum of the AgCu7 sample shows that it contained slightly less copper than expected. The copper content was 5.56% which is 1.44% less than the 7.00% specified. The balance to 100% is 94.44% silver instead of 93.00% silver.

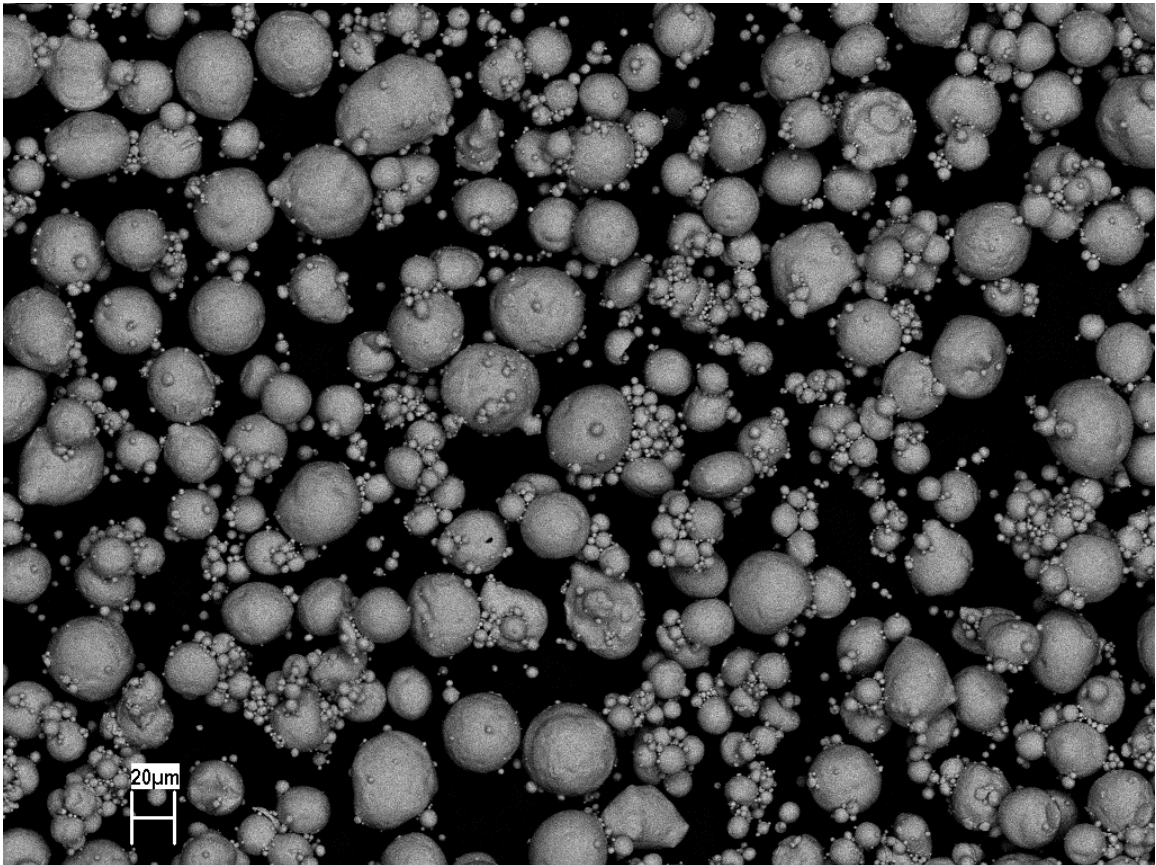


Figure 26: SEM of AgCu28, topography, magnification 500-fold

The topography of AgCu28 shows that the shape of the material was spherical. The diameter of the spheres appeared to be below 45 μm as measured in previous experiments. The topography fit the results obtained from the particle diameter distribution function.

Table 11: Chemical analysis (spectrum) of AgCu28

Element	Atomic number	Series	[Weight%]	[At.%]
Ag	47	L-Series	72.77	61.16
Cu	29	K-Series	27.23	38.84
		Total:	100	100

Table 11 shows that the sample consisted of 72.77% Ag and 27.23% copper. Therefore, the alloying mixture is close to the eutectic composition for AgCu.

4.7 Evaluation of first tracks

With the given information, first line scans were done. The pretests were conducted by the “additive manufacturing” work group at Aachen University of Applied Sciences. [104-109] Since the laser power was comparably low, a preexposure strategy was developed. The aim was the preheating of the spot via multiple laser spots. The number of laser pulses for the same area was varied between the levels two times, four times, and eight times. [108]

“Preexposure” means that the lines are scanned more than once, but the laser power was not necessarily the same for each scan. The preexposure connected powder particles so that the thermal conductivity was increased. It is known that the difference between the thermal conductivity of powder and of solid materials could be as large as a factor of 100. [107]

Initial tests were performed using a double scan strategy. For both runs, 20 μs pulse duration and 5 μm spot distance were used. First, two scans with 50 W laser power and 250 mm/s scan speed were applied. After that, two additional melting scans with 100 W laser power and 250 mm/s scan speed finished the track. [107]

The next step was the alternation of preexposure strategy. For this approach, the preexposure power was increased to 60 W and 70 W, whereas the other parameters were kept constant. The track width appeared more stable and varied between 60 to 70 μm . For both specimens, the weld pools appeared more unstable and the linear connection was unsteady compared to the 50 W preexposed parts. [107]

As a result, it was concluded that the combination of preexposure with 50 W laser power and multiple scans led to the best and thinnest boundaries that could be produced within this test series. For all scans, 20 μs pulse duration and 5 μm spot distance were used.

After that, two different powder size distributions were manufactured by separating coarse powder particles from fine powder particles. Further tracks were manufactured with 50 W, 60 W, and 80 W laser power. The tracks showed unstable melt pool behavior since powder particles were evaporated. [106]

Furthermore, the results showed that the preexposure strategy that was applied successfully for the coarse powder led to poor results for the fine powder. This result is comparable to the work of Morgan et al. [13] (See literature review chapter). Further research on this area was necessary.

4.8 Manufacturing of hollow section parts

Using coarse powder, the manufacture of closed parts and structures was accomplished. Figure 27 shows a wedge and ring that were manufactured using 30 μm hatch distance, 20 μs pulse duration and 5 μm spot distance. [104] The left picture shows the parts as-built, whereas the right picture shows the same parts in a polished version. The wedge was manufactured without any supports. The ring was produced in horizontal and vertical directions. The vertical production was much more accurate. [104]

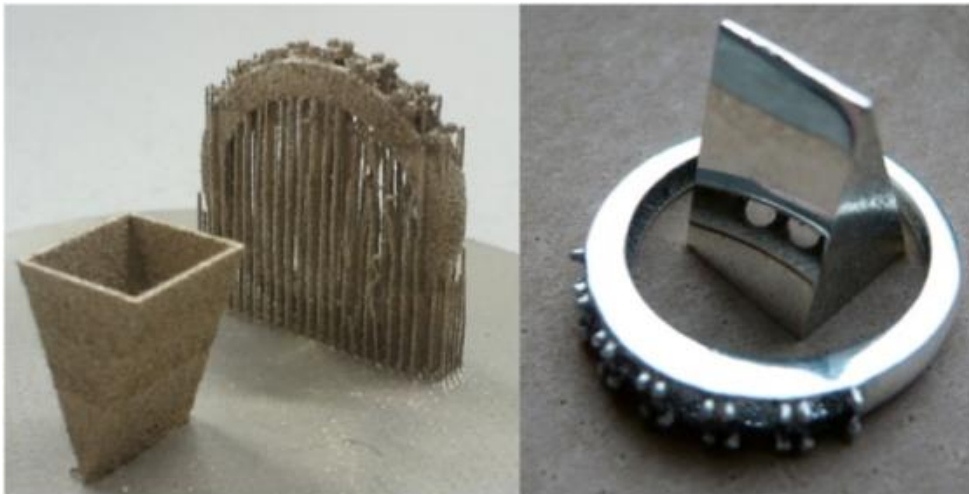


Figure 27: Wedge and ring [110] and [104]

The CAD-data of the bust of Nefertiti was used in previous work [111] and scaled down to fit it into the build chamber. The size is comparable to a regular chess pawn and the height is approximately 3 cm. Figure 28 shows two examples. The polished one can be seen in the image foreground whereas the unpolished version can be seen in the background. Both, the support structure under the chin is visible and the difference in colors due to the unpolished, rough surface compared to the highly reflective surface after finishing.



Figure 28: Silver Nefertiti, manufactured at Aachen University of Applied Sciences

Please note that the polishing of this kind of material with its high ductility needs special skills. Some samples were polished using the experience of a local gold smith. ¹¹

For a numerical comparison, a FEM code was made in order to calculate the heat balances in the weld pool, to compare the results with the predicted values, to match it with the literature and to plan the further experiments. The results of these comparisons and the tests were published in two different conference papers. [110, 112]

¹¹ Thanks to Georg Comouth, jewelry maker from Aachen, Germany

5 SCREENING EXPERIMENTS WITH AGCU7

5.1 Test set up

Based on the results described in sections 4.7 and 4.8, the investigation of AgCu7 continued with systematic parameter analysis. The aim was to eliminate preexposure since other materials were known to be processable without preexposure.

The test series was developed using Design of Experiments methods. Thin, hollow cubes were produced. The optical inspection was carried out using microscopy.

The cubes were arranged on a base plate and were produced using the same layer thickness for each base plate. Figure 29 shows the run order for test series 3 for 30 μm and 60 μm layer thicknesses and test series 4 for 30 μm and 60 μm layer thicknesses. Except for layer thickness, the run order was mixed independently using the randomize function in MINITAB. Randomized parameter sets were necessary in order to reduce the effects of parameters that are difficult or impossible to control. Since an asymmetric wiper system was used, it could be derived from the geometry that the wiper speed linearly increased with increasing radius. That means that the powder application speed was much higher at the outer part (far from the vertical rotating axis) of the build platform compared to the inner region. In order to reduce the effects of the wiper system, the surface of

the powder layer was smoothed by one additional wiping process (for a total of two cycles or four passes of the blade assembly over each portion of the build platform).

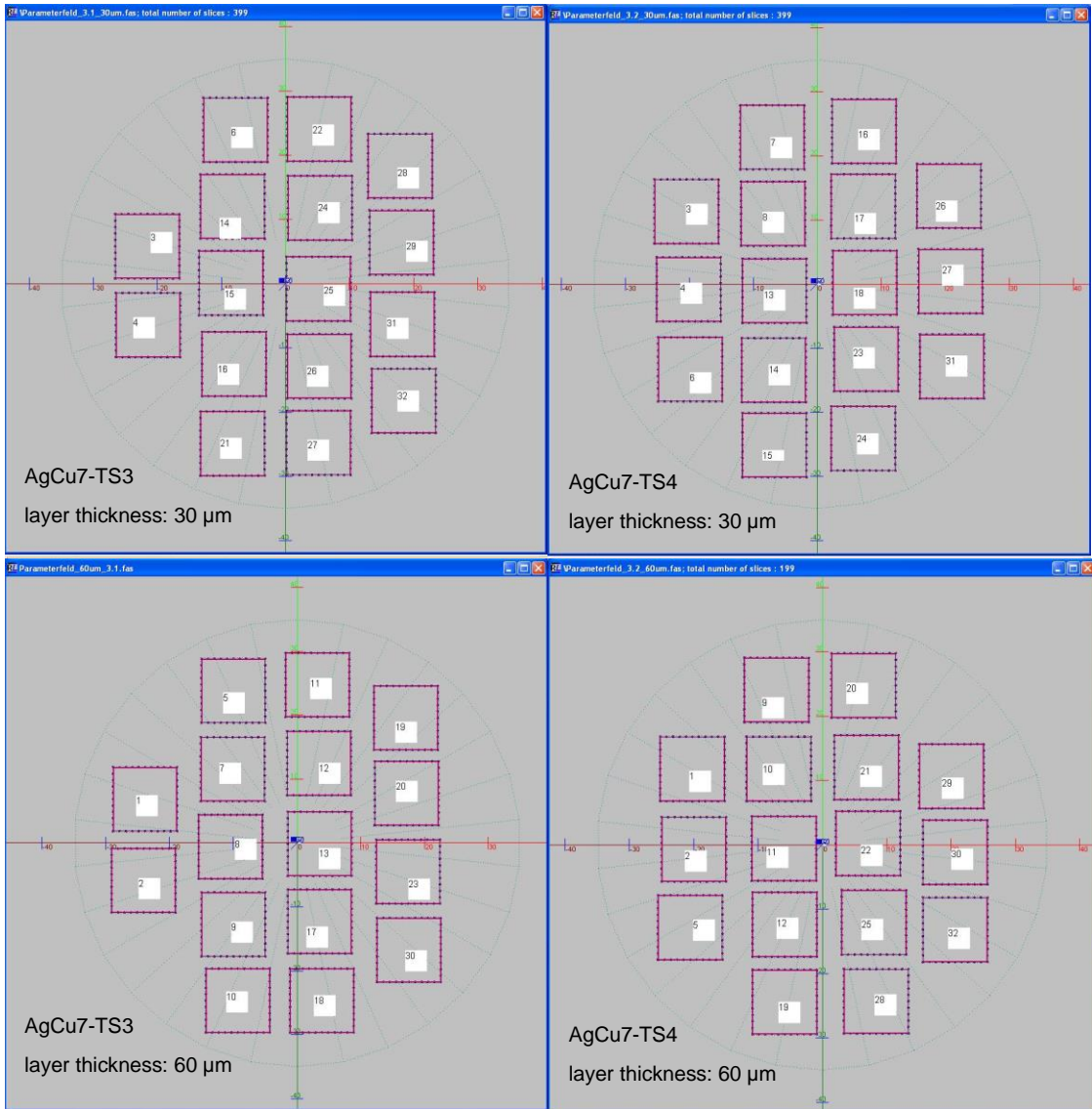


Figure 29: Arrays for test series 3 and 4, separated into 30 µm and 60 µm layer thickness

Milled base plates were used. The material was 1.4301 (X5CrNi18-10) which is an austenitic high alloyed steel with 18% Cr and 10% Ni. Additionally,

copper plates were tested, but no significant differences were observed. The surface was polished to roughness Ra 0.8 (according to DIN EN ISO 4287 Ra is the arithmetical mean deviation of the profile which is $0.8 \mu\text{m}$ or $32 \mu\text{inch}$) as shown in figure 30. [113]

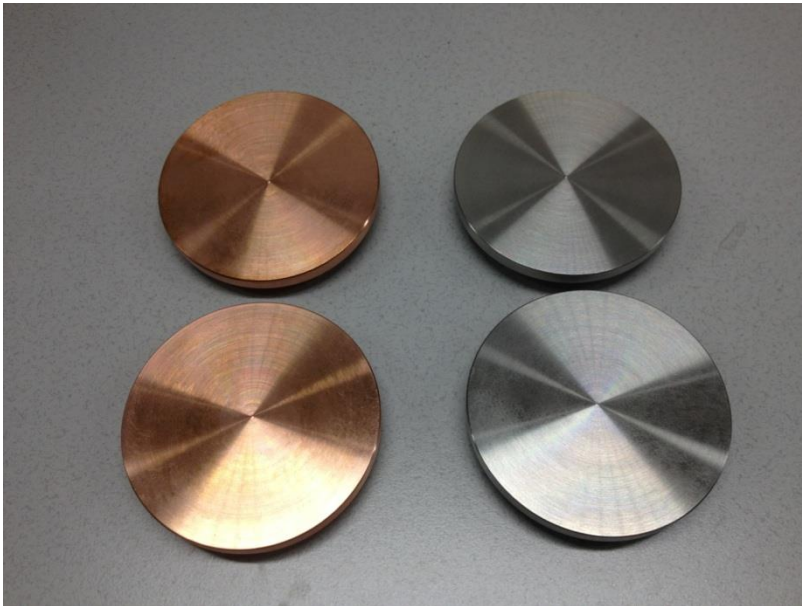


Figure 30: Unused, milled base plates (copper left, stainless steel 1.4301 right)

Figure 31 shows examples of arrays after cleaning for optical inspection. According to the arrays from figure 29, the parameters of the parts were mixed independently. After manufacturing, the base plates were labeled immediately to avoid misinterpretations.

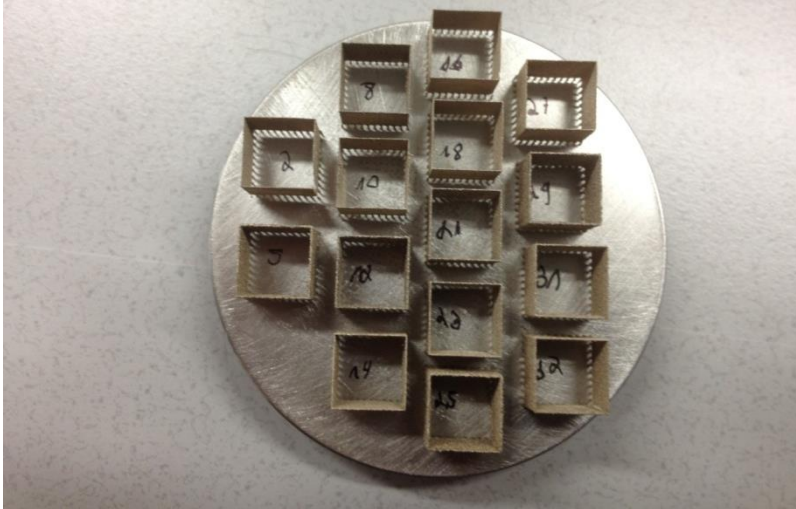


Figure 31: Example of manufactured parts after cleaning, test series 1, 30 μm layer thickness

5.2 Parameter fields

The machine was limited within the range of parameters that could be set up. The setup of the spot distance is shown in the next picture (figure 32). The parameter field was selected based on experience from the pretests (see chapter 4). It is known that the energy distribution of a focused laser spot can be Gaussian, depending on the modes. The illustration (figure 32) shows the proportional dimensions, assuming that the laser spot is a circle. The horizontal axis shows the distance that the laser is moved. The vertical array is valid for a spot distance of 5 μm , 7 μm , 15 μm and 20 μm .

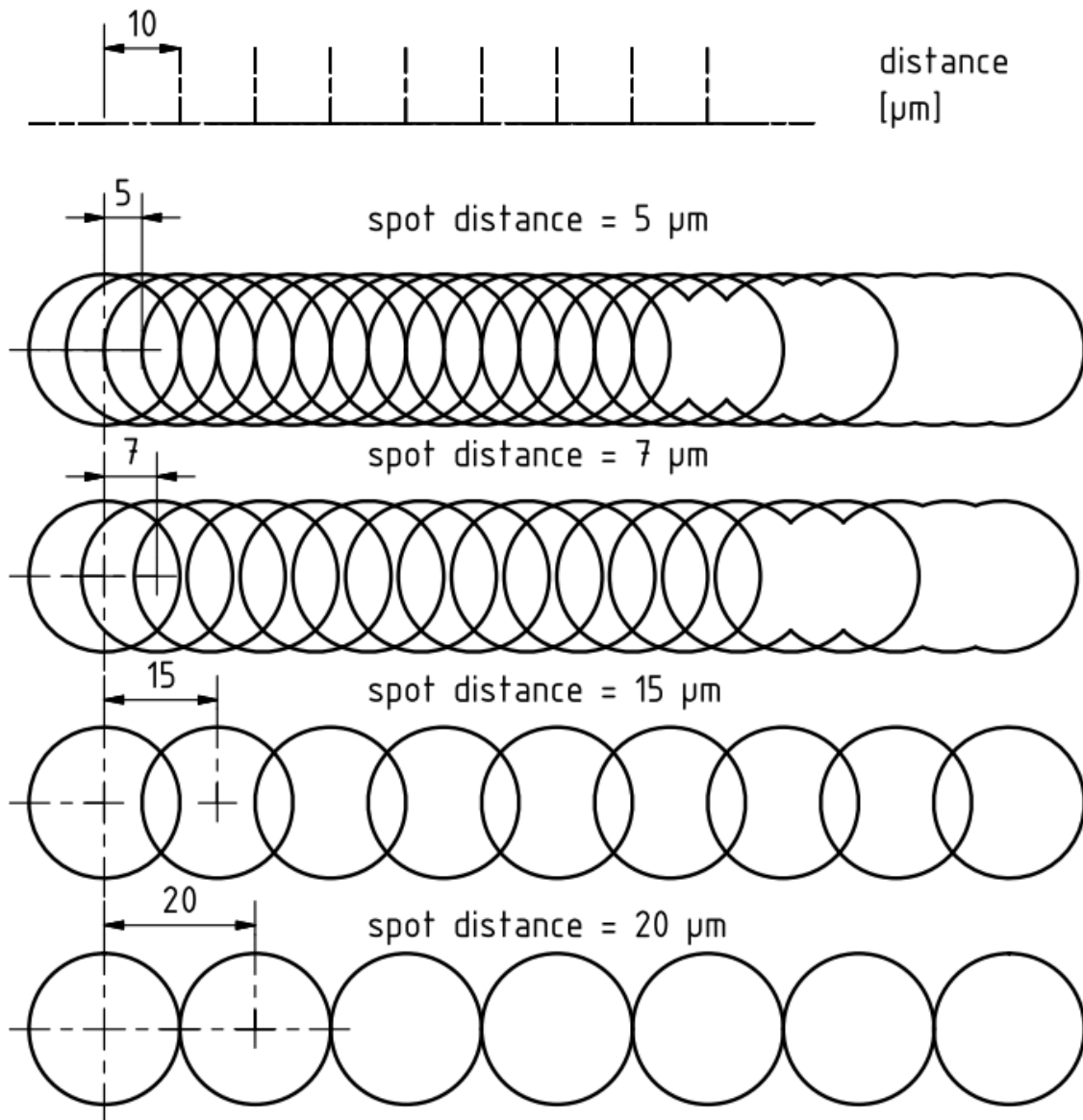


Figure 32: AgCu7- proportional scheme of overlapped spot distances for spot distances = 5 μm , 7 μm , 15 μm , 20 μm (top down)

In figure 32, areas exist where the laser spot is moved in steps which are so narrow that parts of the next spot circle overlap the previous circle. In figure 33, the graph from figure 32 is extended by a third axis that shows the addition of the overlaps. The distances between spots were increased until no intersections were found. The vertical axis represents the theoretical time of exposure:

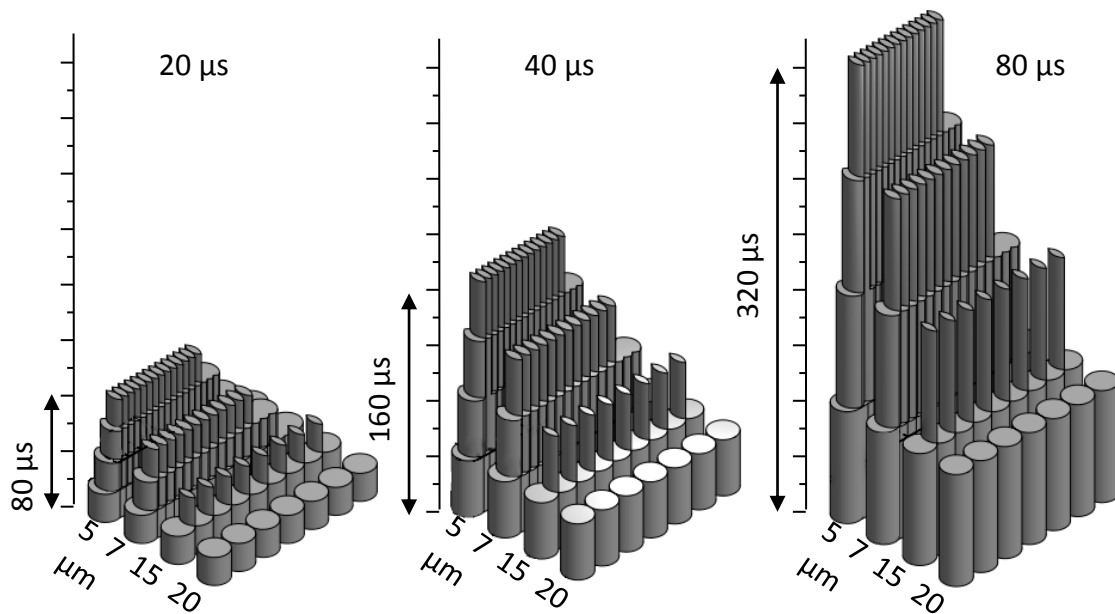


Figure 33: Scheme of exposures, peak time per spot for a pulse time = 20 μs, 40 μs, 80 μs (from left to right) and spot distances = 5 μm, 7 μm, 15 μm, 20 μm (top down)

5.3 Limits of scan speed and linear energy density

The machine could be adjusted using spot distances and pulse time. Pulse time could be changed in steps of 20 μm. Literature usually refers to scan speed and linear energy density as well. Mathematically, the scan speed can be calculated from the distance, the time that it takes to move the laser to the next spot and the time that it takes for the next fusion process. For an edge length of 10 mm, the scan speed can be calculated according to the next graphs.

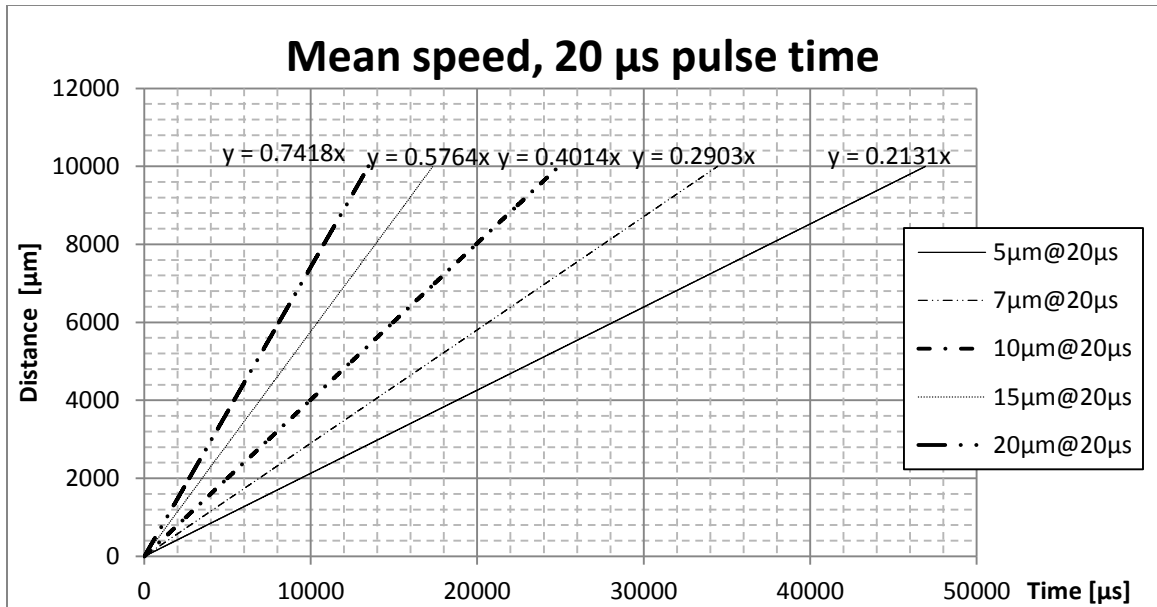


Figure 34: Mean speeds for 20 μs pulse time

Due to the resolution, the lines occur as straight lines. In fact, they are calculated using the following scheme: (figure 35).

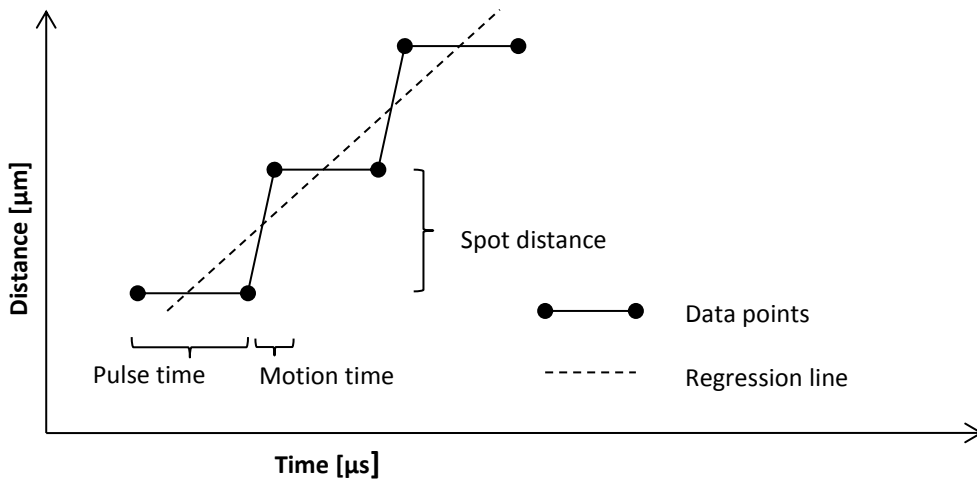


Figure 35: Regression of scan speed (scheme)

Figure 35 depicts the movement of the laser while operating. It started with a pulse at a certain spot with a horizontal line since the pulse occurred without distance movement. Next, the motion to the next spot occurred, giving a motion time over the spot distance where the laser stopped again until the pulse

time was completed. Between the data points, a regression line could be fit. The slope of the regression line represents the average scan speed. According to this scheme, the mean speeds were calculated and displayed in figure 36 to figure 38.

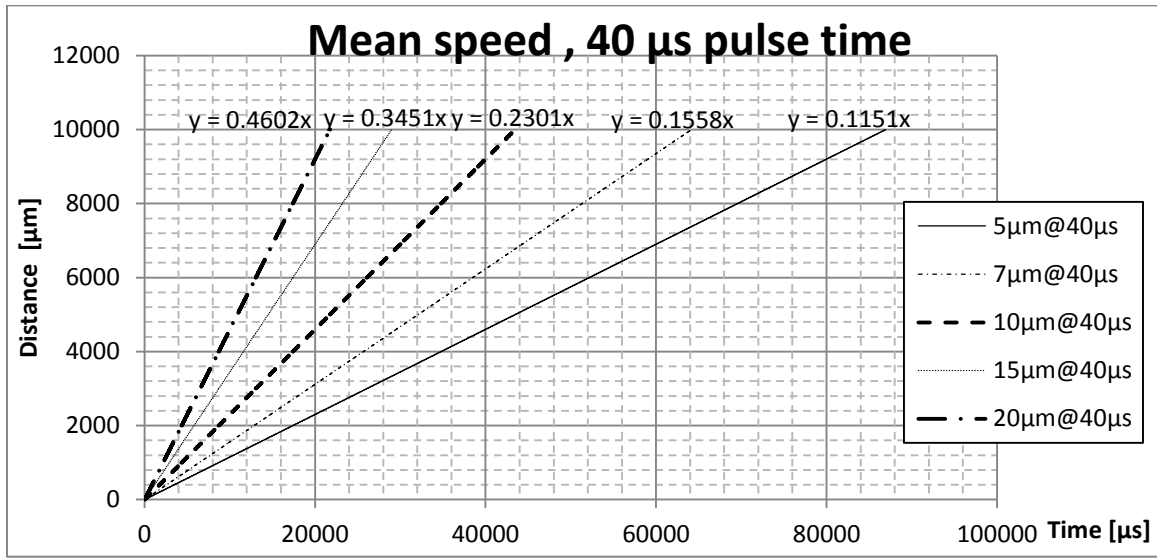


Figure 36: Mean speeds for 40 μs pulse time

For 40 μs pulse time, scan speeds between 115.1 mm/s and 460.2 mm/s could be achieved.

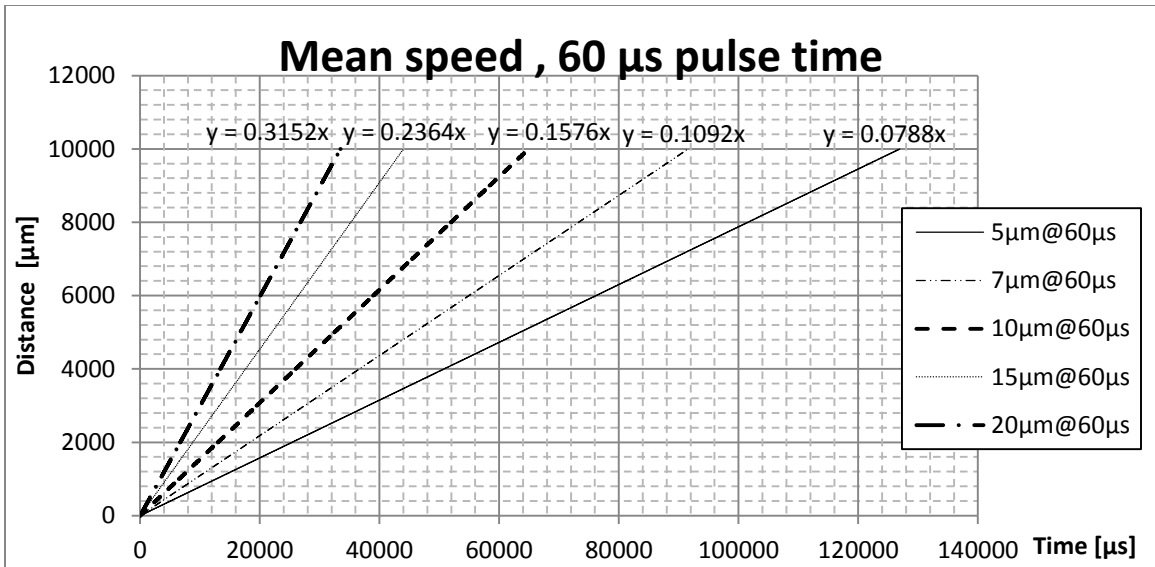


Figure 37: Mean speeds for 60 μs pulse time

Figure 37 shows that for 60 μs pulse time, scan speeds between 78.8 mm/s and 315.2 mm/s could be achieved.

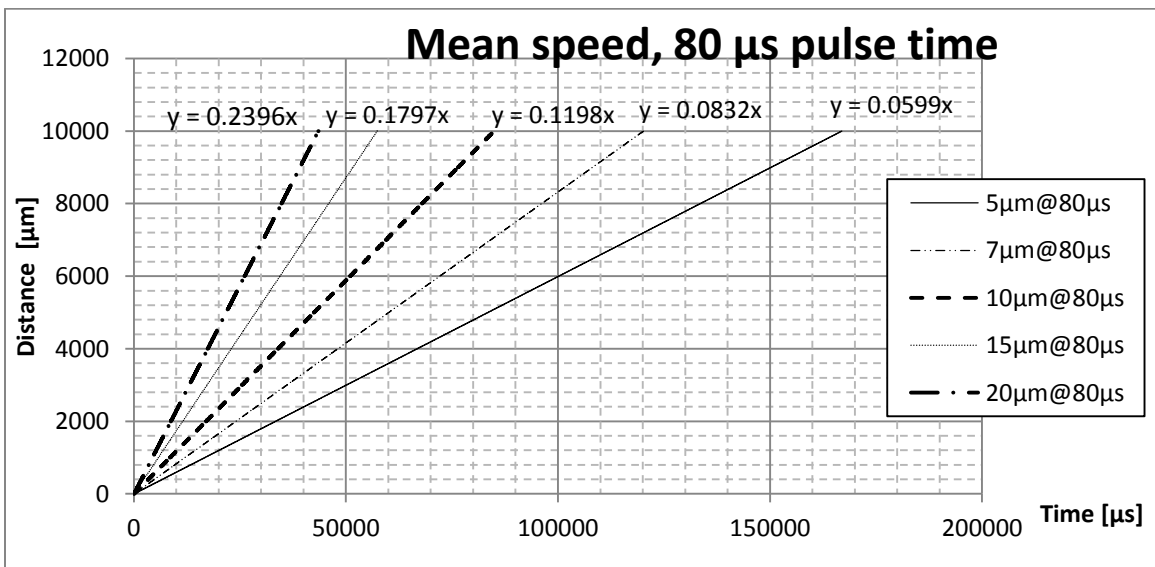


Figure 38: Mean speeds for 80 μs pulse time

Figure 38 depicts the lowest range of scan speeds that were chosen for the tests. For a pulse duration of 80 μs , the nominal scan speed was 59.9 mm/s

for 5 μm spot distance and was 239.6 mm/s for 20 μm spot distance, respectively.

In table 12, the scan speeds of figure 36 to figure 38 are summarized.

Table 12: Summary of scan speeds

spot dist. [μm]	pulse time [μs]	20	40	60	80
	scan speeds [mm/s]				
5		213.1	115.1	78.8	59.9
7		290.3	158.8	109.2	83.2
10		401.4	230.1	157.6	119.8
15		576.4	345.1	236.4	179.7
20		741.8	460.2	315.2	239.6

The difference between e.g. scan speed of 230.1 mm/s (10 μm spot distance at 40 μs pulse time) compared to the scan speed of e.g. 239.6 mm/s (20 μm spot distance at 80 μs pulse time) yielded different material property results although the nominal scan speed difference was only 4%.

5.4 Analysis of produced samples- microscopy

5.4.1 Measurement of surface porosity

The samples were investigated at Aachen University of Applied Sciences using a digital microscope with CCD camera (supplier Keyence, VHX-100 with Keyence VH-Z20 and its on-board inspection software package).

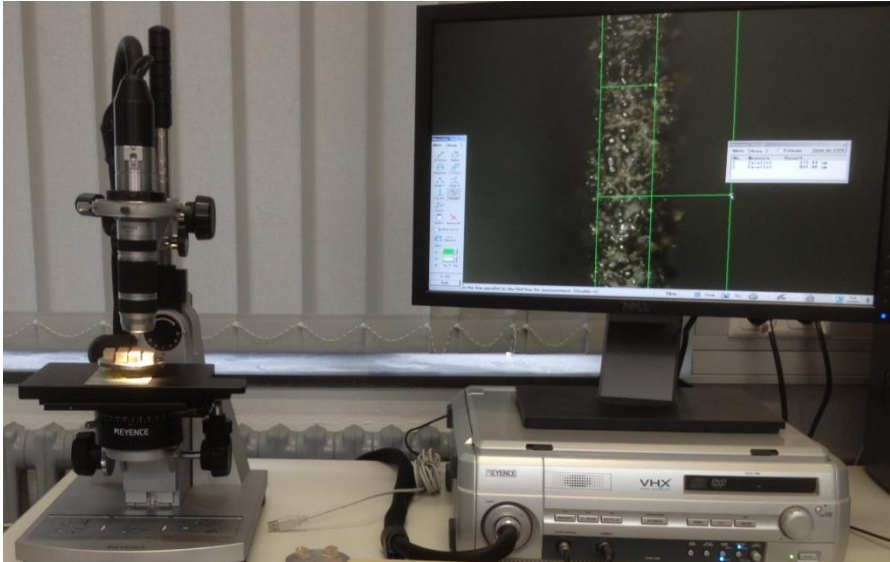


Figure 39: Digital microscope Keyence VHX-100, VH-Z20 with inspection software
 The following scheme shows a section of the test specimen:

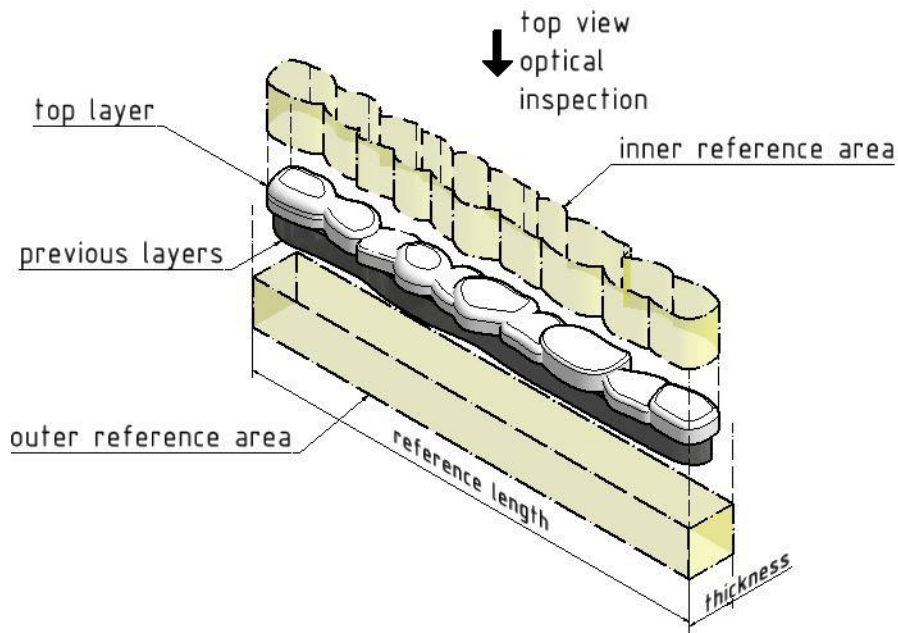


Figure 40: Scheme of optical inspection

Within the focus of the microscope, an area was created using two parallel lines, adjusted at the outer borders of the layer. A reference thickness could be measured between these lines and hence a reference area could be

calculated. In figure 40, the outer reference area is shown at the bottom (rectangular area). After that, the area of the molten layer is measured. In figure 40, this area is shown as the inner reference area. The balance to one of the ratio of inner and outer area returns the “surface porosity”, which was an approach to assess single tracks with numerical values. These values could be used for statistical analysis and selection of the screening experiments for further investigation. Figure 41 shows an example of that method:



Figure 41: Example of optical inspection, test series 3.1, specimen 6, spot OM

5.5 Microsections - sample preparation

Microsections were conducted in order to analyze the parts that were manufactured with higher wall thicknesses. After manufacturing, the parts must be removed from the base plate. Since they were built on supports, they could be easily cut off with a sharp scraper without destroying the structure.

The samples were rinsed and cleaned using an ultrasonic bath if necessary. The next step was to insert one sample in a mold that was filled with castable cold mounting compound afterwards. Varidur 200 from Buehler was used, consisting of a two component synthetic resin, based on methacrylate. The powder to hardener ratio was 2:1. [114, 115] After hardening, the samples were ground with a Buehler grinder polisher at 220 RPM with abrasive papers in the

following steps [grit size]: 220, 320, 400, 600, 800, and 1000 respectively. Before etching, the samples were analyzed using a VHX 100 digital microscope with inspection software. The digital microscope had a maximum resolution of 18 million pixels and a 3D display function for the analysis and 3D plot of surfaces. [116] The samples were suitable for microsections and optical inspection using the automated analysis software. The area of the metal was depicted, and labeled using the software. A reference area was measured to calculate the porosity. For every hollow structure, each of the top edges was measured in the middle. Figure 42 shows a prepared sample and the places at which the measurements occurred.

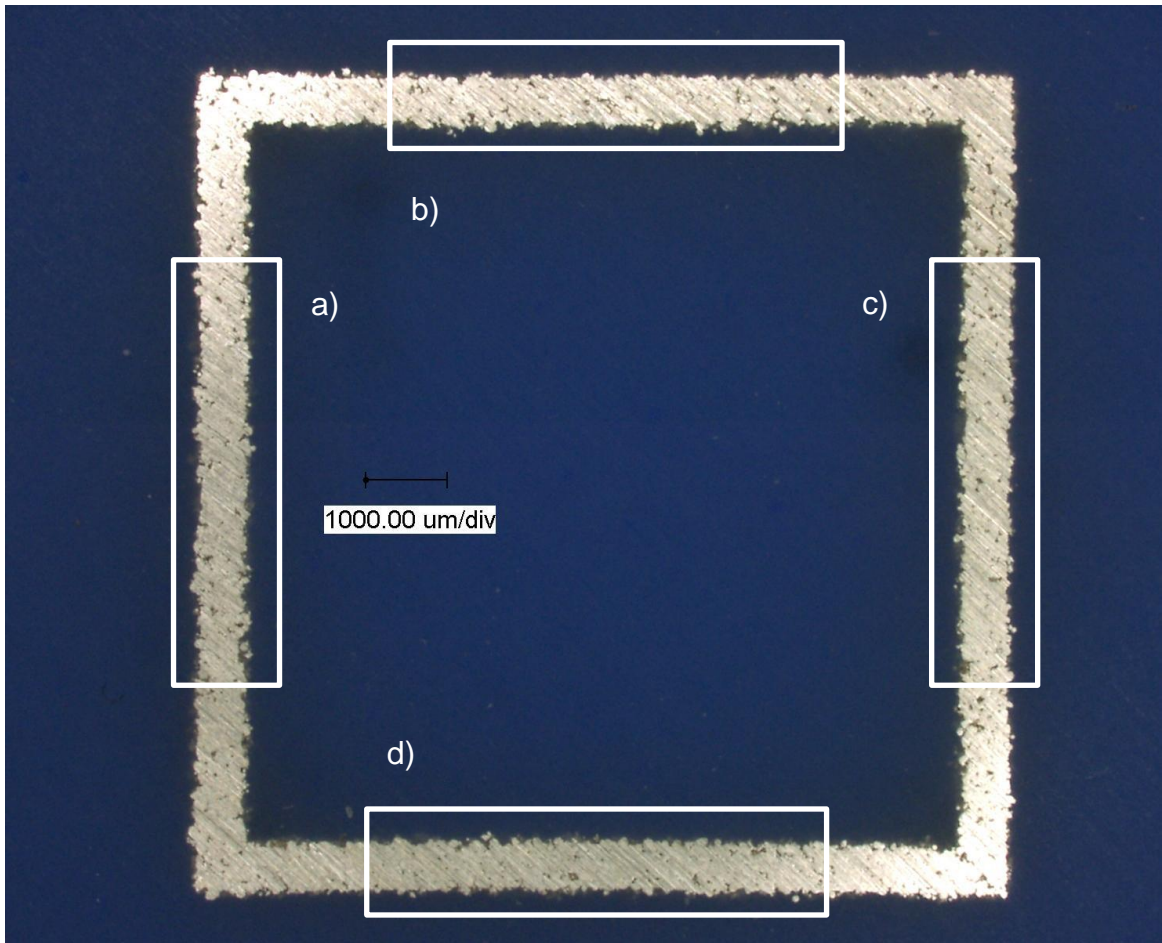


Figure 42: Spots for porosity measurements (a-d)

The sample-ID that is shown in figure 42 is standard order 10, test series 6, replicate 1. The spots were labeled according to the place where the pictures were taken.



Figure 43: Sample of image processing

Figure 43 shows one section that is marked in figure 42 (left box, 90 degrees rotated). In order to eliminate the influence of material that was attached

to the surface, the reference area was selected according to the following scheme: Material that is attached on the boundaries was removed with the program so that a rectangular strip of base material was left. The boundary was cut along the deepest alternating valleys of the surface on both sides. Singular pores like this shown on the right hand, top side, were assessed to contribute to the porosity as well (marked with a red rectangular, see figure 44). Therefore the thickness of the measurement area was typically around 500 μm .



Figure 44: a) Outer boundary removed b) test area c) inner boundary removed

The mean porosity of all four measurements of this sample ID (standard order 10, test series 6, replicate 1) was found to be 7.16%.

5.6 Factorial design - definitions

The results from the previous test series contributed to a better understanding of the range of influencing parameters. The data analysis of the screening tests was conducted using factorial experiments. Two-level factorial designs were chosen. A factorial design is defined to consider all possible combinations of the levels of the factors within a single replicate. [117] The number of combinations is the product of the number of levels: a levels of factor

A and b levels of factor B yields $a*b$ combinations. [117] The effect of a factor is the change in the response due to a change in the factor level. [117] In general, these main effects are the primary factors of interest. [117] If the response is different between the levels of one factor and the levels of another factor, there is an interaction between the factors. [117] That means that the effect of a factor is dependent on the level of another factor. [117]. Factors may be coded (e.g. -1, +1) or uncoded (real data). The advantages of factorial designs compared to designs with just a single change in factors is that fewer experiments need to be conducted and the interactions of the factors can be shown. Therefore, the experimenter receives better data at lower efforts. For Design of Experiments, commercial software packages contribute to the calculation of the models. Within this dissertation, MINITAB was used.

5.6.1 ANOVA

The variability of the data can be analyzed using the fundamental Analysis of Variance (ANOVA) equation:

$$\sum_{i=1}^a \sum_{j=1}^n (y_{ij} - \bar{y}_{..})^2 = n \sum_{i=1}^a (\bar{y}_{i.} - \bar{y}_{..})^2 + \sum_{i=1}^a \sum_{j=1}^n (y_{ij} - \bar{y}_{i.})^2$$

Equation 20: Essential ANOVA equation [118]

In other words, the total sum of squares equals the sum of squares due to treatments and due to errors. The sum of squares due to treatments is calculated by the difference between the treatment mean and the total mean. The sum of squares due to error reflects the differences within the treatment from

the treatment mean. Typically, equation 20 is also denoted in literature in the following manner: [118]

$$SS_T = SS_{\text{Treatment}} + SS_E$$

Equation 21: Symbolic denotation of the fundamental ANOVA equation [118]

For applying an Analysis of Variance, the following assumptions must be checked: [119] The error must be normally distributed and independently distributed. Furthermore, the error has a mean of 0 and has a constant, but unknown variance. In literature, these assumptions are abbreviated as NID (0, σ^2) (normally and independently distributed). The model should satisfy the following equation adequately:

$$y_{ij} = \mu + \tau_i + \varepsilon_{ij}$$

Equation 22: Model to describe the response [119]

The assumptions can be checked if the residuals are investigated. The residuals are the difference between current observation y_{ij} and estimated observation \hat{y}_{ij} for observation j in treatment i . [119]

$$e_{ij} = y_{ij} - \hat{y}_{ij}$$

Equation 23: Calculation of residuals [119]

The residuals e_{ij} are used as estimators of the random error $\hat{\varepsilon}_{ij}$

$$\hat{\varepsilon}_{ij} = e_{ij}$$

Equation 24: Estimation of residuals

The model adequacy checking can be conducted if the residual plots of the data do not violate these assumptions. If the residuals are normally distributed, the normal probability plot of the residuals will fit a straight line. If the

residuals have a mean of zero, the normal probability plot will be centered around zero. In that case, the histogram of the residuals will be centered at zero as well and a normal distribution will fit to the diagram. If the residuals have a constant variance, the diagram “residuals versus predicted value” shows a constant variance. If the residuals are independently distributed, the residuals versus run order plot does not show specific patterns. [119]

5.7 Data analysis

5.7.1 Data analysis of test series 1

Table 13: Data for AgCu7-screening test series 1:

		AgCu7-TS1				
		no offset				
Levels:		power [W]	spot dist. [μm]	pulse time [μs]	layer thickness [μm]	preexposure [W]
high	Factors:	100	20	80	60	50
low		80	5	20	30	0

Responses:				
Thick-ness [μm]	Inner area [μm^2]	Outer area [μm^2]	Ratio inner/ outer area [-]	Surface porosity [%]

The responses “thickness”, “inner area” and “outer area” were measured according to figure 40. The ratio was calculated and the “surface porosity” was simply the balance of this ratio to 1 (in percent).The following run order scheme was used for test series 1:

Table 14: Run order scheme for test series 1

run order	power [W]	spot dist [μm]	pulse time [μs]	layer thickness [μm]	preexposure [W]
1	100	20	80	60	50
2	100	20	20	30	0
3	100	20	20	60	0
4	100	5	80	60	50
5	80	5	80	30	50
6	80	5	20	60	50
7	100	5	20	30	0
8	100	20	80	30	0
9	100	20	80	60	0
10	80	20	20	30	50
11	80	5	80	60	50
12	80	5	80	30	0
13	80	20	80	60	0
14	80	20	80	30	50
15	80	20	80	60	50
16	80	20	20	30	0
17	80	5	80	60	0
18	100	20	20	30	50
19	100	5	20	60	0
20	80	20	20	60	50
21	80	5	20	30	0
22	100	5	80	60	0
23	80	20	80	30	0
24	100	5	20	60	50
25	100	5	80	30	50
26	80	20	20	60	0
27	100	20	80	30	50
28	80	5	20	60	0
29	100	5	80	30	0
30	100	20	20	60	50
31	80	5	20	30	50
32	100	5	20	30	50

5.7.2 Model adequacy checking

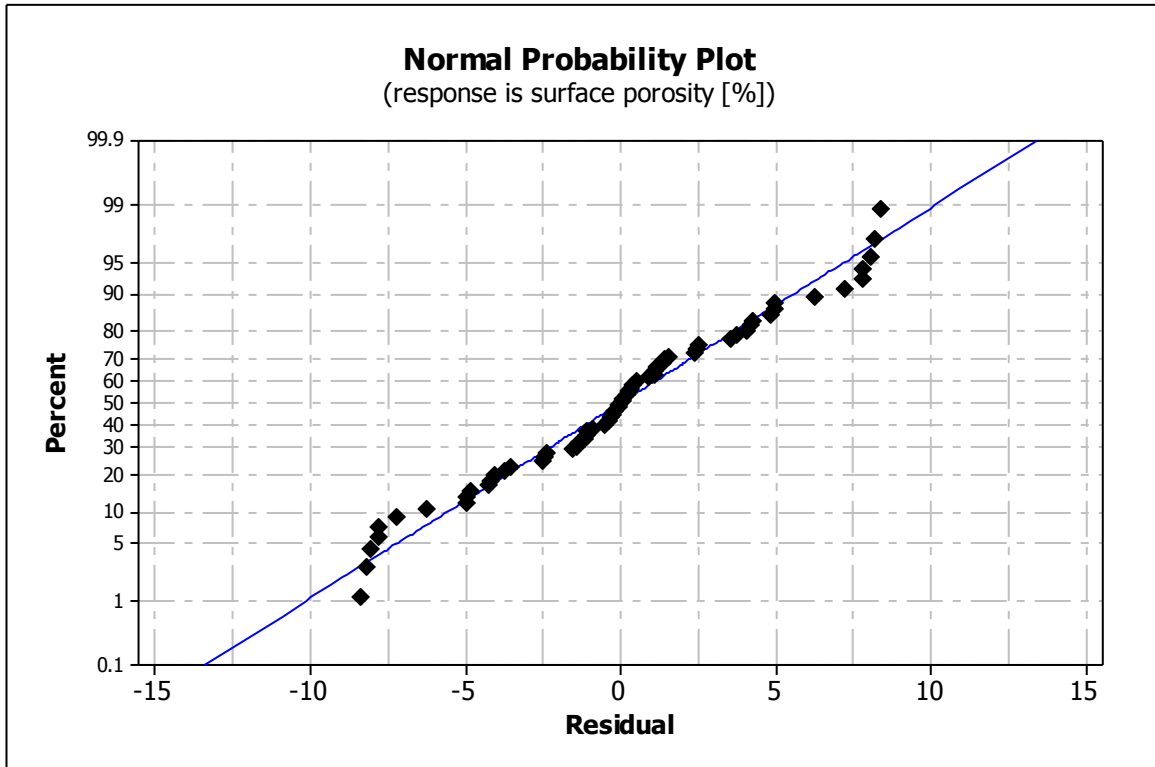


Figure 45: Normal probability plot of the residuals

The normal probability plot of the residuals of test series 1 are shown in figure 45. Although the tails showed a slight curvature, the residuals fit a straight line according to section 5.6. Furthermore, the residuals were centered on zero.

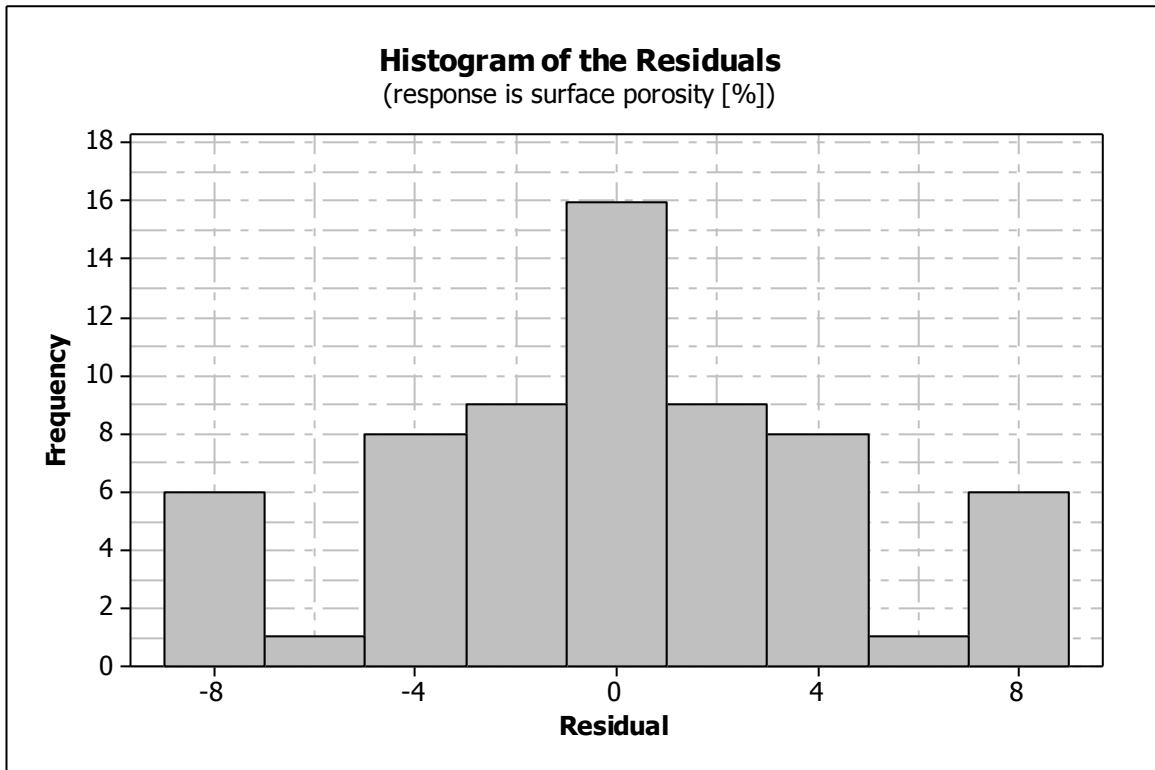


Figure 46: Histogram of the residuals, test series 1

The histogram shows that the residuals were fairly normally distributed. They were centered on zero. The curvature at the end of the tails from figure 45 can be seen in the histogram as well since the frequency at -8 and +8 is increased compared to -6 and +6.

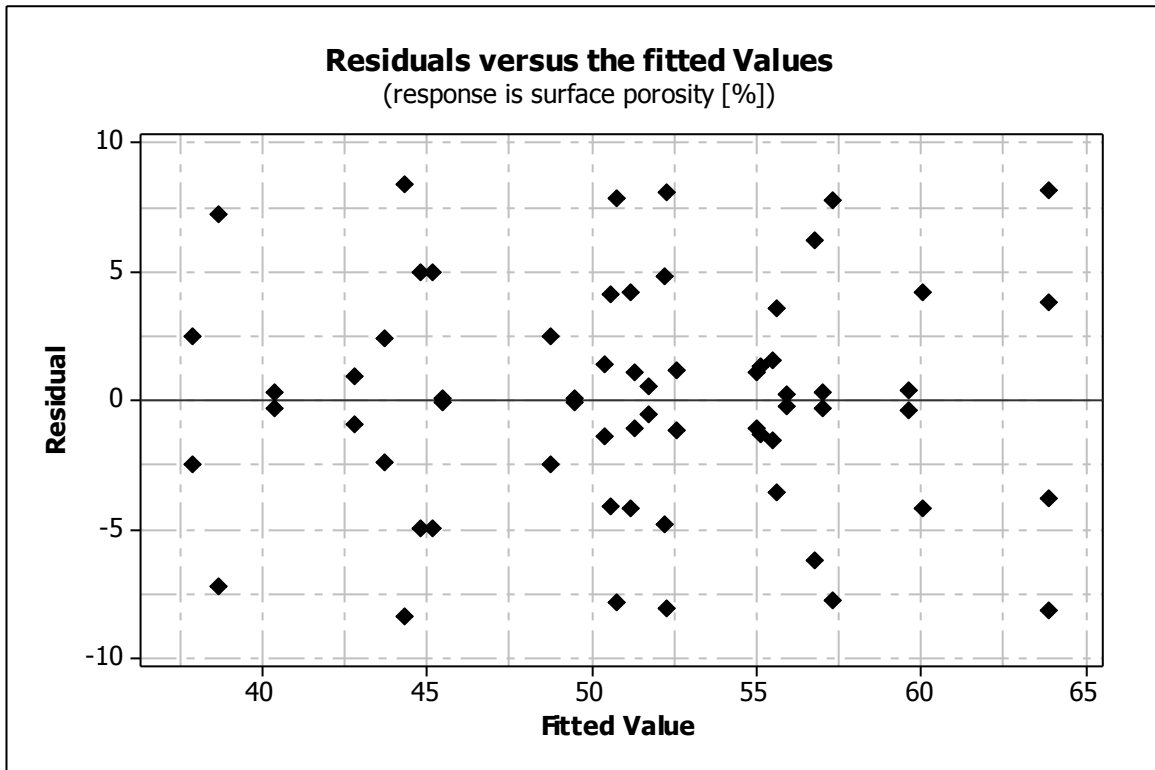


Figure 47: Residuals versus fitted values, test series 1

Figure 47 depicts that the fitted values did not show patterns according to section 5.6. The distance between the outer residuals (-8 and +8) to the center line was similar between the fitted values 35 to 65. This means that the variance could be considered as constant.

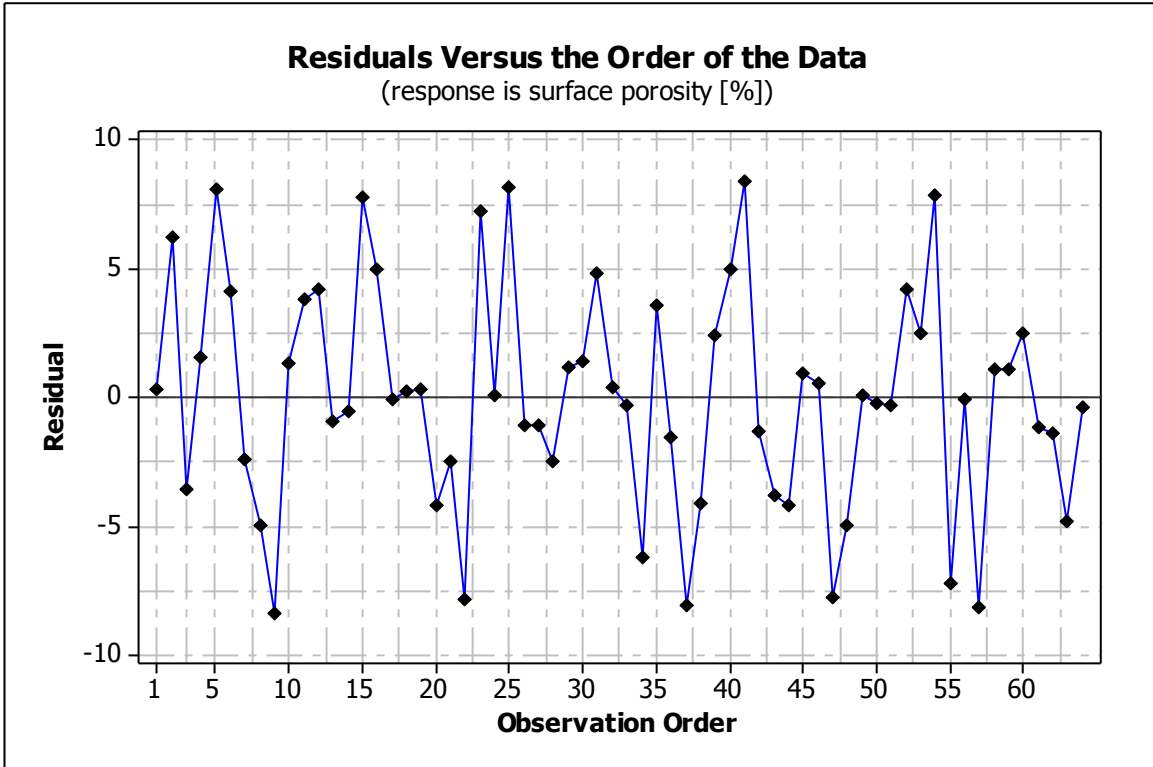


Figure 48: Residuals versus the order of the data

The correct time order presents hints if the data is correlated. For this plot in figure 48, the knowledge about the run order is essential since data might be sorted after the tests were conducted. The plot shows that there was no certain pattern in run order.

Considering figure 45 to figure 48, an ANOVA could be conducted. Table 15 lists the factors and levels for test series 1.

Table 15: Factors and levels for test series 1

Factor	Type	Levels	Values
power [W]	fixed	2	80; 100
spot dist [μm]	fixed	2	5; 20
pulse time [μs]	fixed	2	20; 80
layer thickness [μm]	fixed	2	30; 60
preexposure [W]	fixed	2	0; 50

Table 16: MINITAB output for ANOVA test series 1
General Linear Model: surface porosity versus power; spot distance; pulse time, layer thickness and preexposure with interactions

Source	DF	Seq SS	Adj SS	Adj MS	F	P
Power	1	16.02	16.02	16.02	0.43	0.516
spot dist	1	1	1	1	0.03	0.871
pulse time	1	14.14	14.14	14.14	0.38	0.542
layer thickness	1	3.41	3.41	3.41	0.09	0.764
preexposure	1	966.47	966.47	966.47	25.97	0.000
power*spot dist	1	1.4	1.4	1.4	0.04	0.847
power*pulse time	1	6.11	6.11	6.11	0.16	0.688
power*layer thickness	1	162.59	162.59	162.59	4.37	0.045
power*preexposure	1	35.85	35.85	35.85	0.96	0.334
spot dist*pulse time	1	719.01	719.01	719.01	19.32	0.000
spot dist*layer thickness	1	178.18	178.18	178.18	4.79	0.036
spot dist*preexposure	1	10.64	10.64	10.64	0.29	0.597
pulse time *layer thickness	1	83.84	83.84	83.84	2.25	0.143
pulse time *preexposure	1	64.86	64.86	64.86	1.74	0.196
layer thickness *preexposure	1	0.74	0.74	0.74	0.02	0.888
power*spot dist*pulse time	1	0.43	0.43	0.43	0.01	0.915
power*spot dist*layer thickness	1	0.04	0.04	0.04	0	0.974
power*pulse time * layer thickness	1	0.16	0.16	0.16	0	0.164
power*spot dist*preexposure	1	75.57	75.57	75.57	2.03	0.948
power*pulse time *preexposure	1	4.49	4.49	4.49	0.12	0.731
power*layer thickness *preexposure	1	74.91	74.91	74.91	2.01	0.166
spot dist*pulse time *layer thickness	1	32.67	32.67	32.67	0.88	0.356
spot dist*pulse time *preexposure	1	118.51	118.51	118.51	3.18	0.084
spot dist*layer thickness *preexposure	1	2.8	2.8	2.8	0.08	0.786
pulse time *layer thickness *preexposure	1	40.28	40.28	40.28	1.08	0.306
power*spot dist*pulse time *layer thickness	1	64.5	64.5	64.5	1.73	0.197
power*spot dist*pulse time *preexposure	1	18.23	18.23	18.23	0.49	0.489
power*spot dist*layer thickness *preexposure	1	127.71	127.71	127.71	3.43	0.073
power*pulse time *layer thickness *preexposure	1	1.25	1.25	1.25	0.03	0.855
spot dist*pulse time *layer thickness *preexposure	1	4.86	4.86	4.86	0.13	0.720
power*spot dist*pulse time *layer thickness *preexposure	1	1	1	1	0.03	0.871
Error	32	1190.84	1190.84	37.21		
Total	63	4022.53				
S = 6.10031 R-Sq = 70.40% R-Sq(adj) = 41.72%						

The F-statistic was calculated by the division of mean square and mean error and was reported in the fourth column of table 16. In literature, the F-statistic is tabled separately for (i-1)*(j-1) degrees of freedoms. The F-statistic can be interpreted using the p-value, reported in the last column of table 16.

The p-value represents the percentage of values that is outside the F-statistic. A p-value that is close to zero indicates that the factor is significant, also indicated by a high F-value. Four factors show p-values below $\alpha=0.05$: preexposure (p=0.000), spot dist*pulse time (p=0.000), spot dist*layer thickness (p=0.036), power*layer thickness (p=0.045). These factors are considered to be statistically significant.

R^2 is ratio of sum of squares and is considered as the percentage of variability that can be explained by the model. R^2 is calculated by: [120]

$$R^2 = \frac{SS_{Model}}{SS_{Total}} = 1 - \frac{SS_{Error}}{SS_{Total}}$$

Equation 25: Calculation of Coefficient of Determination (R^2) [120]

In that case, R^2 denotes that 70.4% of the variability in the data is explained by the model. Since R^2 increases with the number of variables that are added to the model, an adjusted Coefficient of Determination can be calculated: [121]

$$R^2_{adjusted} = 1 - \frac{SS_{Error}/(n - p)}{SS_{Total}/(n - 1)}$$

Equation 26: Calculation of Adjusted Coefficient of Determination [121]

R^2_{adjusted} denotes that 41.72% contribute to the variability of the data if the number of variables is considered.

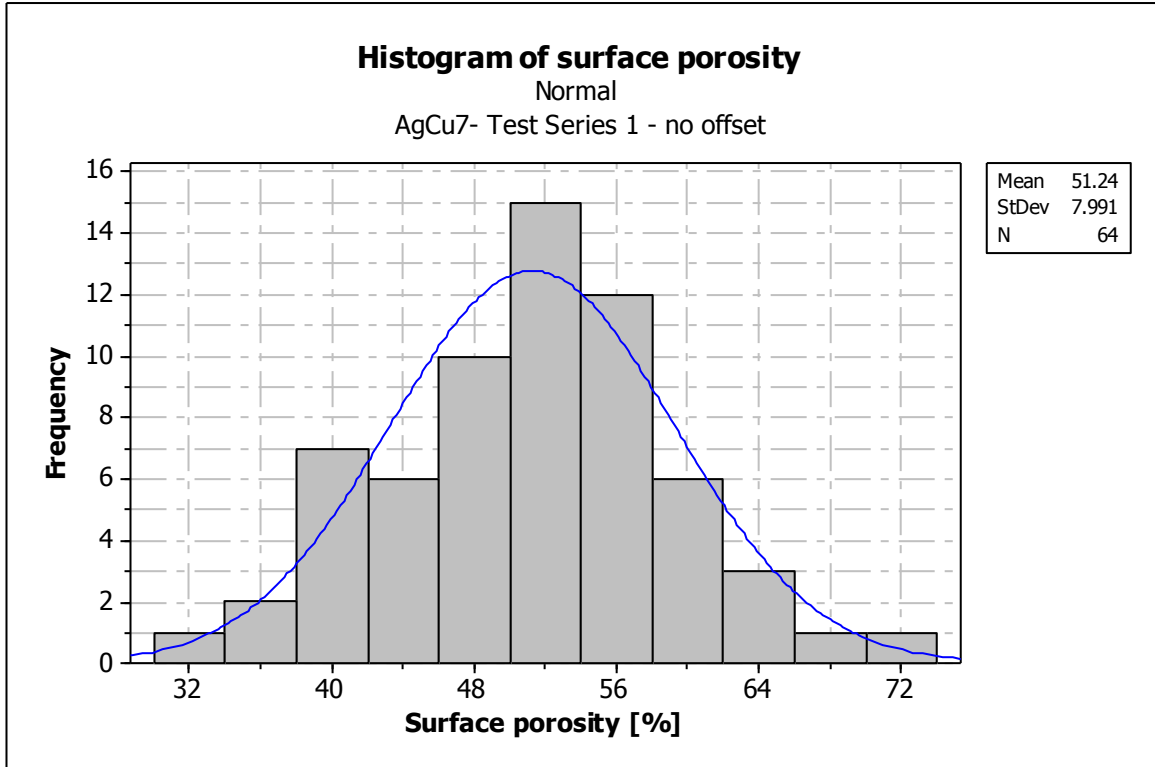


Figure 49: Histogram of surface porosity, AgCu7, test series 1

It can be seen that the mean of the response shows a mean in surface porosity of 51.24% with a standard deviation of 7.991. The response was split into eleven intervals (bins). The vertical axis shows the frequency whereas the horizontal axis shows the intervals. In figure 49, the blue curve shows the normal distribution that was fit to the sample data. The response is considered to be normally distributed.

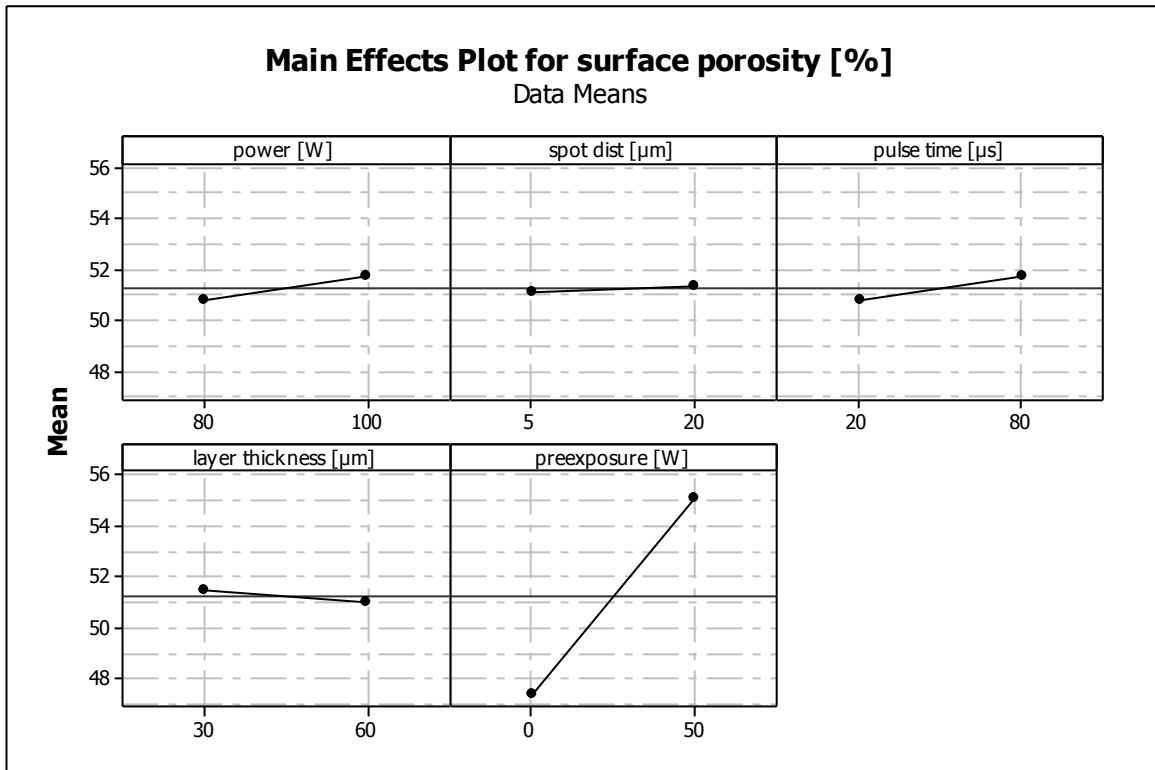


Figure 50: Main effect plot of test series 1, AgCu7

The main effect plot shows the increase or decrease of the mean response for both levels of factors. For this screening experiment, preexposure had the largest effect on the response and is the only factor that is significant. For this set of data points, preexposure increases the surface porosity. The porosity is slightly increased by the factors power, spot distance and pulse time, whereas the porosity is slightly decreased by an increase of the layer thickness.

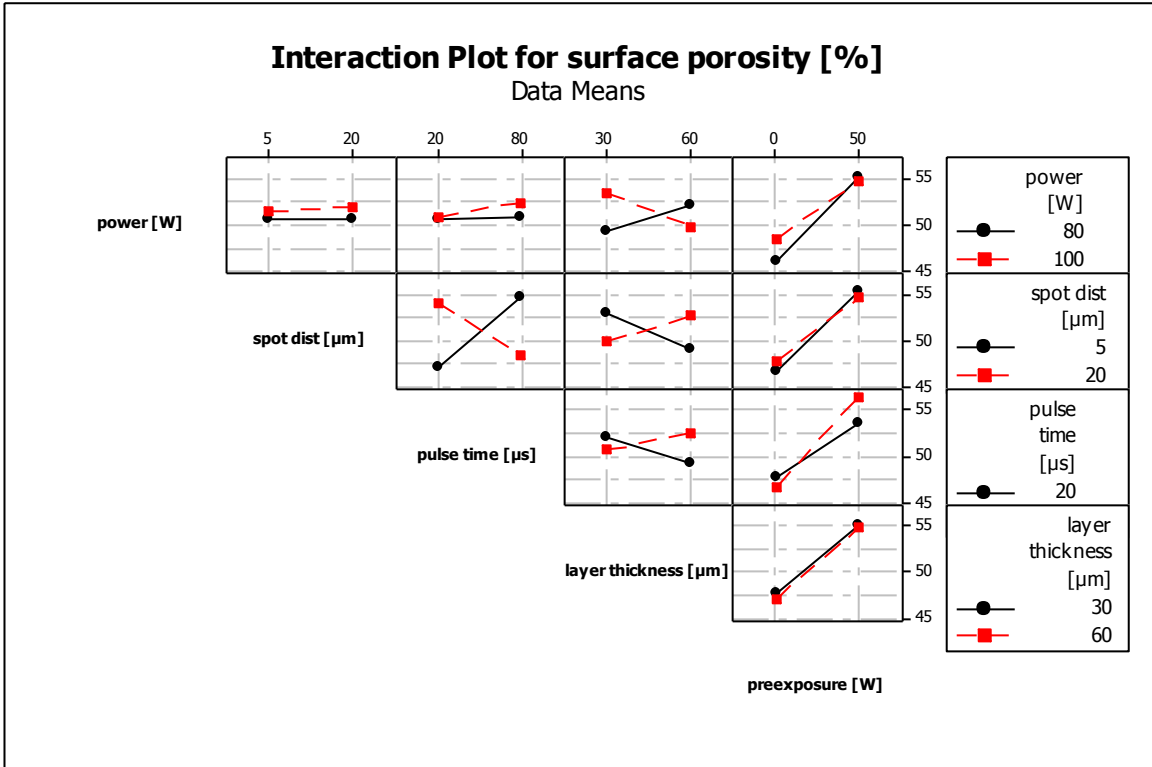


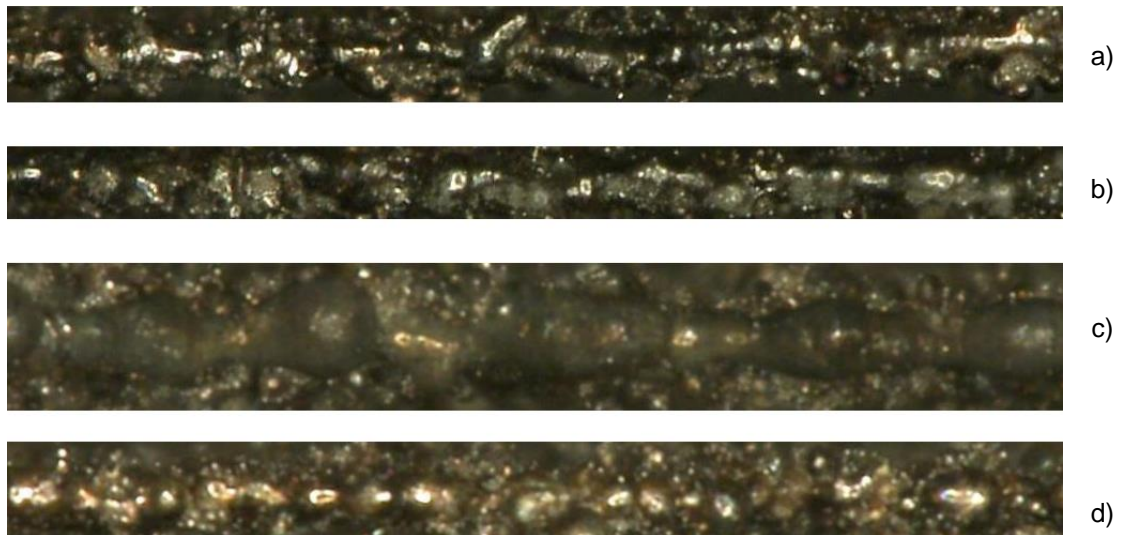
Figure 51: Interaction plot for surface porosity

The interaction plot shows that, for this set of data points, layer thickness interacts with power, spot distance, and pulse time, but not with preexposure. The spot distance interacts with pulse time as well. The interaction of spot distance versus pulse time, and the interaction of layer thickness of each versus power, spot distance and pulse time are considered significant.

Figure 52 shows selected samples from the test series 1. According to table 14, the parameters of the selected samples are shown in table 17. No offset was used.

Table 17: Parameters of selected samples (figure 52)

run order	power [W]	spot dist [μm]	pulse time [μs]	layer thickness [μm]	preexposure [W]
2	100	20	20	30	0
16	80	20	20	30	0
19	100	5	20	60	0
20	80	20	20	60	50



100.00 $\mu\text{m}/\text{div}$
↔

Figure 52: Selected samples of test series 1: a) run order 2, b) run order 16, c) run order 19, d) run order 20

It can be seen that all specimen tended to exhibit the balling phenomenon. Run order 2 and run order 16 only differed in laser power. It can be seen that the appearance of the tracks was similar. Run order 19 and 20 were both conducted using a layer thickness of $60 \mu\text{m}$. The width of the tracks from run order 19 was larger than the width of the other specimens. If sample 20 is compared to sample 16, it can be seen that the surface differed in size and

curvature of the droplets. For these two samples, layer thickness and preexposure were changed.

5.7.3 Data analysis of test series 2, 3, and 4 - failed parts

Test series 2, 3, and 4 were conducted in the same manner as test series 1. For test series 1, every part was built successfully. Changing the parameters to other regions resulted in failed parts. The next graph shows a scatter plot of the data points that failed.

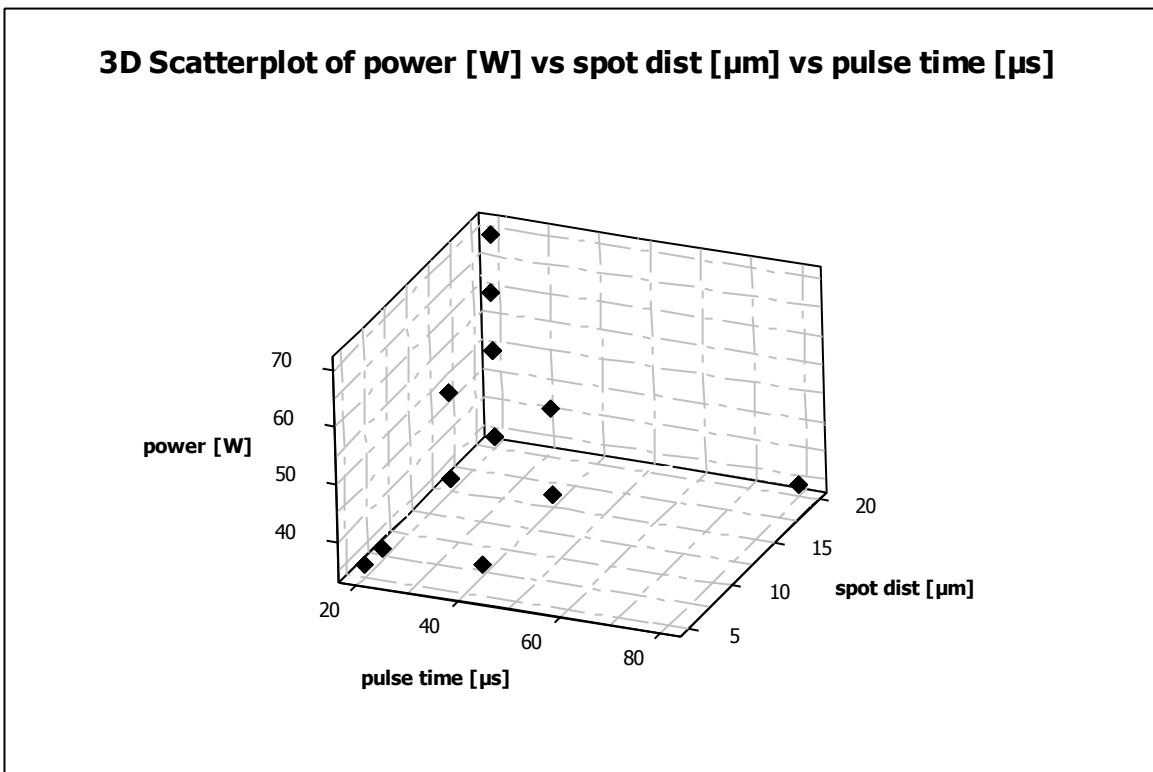


Figure 53: Scatter plot of failed parts test series 2-4, AgCu7

Please note that figure 53 represents 58 data points in total. Since the parameters pulse time, spot distance, and power are exactly the same, the data points are overlaid, so that only 13 data points can be seen.

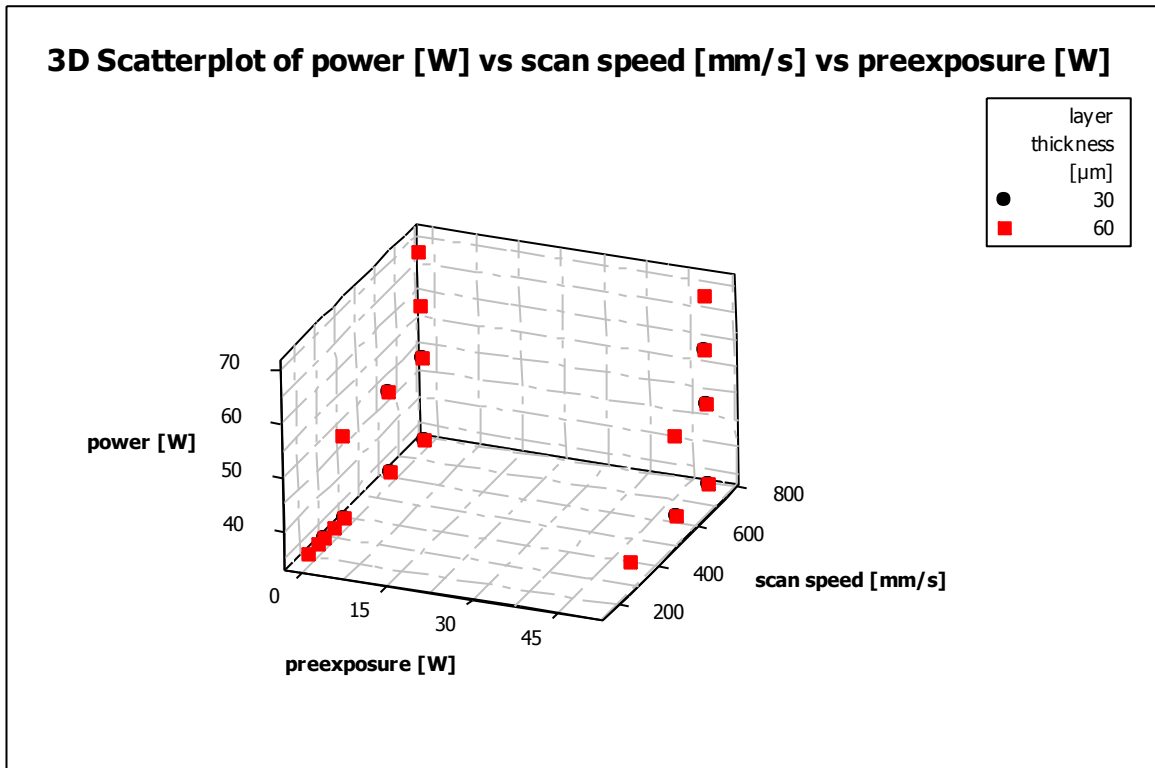


Figure 54: Scatter plot of failed parts, test series 2-4, power vs. preexposure and scan speed

Figure 54 shows the same data points as figure 53, but the axes were changed to preexposure and scan speed instead of pulse time and spot distance. It can be seen that for low laser powers and for high scan speeds parts tended to fail. In case of low scan speeds and low laser powers, the additional energy input using the preexposure reduced the number of failed parts.

The failed parts of the single track screening experiments were not considered in further investigations. The reason could be seen that the energy input was too low to melt the material, so that the wiper system of the SLM 50 simply removed the parts without further building.

5.7.4 Test series 2, 3, and 4

The data of test series 2, 3, and 4 were collected. The test series were analyzed first in a similar manner as test series 1. Please note that the response in case of failed parts was simply not measurable. Even the replacement of the failed parts using a porosity of 100% is not appropriate. In that case, the NID (0, σ^2) assumptions were violated. In order to assess successful parts, data from failed parts were removed from the data sets. Furthermore, in contrast to test series 1, data from the three single tests was summarized in one single model.

Table 18: Data for test series 2, 3, and 4

Test series:		Factors:	power [W]	spot dist. [μm]	pulse time [μs]	layer thickness [μm]	preexposure [W]
Levels							
AgCu7-TS2 no offset	high		50	20	80	60	50
	low		35	5	20	30	0
AgCu7-TS3 no offset	high		50	15	40	60	50
	low		35	7	20	30	0
AgCu7-TS4 no offset	high		70	20	80	60	50
	low		60	5	20	30	0

Responses:				
Thickness	Inner area	Outer area	Ratio inner/outer ar.	Surface porosity
[μm]	[μm^2]	[μm^2]	[-]	[%]

The responses were used in the same manner as described in section 5.7.1: thickness, inner area, and outer area were used to calculate the ratio and the ratio between the areas is used to calculate the surface porosity.

5.7.5 Model adequacy checking of test series 2, 3, 4

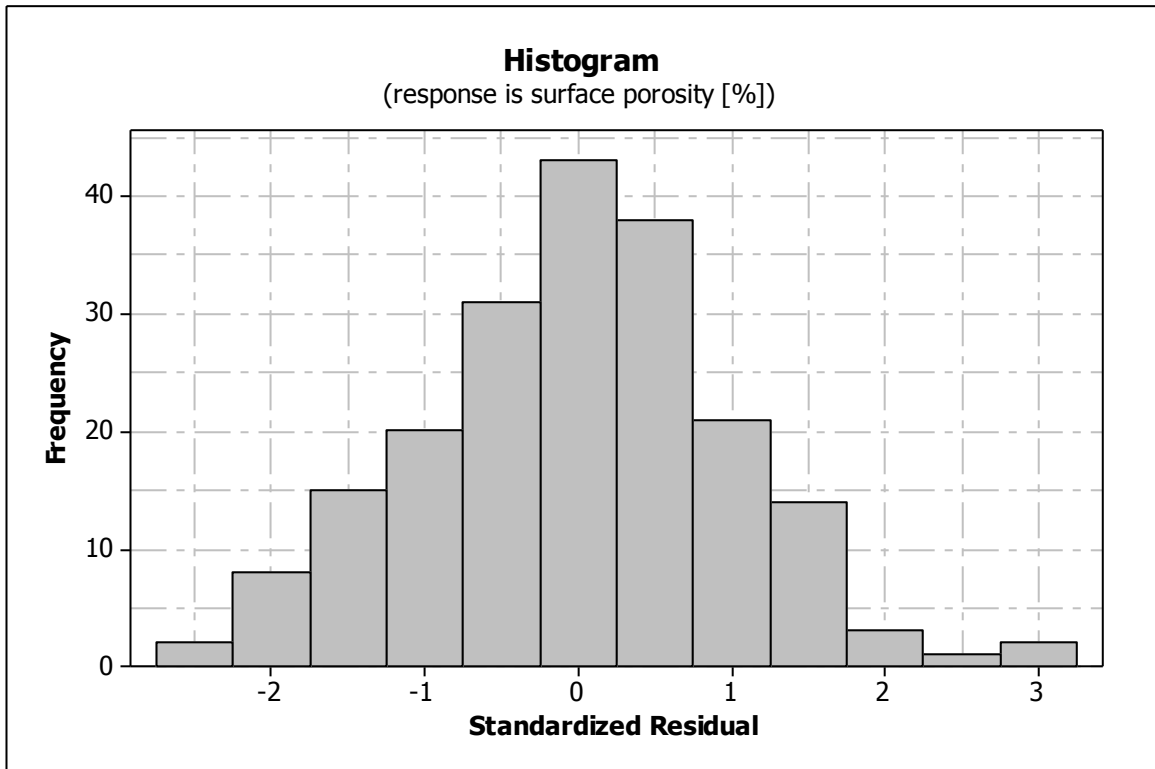


Figure 55: Histogram of standardized residuals, test series 2, 3, 4

The histogram of the residuals shows that the residuals were centered around zero. A normal distribution could be fit to the bars in the first approximation.

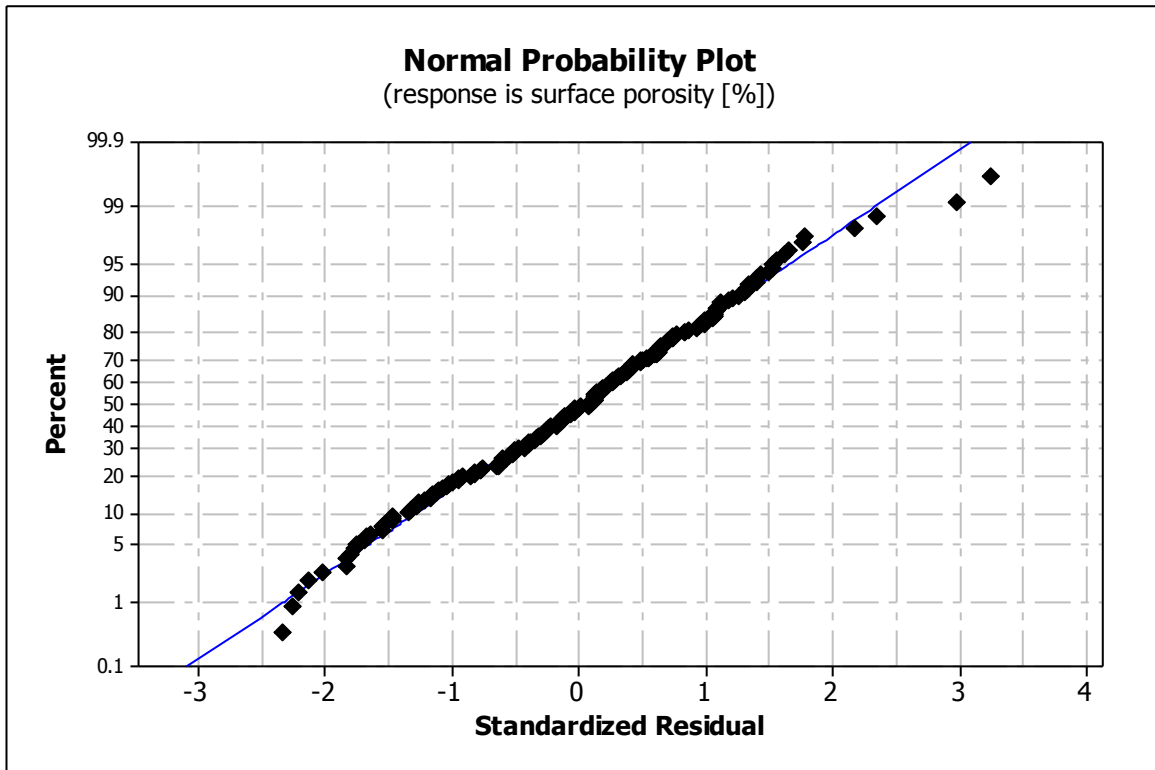


Figure 56: Normal probability plot of standardized residuals, test Series 2, 3, 4

Figure 56 shows the normal probability plot of the standardized residuals.

Besides some outliers at both tails, they fit to a straight line and were centered around zero.

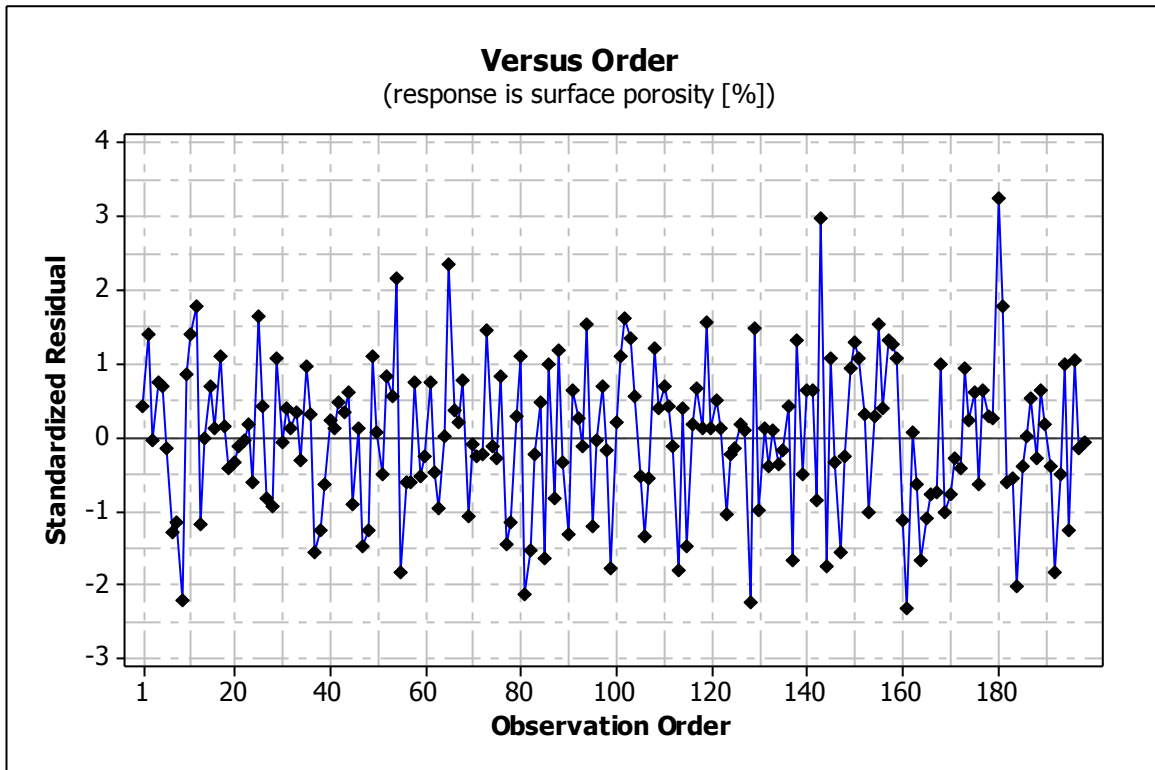


Figure 57: Run order plot of test series 2, 3, and 4

The run order plot (figure 57) did not show patterns in the observation order. The observation order was simply added in correct time order (first test series 2, then test series 3 and 4 following).

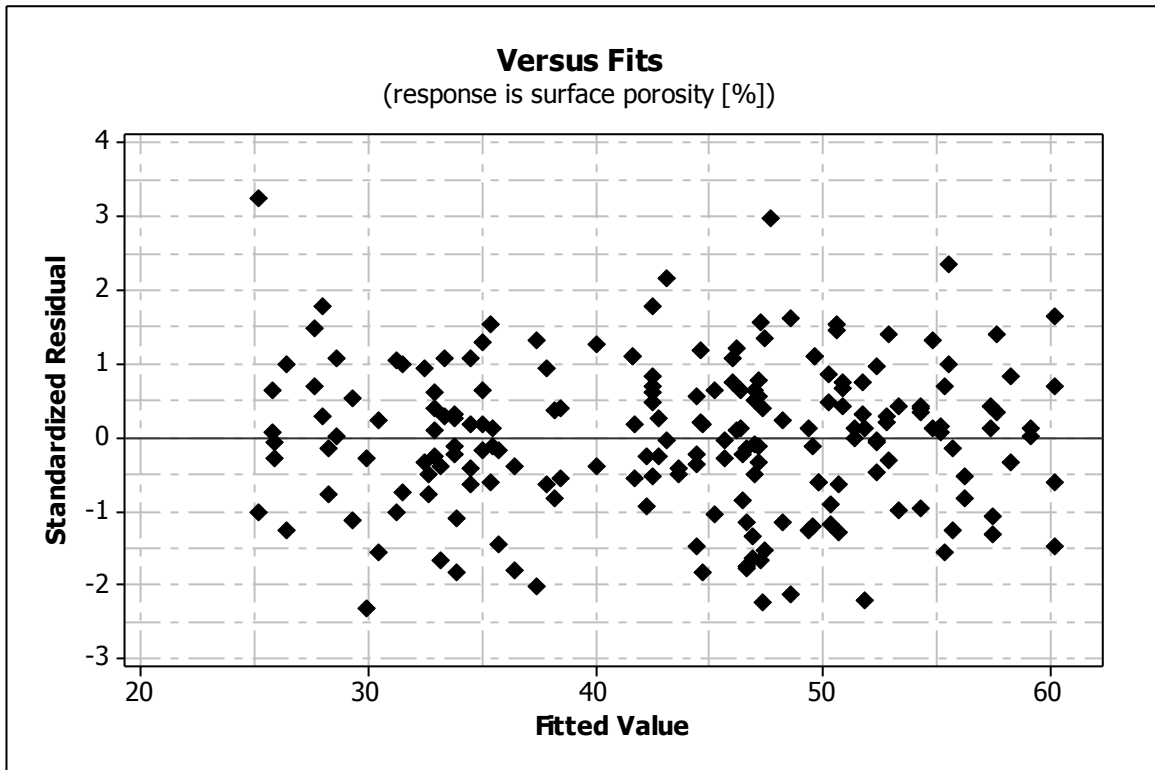


Figure 58: Plot of Standardized Residuals versus Fitted Values

Besides some outliers, the plot of the standardized residuals did not show unusual patterns. Considering figure 55 to figure 58, there was no evidence that the NID $(0, \sigma^2)$ -assumptions were violated. An ANOVA could be conducted. In order to increase the fit, the model was built using all five base parameters (power, spot distance, pulse time, layer thickness and preexposure) and the following interactions:

Table 19: Model of test series 2, 3, 4

Base parameters	interactions
A: power [W]:	A*D
B: spot dist [μm]:	A*E
C: pulse time [μs]:	B*D
D: layer thickness [μm]:	B*E
E: preexposure [W]:	C*D
	C*E
	D*E
	A*D*E
	C*D*E

The following ANOVA output was computed using MINITAB:

Table 20: ANOVA output for test series 2,3,4

Source	DF	Seq SS	Adj SS	Adj MS	F	P
power [W]	5	11392.24	11128.08	2225.62	35.47	0.000
spot dist [μm]	3	321.82	360.93	120.31	1.92	0.129
pulse time [μs]	2	100.34	92.68	46.34	0.74	0.479
layer thickness [μm]	1	884.05	263.31	263.31	4.2	0.042
preexposure [W]	1	8.43	1.05	1.05	0.02	0.897
power [W]*layer thickness [μm]	5	655.5	265.04	53.01	0.84	0.520
power [W]*preexposure [W]	5	1694.23	1281.15	256.23	4.08	0.002
spot dist [μm]*layer thickness [μm]	3	571.57	421.58	140.53	2.24	0.086
spot dist [μm]*preexposure [W]	3	303.33	370.55	123.52	1.97	0.121
pulse time [μs]*layer thickness [μm]	2	207.34	254.95	127.48	2.03	0.135
pulse time [μs]*preexposure [W]	2	179.41	162.42	81.21	1.29	0.277
layer thickness [μm]*preexposure [W]	1	62.56	20.18	20.18	0.32	0.571
power [W]*layer thickness [μm]*preexposure [W]	5	859.04	934.79	186.96	2.98	0.013
pulse time [μs]*layer thickness [μm]*preexposure [W]	2	86.36	86.36	43.18	0.69	0.504
Error	157	9851.15	9851.15	62.75		
Total	197	27177.38				
S = 7.92125 R-Sq = 63.75% R-Sq(adj) = 54.52%						

The factors power and layer thickness were significant, showing a p-value of 0.000 and 0.042 respectively. The interactions power times preexposure and power times layer thickness times preexposure were significant as well since

the p-values were 0.002 and 0.013, respectively. Depending on the confidence interval, the interaction of spot distance times preexposure can be considered to be significant as well since the p-value is close to the α -value which is 0.05 (table 20).

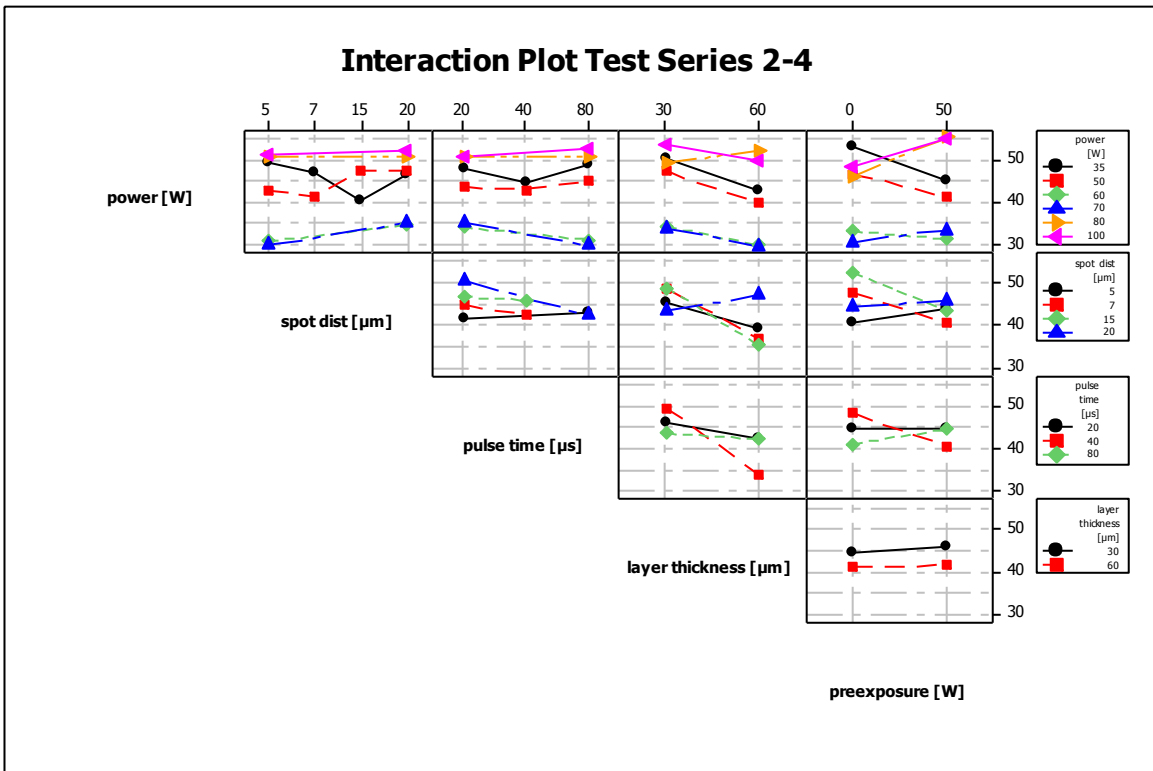


Figure 59: Interaction plot of test series 2, 3, 4

The interaction plot shows interactions for power and spot distance and pulse time with all factors. Besides that, there was no interaction between preexposure and layer thickness. Lines with different slope angles indicate a significant interaction.

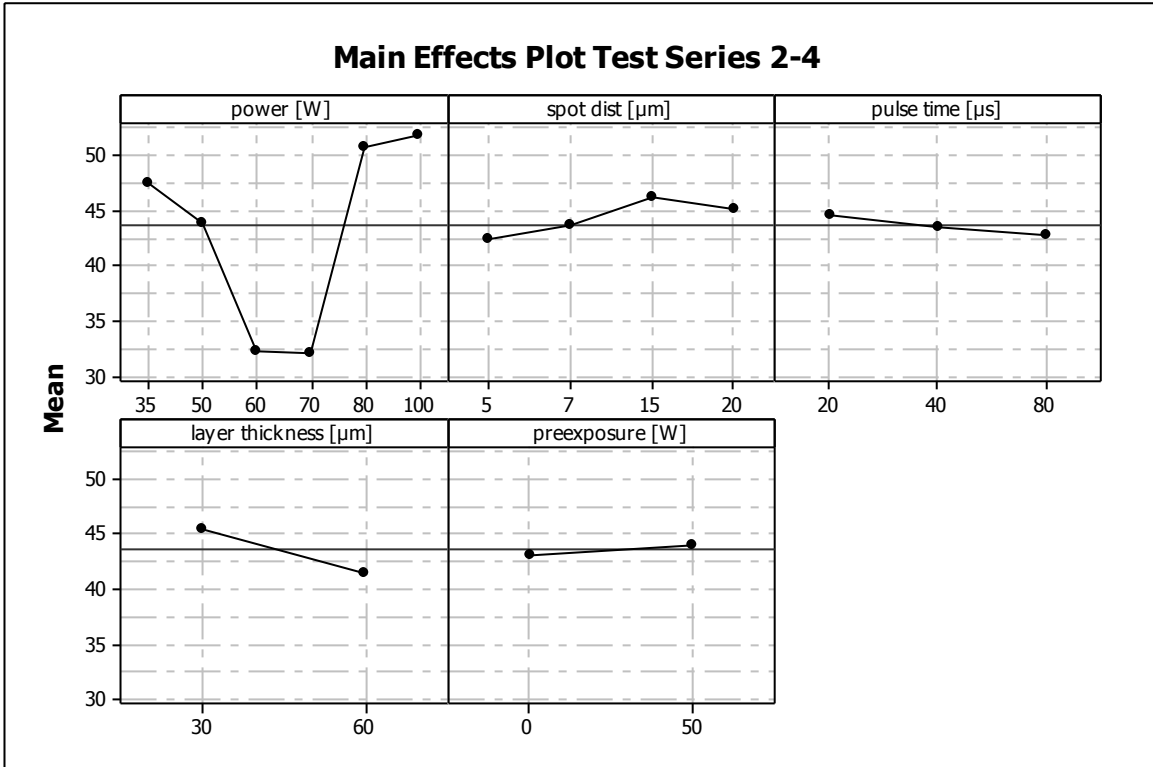


Figure 60: Main effects plot for test series 2, 3, 4

The main effects plot (figure 60) must be analyzed with respect to the interactions and should not be used without considering figure 59. But it can be seen that the power levels of 60 and 70 W obtained the best results regarding the surface porosity. The plot shows that only the power level is significant.

5.8 Microscopy

Besides the assessments using surface porosities, the shape and topography of the molten tracks could be used for sample assessment. The next figures show selections of tracks in order to estimate the results of chapter 5.7. A Keyence VHX 100 digital microscope was used. All pictures (figure 61 to figure 66) were taken with 100-fold magnification.

5.8.1 Test series 2

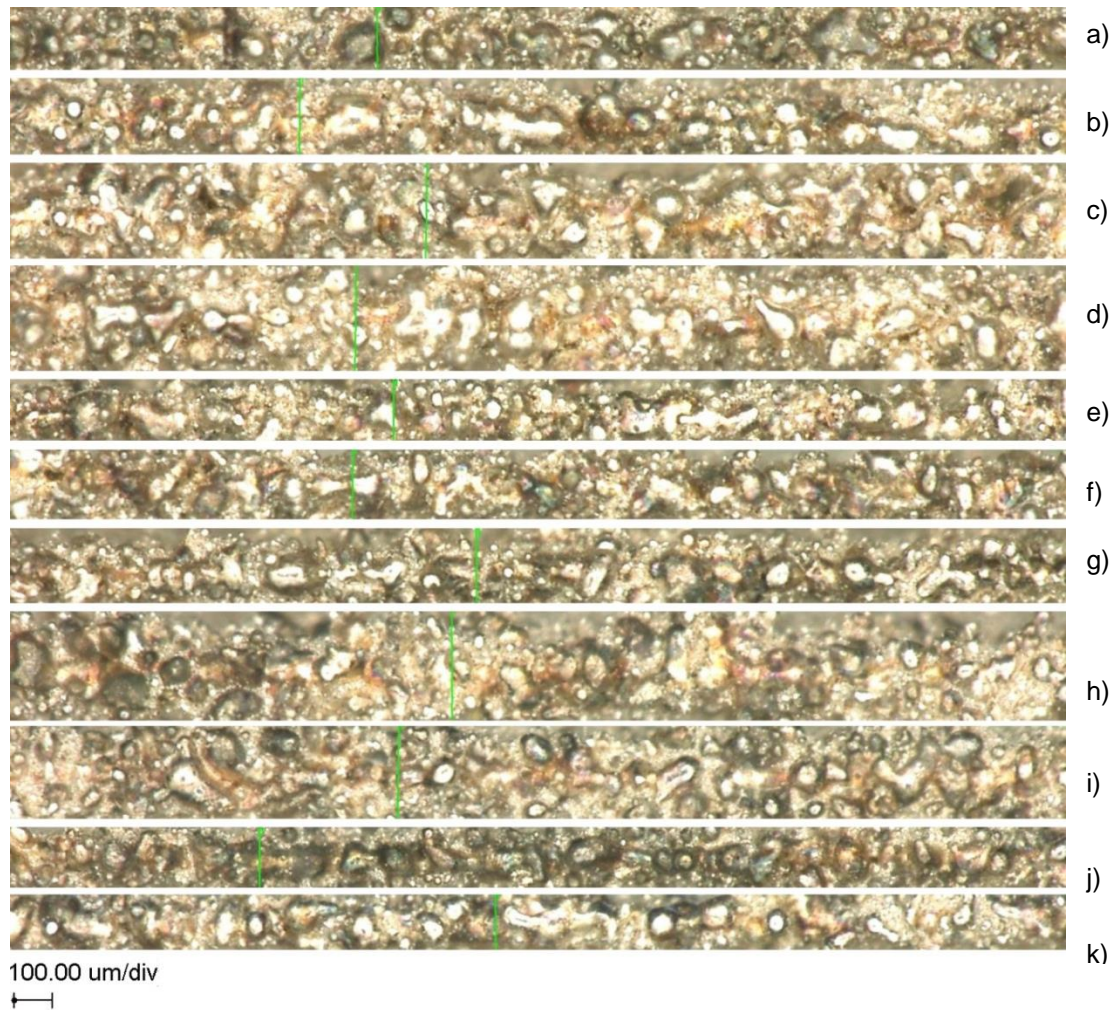


Figure 61: Selected tracks, test series 2 a) 06, b) 27, c) 24, d) 26, e) 18, f) 04, g) 15, h) 31, i) 14, j) 03, k) 23

The tracks were sorted in the following manner: increasing levels of power, increasing levels of spot distance, increasing levels of pulse time and increasing levels of preexposure. Figure 61 depicts samples with a layer thickness of 30 μm . The build parameters are summarized in table 21.

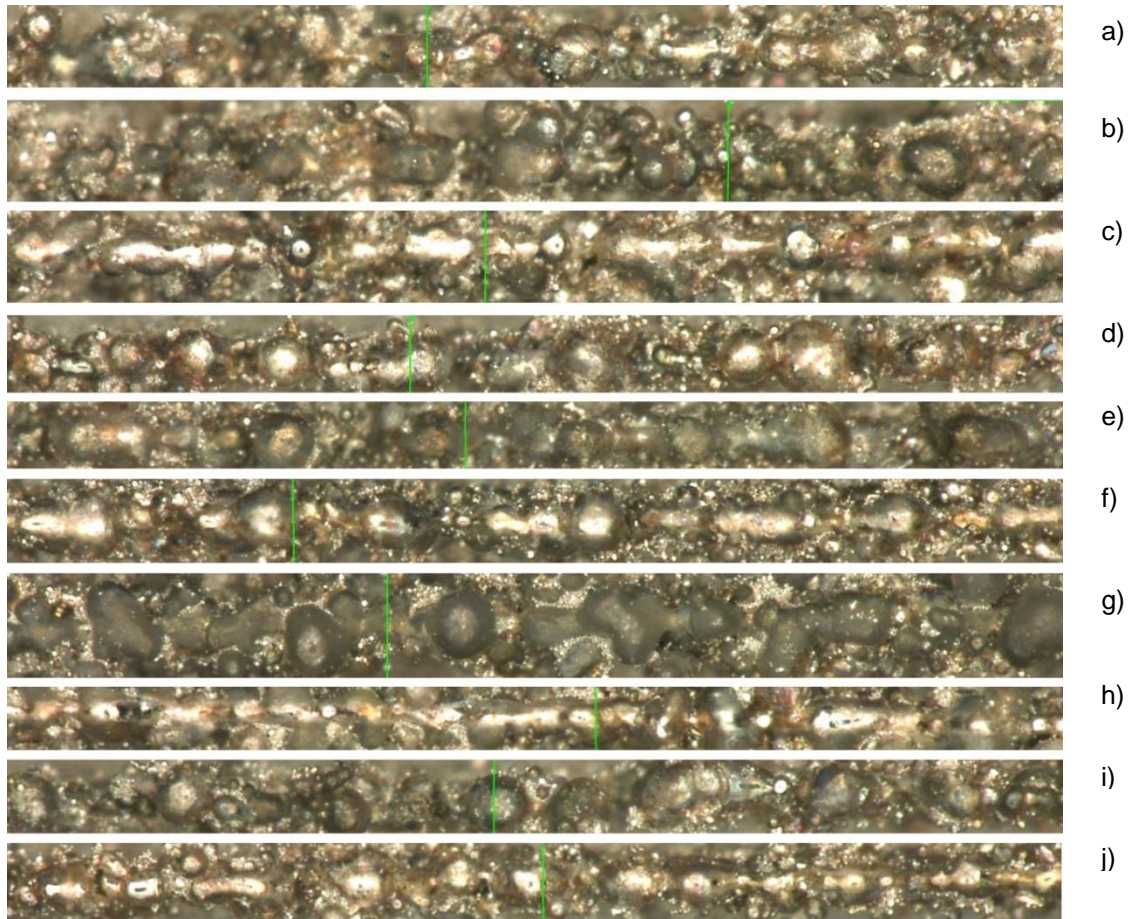
Table 21: Parameters of selected tracks (figure 61)

picture	run order	power [W]	spot dist [μm]	pulse time [μs]	layer thickness [μm]	preexposure [W]	surface porosity [%]
a	6	35	5	20	30	0	48.06
b	27	35	5	20	30	50	33.18
c	24	35	5	80	30	0	54.91
d	26	35	5	80	30	50	57.75
e	18	35	20	80	30	50	43.55
f	4	50	5	20	30	0	52.71
g	15	50	5	20	30	50	48.64
h	31	50	5	80	30	0	46.02
i	14	50	5	80	30	50	61.14
j	3	50	20	80	30	0	46.18
k	23	50	20	80	30	50	38.21

According to figure 61, the tracks in figure 62 were sorted in the following manner: increasing levels of power, increasing levels of spot distance, increasing levels of pulse time and increasing levels of preexposure. Figure 62 depicts samples with a layer thickness of 60 μm . The build parameters are summarized in table 22.

Table 22: Parameters of selected tracks (figure 62)

picture	run order	power [W]	spot dist [μm]	pulse time [μs]	layer thickness [μm]	preexposure [W]	surface porosity [%]
a	19	35	5	20	60	50	47.50
b	10	35	5	80	60	0	44.25
c	30	35	5	80	60	50	48.52
d	9	35	20	80	60	50	46.26
e	29	50	5	20	60	0	56.88
f	12	50	5	20	60	50	32.87
g	32	50	5	80	60	0	35.15
h	21	50	5	80	60	50	25.07
i	1	50	20	80	60	0	62.52
j	2	50	20	80	60	50	40.90




100.00 um/div


Figure 62: Selected tracks, test series 2 a) 19, b) 10, c) 30, d) 09, e) 29, f) 12, g) 32, h) 21, i) 01, j) 02.

If figure 61 is compared to figure 62, it is obvious that over all parameters, the dimension and spread of the droplets strongly depended on the layer thickness. For a layer thickness of 30 μm , the surfaces of the tracks contained more spray than single droplets of molten material. In figure 62, the tracks tended to balling. Besides that, the interruptions of the tracks were larger compared to the interruptions in figure 61.

5.8.2 Test series 3

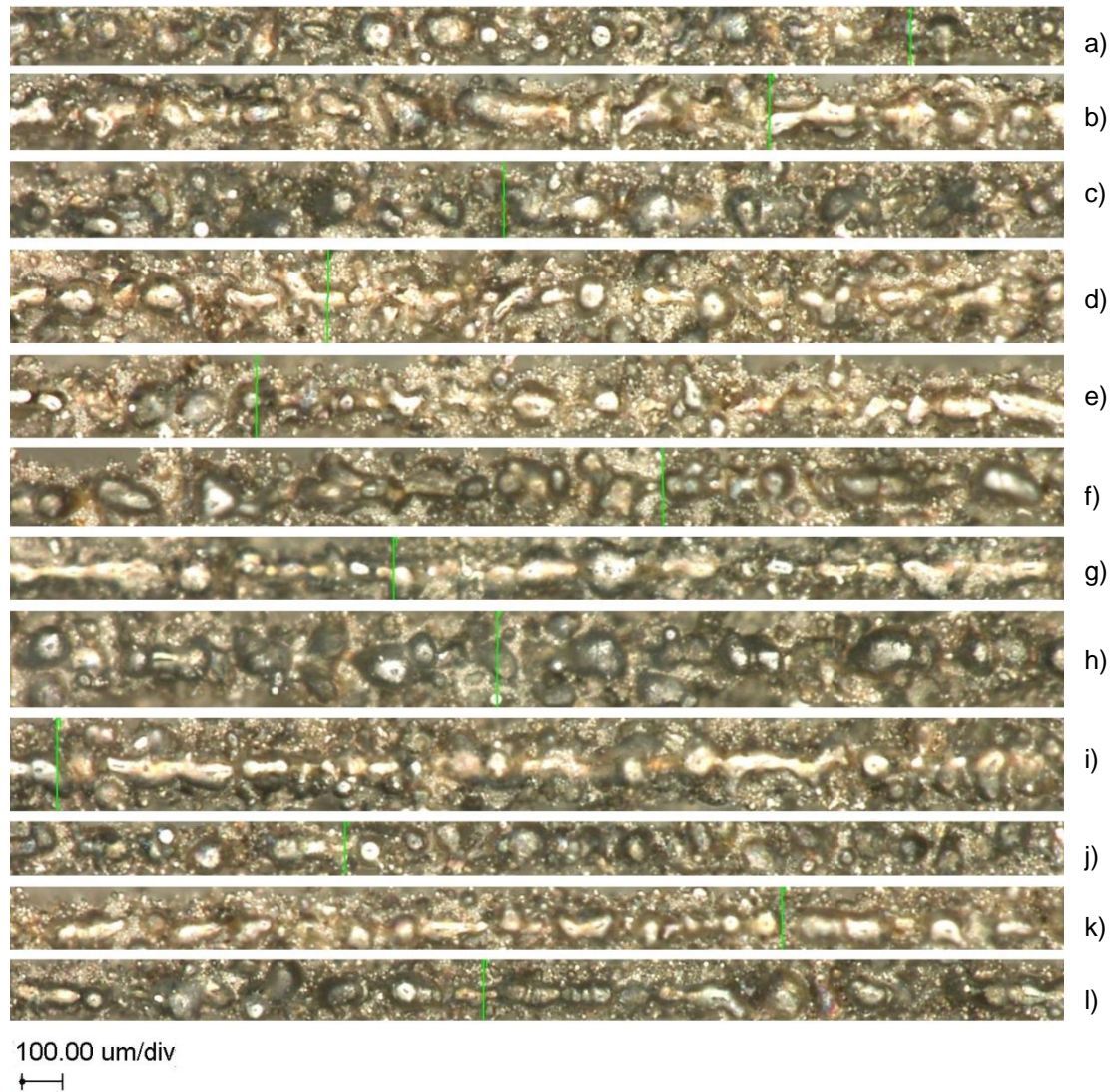


Figure 63: Selected samples of test series 3 a) 25, b) 28, c) 22, d) 27, e) 32, f) 16, g) 03, h) 26, i) 04, j) 21, k) 29, l) 06.

The tracks were sorted in the following manner: increasing levels of power, increasing levels of spot distance, increasing levels of pulse time and increasing levels of preexposure. Figure 63 depicts samples with a layer thickness of 30 μm . The build parameters are summarized in table 23.

Table 23: Parameters of selected samples (figure 63)

picture	run order	power [W]	spot dist [μm]	pulse time [μs]	layer thickness [μm]	preexposure [W]	surface porosity [%]
a	25	35	7	20	30	0	55.65
b	28	35	7	20	30	50	38.05
c	22	35	7	40	30	0	36.57
d	27	35	7	40	30	50	47.31
e	32	35	15	40	30	50	45.69
f	16	50	7	20	30	0	34.40
g	3	50	7	20	30	50	54.71
h	26	50	7	40	30	0	50.82
i	4	50	7	40	30	50	32.13
j	21	50	15	20	30	0	54.53
k	29	50	15	20	30	50	67.58
l	6	50	15	40	30	0	47.08

In figure 63 it can be seen that the tracks where preexposure was applied showed less surface annealing colors. The appearance of the tracks without preexposure was mainly unstable. The laser powers of this test series were comparably low. The additional energy input of the preexposure led to better results for this data set.

Table 24: Parameters of selected samples (figure 64)

picture	run order	power [W]	spot dist [μm]	pulse time [μs]	layer thickness [μm]	preexposure [W]	surface porosity [%]
a	1	35	7	20	60	50	37.95
b	10	35	7	40	60	50	33.81
c	13	50	7	20	60	50	33.56
d	8	50	7	40	60	0	36.12
e	5	50	7	40	60	50	32.29
f	18	50	15	40	60	50	36.02

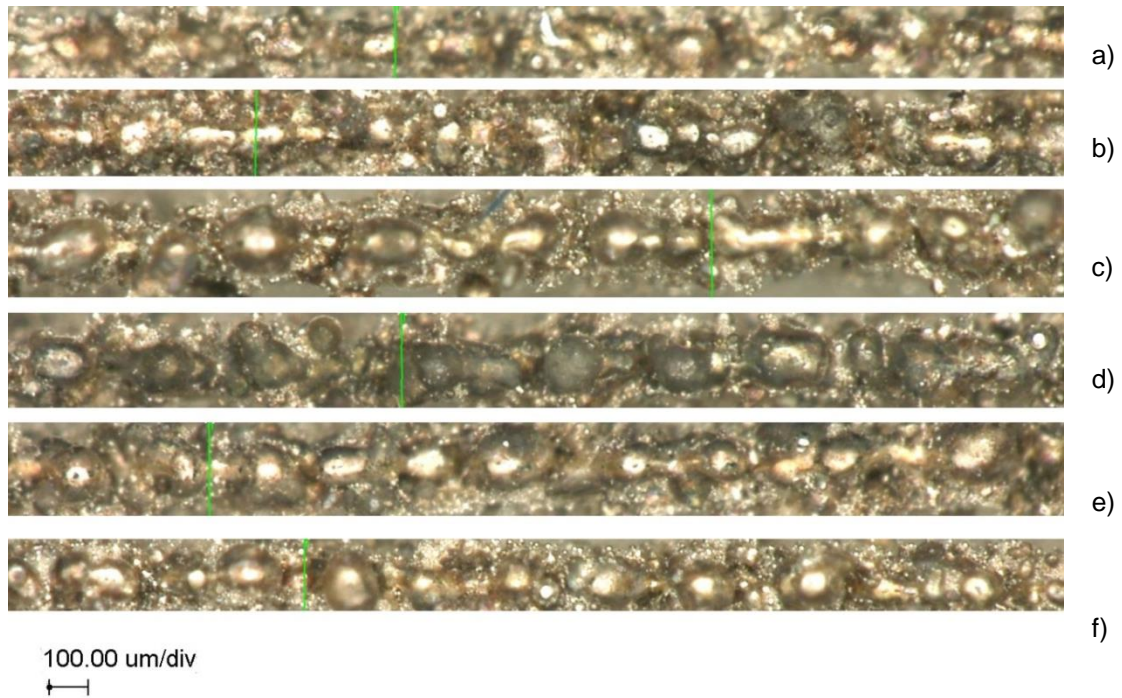


Figure 64: Selected samples of test series 3 a) 01 b) 10, c) 13, d) 08, e) 09, f) 18.

According to the previous figures, the tracks were sorted in the following manner: increasing levels of power, increasing levels of spot distance, increasing levels of pulse time and increasing levels of preexposure. Figure 64 depicts samples with a layer thickness of 60 μm . The build parameters are summarized in table 24.

In figure 64, most parts of the test series were successfully produced using additional preexposure. Only one set of parameters led to successful parts without preexposure with a layer thickness of 60 μm (sample d). Again, one obvious difference could be seen in the annealing colors of sample d) compared to e) which was manufactured using the same parameters except the preexposure.

5.8.3 Test series 4

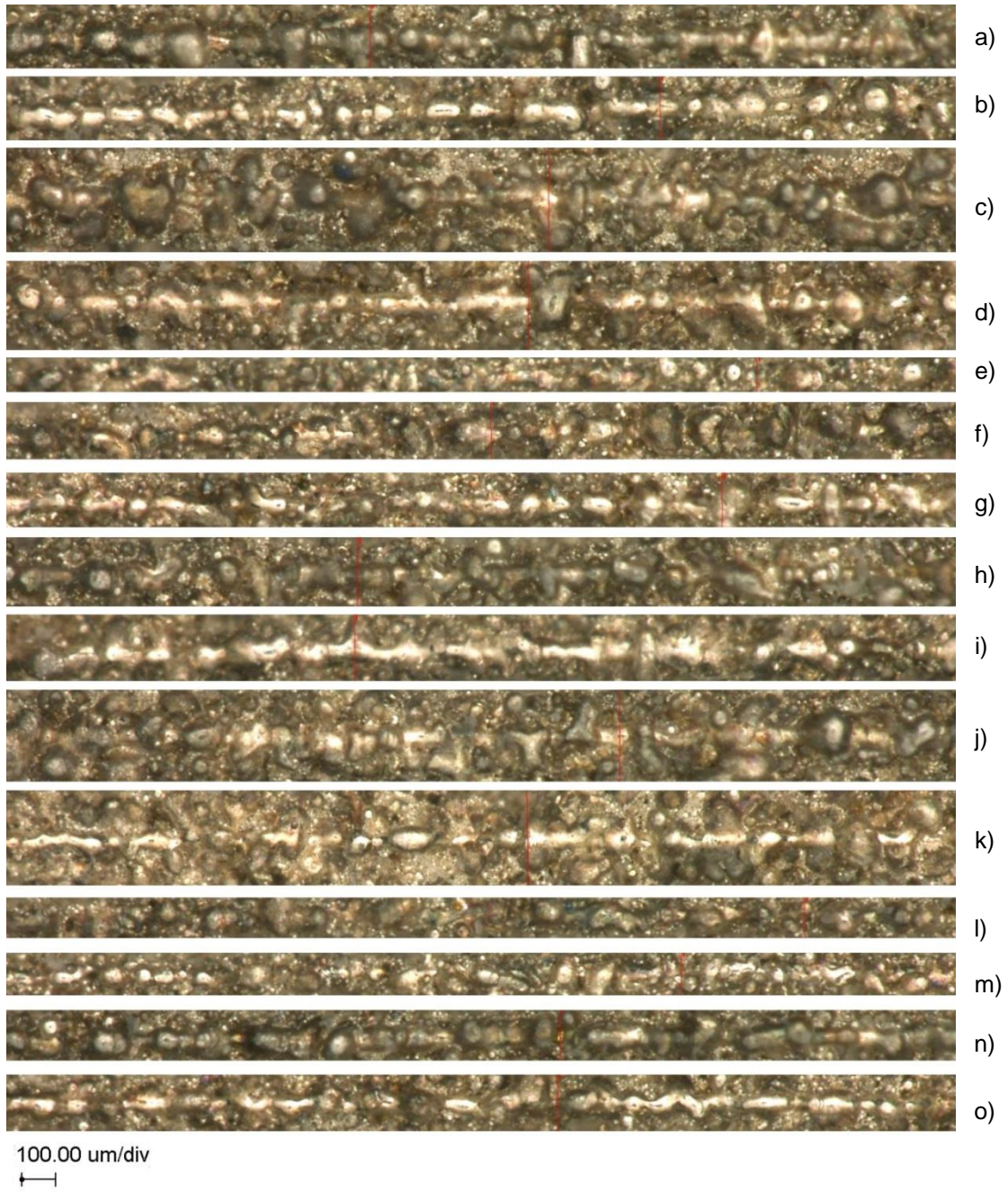


Figure 65: Selected tracks, test series 4 a) 06, b) 27, c) 24, d) 26, e) 16, f) 13, g) 18, h) 04, i) 15, j) 31, k) 14, l) 07, m) 08, n) 03, o) 23

Table 25: Parameters of the scan tracks in figure 65

picture	run order	power [W]	spot dist [μm]	pulse time [μs]	layer thickness [μm]	preexposure [W]	surface porosity [%]
a	6	60	5	20	30	0	33.14
b	27	60	5	20	30	50	38.55
c	24	60	5	80	30	0	30.34
d	26	60	5	80	30	50	28.99
e	16	60	20	20	30	0	37.20
f	13	60	20	80	30	0	30.99
g	18	60	20	80	30	50	28.65
h	4	70	5	20	30	0	37.23
i	15	70	5	20	30	50	22.69
j	31	70	5	80	30	0	27.15
k	14	70	5	80	30	50	34.41
l	7	70	20	20	30	0	39.62
m	8	70	20	20	30	50	35.36
n	3	70	20	80	30	0	32.07
o	23	70	20	80	30	50	35.84

The parameters of figure 65 are displayed in table 25 whereas the parameters of figure 66 are displayed in table 26. Both figures were sorted as the figures before, separated into 30 μm layer thickness and 60 μm layer thickness.

Table 26: Parameters of test series 4, 60 μm (figure 66)

picture	run order	power [W]	spot dist [μm]	pulse time [μs]	layer thickness [μm]	preexposure [W]	surface porosity [%]
a	22	60	5	20	60	0	30.16
b	19	60	5	20	60	50	33.12
c	10	60	5	80	60	0	48.24
d	30	60	5	80	60	50	38.76
e	25	60	20	80	60	0	21.03
f	9	60	20	80	60	50	35.51
g	29	70	5	20	60	0	17.57
h	12	70	5	20	60	50	40.43
i	32	70	5	80	60	0	25.38
j	21	70	5	80	60	50	27.99
k	1	70	20	80	60	0	31.58
l	2	70	20	80	60	50	39.11

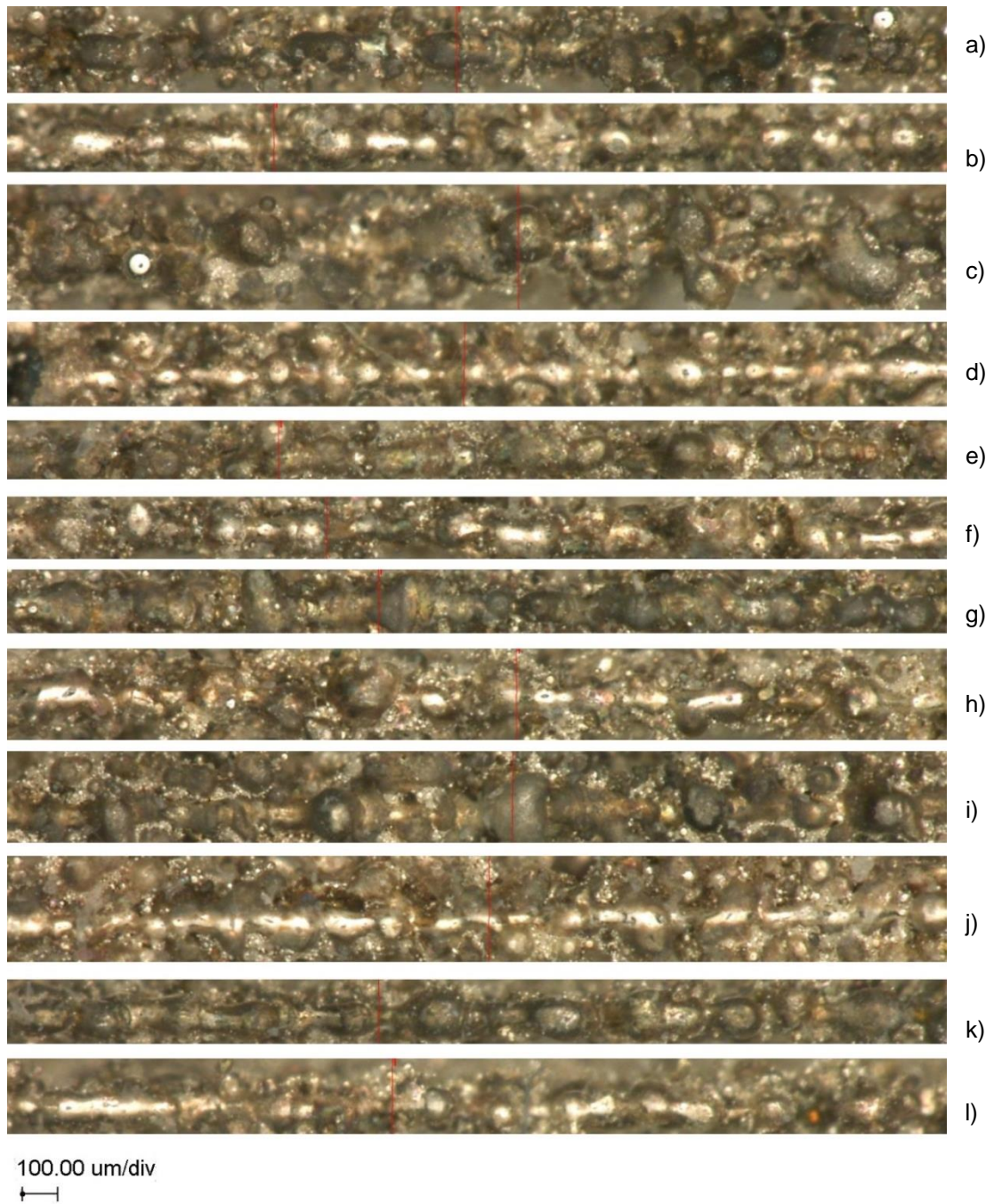


Figure 66: Selected samples, test series 4, 60 μm layer thickness a) 22, b) 19, c) 10, d) 30, e) 25, f) 09, g) 29, h) 12, i) 32, j) 21, k) 01, l) 02.

In comparison to figure 65, figure 66 shows a higher tendency for material agglomerations. The difference in annealing colors between parts that

were treated with preexposure and that were not treated with preexposure could still be seen, although the effect weakened compared to the previous figures. In comparison to all other microscope pictures, the parameter set of figure 65 led to the best results since the surface was comparably smooth and the balling effect was not as distinct as for parameter sets with a layer thickness of 60 μm .

5.8.4 Results and conclusion of the screening experiments

Using the approach to estimate the surface porosity, preexposure was not significant but the interactions of preexposure times power and preexposure times power times layer thickness (see table 20) were significant. In all cases, the effects of preexposure could be seen using microscopy since the annealing color was not part of the model for the surface porosity. Especially in figure 65, good results were obtained without preexposure. From this reason, the next investigations encompassed data sets without preexposure.

Layer thickness and power were considered to be significant factors (see table 20). Comparing the microscope pictures, there was a tendency that a layer thickness of 30 μm led to better results than a layer thickness of 60 μm . The next investigations were done using a layer thickness of 30 μm .

The factor power showed the best results for the levels 60 and 70 W. As a result from these screening experiments, the response surface of chapter 6 was initially started in that region for obtaining good results. 60 W was chosen as the center point, combined with 10 μm spot distance and 40 μs pulse time. In addition to that, the parts were created using a higher wall thickness,

manufactured from 10 offsets. Furthermore, inner results were analyzed using microsections and measuring the porosity of the parts.

5.8.5 Test series 5

In order to investigate the porosity of the parts, test series 5 was designed. It considered all successful parameter sets of the test series 1 to 4, but without the preexposure strategy. The manufacturing of the parts was changed in the following manner:

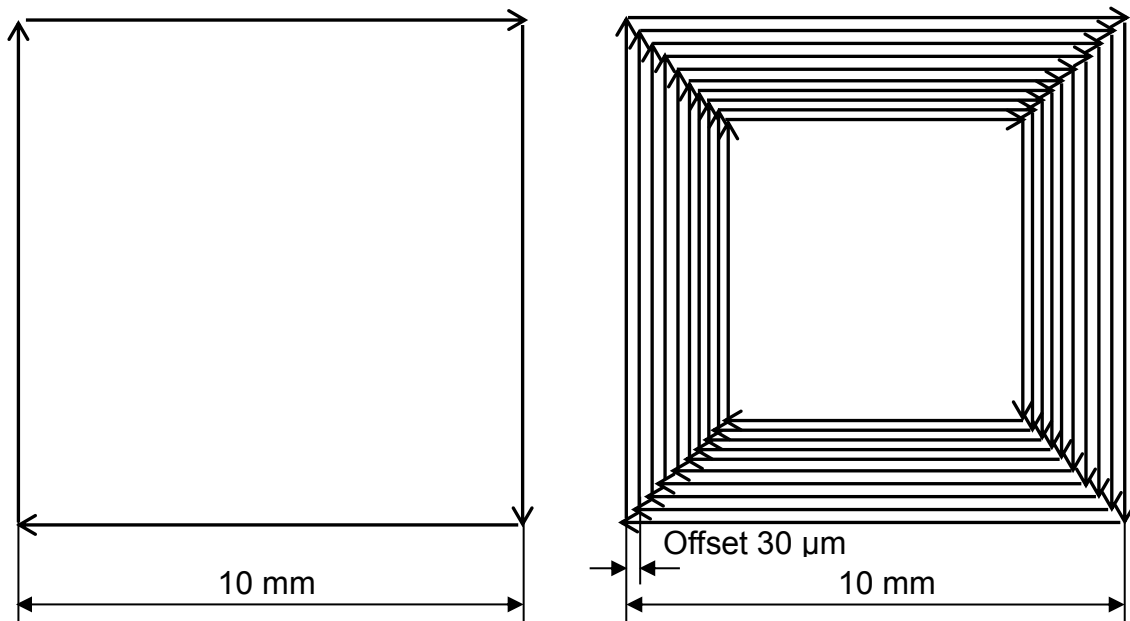


Figure 67: Schematic comparison of test series 1-4 and test series 5

Figure 67 shows that a scan vector length of 10 mm was used. For test series 1 to 4, single scan vectors were investigated. For test series 5, an offset distance of 30 μm was applied, using ten offset vectors. The offsets were shifted to the inner sides of the square so that the edge length of 10 mm times 10 mm remains the same. Figure 68 shows the top view of a manufactured part.

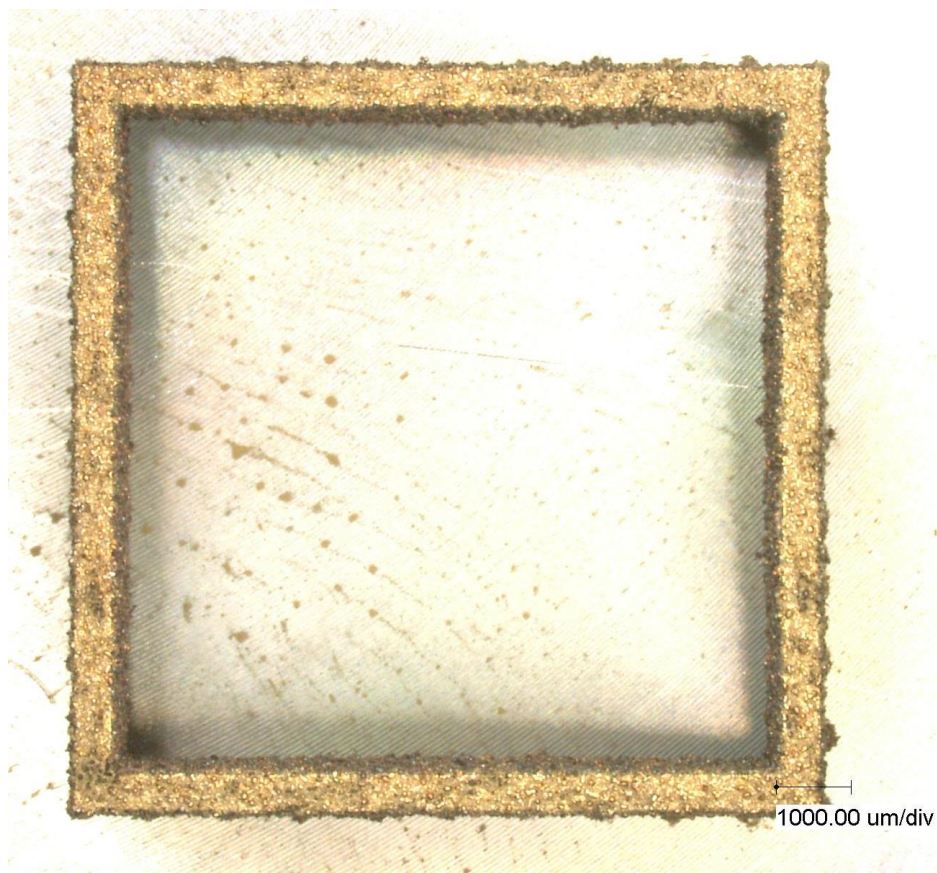


Figure 68: Example of a hollow cube, 10 offsets, height 10 mm

Figure 69 shows the samples of the data collected in table 27. The samples a) to d) were manufactured at power levels of 80 W whereas samples e) to h) were manufactured at a power level of 100 W. Sample a) and g) showed a surface with small droplets, but sample a) was manufactured using 80 W at 5 μm spot distance and 20 μs pulse time whereas sample g) was manufactured using 100 W at 20 μm spot distance and 20 μs pulse time. Samples b), d), f), and h) showed increased droplets on the surface. On the surface of sample c) scan tracks could be seen, overlaid by major droplets. Sample e) compared to sample

a) showed larger droplets on the surface. The difference between these two samples was the difference in power level (80 W versus 100 W).

Table 27: Parameters of test series 5, 30 μm (figure 69)

Picture	run order	power [W]	spot dist [μm]	pulse time [μs]	layer thickness [μm]	preexposure [W]
a	1-21	80	5	20	30	0
b	1-12	80	5	80	30	0
c	1-16	80	20	20	30	0
d	1-23	80	20	80	30	0
e	1-7	100	5	20	30	0
f	1-29	100	5	80	30	0
g	1-2	100	20	20	30	0
h	1-8	100	20	80	30	0

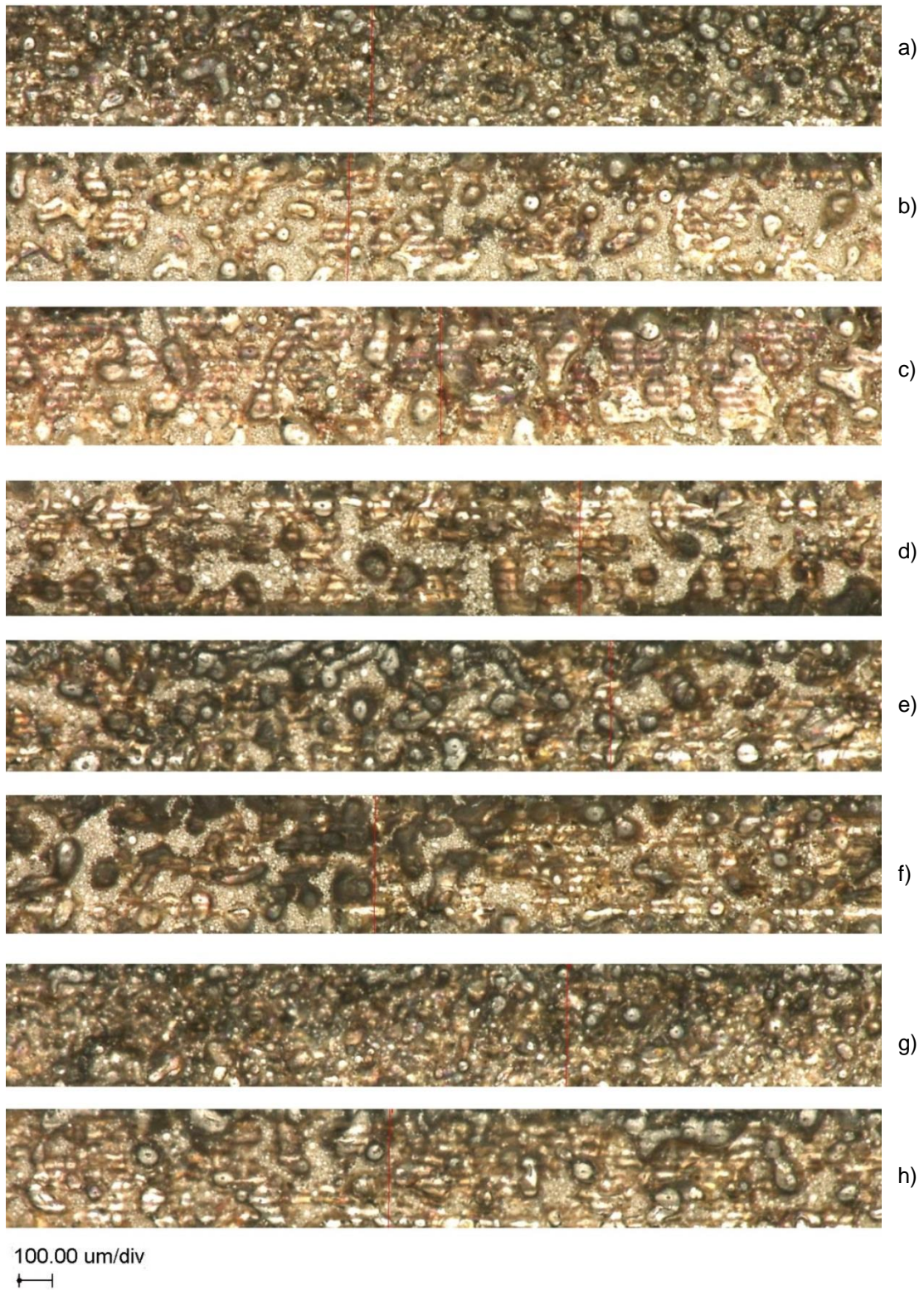


Figure 69: Selected samples, test series 5 a) 01-21, b) 01-12, c) 01-16, d) 01-23, e) 01-7, f) 01-29, g) 01-02, h) 01-08.

Figure 70 shows the samples of the parameters collected in table 28. In comparison to figure 69, figure 70 depicts samples manufactured at a layer thickness of 60 μm . Over all samples, the diameter of the droplets appeared larger than the diameter of the droplets in figure 69. In sample a) and b), scan tracks could be seen, overlaid by large droplets of material. Sample c) showed minor droplets, whereas sample d) and e) showed droplets of similar size. The size of the droplets in sample f) was similar to sample e). The difference was that the scan tracks of sample f) showed rounded edges. All samples except sample c) showed a comparably unstable surface.

Table 28: Parameters of test series 5, 60 μm (figure 70)

Picture	run order	power [W]	spot dist [μm]	pulse time [μs]	layer thickness [μm]	preexposure [W]
a	1-28	80	5	20	60	0
b	1-17	80	5	80	60	0
c	1-26	80	20	20	60	0
d	1-19	100	5	20	60	0
e	1-22	100	5	80	60	0
f	1-9	100	20	80	60	0

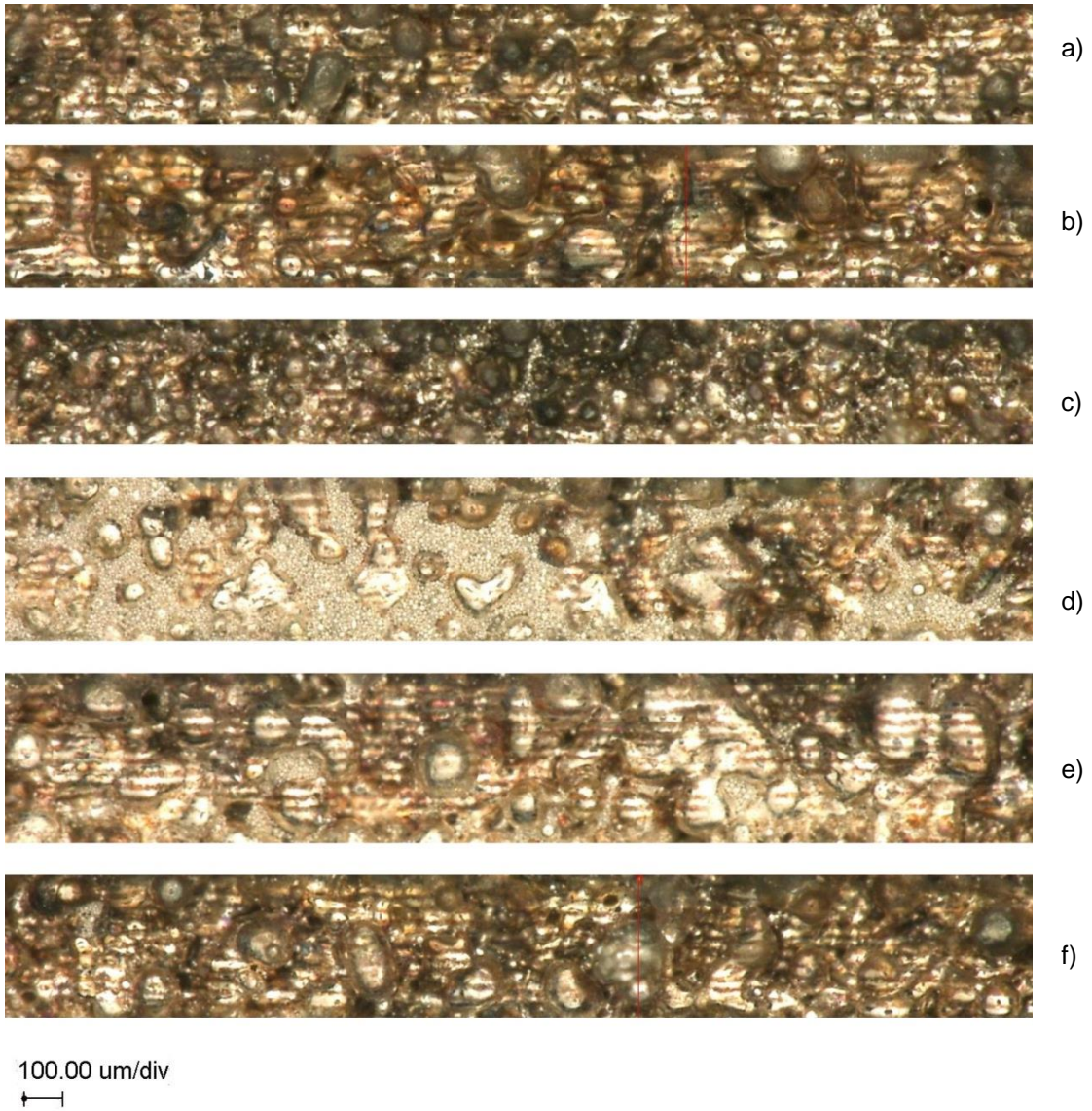


Figure 70: Selected samples, test series 5, 60 μm , a) 1-28, b) 1-17, c) 1-26, d) 1-19, e) 1-22, f) 1-9.

5.8.6 Test series 6

Table 29 lists the build parameters of the samples shown in figure 71. The laser power levels were 35 W and 50 W, respectively. The surface of sample a) showed minor droplets. No scan tracks were visible. Sample b) also showed minor droplets with areas that were filled with base material. Sample c) was manufactured using a laser power level of 50 W, a spot distance of 5 μm and a pulse time of 20 μs . The surface of sample c) was comparably smooth, but no scan tracks were visible. The droplet size of sample d) was increased, but little scan tracks were visible. Sample e) also showed increased droplets, but horizontal scan track lines could be determined.

Table 29: Parameters of test series 6 (figure 71)

picture	run order	power [W]	spot dist [μm]	pulse time [μs]	layer thickness [μm]	preexposure [W]
a	2-6	35	5	20	30	0
b	2-24	35	5	80	30	0
c	2-4	50	5	20	30	0
d	2-31	50	5	80	30	0
e	2-3	50	20	80	30	0

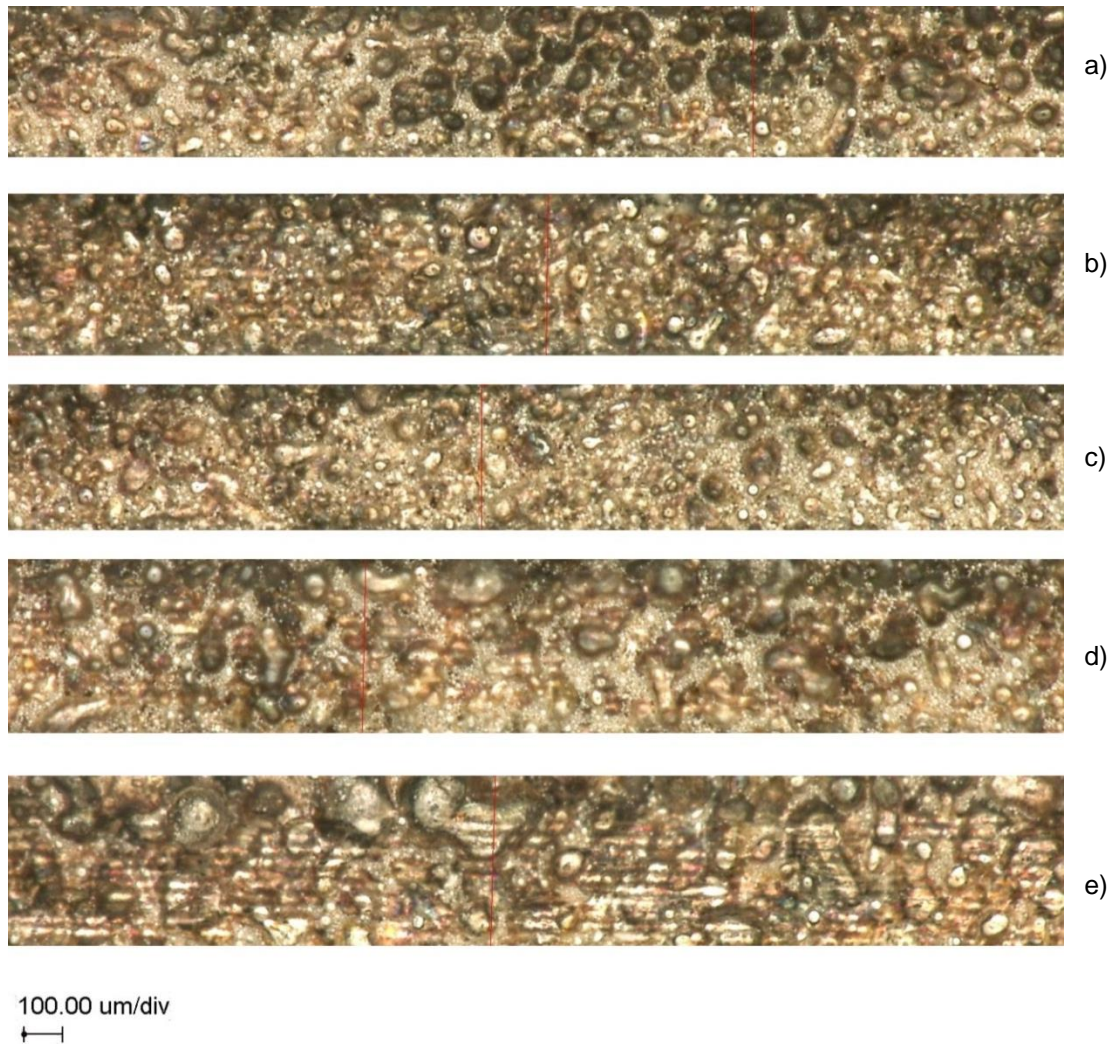


Figure 71: Selected samples, test series 6: a) 2-6, b) 2-24, c) 2-4, d) 2-31, e) 2-3.

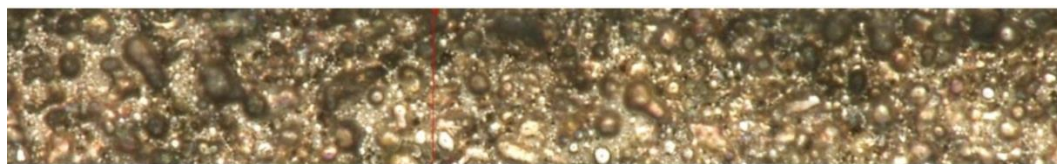
5.8.7 Test series 7

Table 30 collects the build parameters of the samples of test series 7, shown in figure 72. A layer thickness of 30 μm was chosen. The power level was 50 W for all samples. They differed in spot distance and pulse time. Sample a) and c), both manufactured at a pulse time level of 20 μs , did not show scan tracks. The droplets of sample a) appeared a little smaller in diameter than in

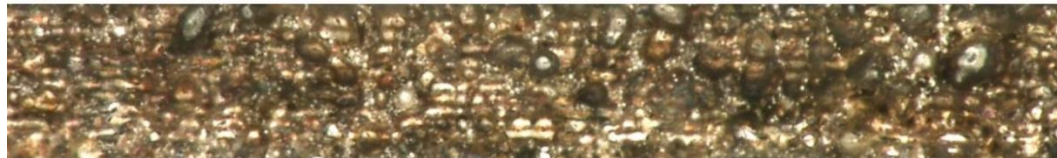
sample c). Sample c) showed areas that were filled with base material. Sample b) and d) both showed scan tracks, overlaid with minor droplets.

Table 30: Parameters of test series 7 (figure 72)

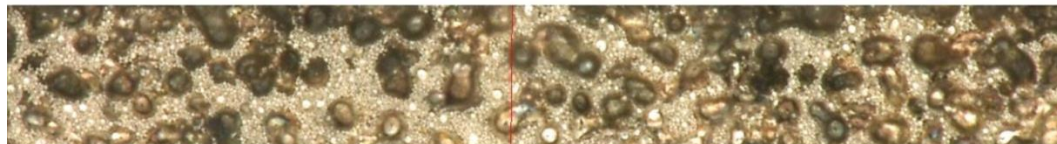
picture	run order	power [W]	spot dist [μm]	pulse time [μs]	layer thickness [μm]	preexposure [W]
a	3-16	50	7	20	30	0
b	3-26	50	7	40	30	0
c	3-21	50	15	20	30	0
d	3-6	50	15	40	30	0



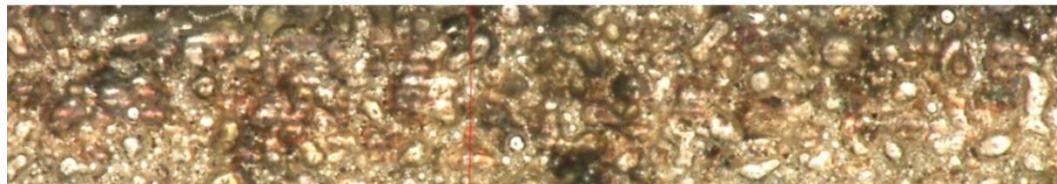
a)



b)



c)



d)

100.00 $\mu\text{m}/\text{div}$



Figure 72: Selected samples, test series 7 a) 3-16, b) 3-26, c) 3-21, d) 3-6.

5.8.8 Test series 8

Table 31: Parameters of test series 8, 30 μm (figure 73)

picture	run order	power [W]	spot dist [μm]	pulse time [μs]	layer thickness [μm]	preexposure [W]
a	4-24	60	5	80	30	0
b	4-16	60	20	20	30	0
c	4-13	60	20	80	30	0
d	4-31	70	5	80	30	0

Figure 73 shows the samples of the parameters collected in table 31.

The layer thickness of 30 μm is depicted.

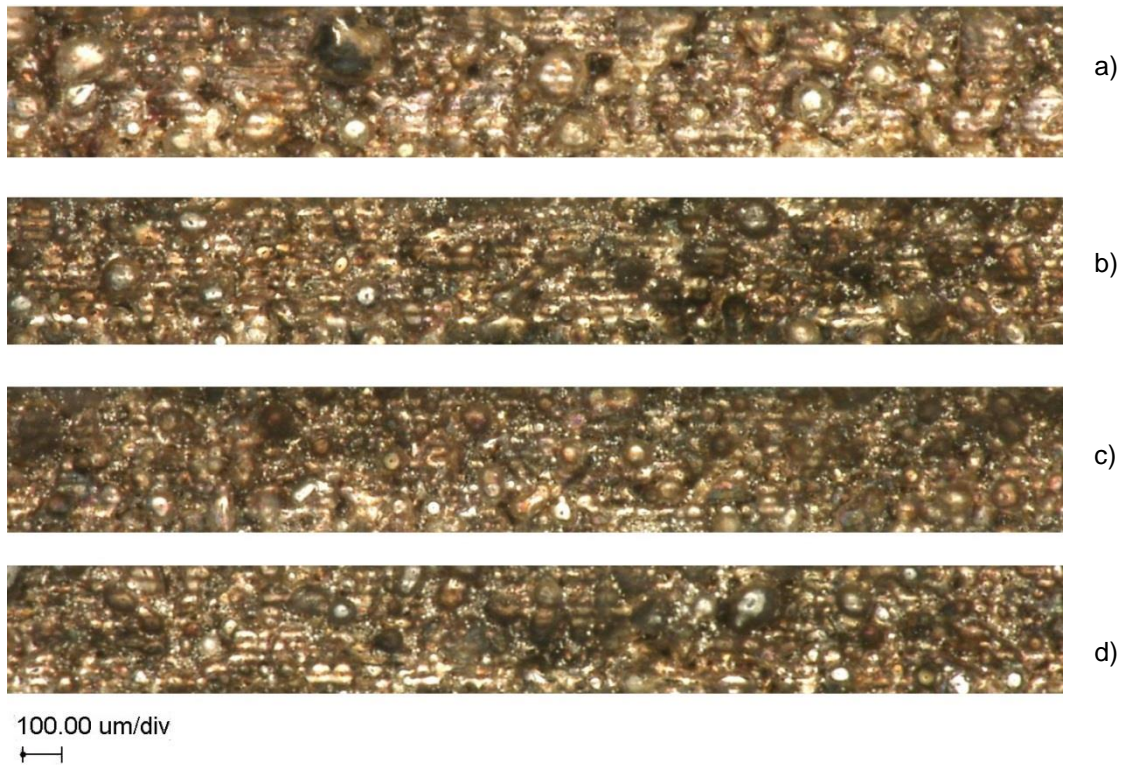


Figure 73: Selected samples, test series 8, 30 μm layer thickness a) 4-24, b) 4-16, c) 4-13, d) 4-31.

In figure 73, all samples showed scan tracks. Sample a) showed the largest droplets on the surface within this parameter sets. The samples b) and c) appeared similar. For sample d), both scan tracks and droplets on the surface

could be seen. Except for the droplets, the microscope picture of this sample showed a similar surface to sample b) and c).

Table 32: Parameters of test series 8, 60 μm (figure 74)

picture	run order	power [W]	spot dist [μm]	pulse time [μs]	layer thickness [μm]	preexposure [W]
a	4-22	60	5	20	60	0
b	4-10	60	5	80	60	0
c	4-29	70	5	20	60	0
d	4-32	70	5	80	60	0
e	4-1	70	20	80	60	0

Figure 74 shows the samples of the parameters collected in table 32. The layer thickness of 60 μm is depicted. In comparison to figure 73, larger droplets were observed due to the balling phenomenon. In sample a) and b), scan tracks were visible. The dimensions of the droplets in sample a) and b) were similar, although the surface of sample a) showed more droplets. Sample c) showed smaller droplets than sample a). The difference between sample a) and c) was a change in the power levels between 60 W and 70 W. Sample d) showed holes on the surface that were filled with base material. The material between the holes showed fragments of scan tracks that were overlaid by large droplets. In comparison to sample d), sample e) showed a similar appearance. Few scan tracks were visible.

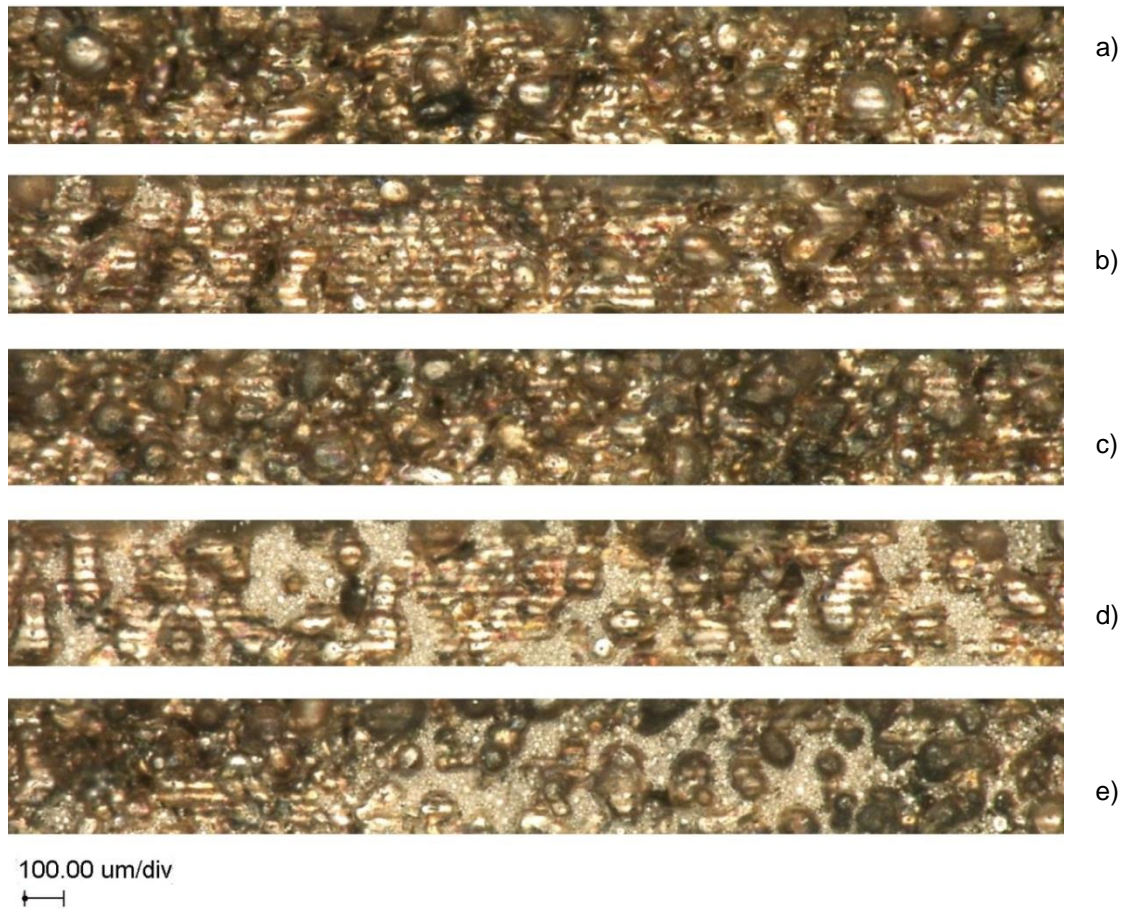


Figure 74: Selected samples, test series 8, 60 μm layer thickness, a) 4-22, b) 4-10, c) 4-49, d) 4-32, e) 4-1.

5.8.9 Results and conclusion of experiments 5 to 8:

Over all tests, the material showed partly unstable behavior in processing and the material was difficult to process. The balling behavior for a layer thickness of 60 μm was worse compared to a layer thickness of 30 μm. For the response surface experiments (chapter 6), the experiments were reduced to a level in layer thickness of 30 μm. According to the screening experiments, best results were obtained using a power level of approximately 60 W, see figure 73. Spot distance and pulse time for the core area were selected with levels of 10 μm and 40 μs and were investigated next.

6 RESPONSE SURFACE METHOD AGCU7

6.1 Theoretical background

The response surface method is a method for optimizing processes. A response surface is built when some parameters are known and a response should be optimized. [122]

A first approximation of the dependency of the variables on the response can be estimated with the first order model [122]

$$y = \beta_0 + \beta_1x_1 + \beta_2x_2 + \dots + \beta_kx_k + \varepsilon$$

Equation 27: First-order model [122]

This first order model is used for a linear approximation within a specific range of data points. In this case, the screening experiments from chapter 4 and 5 were used to detect the area of interest. For many problems, a second-order model is more appropriate: [122]

$$y = \beta_0 + \sum_{i=1}^k \beta_i x_i + \sum_{i=1}^k \beta_{ii} x_i^2 + \sum_{i < j} \sum \beta_{ij} x_i x_j + \varepsilon$$

Equation 28: Second-order model [122]

Figure 75 depicts the general data sets of a response surface approach graphically. It can be distinguished between factorial and axial points. The center point is in the middle of the data set.

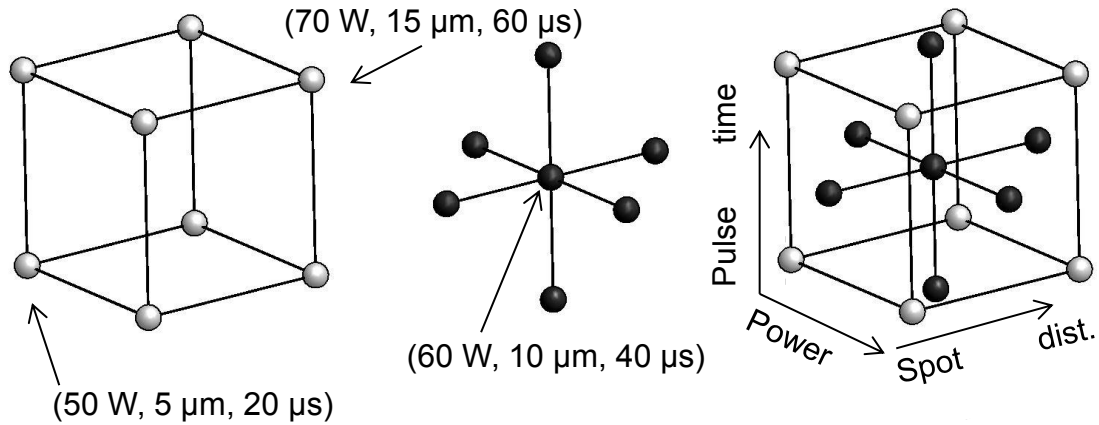


Figure 75: RSM a) factorial points, b) axial points c) factorial and axial points

The factorial points are the outer limits of the design points within the analyzed region. For test series 9, the factorial points were set up using the following values: Power: 50 W and 70 W, spot distance: 5 μm and 15 μm , pulse time 20 μs and 60 μs . The vectors of the factorial points were:

$$\begin{pmatrix} 50 W \\ 5 \mu m \\ 20 \mu s \end{pmatrix}, \begin{pmatrix} 50 W \\ 5 \mu m \\ 60 \mu s \end{pmatrix}, \begin{pmatrix} 50 W \\ 15 \mu m \\ 20 \mu s \end{pmatrix}, \begin{pmatrix} 50 W \\ 15 \mu m \\ 60 \mu s \end{pmatrix}, \begin{pmatrix} 70 W \\ 5 \mu m \\ 20 \mu s \end{pmatrix}, \begin{pmatrix} 70 W \\ 5 \mu m \\ 60 \mu s \end{pmatrix}, \begin{pmatrix} 70 W \\ 15 \mu m \\ 20 \mu s \end{pmatrix}, \begin{pmatrix} 70 W \\ 15 \mu m \\ 60 \mu s \end{pmatrix}$$

In this case, the axial points were centered on the surface since $\alpha = 1$. The vectors of the axial points were set up at the arithmetic mean of the factorial points:

$$\begin{pmatrix} 60 W \\ 5 \mu m \\ 40 \mu s \end{pmatrix}, \begin{pmatrix} 50 W \\ 10 \mu m \\ 40 \mu s \end{pmatrix}, \begin{pmatrix} 60 W \\ 15 \mu m \\ 40 \mu s \end{pmatrix}, \begin{pmatrix} 70 W \\ 10 \mu m \\ 40 \mu s \end{pmatrix}, \begin{pmatrix} 60 W \\ 10 \mu m \\ 20 \mu s \end{pmatrix}, \begin{pmatrix} 60 W \\ 10 \mu m \\ 60 \mu s \end{pmatrix}$$

and the center point

$$\begin{pmatrix} 60 W \\ 10 \mu m \\ 40 \mu s \end{pmatrix}$$

Two replicates were conducted. Per sample, four estimates were taken (see figure 42 on page 87). The sample with the vector

$$\begin{pmatrix} 50 \text{ W} \\ 15 \text{ } \mu\text{m} \\ 20 \text{ } \mu\text{s} \end{pmatrix}$$

failed in both replicates. The reason could be explained by the low linear energy density of 0.09 J/mm which was approximately a factor of 10 lower compared to the highest linear energy density (0.89 J/mm) of the data vector

$$\begin{pmatrix} 70 \text{ W} \\ 5 \text{ } \mu\text{m} \\ 60 \text{ } \mu\text{s} \end{pmatrix}.$$

Therefore, in total 152 measurements were taken (19 samples, four estimates each, two replicates). For the center point, six samples per replicate were measured. The test set up was randomized over both replicates. Power, spot distance and pulse time were adjusted, whereas scan speed and linear energy density were calculated.

6.2 Model and data points for test series 9

Table 33: Initial parameters for the model of the response surface

Base parameters	Squares and interactions
A: power [W]:	A*A
B: spot dist [μm]:	A*B
C: pulse time [μs]:	A*C
	B*B
	B*C
	C*C

Table 33 collects the initial parameters for the response surface. A full quadratic approach was chosen. Therefore, besides all base parameters, the squares of the base parameters and the first grade interactions are included in the model. Table 34 displays a factorial design collection sheet in order to estimate the response R-squared of the estimated regression coefficients. Only squares and interactions are shown. Level 0 represents exclusion from the model, whereas level 1 represents inclusion. For example, row 4 (standard order 3) shows that the interaction BC, spot distance times pulse time and CC, the square of pulse time, were included in the model. A high R-square was desirable. It can be seen from table 34 that the highest values for R-square were obtained for standard order 32 and 64. Standard order 64 included all initial parameters, squares and interactions, given in table 33, whereas for standard order 32, the square of the parameter power (AA) was removed. It could be seen that the value of R-square is 34.94% for both standard orders. From this reason, AA was removed from the model for further investigation. R-square = 34.94% was comparably low and could be increased up to 55% if scan speed was included in the model. Since scan speed was an artificial parameter (see section 5.3), and was correlated to pulse time and spot distance, it was not inserted into the model.

Table 34: Factorial design collection sheet in order to analyze the factors to be included in the model

StdOrder	AA	AB	AC	BB	BC	CC	response R-Sq
1	0	0	0	0	0	0	12.75
2	0	0	0	0	0	1	13.08
3	0	0	0	0	1	0	14.90
4	0	0	0	0	1	1	15.04
5	0	0	0	1	0	0	17.64
6	0	0	0	1	0	1	18.32
7	0	0	0	1	1	0	19.00
8	0	0	0	1	1	1	19.84
9	0	0	1	0	0	0	15.46
10	0	0	1	0	0	1	16.12
11	0	0	1	0	1	0	16.69
12	0	0	1	0	1	1	17.07
13	0	0	1	1	0	0	21.55
14	0	0	1	1	0	1	22.02
15	0	0	1	1	1	0	22.00
16	0	0	1	1	1	1	22.56
17	0	1	0	0	0	0	25.76
18	0	1	0	0	0	1	25.77
19	0	1	0	0	1	0	31.50
20	0	1	0	0	1	1	31.64
21	0	1	0	1	0	0	28.72
22	0	1	0	1	0	1	29.89
23	0	1	0	1	1	0	33.21
24	0	1	0	1	1	1	34.88
25	0	1	1	0	0	0	26.42
26	0	1	1	0	0	1	26.47
27	0	1	1	0	1	0	31.50
28	0	1	1	0	1	1	31.64
29	0	1	1	1	0	0	30.03
30	0	1	1	1	0	1	30.97
31	0	1	1	1	1	0	33.38
32	0	1	1	1	1	1	34.94
33	1	0	0	0	0	0	14.38
34	1	0	0	0	0	1	14.41
35	1	0	0	0	1	0	16.07
36	1	0	0	0	1	1	16.15
37	1	0	0	1	0	0	17.64
38	1	0	0	1	0	1	18.45
39	1	0	0	1	1	0	19.01
40	1	0	0	1	1	1	19.93
41	1	0	1	0	0	0	17.78
42	1	0	1	0	0	1	17.78
43	1	0	1	0	1	0	18.50
44	1	0	1	0	1	1	18.51
45	1	0	1	1	0	0	21.58
46	1	0	1	1	0	1	22.22
47	1	0	1	1	1	0	22.01
48	1	0	1	1	1	1	22.73
49	1	1	0	0	0	0	26.36
50	1	1	0	0	0	1	26.56
51	1	1	0	0	1	0	31.62
52	1	1	0	0	1	1	32.07
53	1	1	0	1	0	0	28.77
54	1	1	0	1	0	1	29.92
55	1	1	0	1	1	0	33.40
56	1	1	0	1	1	1	34.88
57	1	1	1	0	0	0	27.30
58	1	1	1	0	0	1	27.42
59	1	1	1	0	1	0	31.65
60	1	1	1	0	1	1	32.08
61	1	1	1	1	0	0	30.04
62	1	1	1	1	0	1	31.03
63	1	1	1	1	1	0	33.52
64	1	1	1	1	1	1	34.94

Table 35 depicts the MINITAB output of the estimated regression coefficients for porosity. The model was blocked on replicates. The p-value of the block is considered significant if it is less than the α -value, which is set to 0.05. Since the Block p-value of 0.077 is close to the α -value, this indicates that the asymmetric wiper system may have an effect on the results, and thus randomization of location of parts on the base platform was deemed necessary in order to reduce that effect (see section 5.1).

Table 35: MINITAB output: estimated regression coefficients for porosity [%]

Term	Coef	SE Coef	T	P
Constant	33.9985	5.96917	5.696	0.0000
Block	-0.3556	0.19946	-1.783	0.0770
power	-0.384	0.09312	-4.124	0.0000
spot dist	-4.1866	0.6389	-6.553	0.0000
pulse time	0.1181	0.15972	0.74	0.4610
spot dist*spot dist	0.0536	0.02	2.681	0.0080
pulse time*pulse time	-0.0023	0.00125	-1.843	0.0670
power*spot dist	0.0403	0.00775	5.196	0.0000
power*pulse time	0.0007	0.00194	0.339	0.7350
spot dist*pulse time	0.0114	0.00387	2.942	0.0040
R-Sq = 34.94% R-Sq(pred) = 25.03% R-Sq(adj) = 30.81%				

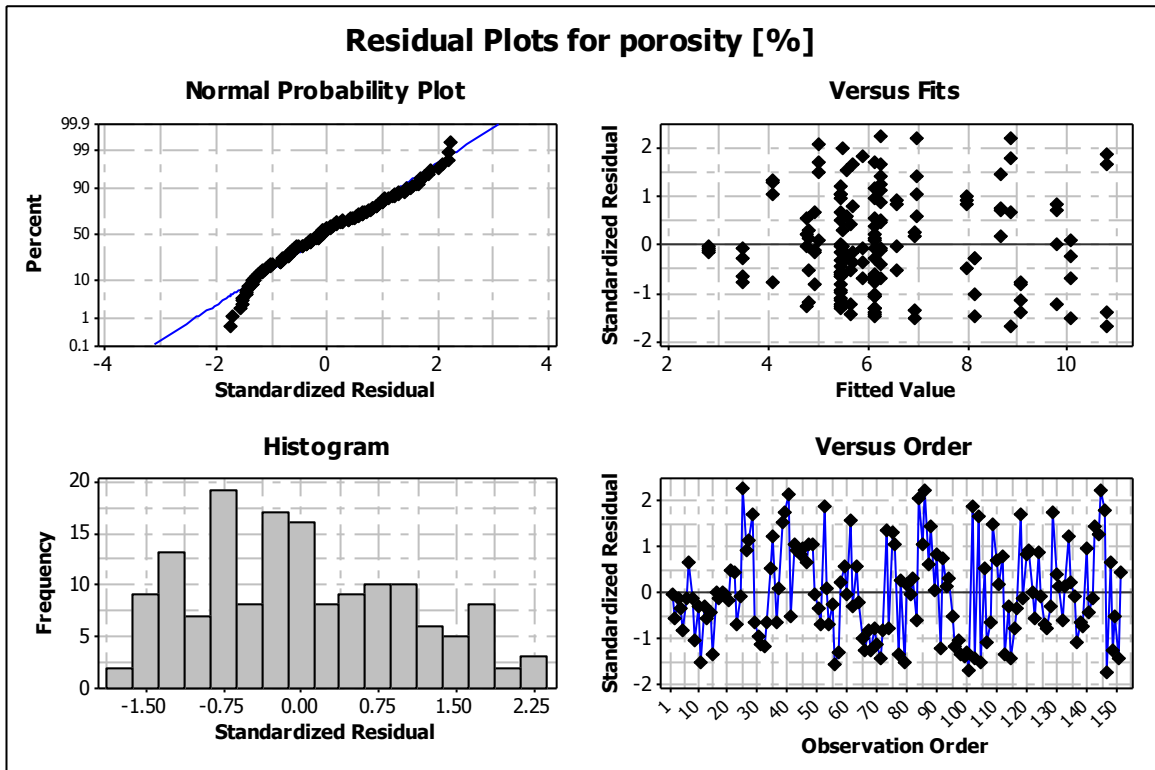


Figure 76: Model adequacy checking of response surface

Figure 76 shows the necessary information for model adequacy checking. The normal probability plot shows that the standardized residuals fit to a straight line. Both tails of the plot show curvature. The histogram of the standardized residuals shows a flat distribution. The plot of the fitted values shows that the variance of the data was acceptable. The plot of the observation order shows some outliers that contributed to the variance of the data.

Model adequacy checking shows that the distribution of the responses was acceptable, and ANOVA could be conducted.

Table 36: MINITAB output: ANOVA of response surface AgCu7

Source	DF	Seq SS	Adj SS	Adj MS	F	P
Blocks	1	19.22	19.222	19.222	3.18	0.0770
Regression	8	441.87	441.866	55.233	9.13	0.0000
Linear	3	149.05	299.788	99.929	16.52	0.0000

power	1	3.8	102.865	102.865	17.01	0.0000
spot dist	1	25.96	259.674	259.674	42.94	0.0000
pulse time	1	119.3	3.309	3.309	0.55	0.4610
Square	2	73.55	45.286	22.643	3.74	0.0260
spot dist*spot dist	1	64.52	43.457	43.457	7.19	0.0080
pulse time*pulse time	1	9.03	20.536	20.536	3.4	0.0670
Interaction	3	219.26	219.259	73.086	12.09	0.0000
power*spot dist	1	152.62	163.277	163.277	27	0.0000
power*pulse time	1	14.31	0.696	0.696	0.12	0.7350
spot dist*pulse time	1	52.33	52.326	52.326	8.65	0.0040
Residual Error	142	858.71	858.71	6.047		
Lack-of-Fit	18	307.72	307.724	17.096	3.85	0.0000
Pure Error	124	550.99	550.986	4.443		
Total	151	1319.8				

Table 36 shows that significant factors were (among others): power, spot distance, the square of spot distance, power times spot distance, and spot distance times pulse time. These factors show low P-values that were shaded gray in table 36.

6.3 Responses

With the model of section 6.2, the response surface could be calculated.

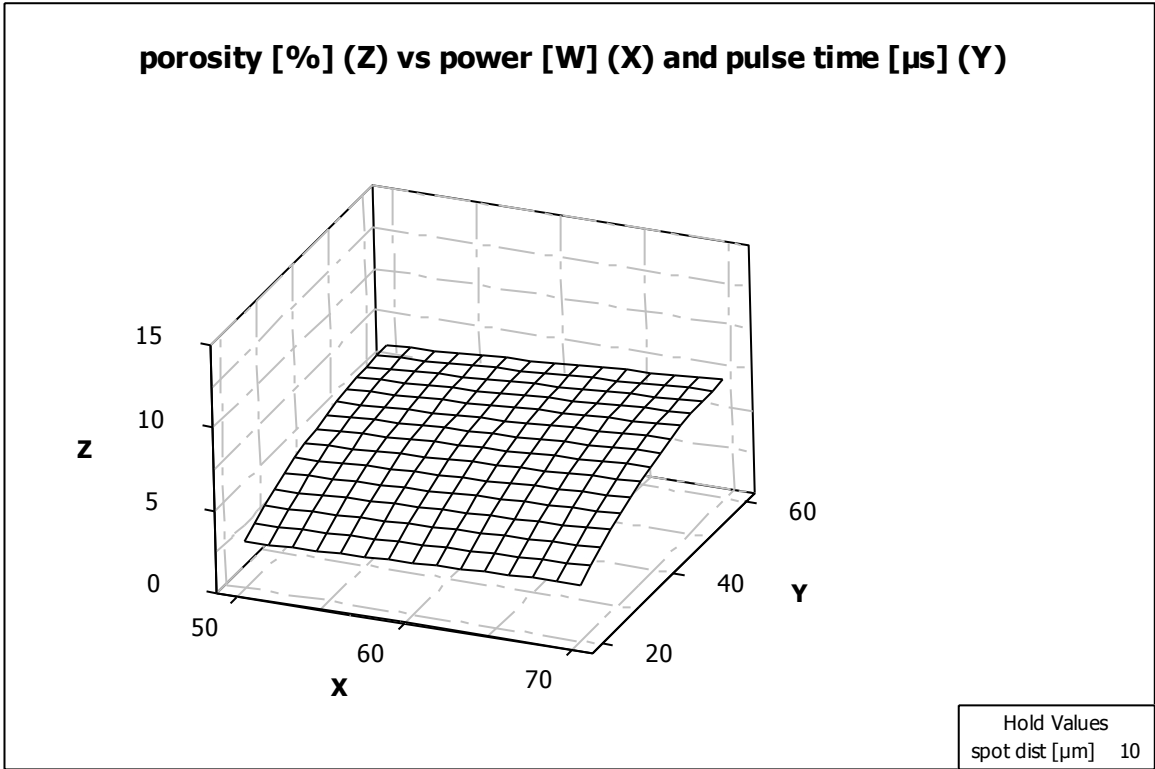


Figure 77: Response surface plot of porosity [%] vs. power [W] and pulse time [μ s]

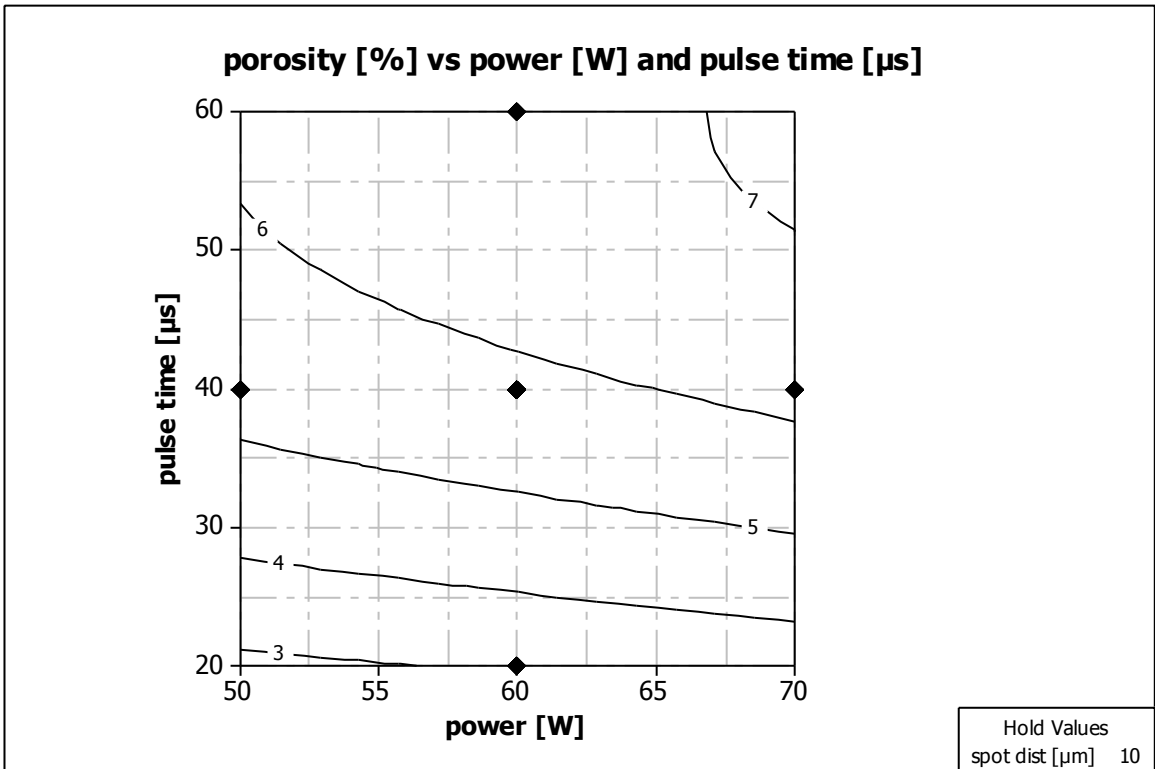


Figure 78: Contour plot of porosity [%] vs. power [W] and pulse time [μ s]

Figure 77 shows the response surface of porosity versus power and pulse time, whereas figure 78 shows the contour plot of the response surface. The Z-axis represents the porosity in [%], the X-axis represents the laser power given in [W] and the Y-axis depicts the pulse time in [μ s]. The response surface is almost linear, but there is a slight curvature around the Y-axis and the Z-axis. This can also be seen in the contour plot of figure 78. According to the response surface, the contour lines depict the porosity in [%]. For a power level of 60 W and 10 μ m spot distance, and for a pulse time of 40 μ s, the model returns values for porosities between 5% and 6%, respectively. If the pulse time level is decreased, the porosity can be decreased as well. If the power level is increased from 60 W to 70 W at 40 μ s pulse time, the model shows that porosities between 6% and 7% are obtained. If the power level is kept constant at 60 W, but the pulse time is increased to 60 μ s, porosities between 6% and 7% can be expected.

If the pulse time is changed from 40 μ s to 20 μ s, the gradient of the curvature is steeper than in the opposite direction from 40 μ s to 60 μ s pulse time. It can be seen from the graph that the distance between the lines of constant porosity is narrower from 40 μ s to 20 μ s pulse time than from 40 μ s to 60 μ s pulse time.

Figure 79 shows the response surface of porosity versus power and pulse time, whereas figure 80 shows the contour plot of the response surface. The Z-axis shows the porosity in [%], the X-axis shows the spot distance given in [μ m], and the Y-axis shows the pulse time in [μ s]. It can be seen from figure 79

that the response surface shows curvatures at all three axes. A linear model could not represent this saddle surface in an adequate manner.

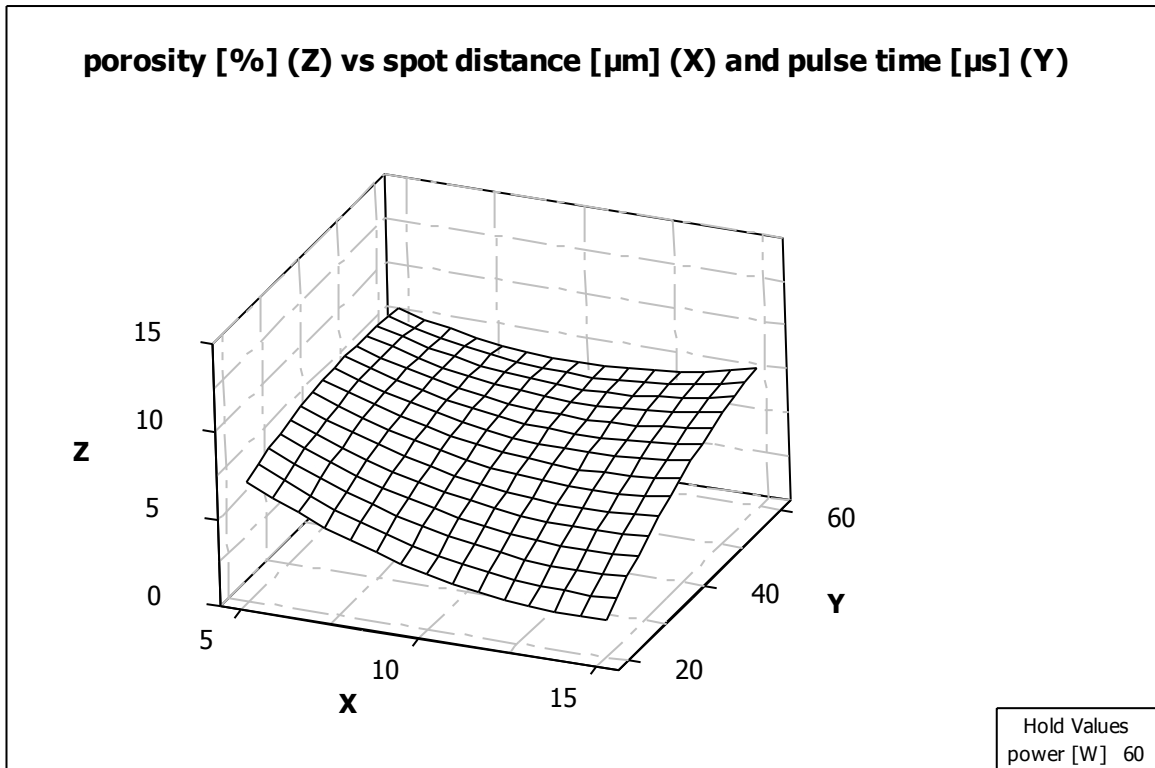


Figure 79: Response surface plot of porosity [%] vs. spot distance [μm] and pulse time [μs]

Figure 79 and figure 80 show, that for this data set, a porosity of at most 8% can be expected. At least 2% porosity can be determined. The saddle point can be determined in figure 80 with coordinates of approximately 11 μm spot distance and 50 μs pulse time. The saddle point shows a porosity of approximately 6%. If the pulse time is reduced from 50 μs to 20 μs and the spot distance is slightly increased at the same time, the region of minimal porosity can be achieved. If starting at the saddle point and moving left at equal pulse time of

approximately 50 μs , the porosity will be increased. The same result occurs if pulse time and spot distance are increased to 60 μs and 15 μm , respectively.

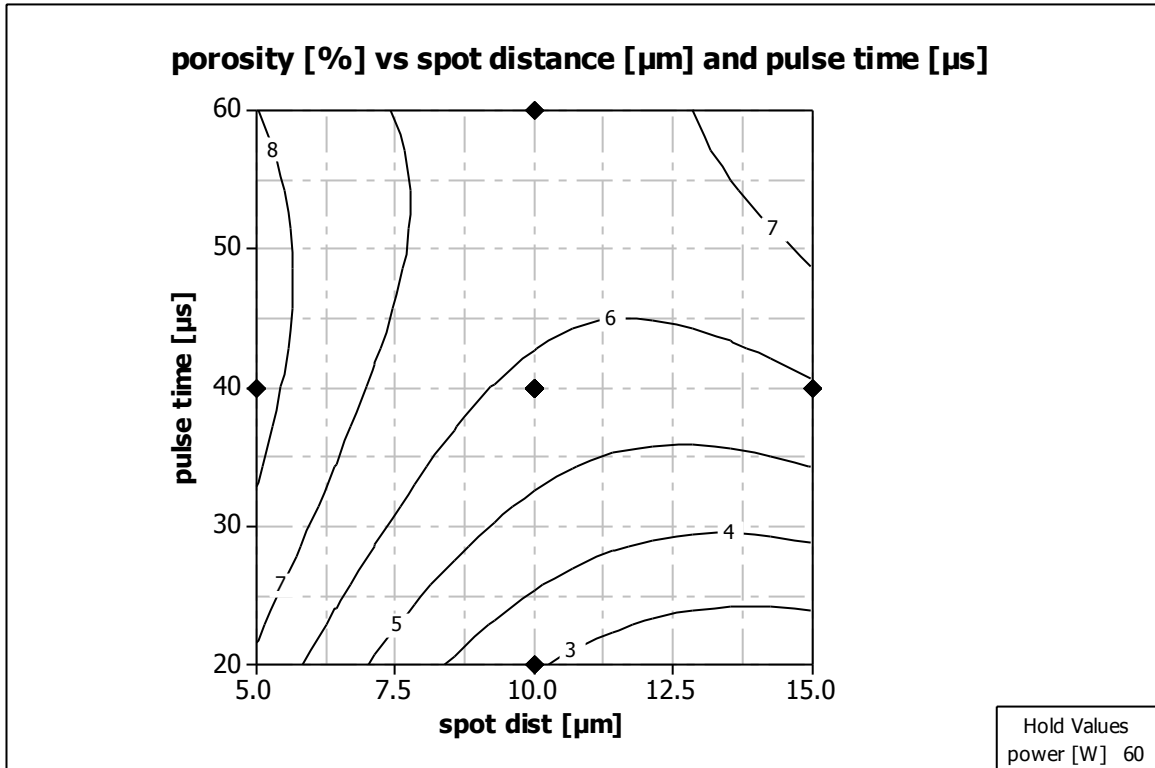


Figure 80: Contour plot of porosity [%] vs. spot distance [μm] and pulse time [μs]

Figure 81 shows the response surface of porosity versus power and pulse time, whereas figure 82 shows the contour plot of the response surface. The Z-axis depicts the porosity given in [%], the X-axis depicts the laser power given in [W], and the Y-axis depicts the spot distance in [μm]. The graph in figure 81 shows curvature in X-, Y-, and Z-directions. The plot was calculated at a constant pulse time of 40 μs . The porosity values of the data set in this response surface are between 4% and 9%.

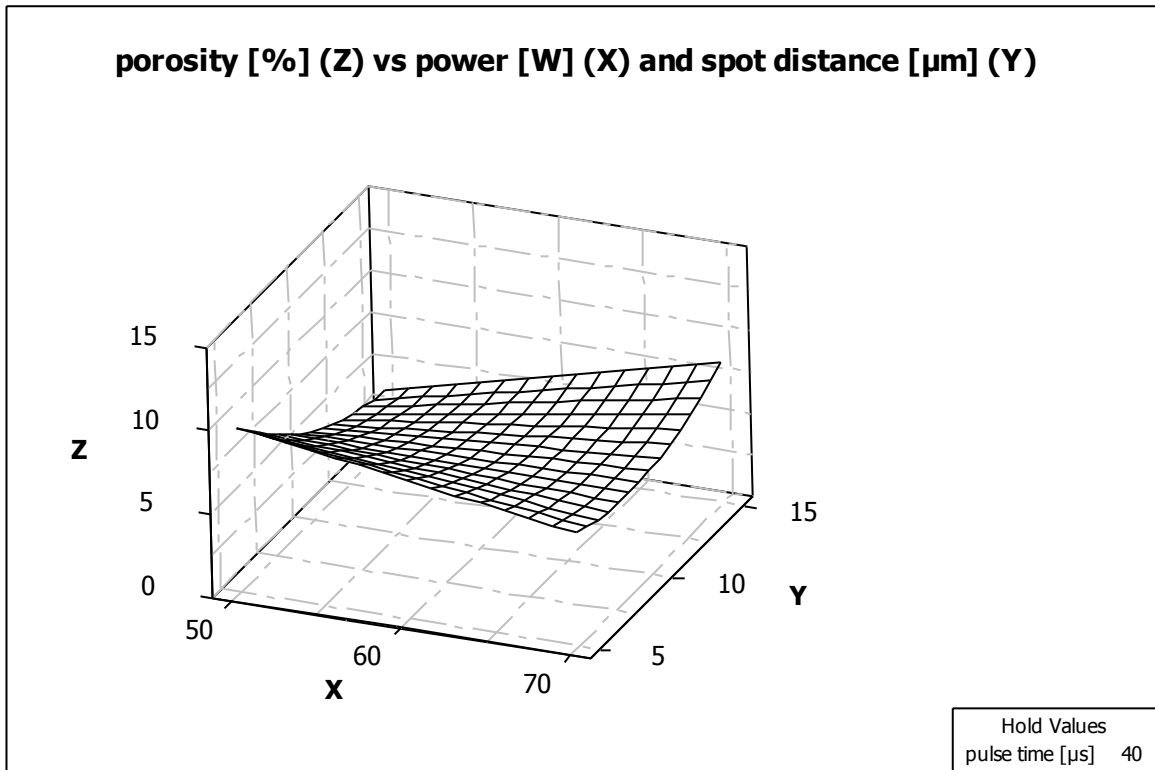


Figure 81: Response surface plot of porosity [%] vs. power [W] and spot distance [μm]

Figure 82 shows that in the center of this contour plot, the porosity can be between 5% and 6%. The center is a spot distance of 10 μm and a power level of 60 W. If one moves from the center to the corner upper left (spot distance increased to 15 μm and power level decreased to 50 W), less porosity can be expected than at the center point. The region of a porosity of 4% can be approached. If one moves from the center point to the corner lower left, the porosity is considered to increase to 8% and above. In the opposite direction, from the center point to the corner upper right, porosities of 7% can be obtained. Related parameters to that region are a level of spot distance of 15 μm and a level of laser power of 70 W.

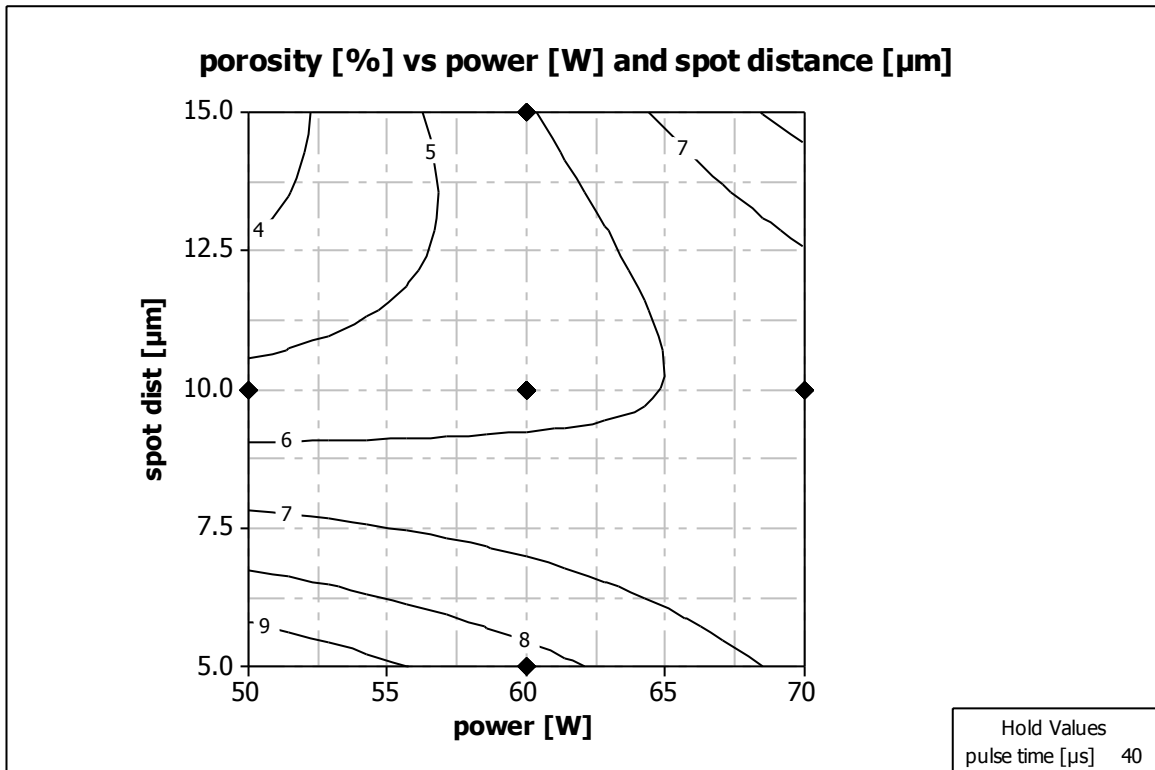


Figure 82: Contour plot of porosity [%] vs. power [W] and spot distance [μm]

With the response surface plots and contour plots of this chapter, porosities were estimated for the test series of AgCu7. It can be considered as a process map within the limits of the parameters. For further usage, at least tendencies can be estimated which porosities can be obtained.

7 RESPONSE SURFACE METHOD AGCU28

7.1 Screening experiments for AgCu28

7.1.1 Test series 10

In order to compare AgCu7 and AgCu28, screening experiments for AgCu28 were conducted in a similar manner as for AgCu7 (test series 10 and 11). Starting with the manufacturing of thin walled, hollow squares, first tracks were manufactured and analyzed using microscopy. The screening experiments resulted in the choice of the parameters for the investigation of the response surface. Initially, the same parameters were chosen as in test series 9.

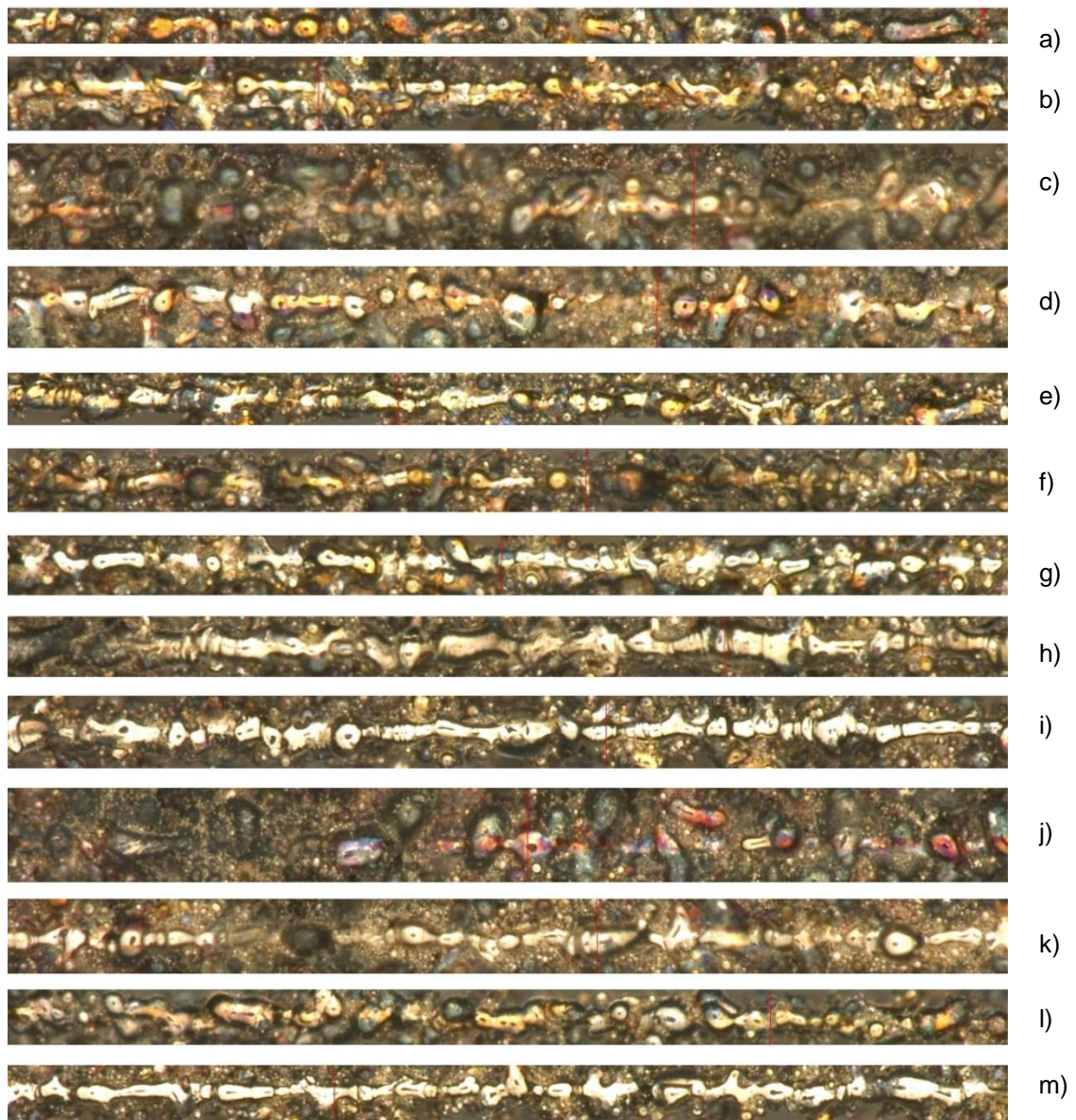


Figure 83: Selected samples, test series 10, a) 21, b) 31, c) 12, d) 5, e) 16, f) 23, g) 14, h) 7, i) 32, j) 29, k) 25, l) 8, m) 27.

Table 37: Parameters of test series 10, 30 μm layer thickness (figure 83)

picture	run order	power [W]	spot dist [μm]	pulse time [μs]	layer thickness [μm]	preexposure [W]
a	21	80	5	20	30	0
b	31	80	5	20	30	50
c	12	80	5	80	30	0
d	5	80	5	80	30	50
e	16	80	20	20	30	0
f	23	80	20	80	30	0
g	14	80	20	80	30	50
h	7	100	5	20	30	0
i	32	100	5	20	30	50
j	29	100	5	80	30	0
k	25	100	5	80	30	50
l	8	100	20	80	30	0
m	27	100	20	80	30	50

Figure 83 shows selected samples of test series 10. The corresponding parameters are listed in table 37. All samples were manufactured at a layer thickness of 30 μm . The samples b), d), g), i), k), and m) were produced using the preexposure method. Besides some interruptions, for these samples continuous tracks were visible. The samples with increased spot distance and increased pulse time (sample g) and m)) yielded better results than samples with lower spot distance (samples d) and k)) at both power levels. Sample i) showed some balling, but it was the most successful sample of test series 10 using the preexposure method.

Samples a), c), e), f), h), j), and l) were produced without preexposure. Between sample a) and c) the pulse time was increased by a factor of 4. It could be seen that the width of the track was increased to more than 200 μm . The surface was uneven and annealed. A similar result was shown if the laser power

was increased to 100 W (sample j)). Most tracks with a pulse time level of 80 μ s showed interruptions, including samples f) and l). Samples e) and h) were manufactured with a pulse time level of 20 μ s. Sample h) showed a comparably thick weld, but the track was almost continuous.

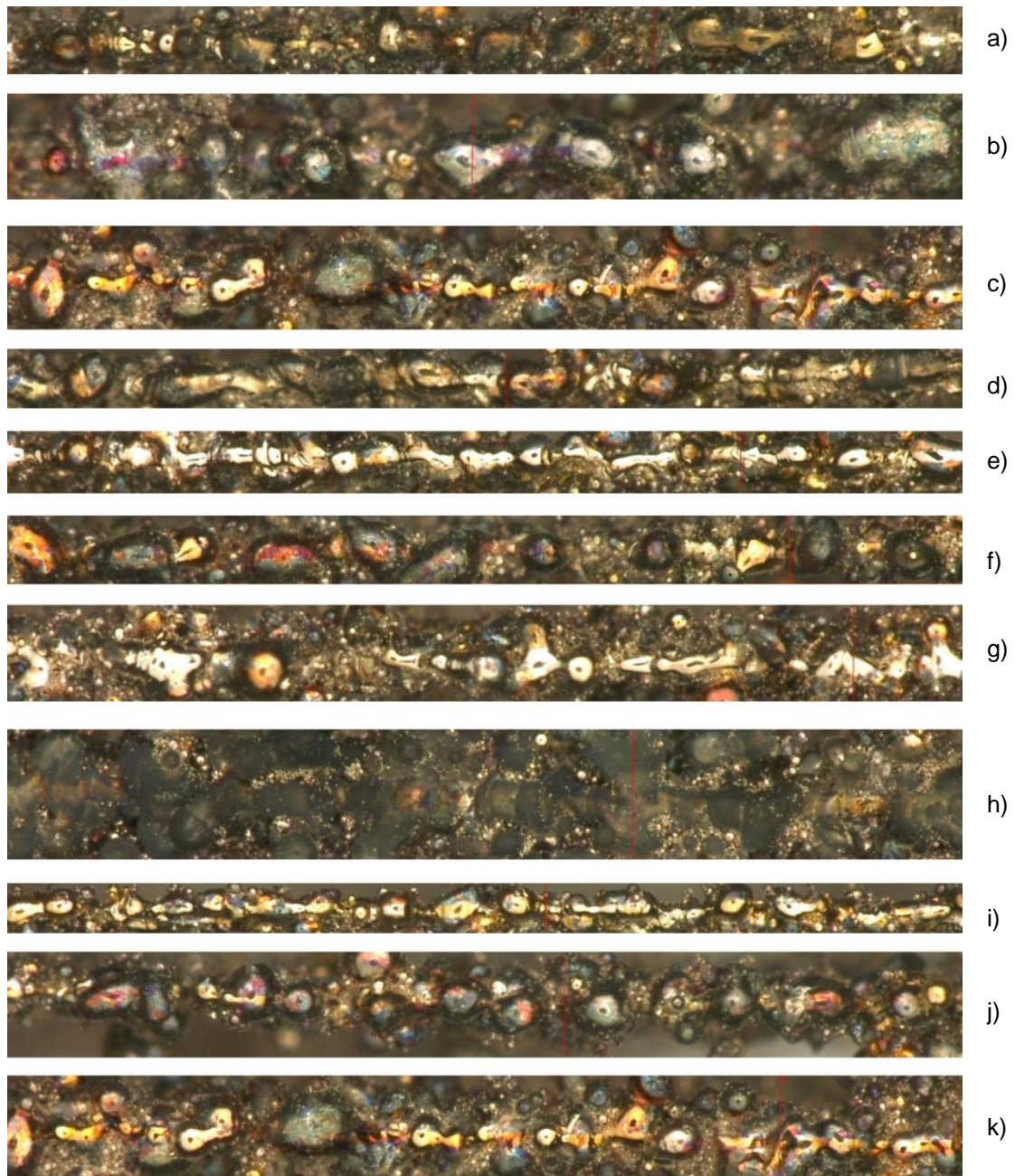


Figure 84: Selected samples, test series 10 a) 28, b) 17, c) 11, d) 13, e) 15, f) 19, g) 24, h) 22, i) 30, j) 9, k) 1.

Table 38: Parameters of test series 10, 60 μm layer thickness (figure 84)

picture	run order	power [W]	spot dist [μm]	pulse time [μs]	layer thickness [μm]	preexposure [W]
a	28	80	5	20	60	0
b	17	80	5	80	60	0
c	11	80	5	80	60	50
d	13	80	20	80	60	0
e	15	80	20	80	60	50
f	19	100	5	20	60	0
g	24	100	5	20	60	50
h	22	100	5	80	60	0
i	30	100	20	20	60	50
j	9	100	20	80	60	0
k	1	100	20	80	60	50

Figure 84 shows selected samples of test series 10 that were manufactured at a layer thickness of 60 μm . The corresponding parameters are listed in table 38. The samples that were manufactured with preexposure were c), e), g), i), and k). The balling of all specimens was worse compared to the layer thickness of 30 μm . For the preexposure tests, samples e) and i) showed the best results.

Samples a), b), d), f), h), and j) were produced without preexposure. Sample b) showed massive balling with diameters above 100 μm . Samples d) and f) showed interruptions between the scanned lines. The width of sample h) was increased due to the high pulse time and the low spot distance. If the spot distance was increased, the track could be narrowed at 80 μs pulse time as well. Sample j) showed the results of the spot distance of 20 μm and 80 μs pulse time.

7.1.2 Test series 11

The parameter sets of test series 11 corresponded with test series 3.

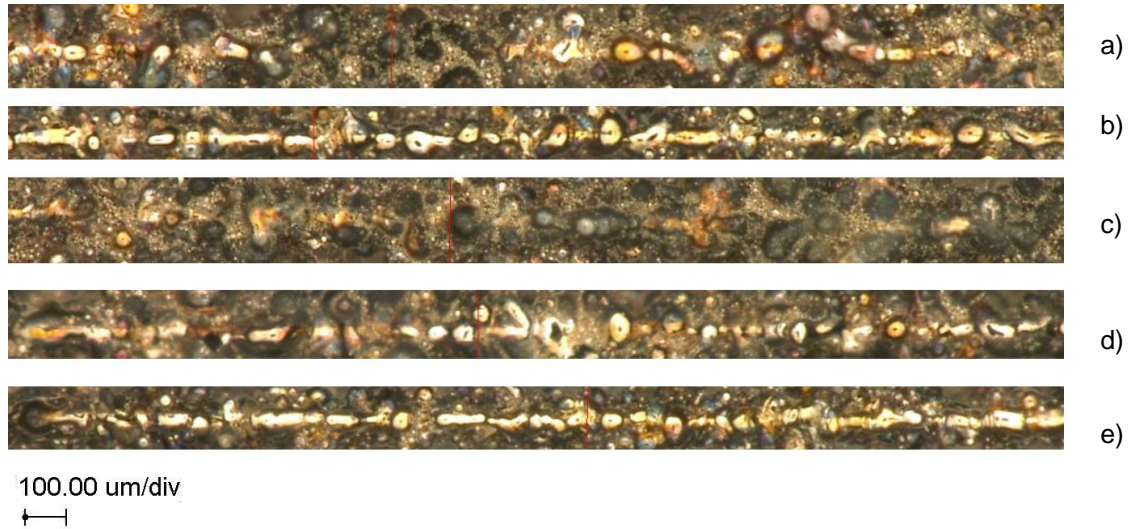


Figure 85: Selected samples, test series 11: a) 24, b) 15, c) 31, d) 14, e) 23.

Table 39: Parameters of test series 11, 30 μm layer thickness (figure 85)

picture	run order	power [W]	spot dist [μm]	pulse time [μs]	layer thickness [μm]	preexposure [W]
a	24	35	5	80	30	0
b	15	50	5	20	30	50
c	31	50	5	80	30	0
d	14	50	5	80	30	50
e	23	50	20	80	30	50

Figure 85 shows selected samples of test series 11 that were manufactured at a layer thickness of 30 μm . The corresponding parameters are collected in table 39. Most samples of this test series failed. Sample a) and c) were produced without preexposure, whereas b), d) and e) were produced with preexposure. Only one sample was successfully manufactured at a layer

thickness of 30 μm and a laser power of 35 W (sample a)). Due to local evaporations, the scan track was interrupted and partially destroyed. Best results were obtained for the parameter sets b) and e).

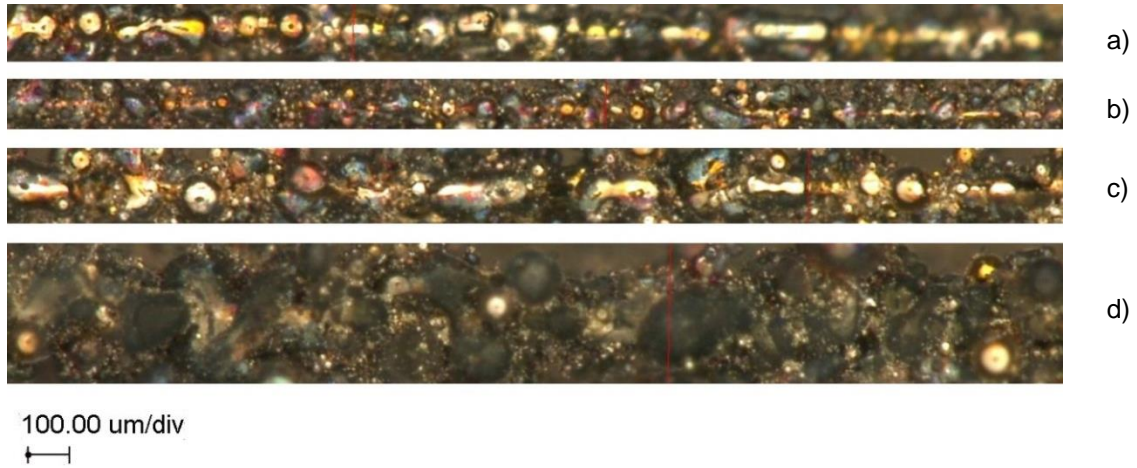


Figure 86: Selected samples, test series 11: a) 19, b) 30, c) 12, d) 32.

Table 40: Parameters of test series 11, 60 μm layer thickness (figure 86)

picture	run order	power [W]	spot dist [μm]	pulse time [μs]	layer thickness [μm]	preexposure [W]
a	19	35	5	20	60	50
b	30	35	5	80	60	50
c	12	50	5	20	60	50
d	32	50	5	80	60	0

Table 40 collects the parameters for the selected samples of test series 11 at a layer thickness of 60 μm . Figure 86 shows the corresponding results. Only four specimens were successfully produced at this layer thickness. Sample d) was the only one without preexposure. As seen in the previous figures, the scan track was annealed due to the low scan speed and the width was increased to more than 100 μm . Sample b) showed fine droplets that were connected to a

fragile hollow cube. Between sample a) and c) only the power was increased from level 35 W to 50 W. The dimensions of the spheres resulting from the balling phenomenon increased as well.

The consequence of test series 11 is that it proved there is no significant reduction in laser energy when using a eutectic material compared to a similar non-eutectic material. In order to obtain comparable results, the same parameter sets were selected for the response surfaces.

7.2 Response surface for AgCu28

Test series 12 contained the same parameters as those in chapter 6 with the exception that AgCu28 was used instead of AgCu7. Table 41 lists the factors and the levels for the experiments.

Table 41 : Factors and levels of the response surface AgCu28

Factor	Levels	Center point			Squares	Interactions
		low	medium	high		
A: power [W]	50	60	70	A*A	A*B	
B: spot dist [μm]	5	10	15	B*B	A*C	
C: pulse time [μs]	20	40	60	C*C	B*C	
Replicates	2	Estimates per point		4		

Two replicates were conducted. Per sample, four estimates were taken (see figure 42 on page 87). The sample with the vector

$$\begin{pmatrix} 50 \text{ W} \\ 15 \mu\text{m} \\ 20 \mu\text{s} \end{pmatrix}$$

failed in both replicates (according to test series 9). The reason was due to the low linear energy density of 0.09 J/mm which is approximately a factor of 10 lower compared to the highest linear energy density of this set (0.89 J/mm). Therefore, in total 152 measurements were taken (19 samples, four estimates each, two replicates). For the center point, six samples per replicate were measured. The test set up was randomized over both replicates. Table 42 lists the randomized data for the response surface. Power, spot distance and pulse time were adjusted, whereas scan speed and linear energy density were calculated.

Table 42: Data of response surface for AgCu28

Sample	Replicate	Power [W]	Spot dist [μm]	Pulse time [μs]	Scan speed [mm/s]	Linear energy density[J/mm]	No. of Estimates	Comment	Sample	Replicate	Power [W]	Spot dist [μm]	Pulse time [μs]	Scan speed [mm/s]	Linear energy density[J/mm]	No. of Estimates	Comment
1	1	60	10	40	230.1	0.26	4	c	21	2	70	5	60	78.8	0.89	4	
2	1	50	15	60	236.4	0.21	4		22	2	50	15	20	576.4	0.09	0	f
3	1	50	5	20	213.1	0.23	4		23	2	70	5	20	213.1	0.33	4	
4	1	60	10	40	230.1	0.26	4	c	24	2	60	10	60	157.6	0.38	4	
5	1	60	10	20	401.4	0.15	4		25	2	50	5	60	78.8	0.63	4	
6	1	70	5	60	78.8	0.89	4		26	2	70	15	20	576.4	0.12	4	
7	1	60	10	60	157.6	0.38	4		27	2	60	10	40	230.1	0.26	4	c
8	1	60	10	40	230.1	0.26	4	c	28	2	70	15	60	236.4	0.30	4	
9	1	60	10	40	230.1	0.26	4	c	29	2	60	10	40	230.1	0.26	4	c
10	1	50	10	40	230.1	0.22	4		30	2	60	5	40	115.1	0.52	4	
11	1	60	5	40	115.1	0.52	4		31	2	60	10	40	230.1	0.26	4	c
12	1	60	10	40	230.1	0.26	4	c	32	2	50	10	40	230.1	0.22	4	
13	1	70	10	40	230.1	0.30	4		33	2	70	10	40	230.1	0.30	4	
14	1	70	15	60	236.4	0.30	4		34	2	60	10	20	401.4	0.15	4	
15	1	50	15	20	576.4	0.09	0	f	35	2	60	10	40	230.1	0.26	4	c
16	1	70	5	20	213.1	0.33	4		36	2	60	10	40	230.1	0.26	4	c
17	1	60	15	40	345.1	0.17	4		37	2	60	10	40	230.1	0.26	4	c
18	1	60	10	40	230.1	0.26	4	c	38	2	60	15	40	345.1	0.17	4	
19	1	50	5	60	78.8	0.63	4		39	2	50	5	20	213.1	0.23	4	
20	1	70	15	20	576.4	0.12	4		2		50	15	60	236.4	0.21	4	
c: center point; f: failed															total:	152	

After conducting the tests, the data was collected and inserted into a MINITAB data sheet. The standard order was the order of the data since the collection sheet was randomized before the tests were conducted. The estimates were reported in the order of measurement. That means that the four estimates of the first sample are followed by the four estimates of the next sample.

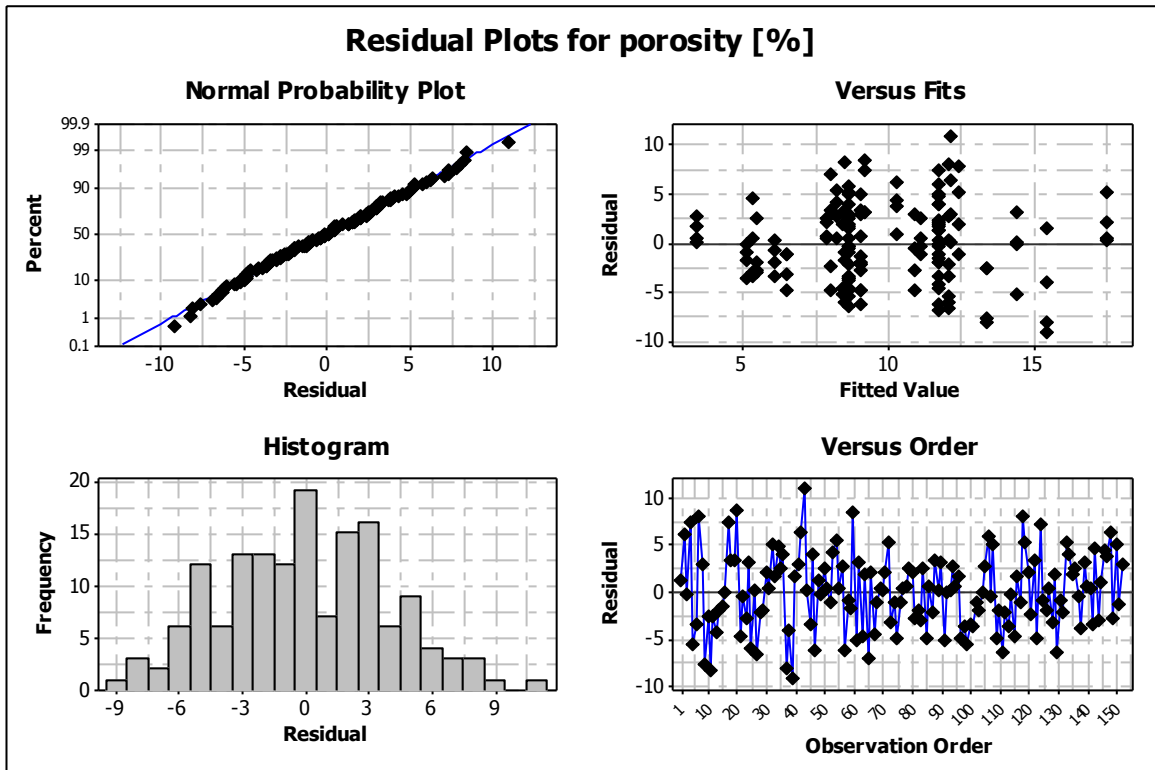


Figure 87: Residual plots for porosity

In order to check the model adequacy, figure 87 shows the residual plots. The normal probability plot shows that the standardized residuals fit to a straight line. Both tails of the plot fit to the line as well. The histogram of the standardized residuals shows a distribution that can be considered a normal distribution. The plot of the fitted values shows that the variance of the data was acceptable. The plot of the observation order shows some outliers, but is acceptable as well.

Model adequacy checking shows that the distribution of the responses was acceptable, an ANOVA could be conducted. Table 43 shows the estimated regression coefficients for porosity. The R-square value is 35.06% and is comparable to the value of the model for AgCu7. Due to the p-values, the factors constant, block, and power are considered significant.

Table 43: MINITAB output: Estimated Regression Coefficients for porosity [%]

Term	Coef	SE Coef	T	P
Constant	71.9744	31.199	2.307	0.0230
Block	1.5345	0.3339	4.595	0.0000
power	-2.1283	1.0841	-1.963	0.0520
spot dist	0.051	1.1272	0.045	0.9640
pulse time	0.4382	0.2711	1.616	0.1080
power*power	0.0155	0.0089	1.742	0.0840
spot dist*spot dist	-0.0583	0.0356	-1.637	0.1040
pulse time*pulse time	-0.0027	0.0022	-1.236	0.2190
power*spot dist	0.0135	0.013	1.036	0.3020
power*pulse time	-0.0021	0.0033	-0.654	0.5140
spot dist*pulse time	-0.0017	0.0065	-0.262	0.7940
R-Sq = 35.06% R-Sq(pred) = 24.26% R-Sq(adj) = 30.45%				

Table 44 lists the ANOVA output of the response surface model of AgCu28. A full quadratic approach was chosen. The factors power, spot distance and pulse time were included in the model, as well as the squares of these factors and the first grade interactions (see table 33 on page 138). Two replicates were included. Each parameter vector point contained four estimates. The ANOVA output shows that power, spot distance and the square of power should be considered as significant since they are close to the α -value which is set to 0.05 for a 95% confidence interval.

Table 44: MINITAB output: ANOVA of response surface AgCu28

Source	DF	Seq SS	Adj SS	Adj MS	F	P
Blocks	1	357.9	357.9	357.9	21.12	0.0000
Regression	9	932.25	932.25	103.583	6.11	0.0000
Linear	3	798.84	100.46	33.487	1.98	0.1200
power	1	538.45	65.32	65.319	3.85	0.0520
spot dist	1	153.24	0.03	0.035	0	0.9640
pulse time	1	107.16	44.28	44.28	2.61	0.1080
Square	3	102.62	108.65	36.215	2.14	0.0980
power*power	1	2.44	51.46	51.455	3.04	0.0840
spot dist*spot dist	1	77.21	45.41	45.413	2.68	0.1040
pulse time*pulse time	1	22.97	25.89	25.885	1.53	0.2190
Interaction	3	30.79	30.79	10.264	0.61	0.6120
power*spot dist	1	18.42	18.2	18.197	1.07	0.3020
power*pulse time	1	11.2	7.26	7.258	0.43	0.5140
spot dist*pulse time	1	1.17	1.17	1.165	0.07	0.7940
Residual Error	141	2389.6	2389.63	16.948		
Lack-of-Fit	17	809.47	809.47	47.616	3.74	0.0000
Pure Error	124	1580.2	1580.15	12.743		
Total	151	3679.8				

Table 45 lists unusual observations for porosity. The unusual observations equal the outliers in the residual vs. observation order diagram of figure 87. They can be found in the left part of the diagram and mainly belong to the first replicate. The model was blocked on replicates.

Table 45: MINITAB output: unusual observations for porosity [%]

Obs	StdOrder	porosity [%]	Fit	SE Fit	Residual	St Resid
7	7	20.136	12.094	1.371	8.042	2.07 R
11	11	5.183	13.384	1.371	-8.201	-2.11 R
20	20	17.675	9.169	1.148	8.506	2.15 R
37	37	7.363	15.466	1.148	-8.102	-2.05 R
39	39	6.291	15.466	1.148	-9.175	-2.32 R
43	43	23.095	12.136	1.098	10.959	2.76 R
60	60	16.834	8.52	1.382	8.314	2.14 R
R denotes an observation with a large standardized residual.						

7.3 Responses

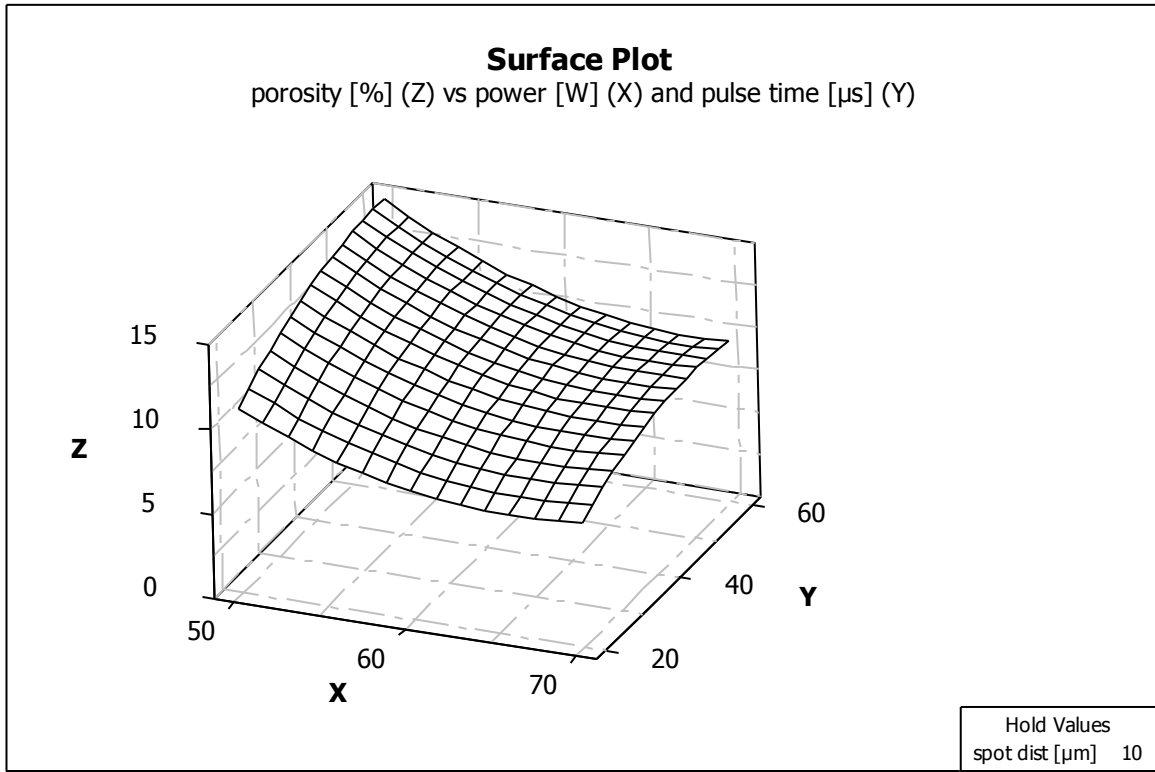


Figure 88: Surface plot of porosity vs. power and pulse time

Figure 88 shows the response surface of porosity versus power and pulse time, whereas figure 89 shows the contour plot of the response surface. The Z-axis represents the porosity in [%], the X-axis represents the laser power given in [W] and the Y-axis represents the pulse time in [μ s]. The response surface shows curvature around the Y-axis and the X-axis. For the entire data set, porosities from 8% to 14% are indicated.

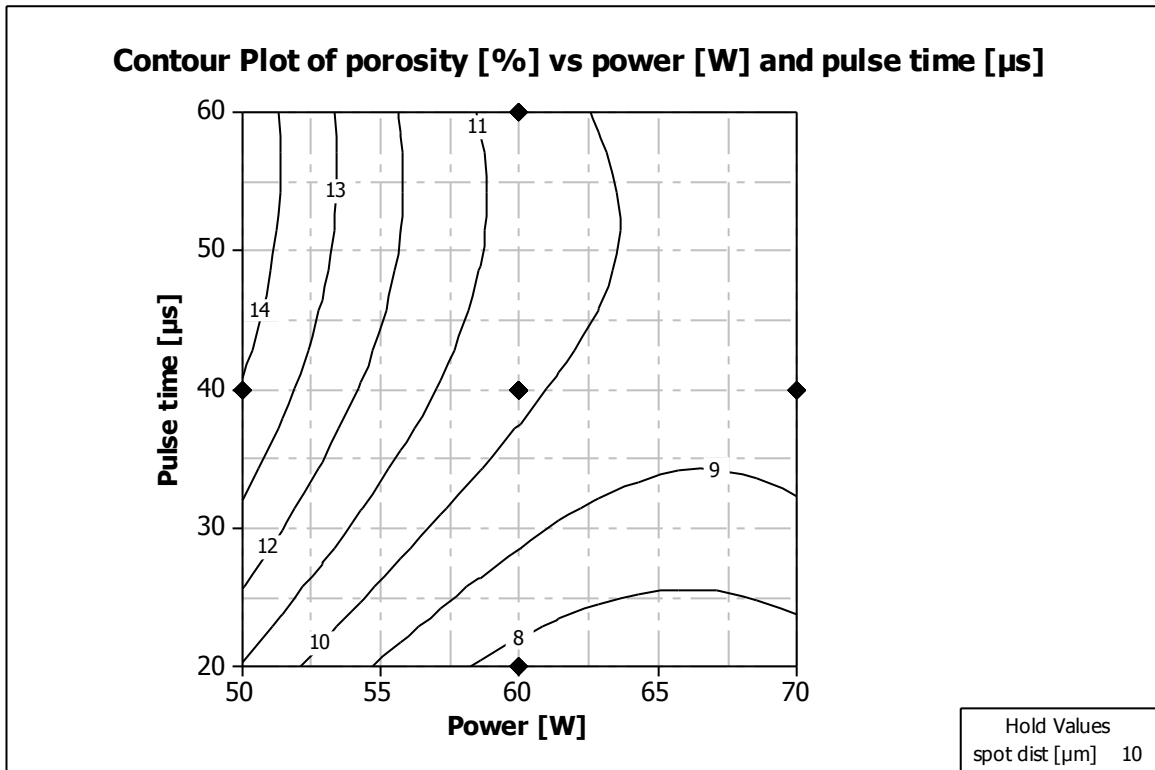


Figure 89: Contour plot of porosity vs. power and pulse time

Beginning with the center in figure 89, porosities between 10% and 11% were calculated. The center point represents a laser power of 60 W, a spot distance of 10 μm and a pulse time level of 10 μs. From there to the corner upper left, the expected porosity indicates increasing values up to 14% or higher. From the center point to the corner upper right, similar values can be expected as at the center point since the surface exhibits a plateau in that area. A slight decrease in porosity is indicated. If the pulse time is kept constant at 40 μs and the power is reduced to 50 W, a steep increase in the response can be expected. If the pulse time is reduced or the laser power is increased, decreasing values for

porosities are indicated. According to the model, the lowest value is approximately 8%.

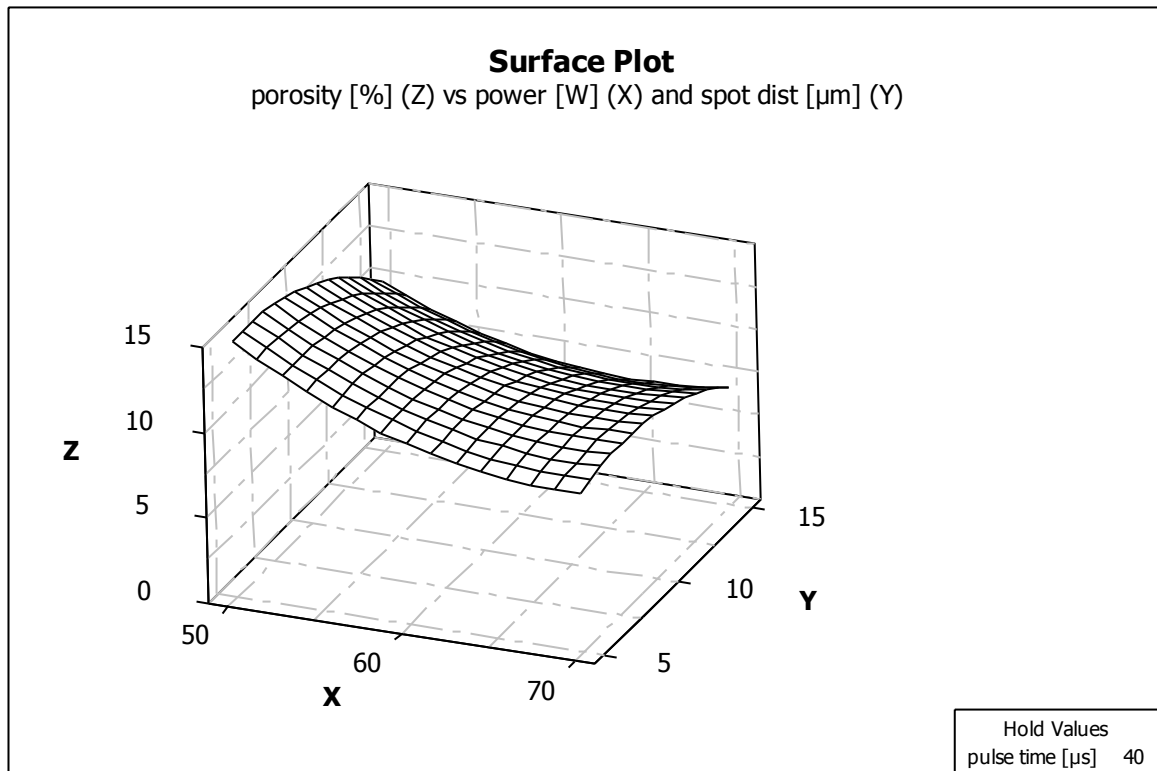


Figure 90: Surface plot of porosity vs. power and spot distance

Figure 90 shows the response surface of porosity versus power and pulse time, whereas figure 91 shows the contour plot of the response surface. The Z-axis represents the porosity in [%], the X-axis represents the laser power given in [W] and the Y-axis represents the spot distance in [μm]. The response surface indicates values for porosity between 6% and 15%.

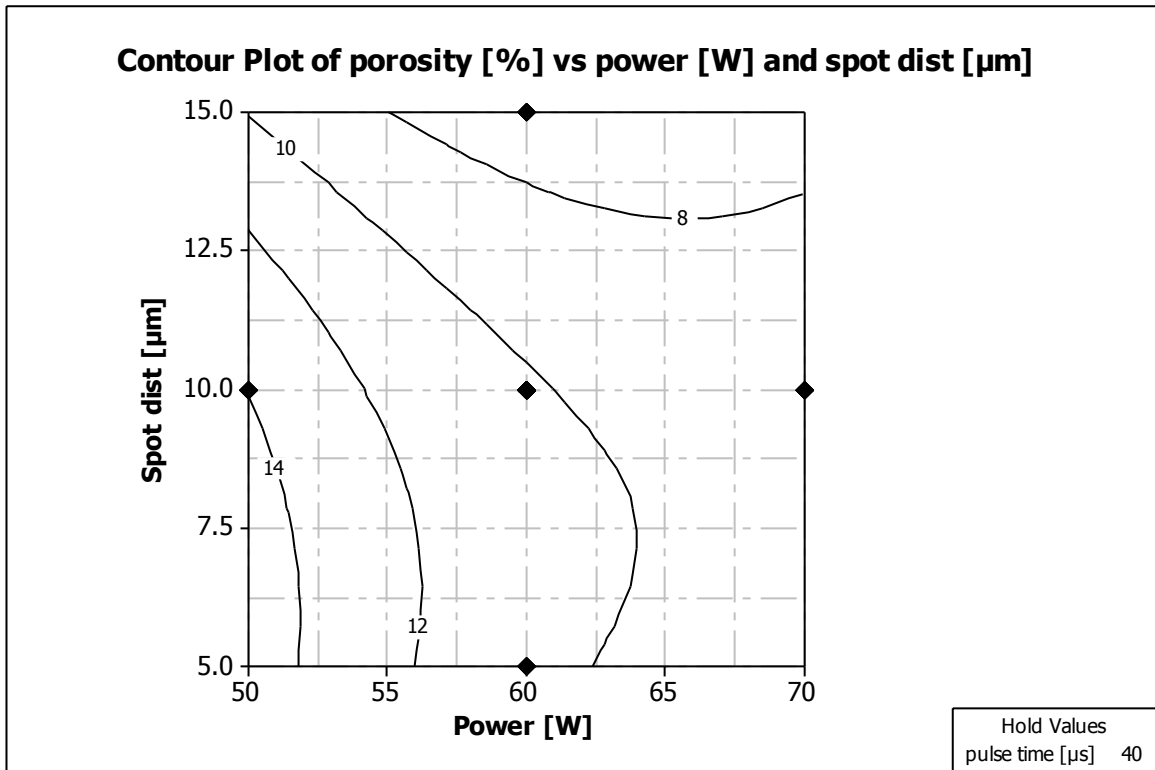


Figure 91: Contour plot of porosity vs. power and spot distance

The contour plot in figure 91 shows the lowest values for porosity at the upper edge of the graph. The spot distance should be adjusted close to 15 μm at a power level of 60 W and above, which is valid for a pulse time of 40 μs . Beginning with the center point to the corner lower left, an increase in porosity can be expected. If the power level is increased to 70 W, less porosity is indicated.

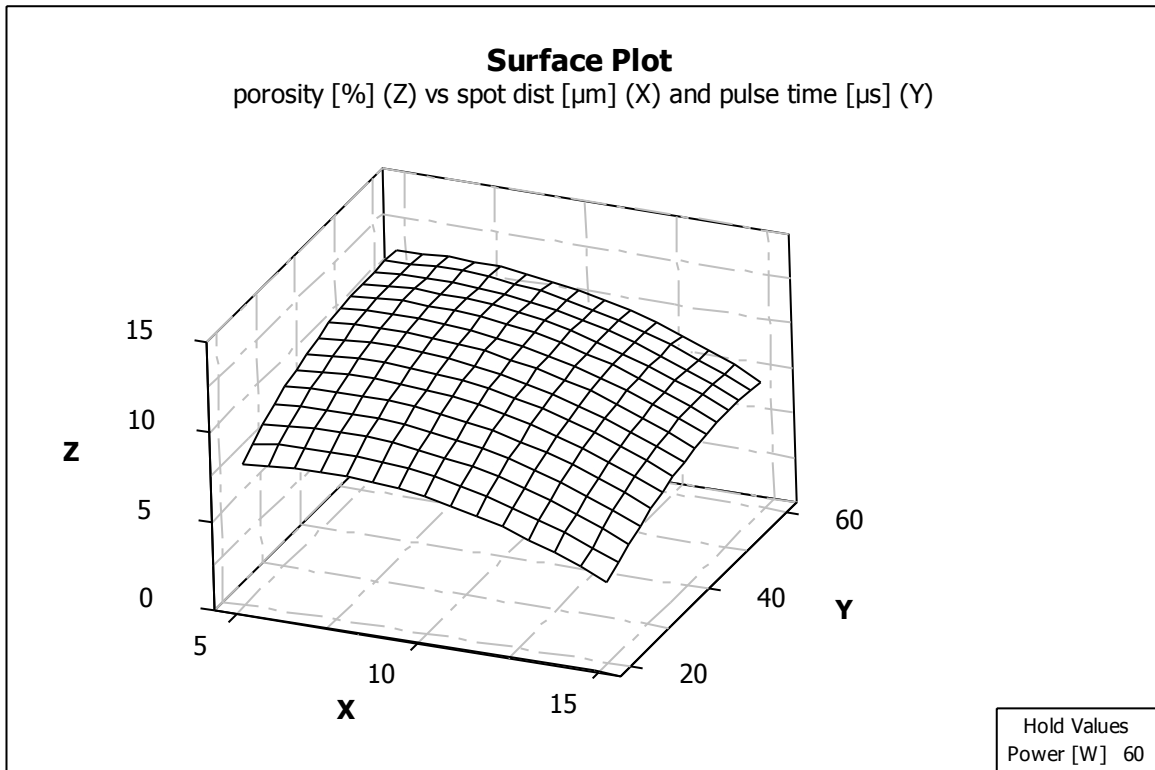


Figure 92: Surface plot of porosity vs. spot distance and pulse time

Figure 91 depicts the response surface of porosity versus power and pulse time, whereas figure 92 depicts the contour plot of the response surface. The Z-axis represents the porosity in [%], the X-axis represents the spot distance measured in [μm] and the Y-axis represents the pulse time measured in [μs].

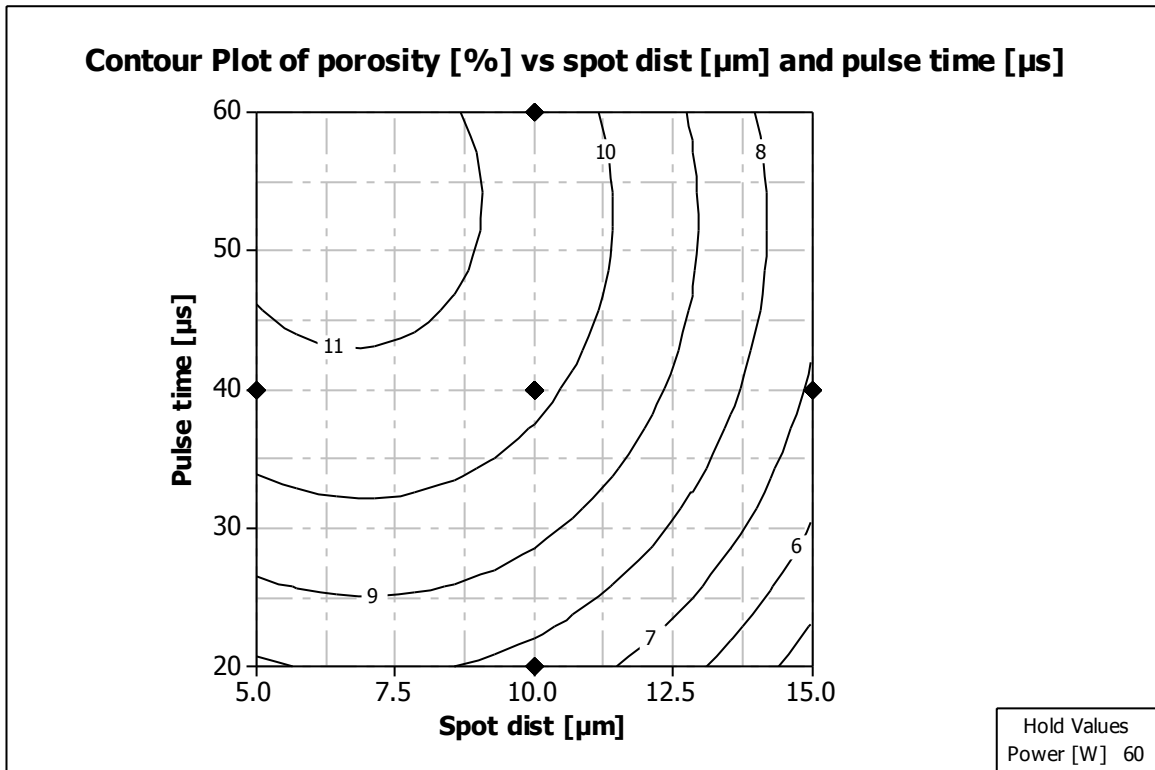


Figure 93: Contour plot of porosity vs. spot distance and pulse time

The contour lines of figure 92 are nearly circular. A peak can be determined around 6 μm spot distance and at approximately 55 μs pulse time, where porosity values above 11% can be expected. Beginning from this maximum, every direction shows lower values. The porosity at 10 μm spot distance and 20 μs pulse time is similar to the porosity at 15 μm spot distance and 60 μs pulse time, since it fits the same contour line. At a spot distance of 15 μm and 20 μs pulse time, the lowest values for porosity can be determined.

8 COMPARISON OF AGCU7 AND AGCU28

8.1 T-test on means

After AgCu7 and AgCu28 were analyzed, a comparison of both materials was of interest. The optical analysis showed that AgCu28 tended to higher porosities than AgCu7 at the same build parameters. A t-test on means was conducted in order to assess both materials. The response porosity showed the following distributions:

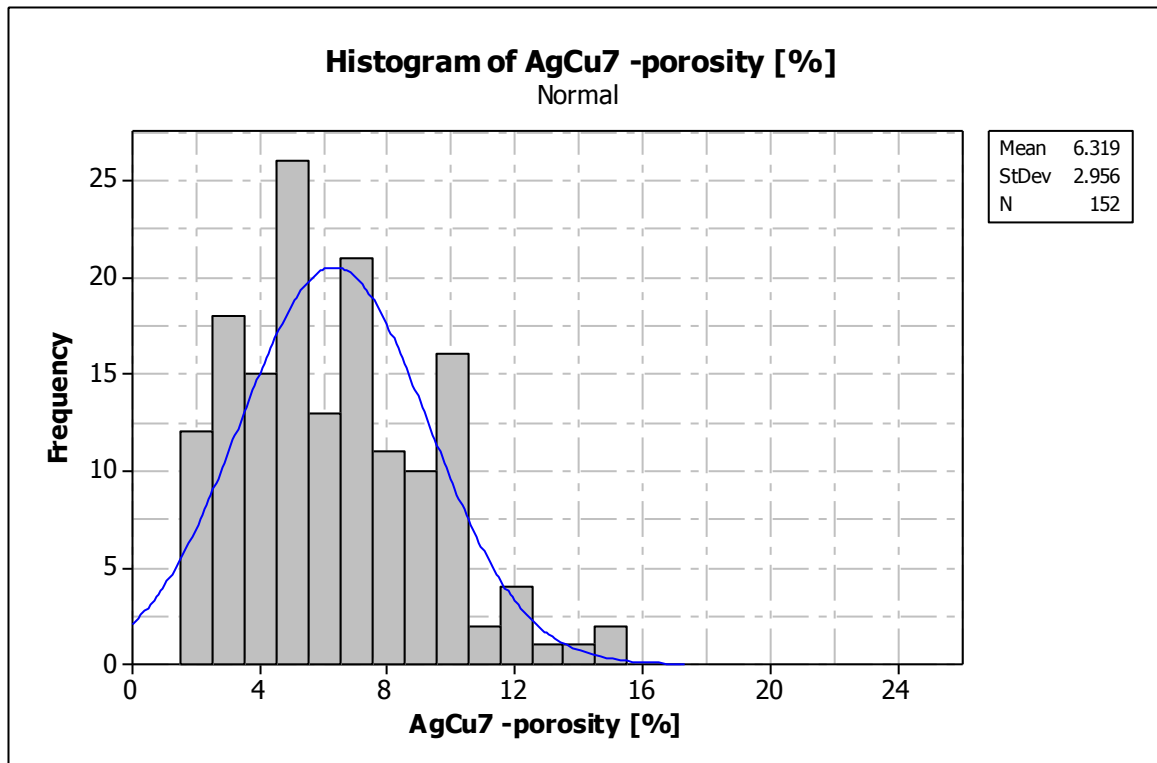


Figure 94: Histogram of the response of AgCu7

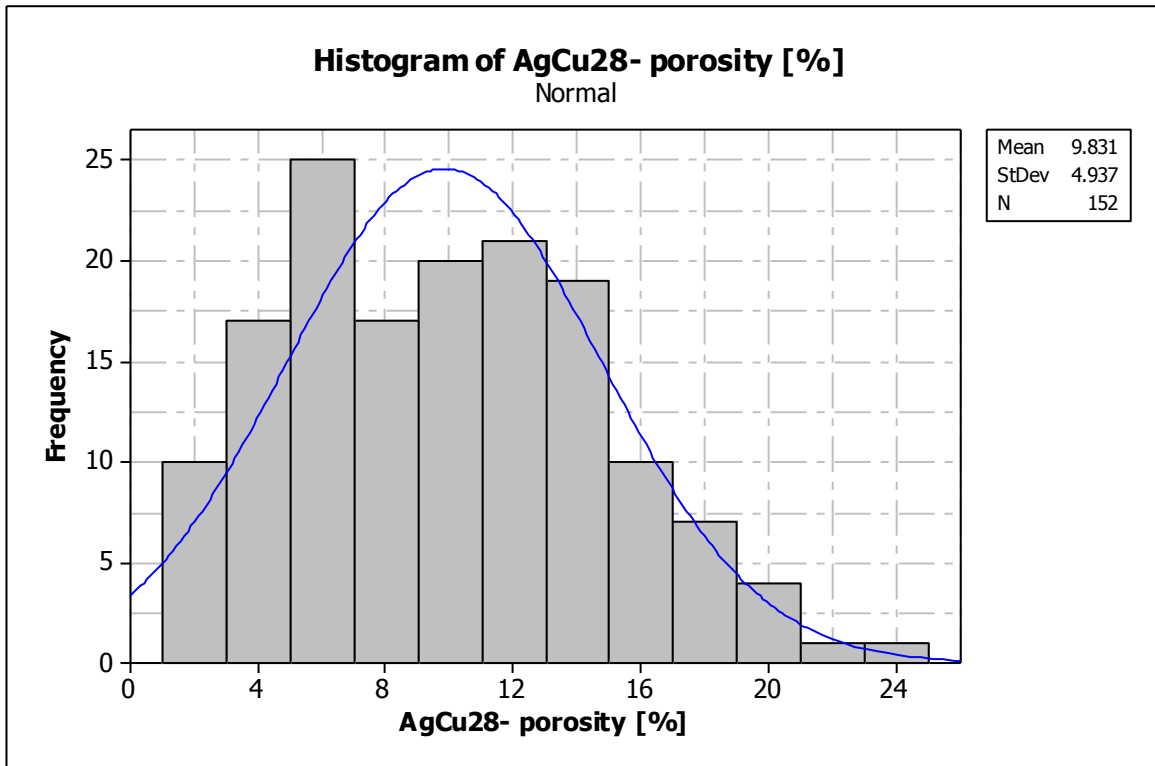


Figure 95: Histogram of the response of AgCu28

The histograms in figure 94 and figure 95 show that the mean porosity over all data points is not the same. Please note that the comparison was based on the same parameter sets, given in test series 9 and 12. The mean response for AgCu7 was a porosity of 6.32% with a standard deviation of 2.96%. The mean porosity obtained in test series 12 for AgCu28 is 9.83% with a standard deviation of 4.94%. The ratio standard deviation to mean was similar for both materials. Table 46 lists the MINITAB output for the test on means. The null hypothesis was “difference in means is zero” whereas the alternative hypothesis was “difference in means is NOT zero”. A 95% confidence interval was between -4.431, and -2.592, with the estimate for the difference -3.512. A P-value of almost zero showed that the null hypothesis must strongly be rejected. There

was no evidence that the alternative hypothesis is false. It could be concluded that both samples showed differences in means.

Table 46: MINITAB output: two sample T-test

Two-sample T for AgCu7-porosity [%] vs. AgCu28-porosity [%]						
	N	Mean	StDev	SE Mean		
AgCu7-porosity [%]	152	6.32	2.96	0.24		
AgCu28-porosity [%]	152	9.83	4.94	0.4		
Difference = mu (AgCu7-porosity [%]) - mu (AgCu28-porosity [%])						
Estimate for difference:	-3.512					
95% CI for difference:	(-4.431; -2.592)					
T-Test of diff. = 0 (vs. not =):	T-Value =	-7.52	P-Value=	0.000	DF	246

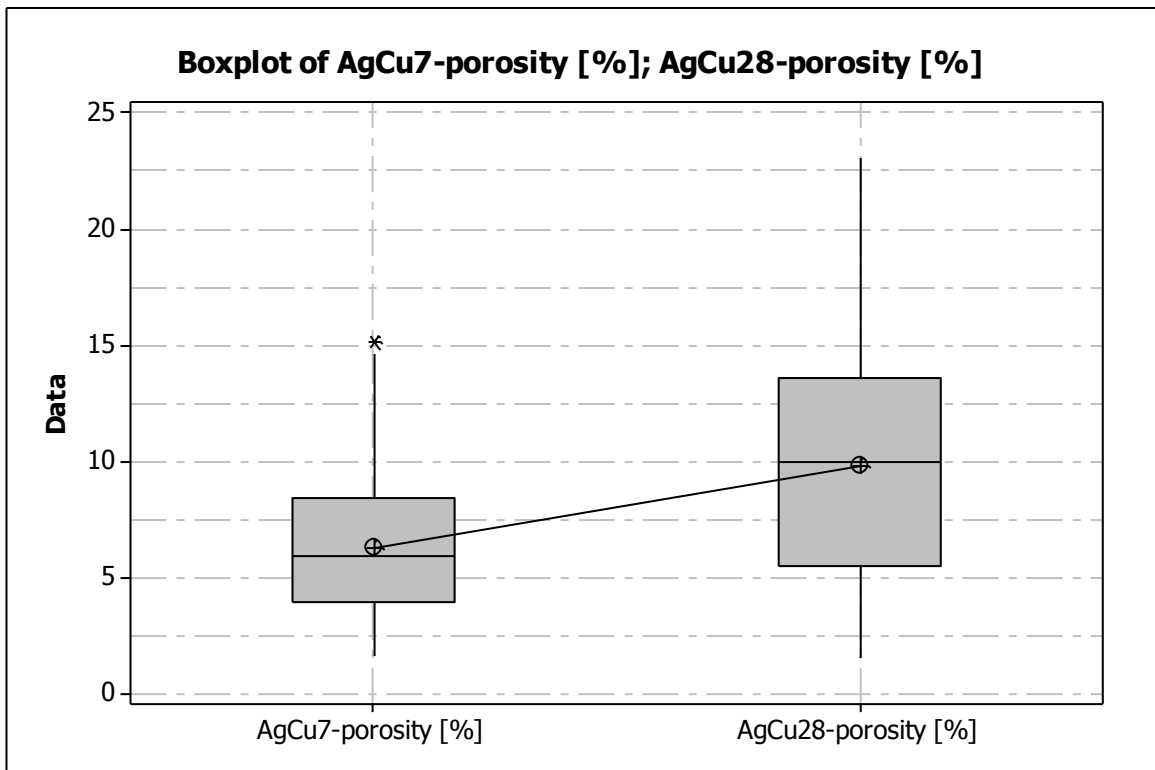


Figure 96: Boxplot of both materials

Figure 96 shows the boxplot of both samples and the comparison. The boxplots contain the minimum and maximum values of both distributions, the median and the first and third quartile. Figure 96 also displays the increase in means between both materials.

Besides the difference in mean porosity the microscopy analysis of the microsection showed that the diameters of the pores were larger for AgCu28 compared to AgCu7. For the best sample set of AgCu7, manufactured with 60 W, 10 μm spot distance and 20 μs pulse time, the five largest pores were measured with 110 μm , 99 μm , 93 μm , 84 μm , and 70 μm , respectively. The mean porosity for this parameter set was 2.45%. In comparison, the best sample set of AgCu28, manufactured with 70 W, 15 μm spot distance and 20 μs pulse time yielded a mean porosity of 4.29%. The five largest pores of sample ID 20 were measured with 159 μm , 123 μm , 92 μm , 89 μm , and 81 μm , respectively. The sample set with the highest porosity of AgCu7 was manufactured with 60 W, 10 μm spot distance and 60 μs pulse time. At sample ID 7, the five largest pores were measured with 144 μm , 136 μm , 102 μm , 97 μm , and 94 μm , respectively. Compared to that, the diameters of the parts with highest porosity of AgCu28 were measured with 251 μm , 218 μm , 215 μm , 201 μm , and 137 μm , respectively.

8.2 Process maps

As stated in the literature review part of this dissertation (see chapter 2), process maps were published by several researchers, e. g. Childs et al. [12], Zhang et. al. [61], Kruth et al.[55] or Khan and Dickens [39]. Childs et al. [12] detected either no fusion, little fusion or balling above a scan speed of approx. 22 mm/s for laser powers up to 200 W. Below approx. 10 mm/s, they detected continuous melt tracks. [12] For iron based powder, [55] Kruth et al. found that balling can be expected between 70 W and 100 W at scan speeds up to 100 mm/s. The melting window is much larger than that of Childs et al. [12] Compared to that, Khan and Dickens [39] found large areas of balling above a power level of 25 W and typical binding problems as weak sintering below that power level. The region with sufficient melting behavior is surrounded by areas with unstable melting behavior. [39]

Figure 97 shows the process map for AgCu7 whereas figure 98 shows the process map for AgCu28, both derived from the experiments described above. For AgCu7 and AgCu28, balling was detected above the minimum fusion line. Below that line, failed parts indicated that the binding energy was too low. The difference between AgCu7 and AgCu28 is that the minimum energy line is shifted to approximately 50 W for AgCu28 compared to AgCu7. For both materials, this threshold is increased compared to Khan and Dickens whose process window was limited to 50 W laser power. [39]

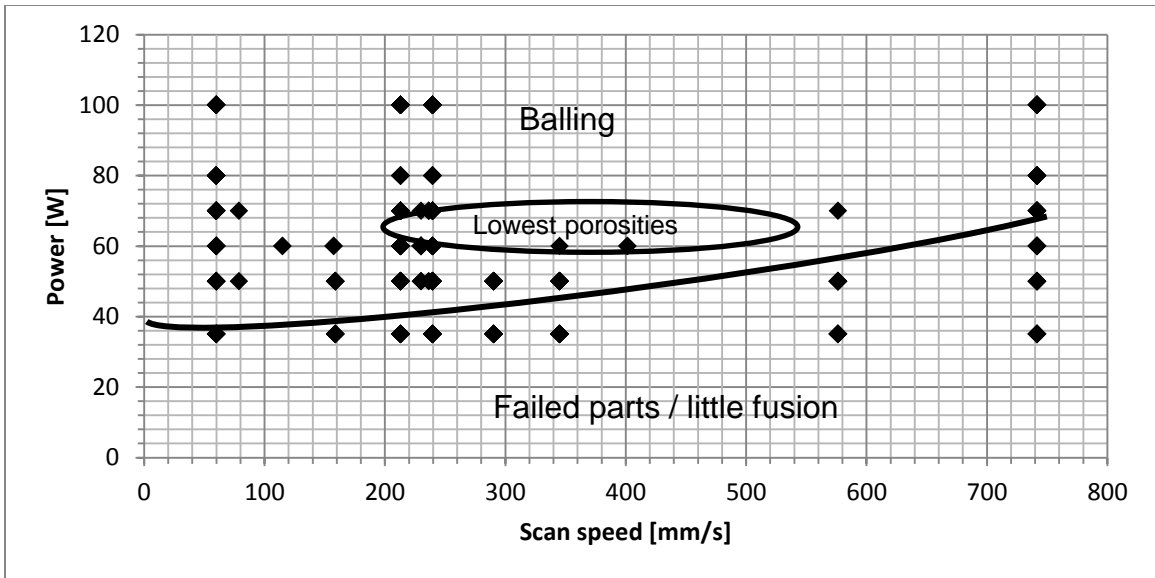


Figure 97: Process map of AgCu7

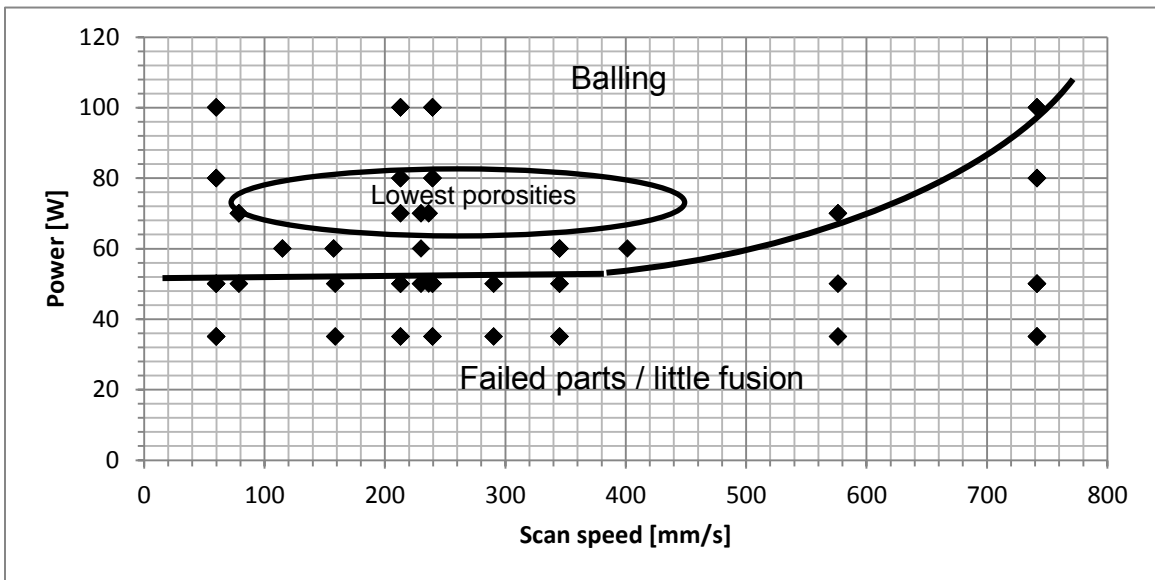


Figure 98: Process map of AgCu28

The location of the region of lowest porosities is comparable related to the line of separation between balling and failed parts for AgCu7 and AgCu28, but in general AgCu28 has a higher percentage of porosity than AgCu7. Future parameter combinations should be investigated near these regions of lowest porosities since high porosities were observed close to the borders of these

regions, indicating that the process window is not stable. These instabilities were also reported by Khan and Dickens [39] and might be related to the decreased absorptivity of gold and silver alloys compared to other materials.

In general, if the process maps for lower thermal conductivity and reflectivity materials (e.g. Childs et al. [12] and Kruth et al.[55]) are compared to higher thermal conductivity and reflectivity materials such as gold (Khan and Dickens [39]) or silver alloys (figure 97 and figure 98), it can be seen that the area for the good melting region is comparably small. Regions with severe balling problems are dominating. In order to overcome this, for highly reflecting and conducting materials, it is essential to minimize the balling effects with the methods that are already known such as optimized scan strategies or the minimization of remaining oxygen.

As explained in section 5.3, the scan speed is an artificial parameter. Since the derivation of the scan speeds for the other process maps mentioned above is not known, there might be an effect on the shape of the process maps as well. Future work might be necessary in order to analyze this.

9 SUMMARY AND FUTURE PERSPECTIVE, CONCLUSIONS

9.1 Summary and findings

This dissertation deals with the production of thin, hollow structures of silver alloys using the Selective Laser Melting (SLM) method. Parts of these alloys are required mainly by jewelry makers in order to produce complex free-form shaped objects with a minimum use of the precious material.

Since silver alloys are rarely used as material for additive manufacturing, the work needed to be based on fundamental investigations about making track structures, which again required redefining and optimizing the material data set of the machine. Therefore, the project is based on a theoretical “cornerstone” that is conducted based upon the elaborated literature research. Important information about silver as a base material, physical properties and its application were gathered. Silver is a unique material due to both its very high thermal conductivity and its high reflectivity.

For the experiments, commercial silver alloy powders were used. The selection encompassed AgCu7 and AgCu28. Therefore material qualification was necessary. The powder size distributions were measured to assure the results using two different physical methods (laser fraction and sedimentation). For AgCu7, two qualities of powder were used, coarse powder with a mean of

approx. 27 μm and fine powder with a mean of approx. 8 μm . The fine powder was separated from the coarse powder by sieving.

As a next step, a multi-track build with an overlap of approx. 30 μm was developed which resulted in dense objects with wall thicknesses of approx. 500 μm . Based on this, 3D objects like a hollow wedge were built and the surface was polished to indicate that the material can be utilized. A scaled bust of the Egyptian queen Nefertiti was made as a thin walled structure from silver alloy AgCu7.

The EDX analysis and SEM analysis of AgCu7 and AgCu28 showed that both powders had spherical morphologies and that the material consisted of silver and copper. Besides some background noise, additional elements like nitrogen or oxygen were not detected in a quantity that is noteworthy.

The next step was the investigation of the porosity using designed experiments. The porosity was investigated by the manufacturing of microsections. Different parameters were tested for optimizing the results. A problem was the repeatability as it was observed that the manufacturing of silver parts was less stable compared to other materials. One reason why production of parts failed was the back reflection that led to a shut-down of the laser source. Another approach to improve the results and to increase the repeatability was the usage of different powders.

Factorial designs were used for the screening experiments. The approach was to reduce the preexposure strategy and to find parameter sets without preexposure. Preexposure is a scanning strategy that consists of at least

two laser scans of the same surface. For AgCu7, this method was state of the art before this work was conducted. The findings of this dissertation were that data sets without preexposure led to successful parts as well. That means for practical applications that less energy can be used. Furthermore, scanning times can be saved which usually are directly related to costs.

Since silver is used as a conductive material and since solid parts can easily be cast, it was determined that thin, hollow structures would be investigated. Due to its comparably high price, silver parts are rarely manufactured using subtractive methods but are cast, or drawn as wire. Silver is usually not used for load-bearing purposes, since there are many materials available that can bear higher loads at much lower prices. Therefore, in addition to jewelry, potential future usage of silver parts using Selective Laser Melting will target thin, light weighting conductive paths, plates or strips. The influence of the build parameters on the porosity was an important question that was answered. Thin walls were manufactured, the porosity was measured and the parameters based on the results of the first track analysis were varied. The manufactured specimens were ground carefully and microsections were analyzed. The response surface method was used in order to determine statistical relationships between the main parameters power, pulse time, and spot distance. Response surface plots and contour plots were investigated.

The limitations of the response surface graphs are that the lowest values are located at the borders of the response surfaces. That means that the areas outside the graphs might contain local minimum values. An investigation of the

areas outside the response surfaces is recommended for future work. In particular, for low linear energy densities, the area between the region of lowest porosities from the response surface maps and an energy that led to insufficient binding needs to be investigated. For this reason, the response surface plots should be considered most accurate for parameter sets well within the borders.

The process maps were derived from both the full factorial screening experiments and the response surface data. The results showed that for the same data sets, the porosity of AgCu28 was significantly higher than the porosity of AgCu7. In fact, both materials were difficult to process. Since AgCu28 has a thermal conductivity of 3.25 W/(cm K) [123] and AgCu7 a thermal conductivity of maximum 3.8 W/(cm K)¹² [123], both materials conduct heat very quickly compared to other metals (see table 1). Due to the high reflectivity, less energy is absorbed compared to other materials (see figure 21). One way this could affect balling is that the combination of high thermal conductivity and high reflectivity causes the melt pool to cool very quickly and hence the geometry of the melt pool is different from that of lower thermal conductivity materials, leading to an increased tendency for balling and porosity. Due to the increased level of porosity for the eutectic material, this study indicates that there is no advantage for eutectic solidification in comparison to non-eutectic solidification. Although the melting point is lower, the threshold for successfully manufactured parts required a higher energy level for AgCu28 compared to AgCu7. One possible explanation is that the solidification of the melt pool without a mushy zone is disadvantageous

¹² Table value for AgCu5 due to deviation of EDX analysis

with respect to the wetting ability and recoiling behavior. The eutectic material cools down at a constant temperature whereas the non-eutectic material cools down at a decreasing temperature interval, and an increasing viscosity. During the cooling process, the surface tension decreases as well. The eutectic material solidifies at a constant temperature so there is little time for sufficient wetting of neighboring areas. For AgCu7, while cooling down the wetting ability might be better compared to AgCu28 because a larger area remains partially molten during solidification. Finally, the recoiling forces of the liquid material would seem to be lower for partially molten material. This combination of factors results in a decreased porosity for non-eutectic materials.

Since the processing of AgCu28 was not investigated before, this work is the first to show detailed processing characteristics for AgCu28. The binding behavior for lower laser powers between 35 W and 50 W shows that AgCu28 is not processable in regions where AgCu7 can be processed. With respect to the hypothesis that the lower melting point of the eutectic material compared to the non-eutectic would enable it to be processed at lower laser powers, this assumption was proven false and thus opens up new areas of research to explain the reasons why.

One new finding from this research was that, in addition to the percentage of porosity, the diameters of the pores in samples of AgCu28 were larger compared to AgCu7. Since many physical properties such as the load bearing behavior, fatigue behavior or the conductivity require a nearly

homogeneous material within desired ranges, this might limit the application of AgCu28 for certain tasks.

The process maps of both, AgCu7 and AgCu28 were not known before this work was conducted. The process maps can be used to guide future processing of silver-copper alloys using SLM. Wide areas of balling were detected. The scan speed versus power regions for least porosities are close to the regions for failed parts due to little fusion and thus there is a narrow process window for these materials, especially when compared to other materials such as iron based powders. The balling behavior leads to increased porosities as balling increases.

9.2 Future work

The work of this dissertation illustrates numerous possible avenues for further research and future work is necessary to fully understand the behavior of AgCu7 and AgCu28 materials. For instance, for this work the scan speed was calculated from the parameters pulse time and spot distance due to limitations of the machine, but the scan speed was applied spot by spot rather than continuously. Therefore, the effect of a continuous scanning strategy needs to be investigated. For that purpose, a different machine might be used. It can be expected that the interaction time between the laser and any location in the powder bed is different for geometric overlaps of laser spots (see figure 33) compared to a continuously moving laser beam. The effect of scan strategy and scan rate should be investigated using a different machine to fully understand the consequences of this difference.

A different machine might be equipped with a different powder distribution system such as a roller or a blade. Since it has been determined that the wiper system may have an effect on the quality of the powder bed, this relation to porosity needs to be investigated as well. The powder distribution system also affects the packing densities of the powder bed, which is another area for investigation in order to analyze the influence of the spreading behavior on the quality of the parts.

For the same parameter sets, the building of solid cubes should be investigated. Due to the different temperature profiles between melt pool, unmelted powder and solid tracks, the parameter sets could lead to different results. Therefore, more research would be necessary if larger components were the aim. Besides manufacturing strategies such as multiple exposures, the influence of higher laser powers would be of interest for further investigations. Furthermore, the manufacturing of conductive paths can be analyzed using the parameter sets that were uncovered in this work.

In summary, suggestions for future work include:

Same parameter sets

- Use of a different machine type,
 - With continuous beam scanning
 - Changes in scan rates
 - Changes in linear energy density
- Analysis of the powder flow behavior,

- Different powder distribution system (e.g. roller)
- Analysis of packing densities

Different parameter sets

- Variation of parameters which were held constant,
- Extension of the studied parameters to other regions,
- Increase in laser power,
- Manufacturing of solid volume parts,
- Analysis of conductivities, and
- Manufacturing of conductors.

REFERENCES

1. Gibson, I., D.W. Rosen, and B. Stucker, *Additive manufacturing technologies. rapid prototyping to direct digital manufacturing*, ed. Springer. 2010, New York, NY.
2. Gebhardt, A., et al. *Additive Manufacturing by Selective Laser Melting: The realizer desktop machine and its application for the dental industry*. in *6th International Conference on Laser Assisted Net Shape Engineering, LANE 2010, September 21, 2010 - September 24, 2010*. 2010. Erlangen, Germany: Elsevier.
3. Piller, F.T., *Profiting from mass customization: Success factors and the role of direct digital manufacturing*, in *Fraunhofer Direct Digital Manufacturing Conference (DDMC) 2012*: Berlin.
4. Gebhardt, A., *Generative Fertigungsverfahren. rapid prototyping - rapid tooling - rapid manufacturing*, ed. Hanser. 2007, München.
5. Meiners, W., *Direktes selektives Laser-Sintern einkomponentiger metallischer Werkstoffe*. Berichte aus der Lasertechnik, ed. Shaker. 1999, Aachen.
6. The Silver Institute. *Silver Facts: Silver in Industry*. 2011 [cited 2011 12-10]; Available from: http://www.silverinstitute.org/in_industry.php.
7. Glasschroeder, J., et al., *3D-Printing of Conductive Paths in Fraunhofer Direct Digital Manufacturing Conference (DDMC) 2012*: Berlin.
8. Hedges, M. and A.B. Marin, *3D Aerosol Jet Printing - Adding Electronics Functionality to RPRM*, in *Fraunhofer Direct Digital Manufacturing Conference (DDMC) 2012*: Berlin.
9. Berry, E., et al., *Preliminary experience with medical applications of rapid prototyping by selective laser sintering*. Medical Engineering and Physics, 1997. **19**(Compendex): p. 90-96.
10. Gebhardt, A., *Understanding Additive Manufacturing*. 2011, Cincinnati: Hanser Publications.
11. Quincieu, J., et al., *Case study: Selective laser sintering of the USUSat II small satellite structure*. Assembly Automation, 2005. **25**(Compendex): p. 267-272.
12. Childs, T.H.C., C. Hauser, and M. Badrossamay, *Mapping and modelling single scan track formation in direct metal selective laser melting*. CIRP Annals - Manufacturing Technology, 2004. **53**(1): p. 191-194.

13. Morgan, R.H., et al., *High density net shape components by direct laser re-melting of single-phase powders*. Journal of Materials Science, 2002. **37**(Compendex): p. 3093-3100.
14. Morgan, R., et al. *Direct Metal Laser Re-Melting (DMLR) of 316L Stainless Steel Powder Part 1: Analysis of Thin Wall Structures*. in *Solid Freeform Fabrication Symposium, Austin, TX*. 2001.
15. Morgan, R., et al. *Direct metal laser re-melting of 316L stainless steel powder. Part 2: analysis of cubic primitives*. in *Proceedings of the 12th Solid Freeform Fabrication Symposium*. 2001.
16. Wei, Q.S., et al. *Effects of the processing parameters on the forming quality of stainless steel parts by Selective Laser Melting*. in *2nd International Conference on Manufacturing Science and Engineering, ICMSE 2011, April 9, 2011 - April 11, 2011*. 2011. Guilin, China: Trans Tech Publications.
17. O'Neill, W., et al. *Investigation of short pulse Nd: YAG laser interaction with stainless steel powder beds*. in *Proc ICALEO 98, , Nov 16-19*. 1998. Orlando, FL, USA: Laser Institute of America.
18. O'Neill, W., et al., *Investigation on multi-layer direct metal laser sintering of 316L stainless steel powder beds*. CIRP Annals - Manufacturing Technology, 1999. **48**(Compendex): p. 151-154.
19. Tolosa, I., et al., *Study of mechanical properties of AISI 316 stainless steel processed by "selective laser melting", following different manufacturing strategies*. International Journal of Advanced Manufacturing Technology, 2010. **51**(Compendex): p. 639-647.
20. Jerrard, P.G.E., L. Hao, and K.E. Evans, *Experimental investigation into selective laser melting of austenitic and martensitic stainless steel powder mixtures*. Proceedings of the Institution of Mechanical Engineers, Part B (Journal of Engineering Manufacture), 2009. **223**(Copyright 2010, The Institution of Engineering and Technology): p. 1409-16.
21. Rombouts, M., et al., *Fundamentals of selective laser melting of alloyed steel powders*. CIRP Annals - Manufacturing Technology, 2006. **55**(1): p. 187-192.
22. Goel, A. and D. Bourell, *Electrochemical deposition of metal ions in porous laser sintered inter-metallic and ceramic preforms*. Rapid Prototyping Journal, 2011. **17**(Copyright 2011, The Institution of Engineering and Technology): p. 181-6.
23. Boeck, T. and A. Thess, *Marangoni-Konvektion in Flüssigmetallen*. Wissenschaftliche Zeitschrift der Technischen Universität Dresden, 1998. **47** (1998)(Heft 2): p. 92-94.
24. Boeck, T. and A. Thess, *Inertial Benard-Marangoni convection*. Journal of Fluid Mechanics, 1997. **350**: p. 149-175.

25. Dongdong, G., et al., *Selective Laser Melting of in-situ TiC/Ti5Si3 composites with novel reinforcement architecture and elevated performance*. Surface & Coatings Technology, 2011. **205**(10): p. 3285-92.
26. Facchini, L., et al., *Ductility of a Ti-6Al-4V alloy produced by selective laser melting of prealloyed powders*. Rapid Prototyping Journal, 2010. **16**(Compendex): p. 450-459.
27. Yasa, E., et al., *Charpy impact testing of metallic selective laser melting parts*. Virtual and Physical Prototyping, 2010. **5**(Compendex): p. 89-98.
28. Fischer, P., et al., *Sintering of commercially pure titanium powder with a Nd:YAG laser source*. Acta Materialia, 2003. **51**(6): p. 1651-62.
29. Zaw, H.M., et al., *Formation of a new EDM electrode material using sintering techniques*. Journal of Materials Processing Technology, 1999. **89-90**(Compendex): p. 182-186.
30. Zhu, H.H., L. Lu, and J.Y.H. Fuh, *Development and characterisation of direct laser sintering Cu-based metal powder*. Journal of Materials Processing Technology, 2003. **140**(1-3): p. 314-317.
31. Zhu, H.H., J.Y.H. Fuh, and L. Lu, *The influence of powder apparent density on the density in direct laser-sintered metallic parts*. International Journal of Machine Tools & Manufacture, 2007. **47**(2): p. 294-8.
32. German, R.M., *Powder metallurgy science*. 1984, New Jersey. 284.
33. Gu, D. and Y. Shen, *Balling phenomena during direct laser sintering of multi-component Cu-based metal powder*. Journal of Alloys and Compounds, 2007. **432**(1-2): p. 163-166.
34. Buchbinder, D., et al., *High Power Selective Laser Melting (HP SLM) of Aluminum Parts*. Physics Procedia, 2011. **12**(Part 1): p. 271-278.
35. Wang, F., *Mechanical property study on rapid additive layer manufacture Hastelloy X alloy by selective laser melting technology*. 2011(Compendex): p. 1-7.
36. Yadroitsev, I., et al., *Strategy of manufacturing components with designed internal structure by selective laser melting of metallic powder*. Applied Surface Science, 2007. **254**(4): p. 980-983.
37. Mumtaz, K.A., P. Erasenthiran, and N. Hopkinson, *High density selective laser melting of Waspaloy*. Journal of Materials Processing Technology, 2008. **195**(1-3): p. 77-87.
38. Khan, M.D., P.M., *Processing Parameters For Selective Laser Melting (SLM) Of Gold*. 2008: p. 278-289.
39. Khan, M. and P. Dickens, *Selective Laser Melting (SLM) of pure gold*. Gold Bulletin, 2010. **43**(2): p. 114-21.

40. Klotz, U.E., *Metallurgy and processing of coloured gold intermetallics - Part I: properties and surface processing*. Gold Bulletin, 2010. **43**(1): p. 4-10.
41. Fischer-Bühner, J., A. Basso, and M. Poliero, *Metallurgy and processing of coloured gold intermetallics — Part II: Investment casting and related alloy design*. Gold Bulletin, 2010. **43**(1): p. 11-20.
42. Kermanidis, A.T., et al., *Effects of temper condition and corrosion on the fatigue performance of a laser-welded Al-Cu-Mg-Ag (2139) alloy*. Materials & Design, 2010. **31**(Copyright 2010, The Institution of Engineering and Technology): p. 42-9.
43. Subramanian, P.R. and J.H. Perepezko, *Alloy phase diagrams*, in *ASM Handbook*, H. Baker, Editor. 1992, ASM International: Materials Park, Ohio. p. 2.28.
44. Beck, D.G., S.M. Copley, and M. Bass, *The constitution and phase stability of overlapping melt trails in Ag-Cu alloys produced by continuous laser melt quenching*. Metallurgical Transactions A (Physical Metallurgy and Materials Science), 1982. **13A**(11): p. 1879-89.
45. Wielage, B., et al., *Kontaktwerkstoffe auf Silberbasis - Gefüge und mechanische Eigenschaften*. Materialwissenschaft und Werkstofftechnik, 2008. **39**(12): p. 940-943.
46. Smith, D.R. and F.R. Fickett, *Low-temperature properties of silver*. Journal of Research of the National Institute of Standards and Technology, 1995. **100**(Copyright 1995, IEE): p. 119-71.
47. Gisario, A., M. Barletta, and R. Stancampiano, *On the interaction mechanisms between a high-power diode laser source and silver alloys: The case of aesthetic welding*. Optics and Lasers in Engineering, 2009. **47**(7-8): p. 821-830.
48. Wohlers, T., *Wohlers report - additive manufacturing and 3D printing state of the industry ; annual worldwide progress report*. 2007, Fort Collins, Colo.: Wohlers Associates.
49. Levy, G.N., R. Schindel, and J.P. Kruth, *Rapid manufacturing and rapid tooling with layer manufacturing (LM) technologies, state of the art and future perspectives*. CIRP Annals - Manufacturing Technology, 2003. **52**(Compendex): p. 589-609.
50. Levy, G.N. *The role and future of the Laser technology in the Additive Manufacturing environment*. in *6th International Conference on Laser Assisted Net Shape Engineering, LANE 2010, September 21, 2010 - September 24, 2010*. 2010. Erlangen, Germany: Elsevier.
51. Sreenivasan, R. and D.L. Bourell. *Sustainability study in selective laser sintering - an energy perspective*. in *Extraction and Processing Division Congress 2010, 14-18 Feb. 2010*. 2010. Warrendale, PA, USA: Minerals, Metals and Materials Society.

52. Yadroitsev, I. and I. Smurov. *Selective laser melting technology: From the single laser melted track stability to 3D parts of complex shape*. in *6th International Conference on Laser Assisted Net Shape Engineering, LANE 2010, September 21, 2010 - September 24, 2010*. 2010. Erlangen, Germany: Elsevier.
53. Gusarov, A.V. and E.P. Kovalev, *Model of thermal conductivity in powder beds*. Physical Review B (Condensed Matter and Materials Physics), 2009. **80**(2): p. 024202 (15 pp.).
54. Simchi, A., *The role of particle size on the laser sintering of iron powder*. Metallurgical and Materials Transactions B (Process Metallurgy and Materials Processing Science), 2004. **35B**(5): p. 937-48.
55. Kruth, J.P., et al., *Binding mechanisms in selective laser sintering and selective laser melting*. Rapid Prototyping Journal, 2005. **11**(Copyright 2005, IEE): p. 26-36.
56. Simchi, A., *Direct laser sintering of metal powders: Mechanism, kinetics and microstructural features*. Materials Science & Engineering A (Structural Materials: Properties, Microstructure and Processing), 2006. **428**(1-2): p. 148-58.
57. Yadroitsev, I. and I. Smurov. *Surface morphology in selective laser melting of metal powders*. in *6th International WLT Conference on Lasers in Manufacturing, LiM, May 23, 2011 - May 26, 2011*. 2011. Munich, Germany: Elsevier.
58. Yadroitsev, I., et al., *Single track formation in selective laser melting of metal powders*. Journal of Materials Processing Technology, 2010. **210**(Compendex): p. 1624-1631.
59. Chandrasekhar, S., *Hydrodynamic and hydromagnetic stability*. 1961: Oxford Clarendon Press.
60. Kruth, J.P. and S. Kumar, *Statistical analysis of experimental parameters in selective laser sintering*. Advanced Engineering Materials, 2005. **7**(Copyright 2006, IEE): p. 750-5.
61. Zhang, B., H. Liao, and C. Coddet, *Effects of processing parameters on properties of selective laser melting Mg-9%Al powder mixture*. 2011.
62. Chatterjee, A.N., et al., *An experimental design approach to selective laser sintering of low carbon steel*. Journal of Materials Processing Technology, 2003. **136**(Compendex): p. 151-157.
63. Hsin-Te, L. and S. Jie-Ren, *Optimization on selective laser sintering of metallic powder via design of experiments method*. Rapid Prototyping Journal, 2007. **13**(Copyright 2007, The Institution of Engineering and Technology): p. 156-62.
64. Bacchewar, P.B., S.K. Singhal, and P.M. Pandey, *Statistical modelling and optimization of surface roughness in the selective laser sintering process*. Proceedings of the Institution of Mechanical Engineers, Part B (Journal of Engineering Manufacture), 2007. **221**(Copyright 2007, The Institution of Engineering and Technology): p. 35-52.

65. Singh, A.K. and R.S. Prakash, *DOE based three-dimensional finite element analysis for predicting density of a laser-sintered part*. Rapid Prototyping Journal, 2010. **16**(Copyright 2010, The Institution of Engineering and Technology): p. 460-7.
66. Kechagias, J., *Investigation of LOM process quality using design of experiments approach*. Rapid Prototyping Journal, 2007. **13**(Compendex): p. 316-323.
67. Yadroitsev, I., P. Bertrand, and I. Smurov, *Parametric analysis of the selective laser melting process*. Applied Surface Science, 2007. **253**(Copyright 2007, The Institution of Engineering and Technology): p. 8064-9.
68. Singh, A.K. and R.S. Prakash, *Response surface-based simulation modeling for selective laser sintering process*. Rapid Prototyping Journal, 2010. **16**(Copyright 2010, The Institution of Engineering and Technology): p. 441-9.
69. Raghunath, N. and P.M. Pandey, *Improving accuracy through shrinkage modelling by using Taguchi method in selective laser sintering*. International Journal of Machine Tools and Manufacture, 2007. **47**(Compendex): p. 985-995.
70. Dingal, S., et al., *The application of Taguchi's method in the experimental investigation of the laser sintering process*. The International Journal of Advanced Manufacturing Technology, 2008. **38**(9): p. 904-914.
71. Matsumoto, M., et al., *Finite element analysis of single layer forming on metallic powder bed in rapid prototyping by selective laser processing*. International Journal of Machine Tools and Manufacture, 2002. **42**(Compendex): p. 61-67.
72. Shiomi, M. and K. Osakada, *Flexible manufacturing of metallic products by selective laser melting of powder*. International Journal of Machine Tools & Manufacture, 2006. **46**(Copyright 2006, The Institution of Engineering and Technology): p. 1188-93.
73. Zaeh, M.F. and G. Branner, *Investigations on residual stresses and deformations in selective laser melting*. Production Engineering, 2010. **4**(Copyright 2011, The Institution of Engineering and Technology): p. 35-45.
74. Kolossov, S., et al., *3D FE simulation for temperature evolution in the selective laser sintering process*. International Journal of Machine Tools & Manufacture, 2004. **44**(Copyright 2004, IEE): p. 117-23.
75. Neela, V. and A. De, *Three-dimensional heat transfer analysis of LENSTM process using finite element method*. International Journal of Advanced Manufacturing Technology, 2009. **45**(Compendex): p. 935-943.
76. Hu, D. and R. Kovacevic, *Modelling and measuring the thermal behaviour of the molten pool in closed-loop controlled laser-based additive manufacturing*. Proceedings of the Institution of Mechanical Engineers, Part B (Journal of Engineering Manufacture), 2003. **217**(Copyright 2003, IEE): p. 441-52.
77. Khailov, A.N., et al., *Nondestructive testing of mechanical characteristics of aluminum alloys on the basis of their electrical conductivity*. Russian Journal of

- Nondestructive Testing, 2006. **42**(Copyright 2007, The Institution of Engineering and Technology): p. 425-42.
78. Lorente, J.A., et al. *Single part microwave filters made from selective laser melting*. in *2009 European Microwave Conference (EuMC), 29 Sept.-1 Oct. 2009*. 2009. Piscataway, NJ, USA: IEEE.
 79. Lin, J.C. and C.Y. Wang, *Effect of surface properties of silver powder on the sintering of its thick-film conductor*. Materials Chemistry and Physics, 1996. **45**(3): p. 253-261.
 80. Heringhaus, F., et al., *On the optimization of the microstructure in powder metallurgical Ag-SnO₂-In₂O₃ contact materials*. Zeitschrift fuer Metallkunde/Materials Research and Advanced Techniques, 2001. **92**(Compendex): p. 784-787.
 81. Ivers-Tiffée, E. and W.v. Münch, *Werkstoffe der Elektrotechnik (Engl: "Materials of Electric Engineering")*. 10., überarb. und erw. Aufl. ed. 2007, Wiesbaden: Teubner. VIII, 266 S. : zahlr. graph. Darst.
 82. Häberle, G., *Tabellenbuch Elektrotechnik*. Vol. 20. 2003: Verlag Europa-Lehrmittel. 442.
 83. finanzen.net GmbH. *Langfristiger Silberpreischart 10 Jahreschart* finanzen.net. 2012 [cited 2012 25-03]; Available from: <http://www.finanzen.net/rohstoffe/silberpreis/Chart>.
 84. finanzen.net GmbH. *Langfristiger Kupferpreischart 10 Jahreschart* finanzen.net. 2012 [cited 2012 25-03]; Available from: <http://www.finanzen.net/rohstoffe/kupferpreis/Chart>.
 85. finanzen.net GmbH. *Langfristiger Silberpreischart 10 Jahreschart* finanzen.net. 2013; Available from: <http://www.finanzen.net/rohstoffe/silberpreis/Chart>.
 86. finanzen.net GmbH. *Langfristiger Kupferpreischart 10 Jahreschart* finanzen.net. 2013; Available from: <http://www.finanzen.net/rohstoffe/kupferpreis/Chart>.
 87. Vogel, H., *Mechanismen der elektrischen Leitung*, in *Gehrtsen Physik*. 1999, Springer: Heidelberg. p. 329.
 88. *VDI-Wärmeatlas*. 10. ed. 2006, Berlin [u.a.]: Springer.
 89. *Thermal conductivity of metals and semiconductors as a function of temperature*, in *CRC handbook of chemistry and physics. 84th edition*. 2003, CRC Press: Washington, DC, USA. p. 12-221.
 90. *Electrical Resistivity of pure metals*, in *CRC handbook of chemistry and physics. 84th edition*. 2003, CRC Press: Washington, DC, USA. p. 12-45-46.
 91. Tolochko, N.K., et al., *Absorptance of powder materials suitable for laser sintering*. Rapid Prototyping Journal, 2000. **6**(3): p. 155-160.

92. *Thermal and physical properties of pure metals*, in *CRC handbook of chemistry and physics*. 84th edition. 2003, CRC Press: Washington, DC, USA. p. 12-219 - 12-220.
93. Robertson, A.R., *Precious Metals and Their Uses in ASM Handbook: Properties and Selection: Nonferrous Alloys and Special-Purpose Materials*. 2000. p. Table 1 Selected properties of precious metals
94. *Property Comparison Tables: Hardness and Tensile Properties in ASM Handbook, Mechanical Testing and Evaluation*. 2000.
95. Hötter, J.-S., *Betriebsanleitung ReaLizer SLM 50 ("User manual, internal Document of FH Aachen")* 2010, Aachen University of Applied Sciences. p. 50.
96. Realizer GmbH. *SLM 50 | Rapid Prototyping Verfahren von ReaLizer*. 2011; Available from: <http://www.realizer.com/startseite/slm-maschinen/slm-50>.
97. Simchi, A. and H. Pohl, *Effects of laser sintering processing parameters on the microstructure and densification of iron powder*. Materials Science & Engineering A (Structural Materials: Properties, Microstructure and Processing), 2003. **A359**(1-2): p. 1 pp.
98. Gibson, I., D.W. Rosen, and B. Stucker, *Powder Bed Fusion Process*, in *Additive manufacturing technologies rapid prototyping to direct digital manufacturing*, Springer, Editor. 2010, Springer: New York, NY. p. 103-142.
99. Castle Island Co. *Commercial Rapid Prototyping System Manufacturers and Technology Providers*. 2012 [cited 2012 03-28]; Available from: http://www.additive3d.com/com3_lks.htm.
100. Kattner, U. *Ag-Cu System*. 2003 [cited 2011 12-21]; Available from: http://matdl.org/repository/eserv/matdl:539/web_agcu-w.jpg.
101. Digilov, R.M., *Prediction of surface properties of metals from the law of corresponding states*. Journal of Crystal Growth, 2003. **249**(1-2): p. 363-371.
102. Micromeritics Instrument Corporation. *Saturn DigiSizer II Micromeritics*. 2012 [cited 2012 03-18]; Available from: <http://micromeritics.com/Product-Showcase/Saturn-DigiSizer-II.aspx>, .
103. Micromeritics Instrument Corporation. *SediGraph 5120 Micromeritics*. 2012 [cited 2012 03-18]; Available from: <http://micromeritics.com/Product-Showcase/SediGraph-5120.aspx>.
104. Rajaratnam, P., *Silberne Zukunft 20120113 (workgroup status report)*, 2012, Aachen University of Applied Sciences.
105. Hötter, J.-S., *Silberne Zukunft 20111124 (workgroup status report)*, 2011, Aachen University of Applied Sciences.
106. Hötter, J.-S., *Silberne Zukunft 20111220 (workgroup status report)*, 2011, Aachen University of Applied Sciences.

107. Hötter, J.-S., *Silberne Zukunft 20111209 (workgroup status report)*, 2011, Aachen University of Applied Sciences.
108. Hötter, J.-S., *Silberne Zukunft 20111207 (workgroup status report)*, 2011, Aachen University of Applied Sciences.
109. Hötter, J.-S., *Silberne Zukunft 20111130 (workgroup status report)*, 2011, Aachen University of Applied Sciences.
110. Gebhardt, A., et al., *Numerical and Experimental Investigation of Selective Laser Melting of Silver*, in *Fraunhofer Direct Digital Manufacturing Conference (DDMC) 2012* 2012: Berlin.
111. Gebhardt, A., *Analysis, Replication and Commercialization of cultural heritage artifacts by Additive Manufacturing*, in *EuroMed2010 – 3rd International Conference Dedicated to Digital Cultural Heritage* 2010: Limassol, Cyprus. p. P-129 ff.
112. Gebhardt, A., et al., *Prozessoptimierung des SLM-Prozesses mit hoch-reflektiven und thermisch sehr gut leitenden Materialien durch systematische Parameterfindung und begleitende Simulationen.*, in *Rapid Tech 2012* 2012: Erfurt.
113. Beuth Verlag GmbH, *DIN EN ISO 4287:2010-07 -Geometrical Product Specifications (GPS) - Surface texture: Profile method - Terms, definitions and surface texture parameters (ISO 4287:1997 + Cor 1:1998 + Cor 2:2005 + Amd 1:2009); German version EN ISO 4287:1998 + AC:2008 + A1:2009*, 2010.
114. ITW Test & Measurement GmbH. *Safety Data Sheet 1907/2006/EC - REACH (GB) VariDur Liquid*. 2012 [cited 2013 03-07]; Available from: http://www.buehler.co.uk/fileadmin/user_upload/pdf/msds/english/VariDur_Liquid_389137_S_gb_gb.pdf.
115. ITW Test & Measurement GmbH. *Safety Data Sheet 1907/2006/EC-REACH (GB) VariDur 200 Powder*. 2012; Available from: http://www.buehler.co.uk/fileadmin/user_upload/pdf/msds/english/VariDur_200_Powder_388466_S_gb_gb.pdf.
116. Keyence Corporation. *VHX-100 Digital Microscope - KEYENCE*. 2013; Available from: <http://www.keyence.co.uk/products/microscope/microscope/vhx100/vhx100.php>.
117. Montgomery, D.C., *162-206 Factorial Experiments*, in *Design and Analysis of Experiments*. 2009, Wiley: Hoboken, NJ. p. 162-206.
118. Montgomery, D.C., *65-75 Analysis of Variance - Analysis of the Fixed Effects Model*, in *Design and Analysis of Experiments*. 2009, Wiley: Hoboken, NJ. p. 65-75.

119. Montgomery, D.C., *75-83 Analysis of Variance - Model Adequacy Checking*, in *Design and Analysis of Experiments*. 2009, Wiley: Hoboken, NJ. p. 75-83.
120. Montgomery, D.C. and G.C. Runger, *418-419 Coefficient of Determination (R^2)*, in *Applied statistics and probability for engineers*. 2007, Wiley ; Chichester : John Wiley [distributor]: Hoboken, N.J. p. 418-419.
121. Montgomery, D.C. and G.C. Runger, *456-458 Test for Significance of Regression*, in *Applied statistics and probability for engineers*. 2007, Wiley ; Chichester : John Wiley [distributor]: Hoboken, N.J. p. 456-458.
122. Montgomery, D.C., *417-485 Response Surface Methodology*, in *Design and Analysis of Experiments*. 2009, Wiley: Hoboken, NJ. p. 417-485.
123. Vinaricky, E., *Datenbuch der elektrischen Kontakte : Kontaktwerkstoffe, Halbzeuge (Engl. translation: "Data book of electrical contacts: contact materials, pre-products")*. 2009, Stieglitz Verlag: Mühlacker. p. 51-61.
124. Retsch GmbH. *Vibratory-Sieve-Shaker-AS-200-basic.pdf*. 2013 [cited 2013 04-20]; Available from: <http://www.retsch.com/products/sieving/sieve-shakers/as-200-basic/function-features/>.
125. TLS Technik GmbH & Co. Spezialpulver KG. *The EIGA Process*. 2012 [cited 2012 03-17]; Available from: http://www.tls-technik.de/e_2.html.
126. TLS Technik GmbH & Co. Spezialpulver KG, *Crucible Free Melting*, in *information provided by Norbert Ludwig, TLS 2012*.
127. *Powder metal technologies and applications*. 1. print. ed. ASM Metals Handbook. Vol. 7. 1998. XV, 1146 S. Ill., graph. Darst.

Sketches and illustrations were produced using MINITAB 16.1 (Minitab Inc.), Maple 16 (Maplesoft), Autodesk Inventor Professional 2012, GIMP 2.8, and the Microsoft office package (Word 2010, Excel 2010, Power Point 2010).

The models were calculated using the following system:

ASUS notebook P50IJ/P81IJ series, 4 GB RAM, Pentium Dual-Core T4500 CPU, 2.3 GHz, operating system: Windows 7 Home Premium, 64 bit.

APPENDICES

Symbols and explanations

Table 47: Chemical elements

Symbol	Explanation
Ag	silver
Au	gold
C	carbon
Cu	copper
Fe	iron
Ge	germanium
Nd	neodymium
O ₂	oxygen
P	phosphor
S	sulphur
Si	silicon
Sn	tin
Ti	titanium
W	tungsten

Table 48: Greek letters

Symbol	Explanation
$\beta_1, \beta_2, \beta_k$	Regression coefficients first order model
$\beta_0, \beta_{ii}, \beta_{ij}$	Regression coefficients second order model
α	Thermal diffusivity
ϵ	Error
γ_{LV}	Surface tension
λ	Wave length, thermal conductivity
ν	Wave number
ρ	Density
ρ_L	Density of large powder diameter
ρ_s	Density of small powder diameter
η	Dynamic viscosity, coupling efficiency
σ	electical conductivity
ψ	Factor for energy input parameters

τ_p Pulse duration

Table 49: Units

Symbol	Explanation
°C	degree Celsius
μin	micro inch
μm	micrometer
μΩ	micro Ohm
cm	centimeter
dT/dr	temperature gradient
g	gram
GPa	Giga Pascal
HB	Brinell hardness
in	inch
K	Kelvin
kJ	kilo Joule
l / min	liter per minute
mm	millimeter
MPa	Mega Pascal
nm	nano meter
RPM	Rounds per minute
s	second
S/m	Siemens/meter
W	Watt

Table 50: Abbreviations

Symbol	Explanation
3D	three-dimensional
A	Absorption
A_b	Absorptivity
a	constant
A_b	absorptivity
ANOVA	Analysis of variance
approx.	approximately
ASTM	American Society for Testing and Materials
CAD	Computer Aided Design
CDF	Cumulative Distribution Function
CO ₂	carbon dioxide
D	Diameter

Symbol	Explanation
d	Beam diameter, layer thickness
cw	continuous wave
DDMC	Direct Digital Manufacturing Conference
DIN	Deutsches Institut für Normung (German Institute for Standardization)
DoE	Design of Experiments
e	elementary charge
E	Extinction
e_{ij}^{\wedge}	random error
e.g.	exempli gratia (for example)
EDM	electrical discharge machining
EDX	energy dispersive X-ray spectroscopy
EOS	Electro Optical Systems, EOS, GmbH, www.eos.info
e_{ij}	residuals
et al.	et alii (and others)
etc.	et cetera (and more)
FEA	Finite Elements Analysis
FEM	Finite Elements Method
GSM	Global System for Mobile Communications
h	Hatch distance
i	Treatment, index
ILT	Fraunhofer-Institut für Lasertechnik, www.ilt.fraunhofer.de
I_{plasma}	estimated empirical plasma formation threshold
I	Intensity of the transmitted light
I_0	Initial intensity
ISO	International Organization for Standardization
j	Observation, index
k	Boltzmann-Constant
L	Length of the melt pool
LBAM	Laser-based additive manufacturing
LENS	Laser-engineered net shaping
Ma	Marangoni effect
min	minimum
n	Number of data points
NID	Normally and independently distributed
NIR	Near Infrared
P_0, P	Laser power
PLC	programmable logic controller
PMMA	Polymethyl Methacrylate
p	Number of terms in the model
P_{rec}	recoil pressure

Symbol	Explanation
Q-factor	Gaussian failure integral
Q	Laser energy density
r_b	laser beam radius
RF	Radio Frequency
R^2	Ratio of Sum of Squares
RSM	Response Surface Method
SEM	Scanning electron microscope
SLM	Selective Laser Melting
SS	Sum of Squares
SS_E	Sum of Squares of the error
SS_T	Total sum of squares
$SS_{\text{Treatment}}$	Sum of squares of the treatments
T	Transmission, Temperature
t_p	pulse duration
t	time
v	Scan speed
v_{plasma}	Plasma speed
v^*	Scan rates
W	Width
W_p	Width of the weld pool
wt	weight
x_i, x_j	Level index i and level index j
\hat{y}_{ij}	estimated observation
YAG	yttrium aluminum garnet
y_{ij}	current observation (jth observation from factor level i)
$\bar{y}_{..}$	Grand average of all observations
$\bar{y}_{i.}$	Average of the observations under ith treatment

Narrow paths

In order to show the usability of this technology, a Louisville Minerva batch was manufactured.

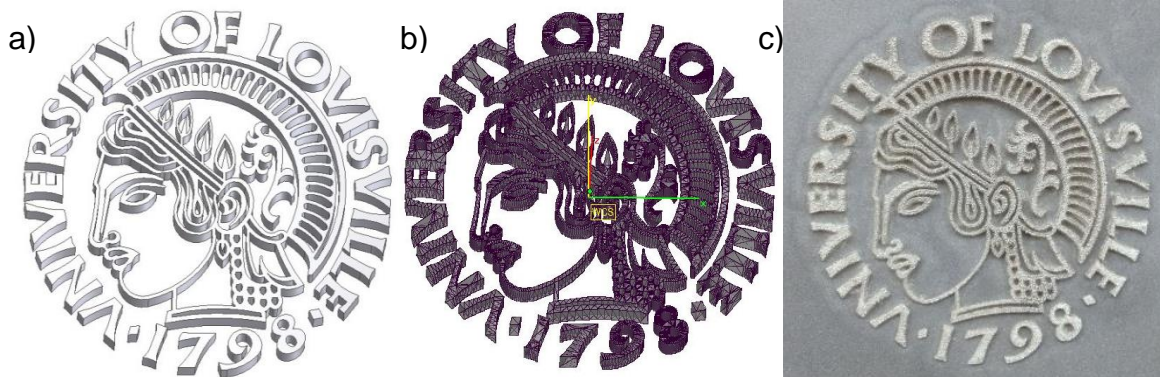


Figure 99: University of Louisville Logo - a) CAD File, b) STL File c) manufactured Minerva batch

The Minerva batch was manufactured using a stainless steel base plate and AgCu7 as material. The Minerva was modeled as a CAD file (Autodesk Inventor, figure 99 a)). This CAD file was transformed to a STL file, (figure 99 b)) that shows the vectors and the contours. The manufactured batch was printed directly onto the base plate without supports (figure 99 c)). Figure 100 shows details of the manufactured paths. It can be imagined that printed circuits can be manufactured in a similar manner.



Figure 100: Manufactured University of Louisville Minerva batch a) as printed b) eyes 20 x magnification c) and d) details 20 x magnification

Selective Laser Melting process

The next picture shows the steps that are necessary to produce a part using the Selective Laser Melting process.

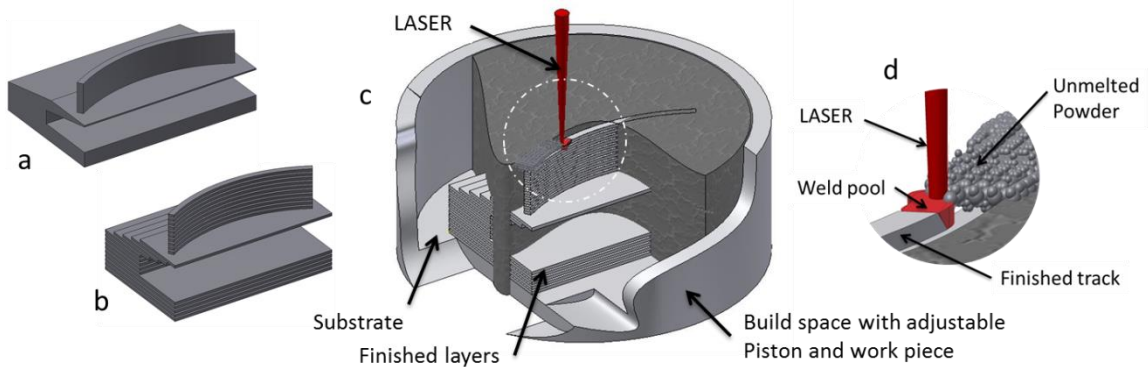


Figure 101: Scheme of Selective Laser Melting process

The parts are manufactured by use of a laser source that is focused and scanned via a powder bed. The geometry from a CAD data file is sliced and applied layer-by-layer onto the powder bed. A powder spreading unit (usually a wiper or roller) smooths the first layer right before the laser selectively melts the first tracks. Scanning distinguishes between boundary (outer lines), offset lines, and hatch scans (fillings). The surplus material (unmelted powder) can be reused. Figure 101 shows the main procedure whereas figure 102 shows the geometrical build parameter.

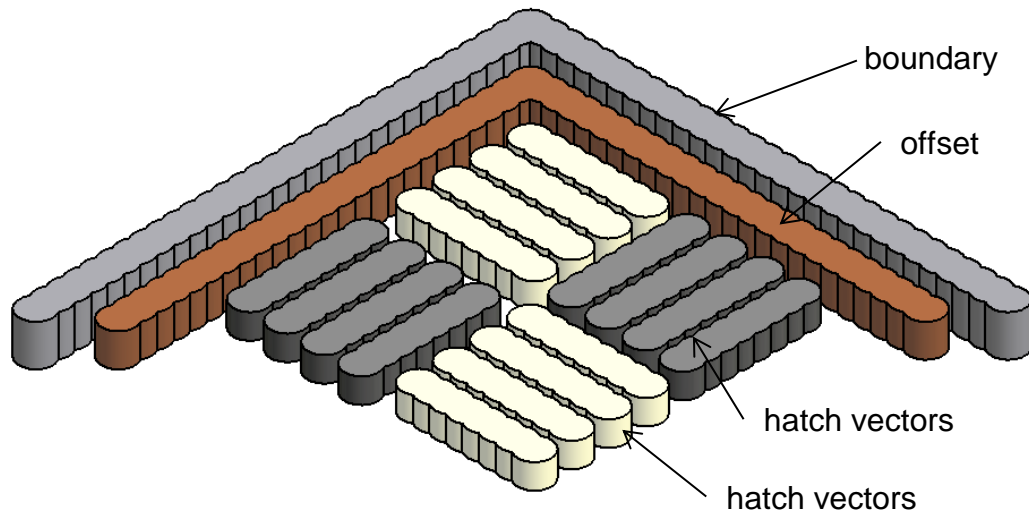


Figure 102: Boundary, offset and hatch vectors

Measurement of laser power

The laser power output was calibrated using a power detector. The power detector was placed in the build chamber. Figure 103 depicts the calibration curve, showing the ideal power output as set-up parameters (dot-dashed line). The solid black line shows the measured power in the build chamber. Some losses due to the lens system and output losses can be expected. The accuracy in the higher region above 50 W shows that the losses are comparably small. Please note that the laser source is a 100 W laser source, but it is possible to set higher laser outputs using the interface. The measurement shows that 100 W is both the nominal and true power threshold.

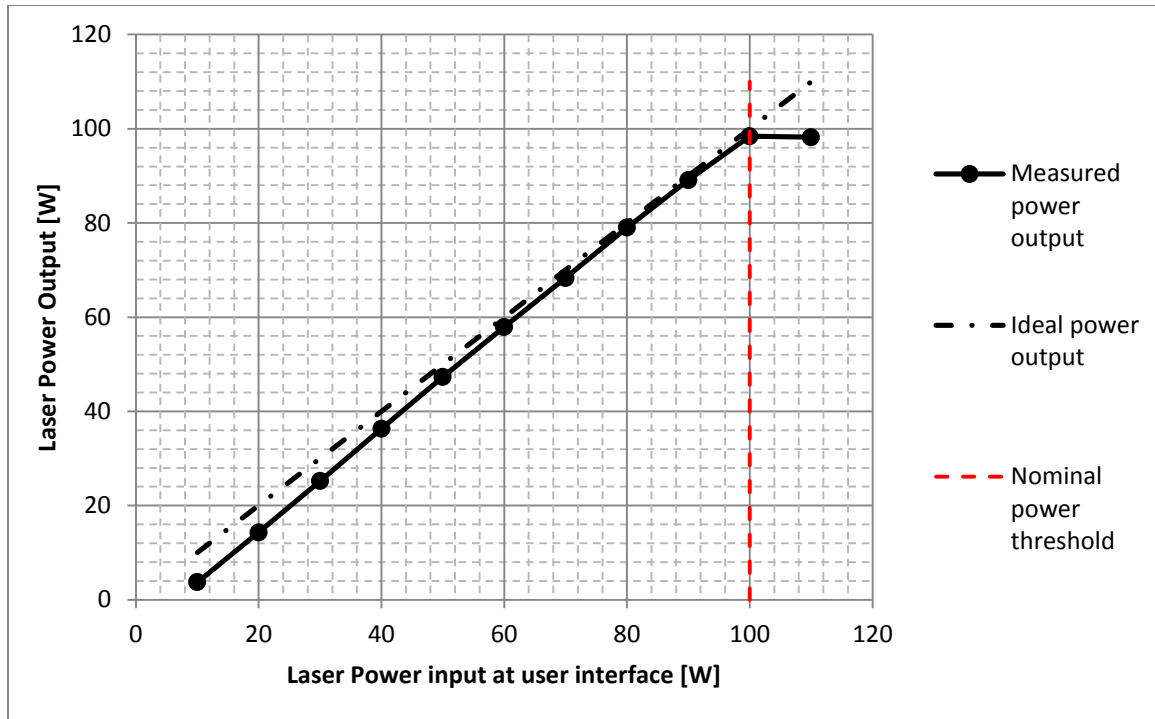


Figure 103: Calibration of laser power [106]

Preparation of powder for additional test runs

After the conduction of a test series, the powder material has to be cleaned and prepared for further usage. A Retsch vibratory sieve shaker AS 200 was used which has a feed capacity of 3 kg. [124] According to the particle size distribution, for AgCu7 a 63 μm test sieve was used, whereas for AgCu28, a 45 μm test sieve was used. To prevent any contaminations, individual sieves for each material were used.



Figure 104: Vibratory sieve shaker with 45 µm test sieve

Manufacturing of silver powder

Spherical silver powder is produced using a gas atomizer, mainly consisting of a melt chamber and a cooling tower. A rotating material rod serves as electrode and is heated up using an inductive melt head. Therefore, the electrode needs to be rotated. The molten material hits a gas nozzle that is shielded by an inert gas stream. The liquid droplets are sprayed and chilled down in a cooling tower and finally collected in a powder tray. Figure 105 shows the fundamental principle of the powder manufacturing process. [125-127]

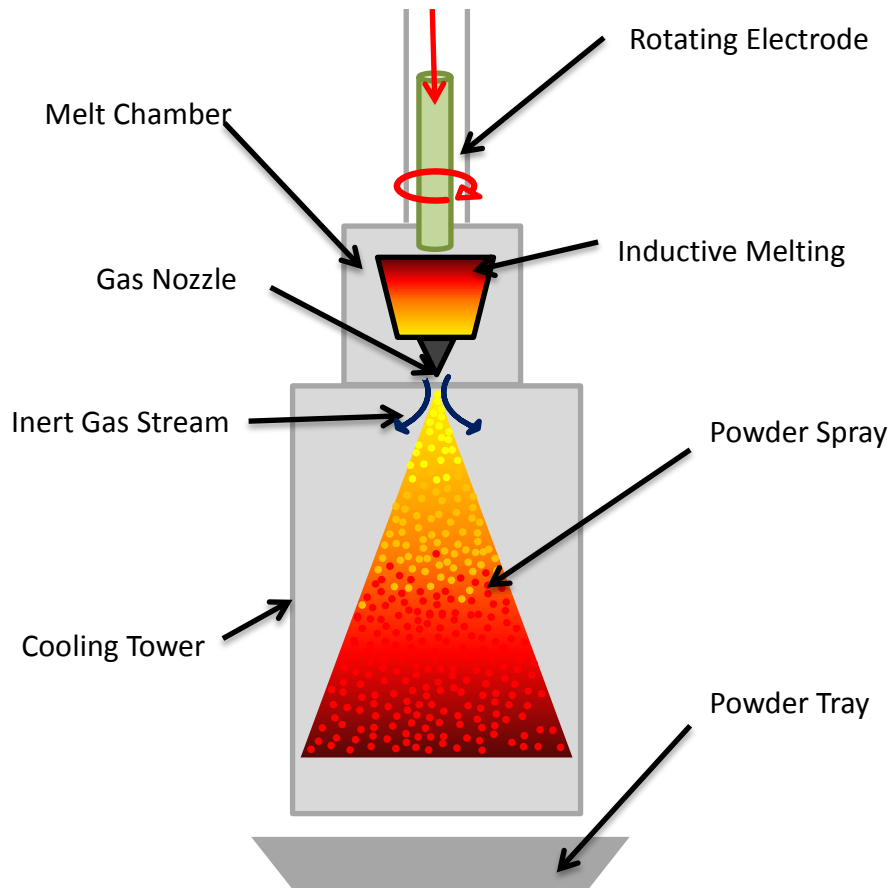


Figure 105: Scheme of the silver powder manufacturing process [125-127]

Comparison of dimensions

For a better understanding of the dimensions that are mentioned in this work, figure 106 might be helpful:

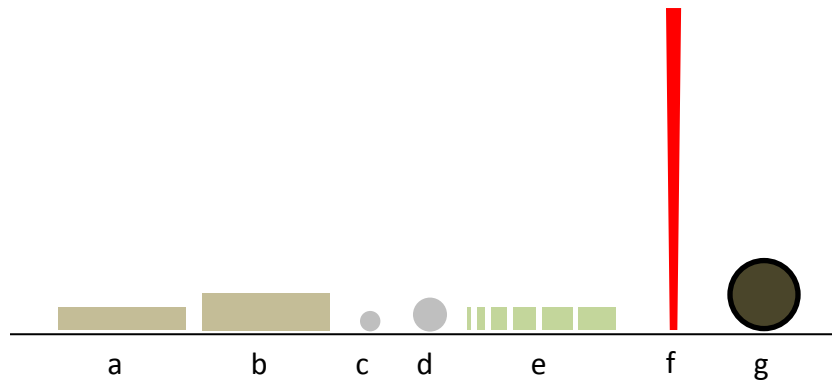


Figure 106: Proportional comparison of dimensions

Symbol (a) shows a 30 μm layer, whereas (b) shows a 50 μm layer. Circles (c) and (d) show 27 μm and 45 μm powder diameters, respectively. Next symbol (e) shows the hatch distance, increasing from 5 μm ; 10 μm ; 20 μm , 30 μm , 40 μm , to finally 50 μm . The red line (f) represents a focused laser beam with 20 μm spot diameter. In comparison, the last circle (g) depicts a cross section through a human hair, sized approximately 90 μm .

CURRICULUM VITAE

NAME: Harald Rieper

ADDRESS: Kruppstr. 14
D-52072 Aachen
Germany

DOB Moenchengladbach, Germany, September 21, 1979

EDUCATION & TRAINING Dipl.-Ing. (FH), Mechanical Engineering
Aachen University of Applied Sciences, Aachen, Germany,
2000 – 2006

IWE, International Welding Engineer,
SLV Duisburg, Germany,
2003

MBA
Aachen University of Applied Sciences, Aachen, Germany,
2006-2008

PHD student
University of Louisville, KY, USA
Since 2009

Design Engineer, JHT, Hückelhoven, Germany
2006-2007

Head of research and development, JHT, Hückelhoven
2008 -2010

Authorized signatory, JHT, Geilenkirchen
Since 2010

AWARDS

Medal of honor, best student

Aachen University of Applied Sciences, Aachen, Germany,
2006

PROFESSIONAL
SOCIETIES

DVS Deutscher Verband für Schweißen und verwandte Verfahren
(German Welding Association)

VDI Verein Deutscher Ingenieure
(German Society of Engineers)